Single Molecule Delivery and Detection into Crowded Environment with a Solid-State Nanopore

Chi Cheng Chau

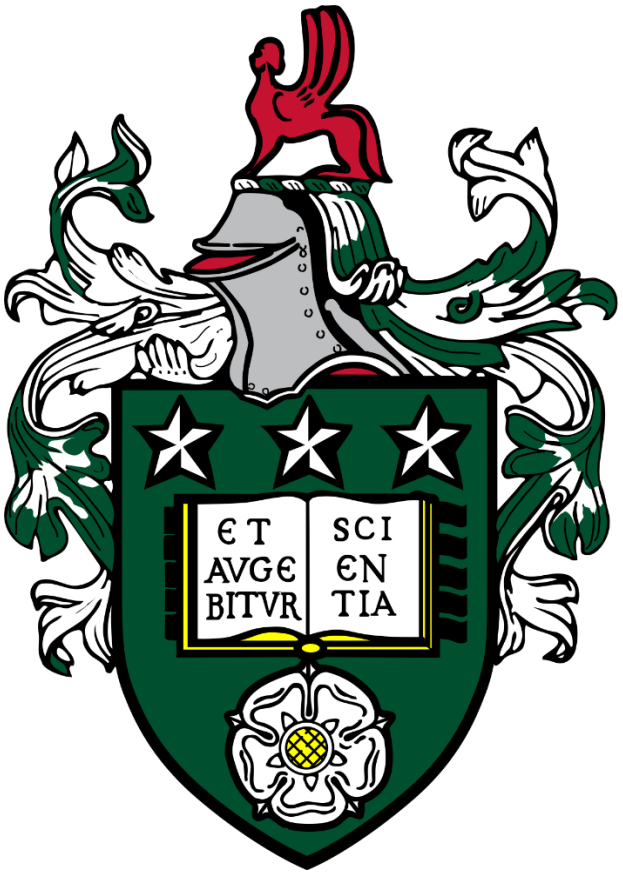

Submitted in accordance with the requirements for the degree of

Doctor of Philosophy in Molecular and Cellular Biology

The University of Leeds

School of Molecular and Cellular Biology

June, 2021

Intellectual Property and Publication Statements

The candidate confirms that the work submitted is their own, except where work which has formed part of jointly authored publications has been included. The contribution of the candidate and the other authors to this work has been explicitly indicated below. The candidate confirms that appropriate credit has been given within the thesis where reference has been made to the work of others.

The work in Chapter 1 of the thesis includes contents and figures that have appeared in publication as follows:

- Chau, C., Actis, P. and Hewitt, E. 2020. Methods for protein delivery into cells: from current approaches to future perspectives. *Biochem Soc Trans.* **48**(2), pp.357-365.

The work in Chapter 4 results of the thesis includes experimental work and data that have appeared in publication as follows:

- Chau, C., Radford, S., Hewitt, E. and Actis, P. 2020. Macromolecular Crowding Enhances the Detection of DNA and Proteins by a Solid-State Nanopore. *Nano Letters.* **20**(7), pp.5553-5561.

The work in Chapter 4 introduction of the thesis includes contents and figures that have appeared in publication as follows:

- Chau, C., Hewitt, E. and Actis, P. 2021. The role of macromolecular crowding in single-entity electrochemistry: Friend or foe? *Current Opinion in Electrochemistry.* **25**, p100654.

I am the first author in the above stated publications, I am the primary lead author from drafting to publishing. For the Nano letters publication entitled "Macromolecular Crowding Enhances the Detection of DNA and Proteins by a Solid-State Nanopore", I contribute all the data and analysis. All advisors including Radford, S., Hewitt, E. and Actis, P. helped and provided advice throughout the process.

Acknowledgements

I would like to thank my supervisors, Professor Sheena Radford, Dr Paolo Actis and Dr Eric Hewitt for allowing me to explore different research ideas, even though some of the ideas sounded absolutely insane. I valued this freedom to explore greatly, and it brings me joy whenever I attempt to do something that is "weird". Also thank you for all the advice given throughout the course of this PhD, despite sometimes going against said advice at my own risk. But mostly for believing in my abilities to complete a PhD degree. This long thesis would not be here, if you had not entrusted and allowed me to do this multi-disciplinary project in 2017.

Then I would like to thank the research group members of the Radford, Actis and Hewitt labs. There are a lot of people in these combined groups whom I am thankful for, but I would like to give special shout outs to the following: Leon Willis, Michael Davies, Atenas Posada Borbon, Madeline Brown, Mukhil Raveendran, Fabio Marcuccio, Dimitrios Soulias, Samuel Confedrat and Francesco Colucci - thanks a lot.

I would not be here if it was not for my past supervisors and advisors, so thank you to all my past supervisors and advisors: My undergraduate advisor Dr Norbert Krauß, I still remember the chat on the day you left QMUL, you believed in my abilities despite me being a troublesome student; My first project supervisor Dr Ping Yip of the Blizard Institute, I only started to like laboratory work because of you and you advised me to pursue research as career because you believed I could do that; My second project supervisor Dr Mark Cooper of UCL, you granted me freedom to explore and allowed me to make suggestions to the project. You insisted on making sure that I understood the nitty-gritty bit of every experimental technique that I used, and you have shaped me into a practical yet methodological researcher that insisted on finding out how things work.

I would like to also thank my parents and especially my brother. I still remember how you have encouraged me to pursue this path and not to worry about anything. Then, I am grateful for people who have supported me during this long journey of PhD, they are: Lucy Bircham, Africa Smith De Diego, Jackie Chan (not the actor), Martina Secone, Simona Caduceo, Vicky Kelly and Lorelai Vennard. It means a lot.

Finally, I would like to include a special celebrities acknowledgement section, since PhD is hard and long journey, and entertainment like movies and TV series are just helpful. I would like to acknowledge: Gordon Ramsay, I have enjoyed all the reality shows since my undergraduate time, especially Hell's Kitchen; Nicolas Cage, the quality of your movies are not up to standard, *i.e.* horrible, but I laughed and enjoyed myself watching others being forced to watch your movies with me; Dwayne Johnson, Seth Rogen, Will Ferrell, Vin Diesel and Mark Wahlberg, the quality of your movies are not up to standard either, *i.e.* bad. But I enjoyed myself and was able to relax whilst watching these bad movies; For Bruce Willis, I have watched Die Hard four times since my PhD started in 2017, I firmly believe it is a Christmas movie, this belief is against everyone's advice; Eurovision 2021 winner – Måneskin, a great band and well-deserved winner from Italy, I enjoyed your music a lot.

I am not thankful for COVID-19, but I am thankful for science.

"Never regret anything you have done with a sincere affection; nothing is lost that is born of the heart."

- Basil Rathbone

Abstract

Cultured cell manipulation by the intracellular delivery of exogenous biomolecules like DNA and proteins is the cornerstone of modern experimental cell biology. The intracellular delivery of biomolecules can be carried out with different methods such as electroporation and microinjection, but these methods lack dosage control.

The nanopipette is a needle with a nanopore size opening and by coupling with the scanning ion conductance microscopy, it has the potential to perform quantitative nanoinjection, *i.e.* intracellular delivery at precise single molecule resolution. When a suitable voltage is applied, the biomolecule moves towards the nanopore and it temporarily disrupts the ionic current flow, which generates a distinctive translocation signal. However, nanopore experiments are typically carried out inside an electrolyte bath, and the electrolyte bath is different from the macromolecular crowded intracellular environment. This work will study whether quantitative nanoinjection in the macromolecular crowded cell is possible, and whether the macromolecular crowded environment alters the translocation dynamic of a single molecule.

Different biomolecules including DNA plasmids, enzyme β-galactosidase and α-synuclein amyloid fibrils are delivered into different cells through the quantitative nanoinjection approach. The nanoinjection of these biomolecules is successful as confirmed by different fluorescence-based assays. Importantly, these biomolecules associated ionic currents were analysed and showed that the number of biomolecules delivered to the cell can be quantified, and thus the concept of quantitative nanoinjection can be realised. The translocation data obtained during the quantitative nanoinjection showed that the translocations of these biomolecules into the cell are slowed down, potentially due to the macromolecular crowded environment. This is further studied by adding the crowders poly(ethylene) glycol (PEG) and bovine serum albumin into the bath electrolyte to generate macromolecular crowded electrolyte bath, in which the translocation experiments are carried out inside. The results showed that the addition of crowders significantly improve the sensitivity of the nanopipette towards both DNA and proteins by nearly a 1000-fold. The use of the PEG crowded bath enables the nanopipette to detect different DNA plasmid topology and α-synuclein fibrils of different lengths.

Table of Contents

Table of Figures

Table of Tables

Abbreviations

Abbreviation	Definition	Abbreviation	Definition
CRISPR/Cas 9 RNPs	Clustered Regularly Interspaced Short Palindromic Repeats / Cas 9 Ribonucleoproteins	**CPPs**	Cell Penetrating Peptides
GFP	Green Fluorescent Proteins	**SICM**	Scanning Ion Conductance Microscopy
AFM	Atomic Force Microscopy	**siRNA**	small interfering RNA
mRNA	messenger RNA	**NanoEP**	Nanopore electroporation
NES	Nanostraws electroporation system	**NLS**	Nuclear localisation signal
RPS	Resistive pulse sensing	**α-HL**	α-hemolysin
PBS	Phosphate Buffered Saline	**PEG**	Poly(ethylene) Glycol
BSA	Bovine Serum Albumin	**EDTA**	Ethylenediaminetetraacetic acid
TAE	Tris-Acetate-EDTA	**SEM**	Scanning Electron Microscopy
S.E.M.	Standard Error of the Mean	**FACS**	Fluorescence-Activated Cell Sorting
SPM	Scanning Probe Microscopy	**NHEK**	Normal Human Epidermal Keratinocytes
HUVEC	Human Umbilical Vein Endothelial Cell	**DRG**	Dorsal Root Ganglion
CTCF	Corrected Total Cell Fluorescence	**EOF**	Electroosmotic flow
EDL	Electrical Double Layer	**dsDNA**	double stranded DNA
SNR	Signal-to-Noise Ratio	**FRET**	Förster resonance energy transfer
ssDNA	single stranded DNA		

Chapter 1

Intracellular Delivery Methods

1.1 Forethought on intracellular delivery

The controlled manipulation of cells by the intracellular delivery of exogenous molecules is a cornerstone of modern cell biology. Among all molecules, the most widely delivered molecule is the DNA expression constructs, *i.e.* the DNA plasmids. The delivery of the DNA plasmids to cells is through a process commonly known as the transfection, in order to manipulate the cells to express any desired proteins, and this is a very common routine in studying cell biology and has enabled the research of the functions of various proteins in a cellular context (Kim, T.K. and Eberwine, 2010; Hunter et al., 2019). Beside the transfection of DNA plasmids, numerous exogenous molecules have been introduced into cells for different purposes, examples include the synthetic intracellular probes (Liu et al., 2015; Chang et al., 2016) and proteins for genome-editing (Doudna and Charpentier, 2014; Cox et al., 2015; Wang, H.X. et al., 2017; Glass et al., 2018). Figure.1.1 depicts the diversity of the molecules that can be delivered into the cells, the expected cellular response and potential applications, it summarizes the potential of intracellular delivery as a way to manipulate and/or analyse cell functions.

The direct delivery of proteins into a cell is important not only because of its potential impacts on the overall cellular functions, but it is also a way to understand, associate and elucidate the protein's structure, function and behaviour inside a cell. As mentioned above, proteins of interest are typically studied by DNA plasmid transfection, although convenient and simple to perform, the transfection relies on the intracellular machinery to produce the protein and thus it has its limitations. For example, it is difficult to control the amount of proteins being produced and the produced protein may fail to fold inside the intracellular environment, a problem exacerbated if the protein is produced at high levels (Halff et al., 2014; Marschall et al., 2014). Furthermore, the transfection of DNA plasmids typically requires many hours before the expression of proteins can be observed, in contrast, the direct delivery of proteins induces phenotypic changes of the cell within an hour (Tang et al., 2013; Wu, G. et al., 2017). Additionally, proteins can be manipulated and characterized before they are delivered into cells. For example, through chemical modification to conjugate small functional fluorescent dye onto the protein, the assembly of defined protein complexes, and the analysis of protein structure using biophysical techniques, and thus establishes a better correlation

between a protein's structure and its cellular function (Fu et al., 2014; Stewart, M.P. et al., 2018; Lee, Y.-W. et al., 2019).

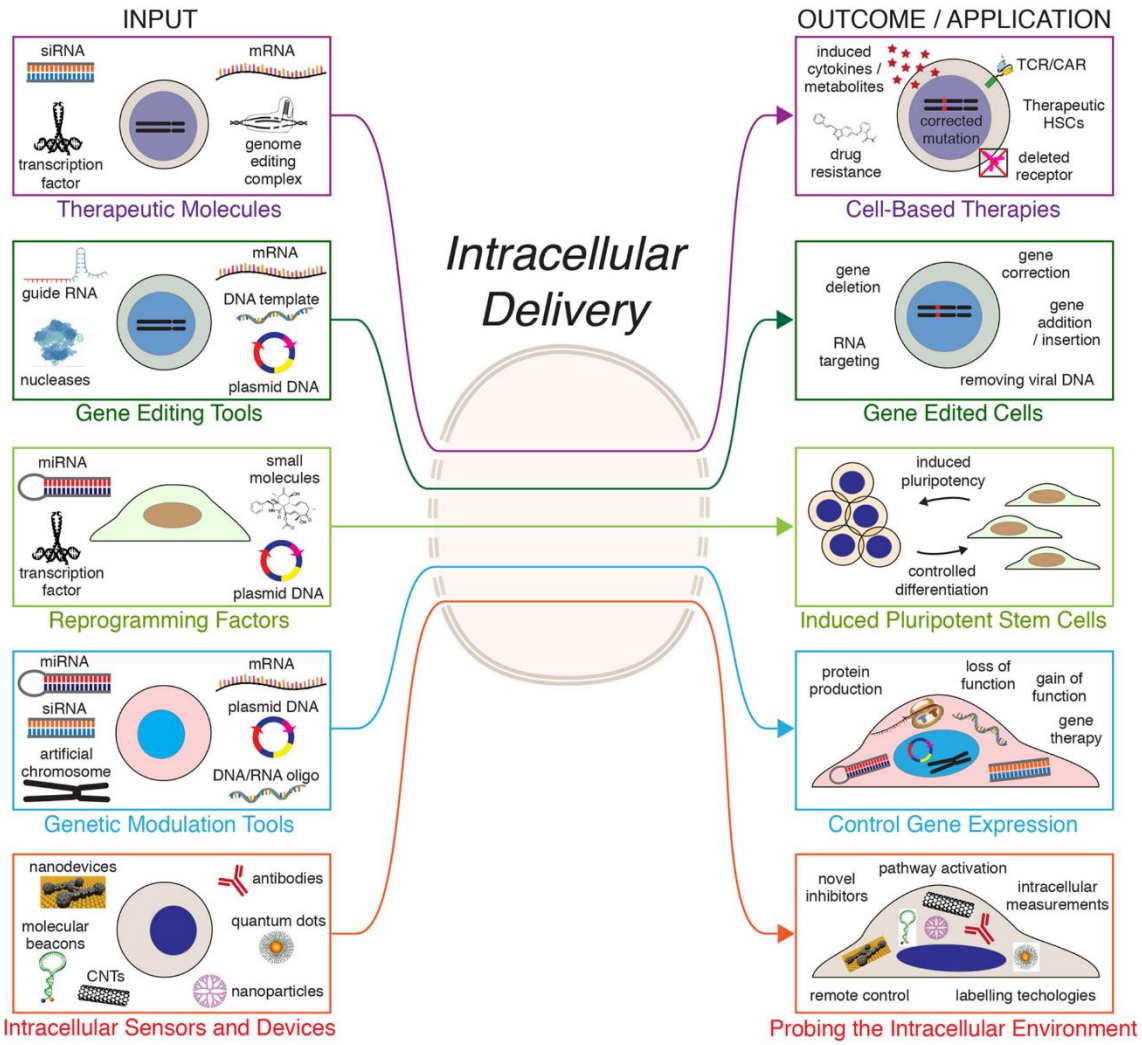

Figure.1.1. The possibilities of the intracellular delivery. *Combinations of cells and exogenous molecules are shown on the left input column. Through intracellular delivery, these molecules are able to exert their functions, consequently manipulate the cell behaviour and/or monitor the intracellular activity as depicted on the right column. The horizontal tiers are not mutually exclusive and substantial overlap exists between them. This "menu" of options reflects the combinatorial potential of intracellular delivery to analyse cell properties and engineer cell function. Abbreviations: TCR, T cell receptor; CAR, chimeric antigen receptor; CNT, carbon nanotube; HSCs, hematopoietic stem cells. Taken from (Stewart, M.P. et al., 2018).*

The intracellular delivery of the gene editing protein Clustered Regularly Interspaced Short Palindromic Repeats (CRISPR)/Cas9 ribonucleoproteins (Cas9 RNPs) is a popular way to manipulate cells at genomic level (Jansen et al., 2002)}. By simply swapping the guide RNA strand, the CRISPR/Cas9 RNPs can perform gene editing efficiently and accurately, however, this requires the CRISPR/Cas9 RNPs to be localised to the nucleus (Adli, 2018). The CRISPR/Cas9 RNPs are

commonly used to insert additional DNA sequence into the genome, but the CRISPR/Cas9 RNPs can also be structurally altered to perform different tasks such as overexpression and repression of certain genes as well as precise single point mutation (Qi et al., 2013; Tanenbaum et al., 2014; Gaudelli et al., 2017).

Antibodies have been used extensively to study the cellular location and to probe the post-translational modifications status of different proteins inside and outside of cells due to their high specificities towards the target proteins. Antibodies are typically used in a technique known as immunocytochemistry, this process involves the irreversible permeabilization of the cell membrane and fixation procedures that consequently kill the cells (Glynn and McAllister, 2006). Alternatively, through the direct delivery of antibodies into the intracellular space, it can be used to monitor the target proteins' cellular location, their dynamics and functions in living cell (Marschall et al., 2014). Furthermore, it can also be used to interfere the assembly of macro intracellular structures such as the cytoskeleton, as an alternative approach to study the function of proteins involves in the assembly process (Keppeke et al., 2015). Antibodies can also be used to control the endogenous target protein level in living cells, via a method known as the Trim-Away, it harnesses the cellular protein degradation machinery to remove the target proteins specified by the intracellular delivered antibodies (Clift, D. et al., 2017; Clift, Dean et al., 2018; So et al., 2019).

Direct intracellular protein delivery also furthers our understanding of cellular pathology on disease such as the amyloidosis, a group of diseases that is characterised by the build-up of the amyloid fibrils intra- and/or extracellularly in different organs. The amyloid fibril is a protein aggregate macromolecule that is formed by the aggregation of numerous protein monomers, an amyloid fibril has a classical cross-β amyloid fold architecture that is composed of numerous monomers forming β-strands, aligned perpendicular to the long axis of the fibril. The accumulation of amyloid fibrils eventually forms an abnormal structure like inclusion bodies, plaques or fibrillary tangles, and in some cases, proteins and other organelles can be found within these abnormal structures (Chiti and Dobson, 2017; Eisenberg and Sawaya, 2017; Iadanza, M. G. et al., 2018; Alam et al., 2019; Ke et al., 2020). The consequence of the build-up and the formation of intracellular amyloid fibrils is often associated with the disruption in cell function and cytotoxicity (Iadanza, M. G. et al., 2018; Chiki et al., 2020). It is known that during

the process of amyloid fibril formation, it generates aggregates of different sizes and structures that are lacking the characteristic organised cross-β amyloid fold architecture, these aggregates can be isolated early on during the aggregation process *in vitro* and these structurally different aggregates have been shown to elicit different cellular responses (Chiti and Dobson, 2017; Eisenberg and Sawaya, 2017; Iadanza, M. G. et al., 2018; Alam et al., 2019; Ke et al., 2020). Whilst the expression of the amyloid-related proteins via DNA plasmids can and has been used as a way to investigate the effects of the amyloid aggregates in living cells, it has an inherent disadvantage of not being able to accurately associate the cellular effects with the structure of the aggregates (Íñigo-Marco et al., 2017; Chiki et al., 2020). Instead, structurally characterised aggregates and/or fibrils can be directly delivered to the cell, to obtain a better correlation between the structure and its associated cellular response (Cremades, N. et al., 2012; Bousset, L. et al., 2013; Peelaerts et al., 2015a; Fusco et al., 2017; Mahul-Mellier et al., 2020).

1.2 The challenges of the intracellular delivery

For any exogenous molecules to reach the intracellular space to exert their intended functions, they must first traverse the highly selective cell plasma membrane (Figure 1.2). This physical barrier limits the entrance and the exit of particles of different sizes, the exogenous molecules often require assistance to gain access into the intracellular space (Doherty and McMahon, 2009; Stewart, M.P. et al., 2018).

Conversely, permeabilizing the plasma membrane with solvents like ethanol or detergents such as saponin, allows the free movement of exogenous molecules into cells, but this process lacks specificity and can result in cell death (O'Dea et al., 2017; Wang, M. et al., 2018). In contrast to the permeabilization approach, there are less intrusive approaches available. For example, cell endocytosis based intracellular delivery, the molecules can be encapsulated inside a lipid vesicle to transverse through the cell membrane, or locally disrupt the cell membrane to access the intracellular space directly (Figure 1.2).

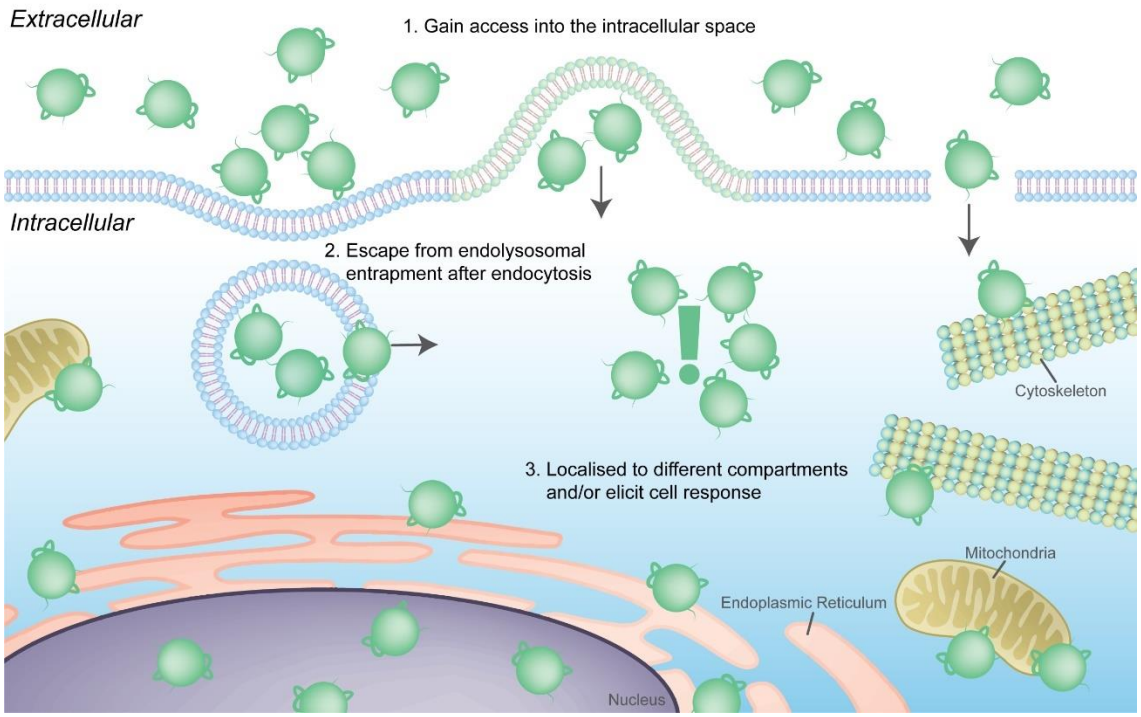

Figure 1.2. The process of intracellular delivery. *The exogenous molecules are unable to access into the intracellular space due to being separated by the cell plasma membrane. For the molecules to exert its intended function inside the cell, they must gain access into the intracellular space first. The majority of the exogenous molecules can gain access either by endocytosis, where part of the cell membrane is internalised alongside with materials stuck on the membrane. However, these molecules are trapped inside the endosomes and must escape from the endosomes, this is termed endolysosomal entrapment. Failure to escape from the endosomes leads to the molecules being degraded by lysosomes. The molecules can bypass the endolysosomal entrapment by using carriers such as liposome, this lipid vesicle can fuse with the cell membrane and discharge the molecules into the intracellular space. Alternatively, the cell membrane can be mechanically disrupted to form pores to allow molecules to access the intracellular space. After gaining access into the intracellular space, depending on the nature of the molecules, some may need to further localise into different cellular compartment to exert its intended function.*

Cell endocytosis is a complicated process, briefly, the cell internalises part of the cell plasma membrane to form a lipid vesicle, any exogenous molecules that interact with the cell membranes will also be internalised at the same time (Doherty and McMahon, 2009; Kumari et al., 2010; Kaksonen and Roux, 2018). However, the membrane wrapped exogenous molecules are encapsulated within the endosomes shortly after the internalisation and shortly trafficked to the lysosomes for degradation, this encapsulation process is termed the endolysosomal entrapment. The exogenous molecules must escape from the entrapment in order to exert their intended functions, however, the probability of these molecules escaping from the entrapment remains less than 5% in most cases, this means that a majority of the internalised molecules are degraded before they exert their intended functions (Kim, J.-s. et al., 2015). Furthermore, the exact mechanism of how molecules escape from the entrapment is unclear, this

subsequently halted the development of more efficient intracellular delivery strategy. There are several models that have been proposed, such as the membrane fusion model, it hypothesizes that the internalised membrane fused with the endosome vesicle to discharge the exogenous molecules into the intracellular space. Alternatively, the budding collapse hypothesis suggests that the internalised molecules bud-off from the endosomes and escape into the cytoplasm (Dougherty et al., 2019; Pei and Buyanova, 2019).

Overall, one further challenge, as well as the goal of the intracellular delivery is to get a specific molecule across the plasma membrane to the desired intracellular location without harming the cell. Various methods have been developed and/or improved to provide a better efficiency, these methods can be categorized into either the membrane disrupted methods or non-membrane disrupted methods. A list of the methods that will be briefly discussed in this chapter has been summarized in Table 1.1.

Table 1.1. Summary of the various approaches to deliver proteins into a cell.

	Description	Pros	Cons	Ref
Non-membrane disrupted methods				
Cell Feeding	Add the exogenous molecules at high concentration into the culture medium for the cell to internalise via endocytosis.	• Gain access without disrupting the cell membrane.	• Endolyosomal entrapment. • Efficiency varies for different molecules. • The delivery location is not controllable. • The number of molecules take up per cell is not controllable.	(Cremades, N. et al., 2012; Bousset, Luc et al., 2013; Peelaerts et al., 2015a; Mao et al., 2016; Fusco et al., 2017; De Cecco et al., 2020; Mahul-Mellier et al., 2020)
Lipofection	Lipofection is performed by liposomes. The exogenous molecules are packaged inside the cationic lipid vesicles known as the liposomes. Liposomes either discharge the molecules directly into the cell via membrane fusion or by endocytosis of the liposome.	• Gain access without disrupting the cell membrane. • Large scale intracellular delivery. • Commercially available.	• Endolysosomal entrapment. • Liposomes can be toxic at high concentration. • Require different liposome composition for different molecules. • The delivery location is not controllable. • The number of molecules take up per cell is not controllable.	(Bangham and Horne, 1964; Bangham et al., 1974; Colletier et al., 2002; Fretz et al., 2007; Xu, X. et al., 2012; Chatin et al., 2015; Ahmed et al., 2016; Kolašinac et al., 2019)
Cell penetrating peptides (CPPs)	The CPPs are conjugated to the exogenous molecules, the structure of the CPPs allow strong interaction with the cell membrane. The CPPs conjugated molecules are taken up by either endocytosis or direct traverse the cell membrane into the cell.	• Gain access without disrupting the cell membrane. • Large scale intracellular delivery. • High delivery efficiency.	• Endolysosomal entrapment. • Conjugation disrupts the structure of the molecules and its intended function. • The delivery location is not controllable. • The number of molecules take up per cell is not controllable.	(Frankel and Pabo, 1988; Eiriksdottir et al., 2010; Hirose et al., 2012; Qian, Z. et al., 2014; Patel et al., 2019)
Virus-like particles (VLPs)	The assembly of VLPs require a co-transfection of DNA plasmids to a fast proliferating cell line, and express the virus envelope and the gag tagged exogenous molecules. The assembled VLPs are released into the culture medium and collected to deliver the gag tagged molecules into different cells. The VLPs are taken up by endocytosis.	• Gain access without disrupting the cell membrane. • Effective escape from endolysosomal entrapment. • Large scale intracellular delivery. • High delivery efficiency.	• The Gag polyprotein is fused with the exogenous molecules in order to pack the molecules inside the VLPs. Potential structural and functional alteration. • Long and complicated preparation process. • The delivery location is not controllable. • The number of molecules take up per cell is not controllable.	(Voelkel et al., 2010; Kaczmarczyk et al., 2011; Patterson et al., 2017)
Membrane disrupted methods				
Microinjection	Glass pipettes with a micron-sized pore is pre-loaded with the exogenous molecules, the pipette approaches the cell by micro/nanomanipulator and mechanically penetrates the cell membrane to reach the intracellular environment. Application of pressure to deliver the molecules into the cell.	• Procedure can be automated. • No limitation on the exogenous molecule's property. • Exogenous molecules reach intracellular space directly. • Pipettes are easy to fabricate and affordable. • Delivery dosage control. • The injection platform is commercially available.	• Low survival rate. • Disruption in the cytoskeleton. • Equipment dependent. • Requires extensive training to operate.	(Barber, 1904; Cho et al., 2013; Keppeke et al., 2015; Chow et al., 2016a; Chow et al., 2016b; Hinchcliffe et al., 2016; Dixon et al., 2017; Chaverra-Rodriguez et al., 2018; Nan et al., 2019)
Nanoinjection	Glass pipettes with nanoscale pore at the tip end penetrates the cell membrane like microinjection. Exogenous molecules are delivered base on their electrical properties.	• Minimum damage to the cell membrane and cytoskeleton. • Couple to the SICM allows injection at precise location. • Exogenous molecules reach intracellular space directly. • Pipettes are easy to fabricate and affordable. • Delivery dosage control. • The injection platform is commercially available.	• Low throughput. • Charge dependent delivery, can be challenging with neutral molecules. • Equipment dependent. • Requires extensive training to operate.	(Adam Seger et al., 2012; Hennig et al., 2015; Simonis et al., 2017; Simonis et al., 2019; Li, B. et al., 2021)

Carbon nanotube endoscope	The micron-sized glass pipette is fitted with a carbon nanotube at the tip end to fabricate the carbon nanotube endoscope. The endoscope gain access into intracellular space, pressure is used to deliver exogenous molecules into the cells like microinjection.	• Minimum damage to the cell membrane and cytoskeleton. • No limitation on the exogenous molecule's property. • Exogenous molecules reach intracellular space directly. • Delivery dosage control.	• Low throughput. • The fabrication of the endoscope is technical, complicated and time consuming.	(Singhal et al., 2011; Orynbayeva et al., 2012)
FluidFM	A hollow channel cantilever of the AFM tip is drilled to form a nanopore ranging from 10 nm to 10 µm. The cantilever is positioned above the cell by AFM and penetrate the cell membrane. The exogenous molecules is loaded into the cantilever and delivered into the cell by pressure.	• Minimum damage to the cell membrane and cytoskeleton. • No limitation on the exogenous molecule's property. • Precise location injection. • Exogenous molecules reach intracellular space directly. • Precise delivery dosage control. • The injection platform is commercially available.	• Low throughput. • Equipment dependent. • Requires extensive training to operate. • The FluidFM probe can be relatively expensive compared to other method.	(Meister et al., 2009; Stiefel et al., 2012; Guillaume-Gentil et al., 2013; Guillaume-Gentil et al., 2016).
Nanostraws	Cells are cultured on numerous protruding hollow nanostructures. These nanostraws penetrate into the intracellular space and gain access. The nanostraws are connected to a liquid reservoir that contains the exogenous molecules. These molecules are delivered into the cell by fluidic pressure and diffusion across a concentration gradient.	• Minimum damage to the cell membrane and cytoskeleton. • No limitation on the exogenous molecule's property. • High throughput injection. • Exogenous molecules reach intracellular space directly. • Delivery dosage control.	• Conflicting evidence on the negative effects of the protruding nanostructures on cellular function. • The penetration of the nanostraws is spontaneous. • Complicated fabrication process. • The delivery location is not controllable.	(VanDersarl et al., 2012; Golshadi et al., 2016; Xu, A.M. et al., 2017)
Bulk Electroporation	Application of multiple high voltage pulses across the suspended cells leads to the formation of numerous nano sized pores on their membranes. Exogenous molecules in the buffer enter the intracellular space by diffusion, electrically driven, or clustered on the cell membrane for endocytosis.	• Very high throughput. • No limitation on the exogenous molecule's property. • Procedures are standardised and easy to perform. • Commercially available	• High cell mortality rate arose due to a very high voltage is needed to perform electroporation. • Molecules entered by endocytosis will be encapsulated by the endolysosomal entrapment. • Compartmental delivery into the nucleus claims to be possible by Nucleofector™ but the compartmental delivery mechanism is not known. • The delivery dosage is not controllable.	(Neumann et al., 1982; Golzio et al., 2002; Kaminski Schierle et al., 2011; Kim, S. et al., 2014; Lin et al., 2014; Richardson et al., 2016; Bai et al., 2017; Conic et al., 2018)
Single-Cell Localised Electroporation	A miniaturised electroporation combined with microfluidic. The cells are in close proximity with the electrodes and localised electroporation is done on each cell flowing through the electrodes inside the microfluidic channel.	• High throughput enabled by rational design of the microfluidic channels. • Higher cell survival rate due to a lower voltage is needed to generate the electric field for electroporation. • No limitation on the exogenous molecule's property.	• Fabrication of the device can be technically challenge. • Molecules entered by endocytosis will be encapsulated by the endolysosomal entrapment. • The delivery location is not controllable. • The delivery dosage is not controllable.	(Adamo et al., 2013; Bürgel et al., 2015)

Nanofountain Probe Localised Electroporation	A hollow cantilever similar to FluidFM is used to perform localised electroporation. The probe is positioned above the cell by AFM and electroporation happens in a small area.	• Higher cell survival rate due to a lower voltage is needed to generate the electric field for electroporation. • No limitation on the exogenous molecule's property.	• Low throughput • Fabrication of the device can be technically challenging. • Equipment dependent • Molecules entered by endocytosis will be encapsulated by the endolysosomal entrapment. • The compartmental location delivery is not controllable. • The delivery dosage is not controllable.	(Kang et al., 2013; Yang et al., 2018)
Nanopore Electroporation (NanoEP)	Cells are cultured on top of a membrane contains numerous nanopores. These nanopores are connected to a liquid reservoir similar to nanostraws. The electroporation happens at the cell membrane in direct contact with the nanopores. The exogenous molecules enter the intracellular space from the liquid reservoir via the nanopore after electroporation.	• High throughput electroporation across multiple cells. • Higher cell survival rate due to a lower voltage is needed to generate the electric field for electroporation. • No limitation on the exogenous molecule's property.	• Fabrication of the device can be technically challenging. • Molecules entered by endocytosis will be encapsulated by the endolysosomal entrapment. • The compartmental location delivery is not controllable. • The delivery dosage is not controllable.	(Cao, Y. et al., 2019; Chen, Z. et al., 2021)
Nanostraws Electroporation System (NES)	Combination of the nanostraws with the nanopore electroporation system. Localised electroporation happens across numerous nanostraws on one cell, the formation of the electroporation induced membrane pores aids the penetration of the nanostraws to reach the intracellular space. Exogenous molecules are delivered via electrophoresis and/or fluid flow pressure.	• High throughput electroporation across multiple cells. • Higher cell survival rate due to a lower voltage is needed to generate the electric field for electroporation. • Exogenous molecules reach intracellular space directly. • No limitation on the exogenous molecule's property. • Delivery dosage control.	• Fabrication of the device can be technically challenging. • Conflicting evidence on the negative effects of the protruding nanostructures on cellular function. • The compartmental location delivery is not controllable.	(Xie et al., 2013; Cao et al., 2018; Schmiderer et al., 2020; Hebisch et al., 2021)

1.3 Non-membrane disrupted method

Non-membrane disrupted methods describe a category of intracellular delivery methods where the cell plasma membrane is kept intact throughout the process. These include cell feeding which does not require any carrier (Figure 1.3), and carrier assisted methods such as liposome of lipofection, cell penetrating peptides (CPPs) and the virus-like particles (VLPs)(Figure 1.3).. These carriers promote the internalisation of the exogenous molecule.

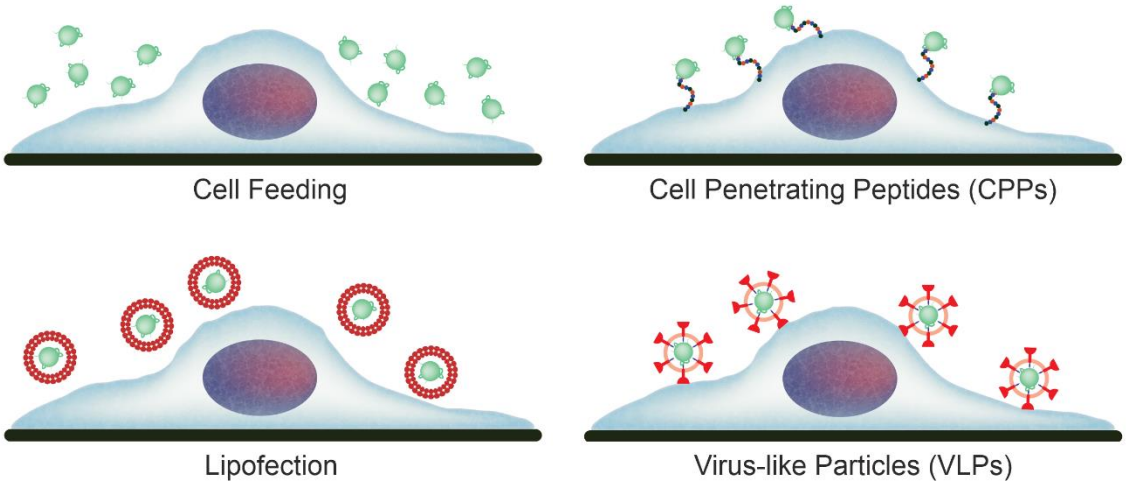

Figure 1.3. Intracellular delivery by the Non-membrane disrupted methods. *Schematic illustrations of the different methods used to deliver exogenous molecules into the cell without disrupting the cell membrane.*

Cell feeding relies on the endocytosis, typically an overwhelmingly high concentration of the exogenous molecules is added to the cell culture medium for the cell to uptake (Figure 1.3). This method is commonly used to deliver biophysically characterised amyloid aggregates and fibrils into the cell (Cremades, N. et al., 2012; Bousset, L. et al., 2013; Peelaerts et al., 2015a; Fusco et al., 2017; Mahul-Mellier et al., 2020). Although endocytosis can happen spontaneously and on any positions of the cell membrane, molecules that are able to interact with cell surface receptors often leads to a higher chance of internalisation (Grant and Donaldson, 2009). These include the lymphocyte-activation gene 3 (LAG3), cellular prion protein (PrP^{C}), triggering receptor expressed on myeloid cells 2 (TREM-2), they have been shown to bind and facilitate the uptake of the *in vitro* generated α-synuclein, tau and amyloid-β amyloid fibrils, this means some of the amyloid related materials can be efficiently delivered into the cell by cell feeding alone (Vaquer-Alicea and Diamond, 2019). However, cell feeding could be less efficient for exogenous molecules that do not interact with the cell membrane strongly or bind to any surface receptor. To facilitate the delivery of these molecules, synthetic molecule carriers can be used.

One of the most widely used synthetic molecule carriers are the liposomes used in the lipofection method. This method was developed in 1964 by Bangham *et al.* (Bangham and Horne, 1964; Bangham et al., 1974) (Figure 1.3). Liposomes are lipid vesicles formed by combining the cationic and neutral phospholipids at a specific ratio depending on the application, the resulting positively charged

vesicles are then used to coat the negatively charged exogenous molecules, *e.g.* the DNA plasmids, the liposome and molecule complex is then delivered to the cell by co-incubating the cells and the liposomes. The positively charged vesicles adhere to the cell plasma membrane via charge attraction as the plasma membrane is negatively charged. The liposomes then traverse the cell plasma membrane either by the endocytosis as described above or by liposome membrane fusion, *i.e.* the liposomes fuse with the cell membrane and directly discharge the exogenous molecules into the intracellular space (Bozzuto and Molinari, 2015; Carter, M. and Shieh, 2015). Direct discharge of molecules into the cell bypasses endolysosomal entrapment, but if the liposome is internalised by the endocytosis pathway then it means that the liposome must escape before its degradation by lysosomes. To improve the escape rate, chemical surface modification of the liposomes and photochemical treatment during the co-incubation period have been shown to increase delivery efficiency (Fretz et al., 2007; Ahmed et al., 2016). Packaging the DNA plasmids into a liposome is standardised and commercially available. However, packaging proteins into the liposome is case dependent as a study shows that different proteins require liposomes made with different lipids and mixing at different ratios (Chatin et al., 2015). The packaging efficiency of proteins can be improved by subjecting the liposome-protein solution mixture to multiple freeze-thaw cycles (Colletier et al., 2002; Xu, X. et al., 2012).

Cell penetrating peptides (CPPs) are another type of synthetic carrier. This was first reported by Frankel *et al.* in 1988 (Frankel and Pabo, 1988). They are short cationic peptides that efficiently interact with the cell plasma membrane, and conjugating the CPPs to the exogenous molecules aid the intracellular delivery process (Figure 1.3). The CPPs do not have a standardised amino acid sequence and different peptides with different amino acid sequences can all be classified as the CPPs, but in general they have less than 30 amino acids in total (Madani et al., 2011; Cleal et al., 2013). The peptides by themselves are random coils in solution but upon interaction with the lipid membrane they adopted the α-helical structures, the structural changes facilitates the interaction between the CPPs conjugated molecules and the plasma membrane (Eiriksdottir et al., 2010). The CPPs conjugated molecules show a size-dependent traverse mechanisms after they bound to the cell membrane (Ruseska and Zimmer, 2020). For example, CPPs' conjugation to a small molecule such as a fluorophore leads to direct penetration

through the cell membrane into the intracellular space (Hirose et al., 2012). In contrast, conjugation to a larger molecule like the green fluorescent protein (GFP) involves the endocytosis pathway to internalise the molecules (Patel et al., 2019). Lastly, the sequence and the structure of the CPPs affect the chances of escape from the endolysosomal entrapment as studies show that a cyclized CPPs are more effective in escaping from the endosomes than that of the α-helical CPPs (Pei and Buyanova, 2019; Ruseska and Zimmer, 2020).

The virus-like particles (VLPs) are artificial engineered non-infectious viruses that act as a carrier (Figure 1.3), and Voelkel *et al.* was the first to use VLPs to deliver proteins to cell in 2010 (Voelkel et al., 2010). It is known that viruses efficiently escape from the endosome via membrane fusion with the endosomal membrane after internalization, similarly, the VLPs retain the ability to escape from the endolysosomal entrapment via fusion (White, J.M. and Whittaker, 2016; Zdanowicz and Chroboczek, 2016). The VLPs have been used to deliver proteins into the cells including enzyme caspases and GFP (Kaczmarczyk et al., 2011; Patterson et al., 2017). However, the generation of VLPs is time consuming. First, the formation of the VLPs requires the gag polyprotein, the sequence of this polyprotein is fused with the sequence of the protein of interest to construct a DNA plasmid. This particular DNA plasmid is then co-transfected to cells with another DNA plasmid that encodes the sequence for the expression of the virus envelope. After the transfection, the co-transfected cells start to produce the gag tagged protein of interest and the virus envelope, and eventually the assembly and the release of the VLPs. The medium is then collected and purified to obtain the VLPs (Kaczmarczyk et al., 2011). The complicated and lengthy procedure is a major hindrance in adopting this method.

Whilst these non-membrane disrupted methods can be relatively easy to adopt, beside the common challenge of overcoming the endolysosomal entrapment, there are additional concerns about the toxicity of the carriers, potential structural alterations and consequently functional alterations of the molecules caused by the carriers (Lappalainen et al., 1994; Hu, X. et al., 2013; Kristensen et al., 2015; Smith, S.A. et al., 2018; Inglut et al., 2020). Furthermore, these methods have little control over the delivery location, this is especially important if the molecules have intended functions at a specific compartment, *e.g.* the delivery of DNA plasmids and CRISPR/Cas9 RNPs both need to be localised to the nucleus to exert the

functions. In contrast, the membrane disrupted methods, which partially disrupt the plasma membrane through physical means during the intracellular delivery process, can provide more control over the location of the delivery. Well known intracellular delivery method that belongs to this category are the electroporation and injection based delivery procedure. Moreover, recent advancements in nanotechnology subsequently enables the electroporation and injection to be performed locally and the procedures are shown to be minimally invasive to the cell.

1.4 Microscale to nanoscale probes cellular injection

Injection based delivery involves the mechanical penetration of the cell plasma membrane with a needle-like probe, the probe is pre-filled with the exogenous molecules through which they can enter the cell (Figure 1.4A). Microinjection uses a conical micron-sized glass micropipette and a pressure controller to control the delivery of the molecules into the cell (Figure 1.4B) (Xu, Q., 2018). The original concept of microinjection was proposed by Barber over a hundred years ago in 1904 (Barber, 1904). Positioning of the micropipette is controlled by a micromanipulator, which enables the injection of cells at a defined site. Successful penetration of the probe through the cell membrane heavily depends on the local cell membrane deformation rate. When the probe approaches the cell membrane at high velocity, the probe impalement rapidly ramps up the local membrane tension, and eventually it becomes energetically favourable to form a pore instead (Figure 1.4A). In contrast, slow penetration allows the membrane to pull lipids from reservoirs and eventually to mould and adopt the shape of the penetrating probe (Figard and Sokac, 2014; Stewart, M.P. et al., 2018). Moreover, a sharper and more cylindrical probe geometry shows to have a higher probability of successful penetration when it is compared to a blunt conical shaped tip, this is because of the sharp cylindrical geometry has a better mechanical advantage over the conical blunt geometry when attempting to penetrate the membrane (Obataya et al., 2005).

Microinjection is typically used for the injection of various different molecules such as DNA plasmids, antibodies and CRISPR/Cas9 RNPs into the nucleus directly (Cho et al., 2013; Keppeke et al., 2015; Chow et al., 2016b; Hinchcliffe et al., 2016; Dixon

et al., 2017; Chaverra-Rodriguez et al., 2018). However, there are significant drawbacks with the microinjection. Most notably the survival rate of the post-injected cells is on average *c.a.* 50%, although this can be improved with the aid of automation (Chow et al., 2016a; Nan et al., 2019). The low survival rate is due to the impact of microinjection on cells by the large tip of the micropipette relative to the cell. Indeed, injection of cell with a 1 µm diameter micropipette results in the significant perturbation of cell, with the majority of the actin filaments being disrupted and the cell develops a deformed morphology (Orynbayeva et al., 2012).

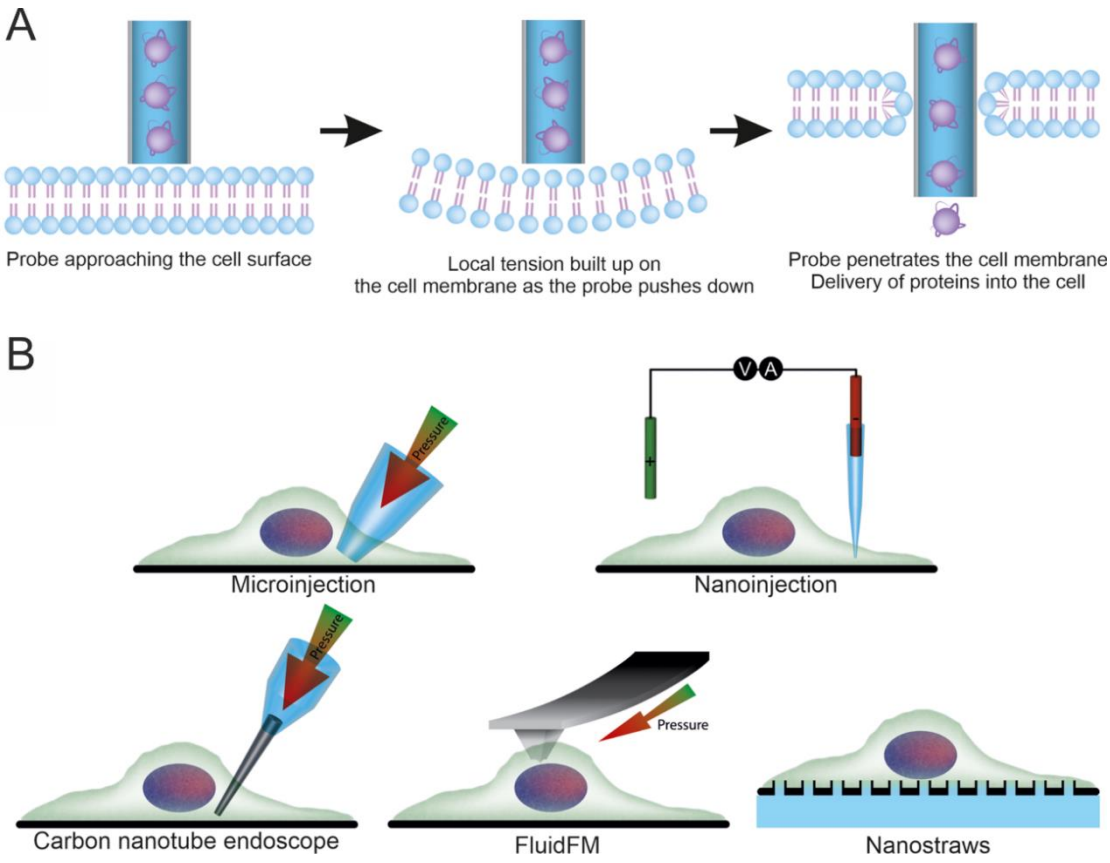

Figure 1.4. Intracellular delivery by injection*. The mechanism of injection (B). The probe approaches the cell surface, it pushes down the cell membrane, leads to a build-up of local tension, eventually penetrating the cell membrane, allows exogenous molecules to access the intracellular space. Schematic illustrations of the different methods for the injection of cells (B). Taken from (Chau, C. et al., 2020).*

One strategy to minimize the cellular impact of the injection process is to reduce the size of the probe to the nanoscale, which has been shown to improve the cell viability after injection (Figure 1.4B) (Singhal et al., 2011; Orynbayeva et al., 2012; VanDersarl et al., 2012; Guillaume-Gentil et al., 2013; Simonis et al., 2017). One such probe-based device is the nanopipette, which is essentially a scaled down

micropipette with a nanometer scale pore, a nanopore, at its tip (Stanley and Pourmand, 2020; Xue et al., 2020). A pair of nanopipettes can be easily fabricated using a laser puller from a single quartz capillary, and the pore diameter can be adjusted within the 10 - 300 nm range (Stanley and Pourmand, 2020; Xue et al., 2020). Nanopipettes can be integrated with nanomanipulators, as used in the scanning ion conductance microscope (SICM), where the vertical position of the nanopipette with respect to surface can be controlled with nanometer precision (Chen, C.C. et al., 2012; Zhu, C. et al., 2020). The SICM has been successfully used for the high-resolution topographical imaging of living cells in culture (Novak et al., 2014; Seifert et al., 2015; Shevchuk, A. et al., 2016; Zhou, Y. et al., 2018; Takahashi et al., 2019). The resultant topographical map can then be used to position the nanopipette anywhere on the cell membrane and precisely insert the nanopipette tip into the cell (Novak et al., 2013; Simonis et al., 2017; Vivekananda et al., 2017; Simonis et al., 2019). Because nanopipettes are fitted with electrodes, the delivery of molecules into cells can be triggered by the application of a voltage of suitable polarity while maintaining a high cell survival rate compared to micropipettes (Hennig et al., 2015; Simonis et al., 2017; Simonis et al., 2019). Antibodies and amyloid aggregates have been delivered into cells using this technique (Simonis et al., 2019; Li, B. et al., 2021). The concept of the SICM and nanoinjection will be discussed in more detail in Chapter 3.

A carbon nanotube endoscope is a micropipette fitted with a carbon nanotube at its tip, the carbon nanotube typically has an inner tube diameter of 50 – 200 nm (Figure 1.4B) (Singhal et al., 2011; Orynbayeva et al., 2012). The endoscope is coupled with a pressure controller to regulate the delivery duration as well as delivery liquid volume. Quantum dots and fluorescent dyes can be delivered into cells with minimum disruption to the cytoskeleton and cell morphology (Singhal et al., 2011; Orynbayeva et al., 2012). An alternative tool is the FluidFM platform, which is an adaptation of atomic force microscopy (AFM) (Figure 1.4B) (Meister et al., 2009; Stiefel et al., 2012; Guillaume-Gentil et al., 2013). The injection probe of the FluidFM is a hollow AFM cantilever that is connected to a liquid reservoir coupled with a pressure controller, the opening of the pore can be manufactured with a diameter ranging from 10 nm to 10 µm. Upon the penetration of the plasma membrane, the pressure controlled injection is used to deliver molecules into the cells including the nuclear injection of DNA plasmids, to demonstrate that the

intranuclear delivery by the FluidFM does not affect the cell viability. Besides the DNA plasmids, cell impermeant fluorescent dyes and vaccinia virus have been delivered to the cytoplasm and cell surface using the FluidFM (Meister et al., 2009; Stiefel et al., 2012; Guillaume-Gentil et al., 2013; Guillaume-Gentil et al., 2016).

Without automation, the injection of cells with nanoscale probes has a low throughput, as the user can only inject one cell at a time. One solution is to use arrays of nanoscale probes to perform simultaneous injection of hundreds of cells at once (VanDersarl et al., 2012; Golshadi et al., 2016). Nanostraws are arrays of hollow elongated nanostructures which protrude from a polycarbonate or alumina membrane surface (Figure 1.4B) (VanDersarl et al., 2012). They typically have a diameter of hundreds of nanometers or less and lengths on the micrometer scale, and a straw density ranges from 0.01 to 1 straw per μm^2 (VanDersarl et al., 2012). Cells are grown on top of the nanostraws, which are connected to a fluidic reservoir that allows the intracellular delivery via fluidic pressure and concentration gradient diffusion. Molecules such as the cell impermeable fluorescent dyes, probes and DNA plasmids have been delivered into the cells via the nanostraws (VanDersarl et al., 2012; Golshadi et al., 2016; Xu, A.M. et al., 2017). Due to the design of this device, it lacks specificity at the delivery location. The nanostraws have shown to cause minimal impact on the genetic profile of the cell as revealed by analysing the expression of genes associated with cellular functions (VanDersarl et al., 2012), and yet some studies reported that long term culturing of cells on top of these protruding nanostructures can have undesired effects on cells. For example, the alteration in the cell growth rate and cell cycle progression, interferes with the cell division mechanism and leads to the formation of the abnormal multinucleate cells (McKnight et al., 2004; Persson et al., 2013; Persson et al., 2015).

1.5 Bulk and localized electroporation

Electroporation utilises a strong electric field to temporarily permeabilize the cell plasma membrane, allowing the entrance of the exogenous molecules from the solution into the cells (Santra and Tseng, 2016) (Figure 1.5A). Electroporation was first used to deliver genetic materials in 1982 by Neumann *et al* (Neumann et al., 1982). Nowadays, electroporation is a well-established technique and typically involves the use of an electroporation cuvette, a cuvette that has a set of parallel electrodes on the cuvette walls (Figure 1.5B). The cells are suspended in a conductive electrolyte inside the electroporation cuvette, and upon the application of a voltage, an intense electric field is instantly generated. This electric field is maintained for only several microseconds to a second, the on-and-off electric field is often described as a pulse. Depending on the applications and cell types, different combinations on the number of the pulses, the duration of the pulse and the electric field strength of the pulse can be tailored (Santra and Tseng, 2016; Stewart, M.P. et al., 2018). The mechanism which allows the intracellular space to become accessible is that the intense electric field causes the cell plasma membrane to undergo a phenomenon known as the thermal fluctuation, which leads to the formation of numerous membrane pores ranging from 0.5 to 50 nm in diameter, these pores connects the intracellular space to the extracellular space (Figure 1.5A) (Smith, K.C. et al., 2014). Electroporation has been widely used to deliver DNA plasmids into the cell, the negatively charged DNA plasmids migrate towards the intracellular space by electrophoresis under the influences of the electric field (Stewart, M.P. et al., 2018). However, the typical physical dimension of a DNA plasmid is usually bigger than the electroporation induced membrane pores, thus the majority of these plasmids will be found clustered on the surfaces of the cell membrane, threading themselves through the electroporation induced membrane pores (Golzio et al., 2002). These clusters of DNA plasmids are internalised by cell endocytosis, eventually some of the endocytosed DNA plasmids will make its way to the nucleus and consequently transfect the cell (Bai et al., 2017). Electroporation often utilises a short pulse duration and the electroporation induced membrane pores immediately shrink and reseal when the electric field is off (Venslauskas and Satkauskas, 2015). This limitation affects the delivery of smaller, less charged molecules, for example, proteins migrate towards the intracellular space mainly by diffusion rather than the electrophoresis, this

together with the short accessible time frame for the proteins to be diffused into the intracellular space through the pore makes it extremely challenging for protein delivery through bulk electroporation (Stewart, M.P. et al., 2018). However, various proteins including antibodies, CRISPR/Cas9 RNPs and amyloid related proteins such as α-synuclein have also been successfully delivered into cells by bulk electroporation (Kaminski Schierle et al., 2011; Kim, S. et al., 2014; Lin et al., 2014; Richardson et al., 2016; Conic et al., 2018).

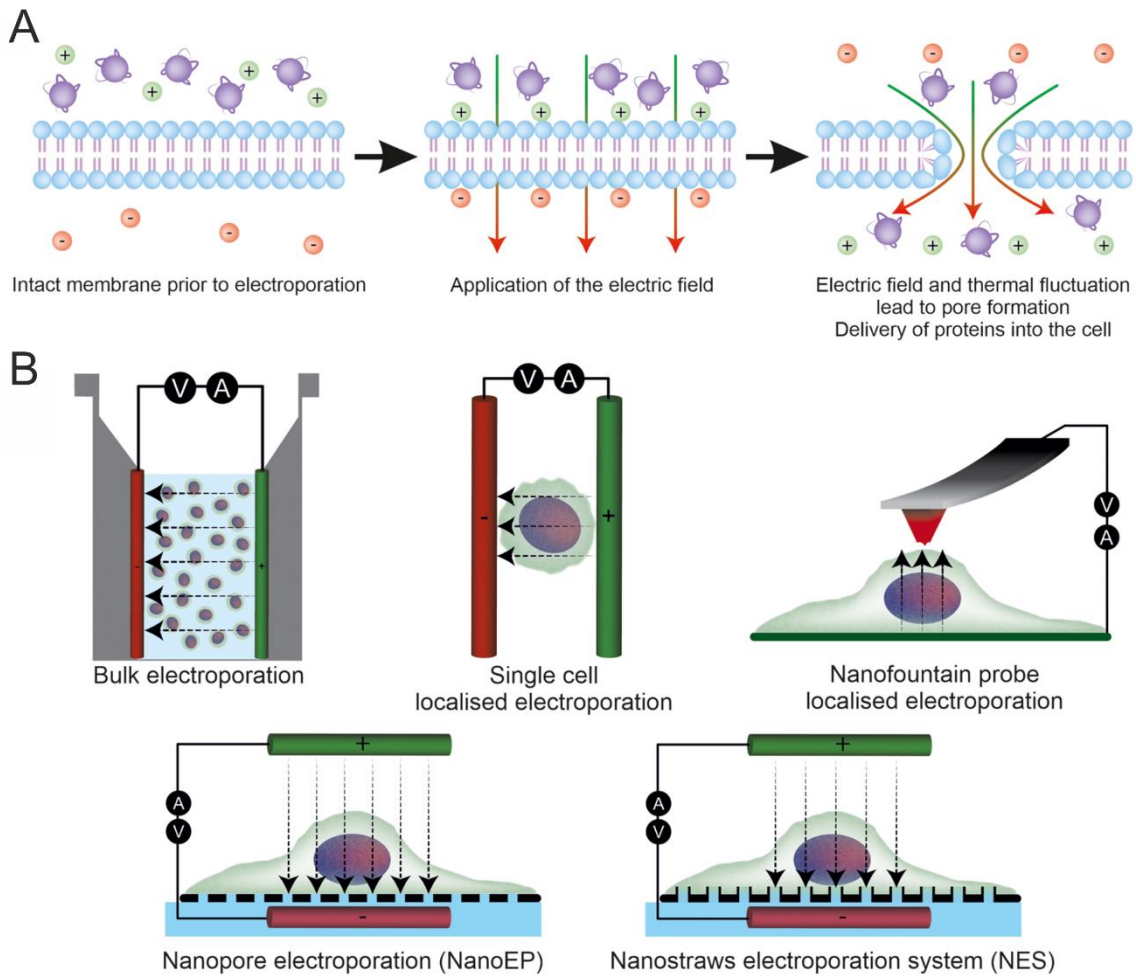

Figure 1.5. Intracellular delivery by electroporation. *The mechanism of electroporation (A). An electric field is applied across the cell's plasma membrane, the electric field and membrane thermal fluctuation lead to the formation of transient pores, allowing access into the intracellular space of exogenous molecules. Schematic illustrations of the different electroporation methods (B). Taken from (Chau, C. et al., 2020).*

Besides the issue of delivery, the existence of a relatively large gap (1 mm to 4 mm) between the electrodes of the electroporation cuvette is a major issue in retaining a high cell survivability rate after the bulk electroporation. To maintain a consistently strong enough electric field to electroporate the cells across a long

distance through the conductive electrolyte will require the input of a high voltage (Figure 1.5B) (Santra and Tseng, 2016). The prolonged exposure to the intense electric field causes lipid peroxidation and the generation of reactive oxygen species, which can cause massive damage to the protein and DNA inside the living cell (Luft and Ketteler, 2015; Kotnik et al., 2019). Moreover, the need of the high voltage to maintain the intense electric field leads to an increased in the local temperature and local pH changes in the area close to the electrodes (Kurata et al., 2012; Li, Y. et al., 2015). As the consequences of the above effects brought by the electric field and high voltage, many cells die immediately after the procedure, whereas the surviving cells have been shown to have a reduced viability and proliferative potential (Lenz et al., 2003). To improve the survival rate and the overall health of the cells post-electroporation, developments in micro and nanofabrication technologies have enabled the production of a localised electroporation device. The localised electroporation device is any device that places the electrodes in a much closer proximity, almost adhering to the cell membrane (Figure 1.5B). The significant reduction in the distance between the electrodes means that a much lower voltage can be used to maintain the same electric field strength for electroporation and consequently minimizes the localised heating and pH changes issues caused by the high voltage (Zhu, T. et al., 2009; Zhao, D. et al., 2016). As a result, the overall survival rate and cell viability after electroporation as well as the DNA plasmids transfection efficiency have all been shown to be increased (Cao et al., 2018; Mukherjee et al., 2018; Yang et al., 2018; Cao, Y. et al., 2019; He et al., 2019; Tay and Melosh, 2019; Santra et al., 2020).

A variety of devices have been developed to perform localized electroporation (Figure 1.5B). For example, this can be achieved by incorporating electrodes containing microchips inside a microfluidic channel to perform single cell localised electroporation. The microfluidic channel allows the cells to flow through whilst simultaneously being subjected to localized electroporation, this has been shown to enable cell impermeable fluorescent dyes and small interfering RNAs (siRNAs) to be delivered into single cells as they pass through the channel and electric fields (Adamo et al., 2013; Bürgel et al., 2015). Alternatively, a probe can be used to perform localized electroporation (Figure 1.5B). The nanofountain probe system is similar to the above described FluidFM, with a hollow cantilever-based probe and coupled with the (AFM) for positioning (Kang et al., 2013). In this approach, the

nanofountain probe is positioned in close proximity to the plasma membrane, then the application of an electric field allows the delivery of molecules ranging from DNA plasmids to proteins such as bovine serum albumin, and CRISPR/Cas9 RNPs into the cells (Kang et al., 2013; Yang et al., 2018).

Array based methods can also be used to perform the localized electroporation with the main advantage of electroporating multiple cells simultaneously at the same instant. In one such device, known as the nanopore-electroporation (NanoEP) platform, the cells are deposited and cultured on top of a polycarbonate membrane which contains 100 nm diameter nanopores at a density of 0.2 pores per μm^2 (Figure 1.5B). These nanopores are connected to a liquid reservoir containing the exogenous molecules similar to the nanostraws, the localised electroporation through numerous nanopores induced the formation of the membrane pores and allow the exogenous molecules to enter the cell (Cao, Y. et al., 2019; Chen, Z. et al., 2021). The NanoEP has been used to deliver a variety of exogenous molecules, including mRNAs, DNA plasmids, CRISPR/Cas9 RNPs, functional stromal interaction molecule 1 (STIM1) proteins, as well as fluorescently labelled proteins into the cell cytoplasm (Cao, Y. et al., 2019; Chen, Z. et al., 2021). The nanostraws electroporation system (NES) has essentially the same set-up as the nanostraws system previously described, with the addition of electrodes in the liquid reservoir underneath the straws and in the cell culture medium reservoir to enable the localised electroporation (Xie et al., 2013; Cao et al., 2018). This increases the delivery efficiency over that of fluidic delivery by nanostraws alone, and has been used to deliver DNA plasmids, nanoparticles, proteins CRISPR/Cas9 RNPs and STIM1 into the various cells at high viability rate including the primary stem cells (Xie et al., 2013; Cao et al., 2018; Schmiderer et al., 2020; Hebisch et al., 2021).

The most well-known location controlled delivery based on the electroporation is the Nucleofector™ Technology, a highly optimised electroporation parameter accompanied with specially formulated buffers to maintain high cell viability as well as high delivery efficiency of DNA plasmids directly into the nucleus (Distler et al., 2005). However, the exact mechanism of the nucleus targeted electroporation delivery is unclear. Several studies have adopted the Nucleofector™ technology to deliver CRISPR/Cas9 RNPs into the nucleus but the advantages of such technology is not demonstrated properly (Kim, S. et al., 2014;

Lin et al., 2014; Richardson et al., 2016). The CRISPR/Cas9 RNPs proteins used in these studies are tagged with the nuclear localisation signals (NLS), the NLS tagged molecules will be directed and imported into the nucleus via the intracellular machinery (Marfori et al., 2011), this affects the interpretation on the localised compartmental delivery ability of the Nucleofector™ technology.

1.6 Quantitative intracellular delivery?

The above sections highlight some of the commonly used intracellular delivery methods, these methods are constantly being improved to address issues such as cell viability and improving the intracellular delivery efficiency. However, the dosage control of these methods are usually not the main focus. Controlled dosage delivery is important, particularly for protein functional analysis as excess proteins may cause undesired effects while insufficient protein may lead to no cellular response. There are several ways to reasonably estimate the number of molecules delivered. For example, an estimate can be extrapolated from the delivery duration and molecules' concentration at that time. Alternatively, fluorescent signals can be quantified and used to estimate the number of fluorescent particles delivered, providing that the exogenous molecules are fluorescent molecules or conjugated to a fluorophore or dye (Guillaume-Gentil et al., 2013; Chow et al., 2016b; Drews et al., 2016; Cao et al., 2018). However, estimation can be error prone as the intracellular environment is vastly different from an *in vitro* mimic environment (Minaschek et al., 1989; Guillaume-Gentil et al., 2013). To avoid the estimation based approach, instead, the delivery can in theory be performed at single molecule resolution with the use of the nanopore of a narrow nanopipette. The molecules passing through the nanopore can be detected at single molecule resolution based on the well-established technology known as the resistive pulse sensing (RPS).

1.6.1 Nanopores

Nanopore is an exciting and promising platform for the development of rapid biochemical related assays at single molecule resolution (Miles et al., 2013; Muthukumar et al., 2015; Varongchayakul et al., 2018; Xue et al., 2020). The

fundamental principle and set-up of a nanopore single molecule sensor is simple (Figure 1.6), two chambers of conductive electrolyte are separated by a nanopore such that the only connection between these two chambers is through the nanopore opening. Each separated chamber is fitted with an electrode and when a voltage is applied between the two electrodes, an electric field is established through the nanopore. Depending on the charges of the ions and molecules present in solution, they either move towards to the anode or cathode through the nanopore via electrophoresis. Since the pore dimension of the nanopore restricts the number of ions that can flow through the nanopore at the same instant, the dimension of the nanopore acts as the main resistor in the equivalent electric circuit.

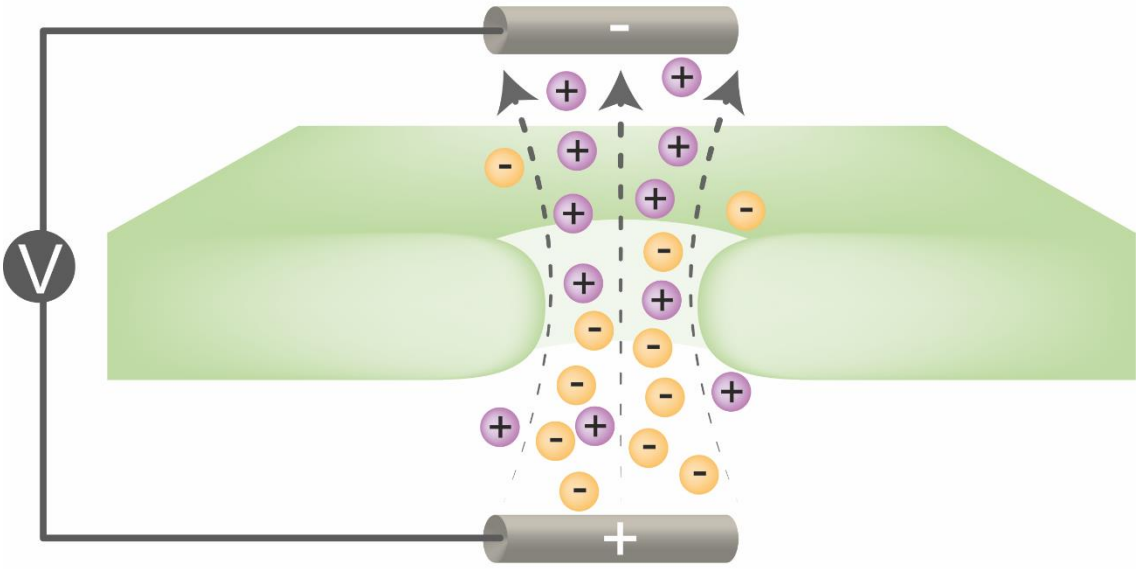

Figure 1.6. The set-up of the nanopore detection system*. The nanopore is the only connection between two separate chambers containing conductive electrolyte. Appling voltages across the nanopore leads to an establishment of an electric field (dotted arrows) and ions move towards the electrode by electrophoresis.*

There are two main types of nanopore that are used for the single molecule detection purpose: the biological nanopore and the solid-state nanopore. The biological nanopores are typically found and embedded in the cell membrane of living cells and organelles, these biological nanopores typically have a β-barrel structure where multiple protein domains assemble to form a single channel structure. Some of the commonly used biological nanopores include the pore forming toxin α-hemolysin (α-HL) from *Staphylococcus aureus* (Clarke, J. et al.,

2009; Stoddart et al., 2009), and the mycobacterial porin A of *Mycobacterium smegmatis* (Figure 1.7A) (Mathe et al., 2011; Laszlo et al., 2016). Others include the voltage dependent anion channel of the mitochondria (Jacobs et al., 2019) and Fragaceatoxin C of *Actinia fragacea* (Huang, G. et al., 2019). These biological nanopores have an inner pore diameter of typically less than 5 nm, measured on their resolved crystal structures (Song et al., 1996; Faller, 2004; Bayrhuber et al., 2008; Tanaka et al., 2015). The advantages of biological nanopores as a single molecule sensor are that the pore dimension and geometry are always consistent regardless of the production batch, and the properties of the nanopore can be engineered by mutations to improve the pore sensitivity (Wang, S. et al., 2018). Solid-state nanopores can be fabricated in membranes, for example the commonly used silicon nitride (Figure 1.7B) (Kong et al., 2013; Niedzwiecki et al., 2020), graphene (Merchant et al., 2010) or molybdenum disulfide (Graf et al., 2019). Solid-state nanopores can be fabricated on these membranes by different methods including drilling with electrons from a transmission electron microscope (TEM), focused ion beam milling, reactive ion etching, laser-etching and dielectric breakdown (Chen, Q. and Liu, 2019; Xue et al., 2020), these procedures result in the formation of nanopores from 1 nm to 10s of nanometers in diameter. Alternatively, a solid state nanopore of <10 nm in diameter and above can be fabricated by laser assisted pulling of glass capillaries to form a pair of conical glass nanopores, commonly known as the nanopipettes, as mentioned previously (Figure 1.7B) (Stanley and Pourmand, 2020; Xue et al., 2020). The dimension of the solid-state nanopore varies slightly each time, this is different from the biological nanopore where the inner pore dimension is determined by its amino acid sequence. However, the solid-state nanopores generally exhibit greater mechanical robustness, finer control over the pore geometry and opportunities for chemical functionalization compared to the biological nanopores (Varongchayakul et al., 2018; Fragasso et al., 2020).

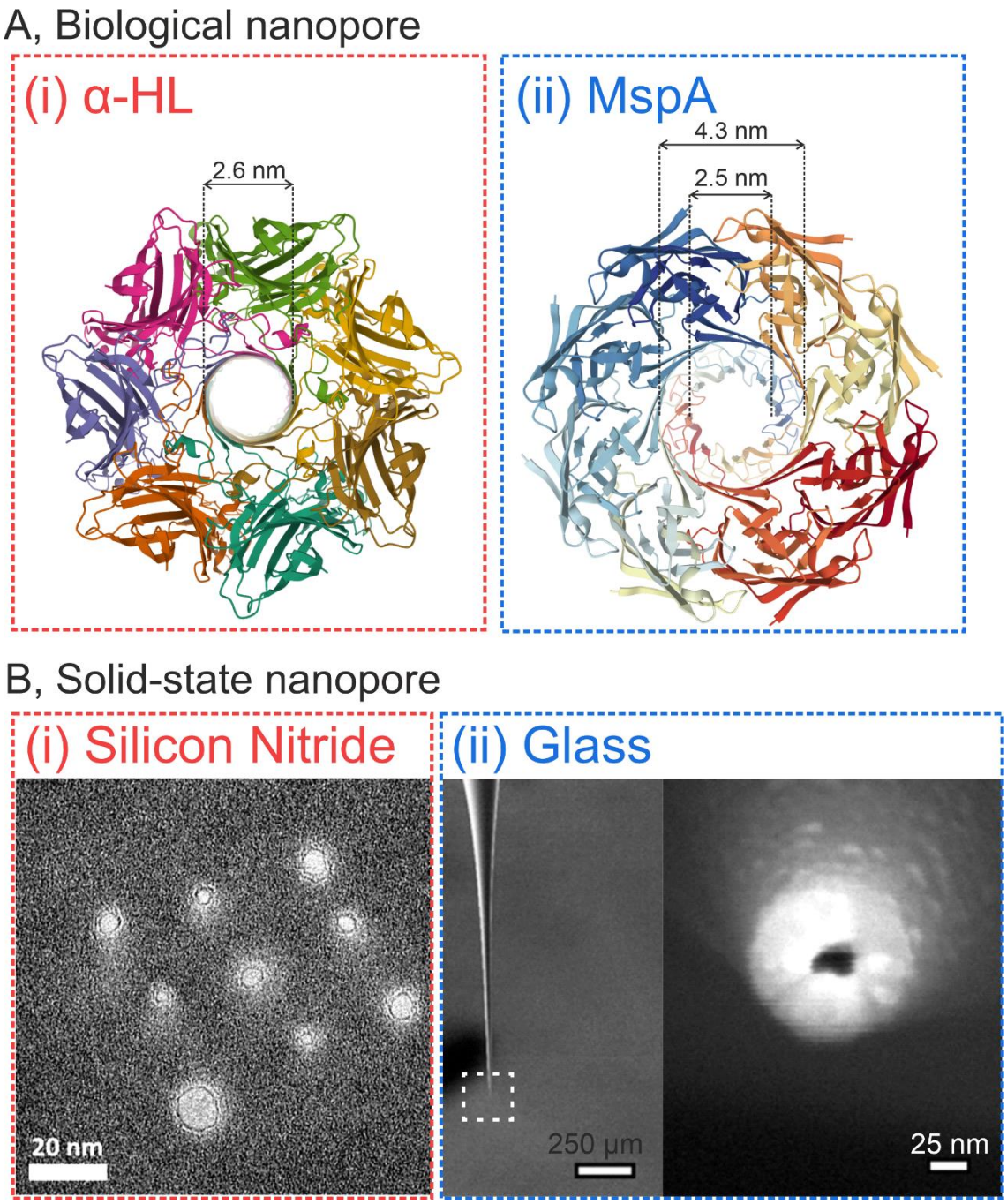

Figure 1.7. Biological and solid-state nanopores. *The α-hemolysin (α-HL) has a nanopore of 2.6 nm in diameter (A(i)) and mycobacterial porin A (MspA) has a pore diameter of 2.5 nm and 4.3 nm at the bottom and the top respectively (A(ii)). The diameter measured is based on the crystal structure. Protein Data Bank ID: 7AHL for α-HL and 1UUN for MspA. The solid-state nanopore can be fabricated by using focused electron beam to drill on the silicon nitride membrane, they have nanopore diameter ranging from 2 to 20 nm imaged by transmission electron microscopy (B(i)). Solid-state nanopore can also be fabricated by pulling capillaries to form nanopipettes. The scanning electron microscopy image showed a nanopipette with a pore size of c.a. 20 nm diameter (B(ii)). (B(i)) is taken from (Niedzwiecki et al., 2020), (B(ii)) is taken from (Ivanov et al., 2015).*

1.6.2 Single molecule detection

Recent advancements in the single molecule detection via the nanopore have enabled the development of nanopore-based platform for DNA sequencing which

was first demonstrated by Kasianowicz *et al.* in 1996 (Kasianowicz et al., 1996), this technology ultimately led to the commercialisation of the MinION nanopore DNA sequencing device from Oxford Nanopore Technologies in 2015, a small portable device that can be used to sequence DNA at high precision (Howorka et al., 2001; Jain et al., 2015; Loman and Watson, 2015), Since then, the community has focused on the development of protein peptide sequencing technology with the nanopore (Ouldali et al., 2019; Howorka and Siwy, 2020). Besides sequencing technology, the nanopore enables single molecule structure investigation such as discerning the topological state of DNA plasmid and DNA knots (Fologea et al., 2007; Steinbock et al., 2010; Kumar Sharma et al., 2019), ribosome and poly-ribosome differentiation (Raveendran et al., 2020a), protein structural investigation *e.g.* post-translational modification detection (Restrepo-Pérez et al., 2019), unfolding kinetics (Si and Aksimentiev, 2017), protein-protein binding affinity (Wloka et al., 2017), and protein aggregation (Yusko, Erik C. et al., 2012; Martyushenko et al., 2015; Giamblanco et al., 2018a; Giamblanco et al., 2018b; Giamblanco et al., 2020a; Giamblanco et al., 2020b). These are all enabled by utilising the resistive pulse sensing (RPS) technology with the nanopore.

The translocation of biomolecules can be detected by RPS technology. Using nanopipette as the example: the established electric field allows ions to flow through the nanopore, when a single molecule passes through the nanopore under the influence of the electric field, the flowing ions are temporarily excluded by the molecule, this causes an geometrical exclusion phenomenon and disrupts the ionic current flow, and thus increases the resistivity of the nanopore at that instant and consequently a temporarily drop in the ionic current baseline, this drop is known as the RPS (Figure 1.8A) (Varongchayakul et al., 2018; Xue et al., 2020). This type of detection technology was first proposed by W.H. Coulter in 1953 (Coulter, 1953), this technology was then adopted and commercialised – the Coulter counter, an instrument for counting and sizing particles suspended in the electrolytes (DeBlois and Bean, 1970). The nanopore detection is essentially a scaled down Coulter counter for the analysis of single molecules. Each RPS event is defined by two parameters: the relative change in the ionic current baseline due to the geometrical exclusion – the current peak maxima and the duration of the geometrical exclusion caused by the translocating analyte molecule – the dwell time (Figure 1.8B). This information can be used to define the physical properties

of the molecule at that particular instant as it passes through the nanopore (Yusko, E. C. et al., 2017; Houghtaling, Jared et al., 2019).

Geometrical exclusion will always lead to a disruption in the ion flow and consequently a decrease in the ionic current baseline, however in some cases, the translocation events are current enhancing instead of dropping as demonstrated in multiple molecule translocation studies (Smeets et al., 2006; Aksimentiev, 2010; Kowalczyk and Dekker, 2012; Lan et al., 2014; Ivanov et al., 2015; Raveendran et al., 2018; Raveendran et al., 2020b). The current enhancement event can be attributed to factors including the geometry of the nanopore, the electrolyte salt concentration and the properties of the translocating molecules (Smeets et al., 2006; Chen, K. et al., 2017). The geometry and the salt concentration affect the thickness of the electrical double layer (EDL), and the thickness of the EDL determines the magnitude of the ion concentration polarization phenomenon at the tip of the nanopipette. This polarization leads to the enhancement in the current during the translocation of molecule (Chen, K. et al., 2017). The properties of the translocating molecules also contribute to the formation of the current enhancing translocation event, as highly negatively charged molecules like DNA, the surrounding environment of the DNA is shielded with cations (Smeets et al., 2006; Gebala et al., 2015; Gebala et al., 2016). The migration of this highly shielded molecule brings in excess ions to the tip of the nanopipette and these excess ions lead to the formation of the current enhancing event during the translocation of DNA (Smeets et al., 2006). The relationship between the nanopore and the analyte molecules will be discussed in more detail in Chapter 4.

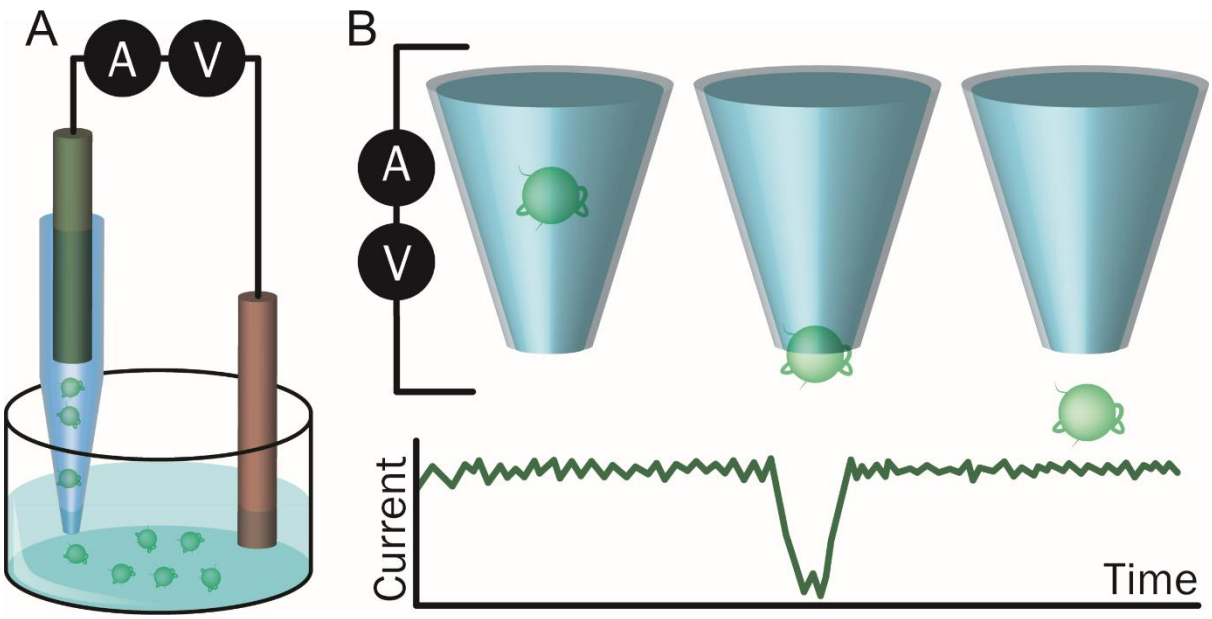

Figure 1.8. Nanopipette as the single molecule sensing tool. *The schematic set-up of the single molecule sensor using the Nanopipette as the example (A). An electric circuit is established by immersing two electrodes into the conductive electrolyte. The electrodes are separated by a nanopore, in this case the nanopipette. Molecules of interest are driven towards their polar opposite electrode due to the electric field. Illustration of the formation of the resistive pulse sensing (RPS) event signal (B). The upper panel illustrates how a molecule pass through the nanopore from reaching the pore, passing through the pore and passed the pore. The passing of the molecule through the pore affects the current baseline led to a sudden increased in resistance. This is visualised as a drop in the current size, the duration of the drop correspond to the time the molecule spent passing through the pore. These two parameters together formed the RPS event signal. Taken from (Chau, C. et al., 2020).*

Since each individual RPS event is associated with the translocation of a single molecule, the number of the molecules passed through the nanopore can be quantified by simply counting the RPS events (Figure 1.8B) (Charron et al., 2019). Furthermore, the nanopore was able to fully control the number of DNA delivered into an electrolyte bath through the nanopipette by manipulating the applied voltage (Ivanov et al., 2015). Moreover, the recently developed nanopore-optofluidic chip device combines the nanopore with a optofluidic system and a microcontroller feedback control circuit module, this chip device shows that it detects and restricts down to only one molecule (DNA or ribosome) to pass through the nanopore. In this device, when a defined number of the RPS events were detected (as low as 1 RPS event), the microcontroller immediately applies 0V to immobilise the remaining molecules in the chamber that has yet to pass through the nanopore. This single molecule then diffuses through a microfluidic channel and confirms by the optical measurement (Rahman et al., 2019). These studies demonstrate that complete control over the number of molecules delivered is possible in an electrolyte bath. To date, two studies have demonstrated that

nanopore sensing can quantify the number of molecules delivered into the cell during intracellular delivery. The first one uses an optical tweezer to immobilize the cell on top of a 2.5 nm diameter nanopore for the quantitative delivery of the DNA plasmids to transfect the cell (Kurz et al., 2014). In the other study, a NES-like system with 200 nm hollow electrodes is able to detect multiple RPS events caused by the delivery of gold nanorods into the cells (Huang, J.A. et al., 2019).

1.6.3 Potential applications

The precise controlled delivery of materials into the cell can be used to aid biological research and potentially be used to investigate important biological questions.

Allowing the researchers to precisely deliver a certain number of molecules can be used as a tool to control the intracellular environment. This can be achieved by combining the quantitative approach with the established Trim-Away method where certain proteins will be targeted for degradation as previously discussed (Clift, D. et al., 2017; Clift, Dean et al., 2018; So et al., 2019). As an example, cell signalling related proteins can be depleted to a desire level by the quantitative intracellular delivery of the Trim-Away antibodies which can help researchers to further understand the cell signalling process.

The quantitative delivery approach can be used to perform single cell transfection of plasmid. It has been estimated that in order to transfect a cell with plasmid, approximately 20 copies of DNA plasmids will be needed to be localised to the nucleus (Lechardeur et al., 1999; Bai et al., 2017). However, the commonly used lipofectamine approach delivers approximately 20,000 copies of the plasmids to the cell cytoplasm (Lechardeur et al., 1999; Bai et al., 2017). A high number of plasmids delivered to a cell inevitably affects the cell viability (Geiler-Samerotte et al., 2010; Park et al., 2013; Kafri et al., 2016; Kintaka et al., 2016), this is due to the overloading of the protein translation process and exhausting resources for protein turnovers (Moriya and Cohen-Fix, 2015). This can be problematic, *e.g.* the investigation of protein function inside the cell via transfection, overexpressing the protein of interest leads to a reduction in cell viability, and consequently leads to researchers to establish a potentially false positive correlation between the protein of interest and cell viability. In contrast, a controlled dosage delivery of plasmid at

low number directly to the nucleus minimise the probability of overloading the cell and its protein production process and resources.

Alternatively, this quantitative approach may have important application as a key tool to understand key biological question, *e.g.* the amyloid diseases. Amyloid diseases such as Parkinson's and Alzheimer's are associated with the formation of amyloid fibrils through abnormal protein aggregation, and the abnormal build-up of the amyloid fibrils can disrupt the function and viability of cells (Chiti and Dobson, 2017; Eisenberg and Sawaya, 2017; Iadanza, M. G. et al., 2018; Alam et al., 2019; Ke et al., 2020). Amyloid fibrils can be formed by the aggregation of different proteins, *e.g.* α-synuclein in Parkinsons' disease and amyloid-β in Alzheimer's disease, however, these fibrils share a common underlying cross-β amyloid fold architecture (Chiti and Dobson, 2017; Eisenberg and Sawaya, 2017; Iadanza, M. G. et al., 2018; Alam et al., 2019; Ke et al., 2020). Amyloid proteins like α-synuclein aggregate inside the intracellular compartment, and subsequently lead to the formation of the intracellular Lewy body, an inclusion body that contains different intracellular components (Spillantini et al., 1997; Mahul-Mellier et al., 2020; Fares et al., 2021). Since the protein α-synuclein can aggregate inside the cell, the intracellular delivery of structurally characterised fibrils and aggregates is crucial to understand the correlation between protein structure and how the cell responds, and the structure and cell viability relationship has been demonstrated before in different studies (Cremades, Nunilo et al., 2012; Bousset, Luc et al., 2013; Paslawski et al., 2014a; Paslawski et al., 2014b; Chen, S.W. et al., 2015; Peelaerts et al., 2015b; Fusco et al., 2017; Alam et al., 2019; Guerrero-Ferreira et al., 2019; Chakroun et al., 2020; Guerrero-Ferreira et al., 2020; Schweighauser et al., 2020; Chou et al., 2021).

The commonly used method to investigate the effects brought by the amyloid fibrils in cell biology is to incubate cells with amyloid fibrils by adding the fibrils to the culture medium (Cremades, N. et al., 2012; Bousset, L. et al., 2013; Peelaerts et al., 2015a; Fusco et al., 2017; Ke et al., 2020; Mahul-Mellier et al., 2020). Other methods have also been used to deliver amyloid materials into the cell directly, such as the electroporation and injection (Kaminski Schierle et al., 2011; Li, B. et al., 2021). These methods are of particular interest as they bypass the cell membrane and deliver the amyloids directly into the intracellular space, which not only improves the efficiency of delivery, but also eliminates cell responses

associated with the endocytosis of the amyloids and amyloid-lipid interaction. It provides a direct way to correlate the intracellular responses to the structure of the amyloids, *i.e.* a way to understand how the cell responds when the amyloid initially starts to aggregate inside the cell. Similarly, the quantitative nanoinjection approach also bypass the lipid membrane and deliver the molecules directly to the intracellular space.

The advantage of the quantitative approach is the control over the number of molecules delivered which is important in the field of amyloid disease. It is known that certain amyloid aggregates, *e.g.* the *in vitro* generated aggregates of α-synuclein can be used as to seed the formation of larger aggregations inside cells and animals (Danzer et al., 2009; Freundt et al., 2012; Luk et al., 2012; Rey et al., 2013; Witt et al., 2016; Gribaudo et al., 2019; Rey et al., 2019; Hijaz and Volpicelli-Daley, 2020; Mahul-Mellier et al., 2020; Sang et al., 2021). Recent study has calculated that on average less than 100 intracellular α-synuclein aggregates would be sufficient to seed the formation of additional intracellular aggregates (Sang et al., 2021). The quantitative nanoinjection method has potential to be used as a tool to further understand the complicated relationship between the number of aggregates, the structure of aggregates and the cell response.

Thesis Aims

The first aim of this thesis was to develop a quantitative nanoinjection platform and workflow, to enable the delivery of biomolecules from a nanopipette into the intracellular space of the cell and to simultaneously quantify the number of biomolecules injected using resistive pulse sensing technology (Figure 1.9).

This platform was comprised of two main components: the scanning ion conductance microscopy (SICM) with an integrated nanopipette of <30 nm in diameter and an inverted confocal fluorescent microscope. The SICM provides high spatial resolution for positioning the nanopipette and can lower down the nanopipette at a defined distance to penetrate the cell membrane and access the intracellular space. The nanopipette was used to nanoinject cells with different biomolecules in order to demonstrate the quantitative nanoinjection concept. The biomolecules injected included dextran conjugates, DNA plasmids, enzymes and amyloid fibrils. The nanoinjection associated ionic current trace was analysed and the number of translocated molecules will be quantified. Successful delivery of these biomolecules was then confirmed by fluorescent microscopy.

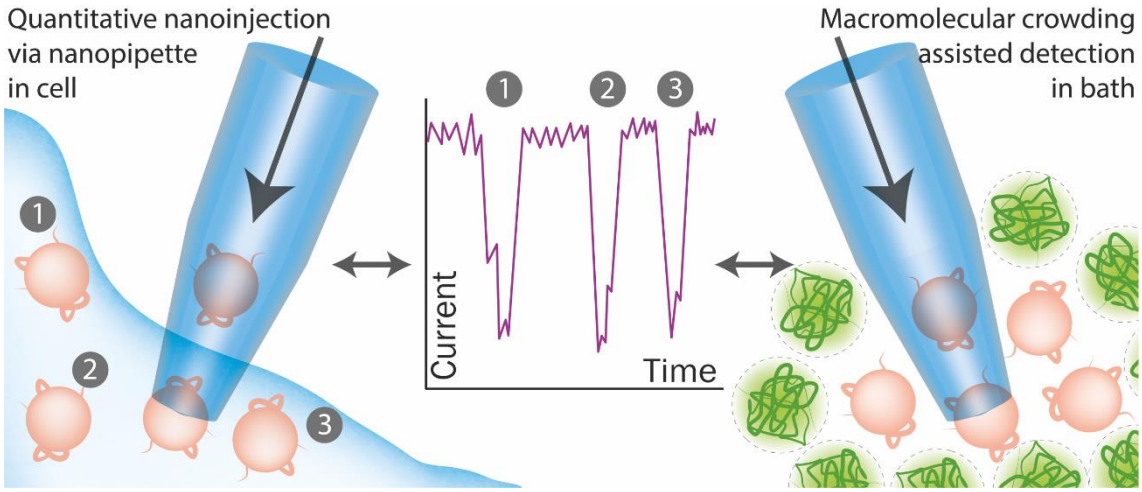

Figure 1.9. Schematic illustrations of the two aims of the thesis. *On the left, aim 1 is depicted i.e. quantitative nanoinjection in which biomolecules will be delivered into the cell via the nanopipette. The ionic current will then be analysed and the number of molecules will be quantified by counting the number of the translocation events as shown in the middle. On the right, aim 2 is depicted in which the translocation experiments are carried out using a macromolecular crowded environment. The ionic current and the translocation events will be analysed and characterised in order to understand the role of macromolecular crowding in the electrolyte bath on the translocation signals.*

The second aim of this thesis was to investigate the role of the bath environment on the translocation dynamics of biomolecules through the nanopore of a nanopipette, in particular the effect of macromolecular crowding (Figure 1.9).

The intracellular space is filled with macromolecules at high concentration, resulting in a macromolecular crowded environment, which is different from the pure electrolyte such as the Phosphate Buffered Saline (PBS) used in electrolyte baths. To mimic this *in vitro*, the crowding agents poly(ethylene) glycol (PEG) and bovine serum albumin (BSA) were used to generate macromolecular crowded PBS baths. The nanopipette was filled with different biomolecules and translocation experiments were performed into the macromolecular crowded baths to study whether macromolecular crowding affects the translocation dynamics of biomolecules.

Chapter 2

Methods

2.1 Plasmids preparation and analysis

2.1.1 Plasmids production

The pMaxGFP plasmids from the Cell Line Nucleofector™ Kit V (VVCA-1003; Lonza) and pmCherry-NLS (the pmCherry-NLS from Martin Offterdinger; #39319; Addgene; RRID: Addgene_39319)(Micutkova et al., 2012) were used. The pMaxGFP was provided as solution at 0.5 µg/µl. The pmCherry-NLS arrived as a *E. coli* bacterial stab from Addgene. The Luria broth medium was generated by dissolving 25% (w/v) of Luria broth powder (L24020; Melford) in ddH_2O followed by autoclave sterilisation. Colonies of the *E. coli* stab was picked using a clean pipette tip and inoculated inside 2 ml of 25% (w/v) Luria broth medium containing 50 µg/ml of kanamycin overnight at 37°C at 200 rpm shaking. The 2 ml overnight inoculated culture was transferred to 1 L of 25% (w/v) Luria broth medium containing 50 µg/ml kanamycin and allowed to further inoculate overnight 37°C at 200 rpm shaking. The overnight *E. coli* culture was collected, lysed and the pmCherry-NLS plasmids were isolated using the Qiagen Plasmid Maxi Kit (12162; Qiagen) as per manufacturer's instructions. All plasmids were stored at -20°C.

2.1.2 Restriction digestion

To confirm the length of the plasmids, they were linearized by restriction digestion using the enzyme Kpn I (R0142S; New England Biolabs) in the NEBuffer™ r1.1 (B6001; New England Biolabs). A 20 µl reaction mixture was made by combining 1 µg of plasmid, 1U final concentration of restriction enzyme Kpn I, 1× NEB Buffer™ r1.1 and ddH_2O. The reaction mixture was incubated at 37°C for 1 hour. The restriction digestion process was inactivated by incubating the reaction mixture at 65°C for 15 minutes immediately after the digestion reaction. The resultant linearized DNA was kept at -20 °C for storage.

2.1.3 Agarose gel electrophoresis

The plasmid concentration was measured by UV absorbance at 260 nm with a NanoDrop™ 2000 (Thermo Fisher). For gel electrophoresis, a 10× Tris-acetate ethylenediaminetetraacetic acid (EDTA) buffer (1× TAE buffer; 400 mM Tris-

acetate, 10 mM EDTA, pH 8.3) was used to cast agarose gel and as the running buffer. 0.8% (w/v) of agarose (A9539; Sigma Aldrich) was dissolved in 1× TAE buffer under high heat inside a microwave, 1× SYBR safe (S33102; Thermo Fisher) was incorporated into the solution mixture before it was solidified, the solution was poured into a gel caster and a gel comb was used to create wells in the gel. Once set, the gel was immersed into the 1× TAE buffer inside the horizontal electrophoresis apparatus, and the comb was removed. 1 μg of the sample DNA was loaded into the gel well, and an voltage of 80V was applied for 90 minutes to cause the DNA to migrate to the anode. 1 μg of either TrackIt™ 1 Kb Plus DNA Ladder (10488085; Thermo Fisher) was used as the DNA size standard.

2.2 Protein preparation and analysis

2.2.1 β-galactosidase purification

β-galactosidase of *E. coli* (G5635; Sigma-Aldrich) was further purified and characterised by gel filtration using a calibrated Supderdex 200 10/300 GL column (GE Healthcare Life Sciences). The column was equilibrated with Dulbecco's PBS (D8537; Sigma Aldrich), the column was calibrated by three separate analyses of standards: vitamin B12 (1 kDa; V2876; Sigma-Aldrich) and blue dextran (2000 kDa; D5751; Sigma-Aldrich); cytochrome C (12 kDa; C2506; Sigma-Aldrich), bovine serum albumin (66 kDa; A7030; Sigma-Aldrich) and ferritin (440 kDa; F4503; Sigma-Aldrich); and ovalbumin (43 kDa; A5503; Sigma-Aldrich) and alcohol dehydrogenase (150 kDa; A7011; Sigma-Aldrich). β-galactosidase was eluted at the expected elution volume for a tetramer of *c.a.* 491 kDa, this molecular weight is close to the actual molecular weight of tetrameric β-galactosidase of 465 kDa, the collected fractions were concentrated using a Vivaspin protein concentrator (Z614092; Sigma-Aldrich), snap frozen and stored at -80˚C for future use.

2.2.2 Measurement of β-galactosidase activity using a plate reader

The snap frozen β-galactosidase was thawed, serial diluted and incubated with final concentration of 2.5 μM fluorescent substrate SPiDER-βGal (SG02-10; Dojindo) for 30 minutes at room temperature inside a 96-well black clear bottom

microplates (3631; Corning). The fluorescent signal was measured using the CLARIOstar Plus plate reader (BMG LABTECH).

2.2.3 α-synuclein protein expression

BL21(DE3) (carries the gene for T7 RNA polymerase under control of the lacUV5 promoter) competent *E. coli* (C2527; New England BioLabs) was transformed with carbenicillin resistant pET23a encoding a codon optimised gene encoding full length human α-synuclein using the heat shock transformation. Briefly, 1 µl of 200 ng/ml plasmid was added to 50 µl of the *E. coli*, followed by incubation on ice for 30 minutes and immediately followed by heat shock procedure at 42°C for 45 seconds in a heat block. The transformed *E. coli* was then inoculated in a 25% (w/v) Luria broth medium for 60 minutes at 37°C, and then grown overnight at 37°C on 25% (w/v) Luria broth agar plates containing 25 µg/ml of carbenicillin. A single bacterial colony was picked and grown overnight at 37°C with constant shaking at 200 rpm in 150 ml 25% (w/v) Luria broth containing 25 µg/ml of carbenicillin. The bacterial culture was mixed with 30% (v/v) autoclaved glycerol at the ratio of 1:1, and aliquoted into 1 ml cryotube vials (V7884; Sigma-Aldrich) and stored at -80°C as a glycerol stock for future use.

For the large scale expression of the α-synuclein, approximately 1 µl of the transformed bacteria glycerol stock was added to 1 ml of 25% (w/v) Luria broth containing 25 µg/ml of carbenicillin and was grown overnight at 37°C with constant shaking at 200 rpm. This starter culture was then added to 1 L of 25% (w/v) Luria broth containing 25 µg/ml carbenicillin under constant 200 rpm shaking at 37°C. Protein expression was induced by adding isopropyl β-D-1-thiogalactopyranoside to a final concentration of 1 mM when the culture reached an OD_{600} of 0.6, followed by incubation for 4 hours.

The pET23a plasmid encoding A90C α-synuclein single mutated version (expression under control of T7 expression) of the wild type human full length α-synuclein was transformed and expressed by Dr Michael Davies, the expression procedures of the A90C α-synuclein are the same as the wild-type full length human α-synuclein.

2.2.4 α-synuclein protein purification

The purification of monomeric α-synuclein was performed as following. After the IPTG induction the *E. coli* was collected by continual action centrifuge (Heraeus™ Biofuge™ Stratos™ Centrifuges; HCA 10.300 centrifuge rotor; Thermo Scientific) at 15,000×rpm. The collected *E. coli* was lysed by resuspending the *E. coli* into lysis buffer (25 mM Tris-HCl, pH 8.0; 100 µg/ml lysozyme; 50 µg/ml phenylmethylsulfonyl fluoride; 20 µg/ml deoxyribonuclease (DNase); 1 mM EDTA and frozen overnight at -20°C.

The lysed bacteria were then thawed and lysed by mechanical homogenisation followed by 10 minutes incubation at 70°C in water bath. The bacteria debris pellet was removed by centrifugation at 35,000×rcf for 30 minutes at 4°C (JLA 16.250 rotor; Beckman). The supernatant was titrated to pH 3.5 with 1 M HCl and incubated for 30 minutes with gentle stirring using a magnetic stirrer inside 4°C cold room. Then, the supernatant was collected by centrifugation at 35,000×rcf (JLA 16.250 rotor; Beckman) for 30 minutes at 4°C and the supernatant titrated with 1 M NaOH to pH 7.5. The solution was dialysed against 20 mM Tris-HCl pH 7.5 using a 3.5 kDa dialysis membrane (68035; Thermo Scientific) overnight at 4°C with gentle stirring constantly with a magnetic stirrer.

α-synuclein was purified from the dialysed protein solution by anion-exchange chromatography, followed by size exclusion chromatography to increase the purity. The XK 50/20 column (Amersham Bioscience) packed with Q-Sepharose (GE Healthcare) were used for anion-exchange chromatography on the AKTA Prime column purification system (GE Healthcare). The column was equilibrated with 20 mM Tris-HCl, pH 7.5 buffer (Buffer A) with 15% (v/v) of 1 M NaCl, 20 mM Tris-HCl, pH 7.5 (Buffer B). After stable A_{280} and conductivity values were obtained, the protein solution was loaded onto the column and then followed by 1 column volume (approximately 300 ml) of buffer A with 15% (v/v) of buffer B, this is equivalent to a total of 150 mM of NaCl throughout the entire column. Proteins were eluted under constant gradient of 3 column volume of buffer B from 15 to 50%, *i.e.* 150 mM to 500 mM NaCl. Eluted fractions were collected at between 30 to 37% of the buffer B, *i.e.* 300 to 370 mM NaCl concentration. The collected anion-exchange fractions were then further purified by size exclusion chromatography. The eluted fractions were pooled and stored at 4°C for short term storage. The Superdex 75 10/300 GL column (GE Healthcare) was used with the AKTA Prime

column purification system (GE Healthcare) and equilibrated with buffer A. The protein solution was loaded onto the column and the α-synuclein containing fractions were collected and pooled together, the fractions were dialysed against 30 mM ammonium bicarbonate using a 3.5 kDa dialysis membrane at 4°C with gentle stirring using the magnetic stirrer overnight. The protein was then lyophilized and stored at -20°C for future use. The molecular weight of the lyophilized α-synuclein was confirmed by mass spectrometry.

The purification procedure for the A90C mutated human full-length α-synuclein monomers followed the same procedure as the wild-type full length α-synuclein. This was carried out by Dr Michael Davies.

2.2.5 Mass spectrometry

Mass spectrometry was carried out to identify the molecular mass of the purified α-synuclein. Molecular mass was calculated using liquid chromatography electrospray ionisation mass spectrometry. Samples were submitted at 100 μM in 1× Dulbecco's PBS (D8537; Sigma-Aldrich) and filtered through 0.22 μm prior to mass spectrometry measurement. The measurement and analysis of the sample were carried out by Rachel George in the University of Leeds Mass Spectrometry Facility.

2.2.6 α-synuclein fibril formation

To generate the α-synuclein fibril seeds the lyophilised monomeric protein was rehydrated in 1× Dulbecco's PBS at a concentration of 500 μM and filtered through a 0.22 μm syringe filter. 500 μl of the filtered protein was transferred to a 2 ml glass vial (27267-U; Sigma-Aldrich) and a sterile magnetic stirrer bar added before the vial was sealed. The vial was then placed inside a mineral oil bath on top of a magnetic stirrer with heating (N2400-3010; STARLAB) and stirred for 3 days at 1500 rpm at 40˚C. The resultant α-synuclein fibril seeds were pelleted down by centrifugation at 16,000×rcf for 1 hour inside a table top centrifuge. The protein concentration of the pellet was checked by BCA assay (J63283; Alfa Aesar) and was diluted down to 200 μM monomeric equivalent concentration with 1× Dulbecco's PBS, snap frozen and stored at -80˚C for future use.

To generate fibrils by elongating the seeds, thawed fibril seeds in Eppendorf tubes were first sonicated inside a water bath sonicator at maximum power at 25 ºC (U500H; Ultrawave) for 5 min prior to use. Lyophilised monomeric α-synuclein was rehydrated with 1× Dulbecco's PBS at a concentration of 200 μM and filtered through 0.22 μm syringe filter. The freshly thawed sonicated fibril seeds were mixed with filtered monomeric α-synuclein such that the final solution contained 10% (v/v) fragmented fibrils and 100 μM of α-synuclein monomers in 500 μl inside a 1.5 ml Eppendorf tube. The sample was then incubated at 37˚C under intermittent shaking conditions (600 rpm shaking for 5 seconds followed by every 4:55 minutes without shaking) for 5 days using the Thriller shaking incubator (91-7010; Peqlab). The resultant fibrils were stored at room temperature for future use.

To generate the Alexa Fluor 594 labelled A90C α-synuclein fibril seed, the A90C α-synuclein fibril seed was generated following the same procedure as the wild-type α-synuclein. After 3 days of stirring at 1500 rpm at 40°C, the resultant A90C α-synuclein fibril seeds were collected by centrifugation at 16,000×rcf for 1 hour. The protein concentration of the pellet was checked by BCA assay and was diluted down to 100 μM monomeric equivalent concentration with 1× Dulbecco's PBS. Dithiothreitol (DTT) was added to the fibril seeds to a final concentration of 5 mM and incubated for 30 minutes on bench. After incubation, the fibril seeds were pelleted down by centrifugation at 16,000×rcf for 40 minutes, the pellet was kept and washed with 1× Dulbecco's PBS by pipette aspiration mixing. The pelleting and washing processes were then repeated for 3 times to remove DTT. The resultant pellet was then labelled with the Alexa Fluor 594 dye by incubating with 10 mM Alexa Flour 594 Maleimide (A10256; Thermo Fisher) at 4°C for 16 hours. Unbound Alexa Fluor 594 Maleimide dye was removed by pelleting and washing processes for 3 times to remove the dye similar to the removal of DTT. The protein concentration of the Alexa Fluor 594 labelled A90C fibril seed pellet was checked by BCA assay and diluted down to 200 μM monomeric equivalent concentration with 1× Dulbecco's PBS, snap frozen and stored at -80˚C for future use. The generation of the Alexa Fluor 594 A90C α-synuclein fibril seed was carried out by Dr Michael Davies.

2.2.7 Atomic Force microscopy (AFM) and sample preparation

1 µl of the 100 µM (monomeric equivalent) fibril samples was added to 99 µl of 1 M $MgCl_2$ and incubated for 15 minutes, then the solution was deposited onto a freshly cleaved mica (AGG250-1; Agar Scientific) and incubated for 30 minutes. The solution was drained, and the mica surface was washed 3 times with ddH_2O and dried with streams of nitrogen, followed by overnight drying at room temperature. The α-synuclein fibrils were imaged using a Dimension Fastscan (Bruker) in air tapping mode using the Fastscan A Silicon Nitride cantilever (FASTSCAN-A; Bruker). The probes were driven at resonance (1400 kHz in air). Images were acquired with a scan rate of 8-15 Hz (1024 X 1024 pixels) and processed with Nanoscope Analysis v1.9. The length and height data of the fibrils were analysed by FiberApp (Usov and Mezzenga, 2015).

2.3 Single molecule detection with nanopipette

2.3.1 Electrolyte bath preparation

The reagents used for the generation of the PBS electrolyte bath are shown in Table 2.1.

Table 2.1. Reagents used for the preparation of the electrolyte bath

Chemical	Catalogue	Supplier
Dulbecco A PBS Tablets (Composition at 1 × concentration: 137 mM NaCl, 3 mM KCl, 8 mM Na_2HPO_4, 1.5 mM KH_2PO_4)	BR0014	Oxoid
Polyethylene Glycol 4000 (PEG 4000)	A16151	Alfa Aesar
Polyethylene Glycol 8000 (PEG 8000)	043443	Alfa Aesar
Glycerol	G2025	Sigma Aldrich
Bovine Serum Albumin (BSA) >99%	BS9808K	BioServ UK Limited

A 10× concentrated PBS solution was made by dissolving the PBS tablets in ddH_2O, followed by autoclaving, then the 10× concentrated PBS was diluted to 1× with ddH_2O.

To generate 10 ml of 50% (w/v) PEG crowded bath, 5 g of PEG of desired molecular weight was added to 1 ml of 10× PBS and 4 ml of ddH_2O. The solution mixture was put inside a 70°C oven for 2 hours to completely dissolve the PEG, followed by overnight incubation at 37°C. The PEG solution was allowed to cool

down to room temperature prior to usage. To generate 10 ml of a 50% (v/v) glycerol PBS bath, 5 ml of glycerol was added to 1 ml of 10× PBS and 4 ml of ddH_2O. For a BSA PBS bath, lyophilized BSA powder was dissolved in ddH_2O to 0.4 g/ml (40% w/v) concentration overnight at 4°C and then diluted with 10× PBS and ddH2O to obtain a concentration of 30% (w/v).

The 50% (w/v) PEG solution, 50% (v/v) glycerol solution and 30% (w/v) BSA PBS solution were diluted with 1× PBS to change the concentration of the PEG, glycerol and BSA without altering the ionic strength of the solution.

2.3.2 Nanopipette fabrication and ion current measurement

Quartz glass with filaments with an outer and inner diameter of 1.0 mm and 0.5 mm respectively were used to fabricate nanopipettes (QF100-50-7.5; Sutter Instrument). Nanopipettes were fabricated by using the SU-P2000 micropipette puller (World Precision Instruments), the fabrication of the nanopipette involves laser melting the centre of the quartz glass while simultaneously pulling the nanopipettes apart (Figure 2.1A), each quartz capillary produce a pair of nanopipettes with an almost identical pore size and geometry.

For the production of the 25 nm nanopipette, the two-line parameter used was: (1) HEAT, 750; FIL, 4; VEL, 30; DEL, 145; PUL, 80, followed by (2) HEAT, 625; FIL, 3; VEL 40; DEL 135; PUL, 150. For the 80 nm nanopipette, two-line parameter used was: (1) HEAT, 750; FIL, 4; VEL, 30; DEL, 150; PUL, 80, followed by (2) HEAT, 500; FIL, 3; VEL 40; DEL 135; PUL, 150. It should be noted that the pulling protocol is instrument specific and there is variation between each laser puller. The fabricated nanopipette typically has a cone shaped geometry, the cone angle θ can be approximated by using the taper length and the shank radius, these parameters are obtained by scanning electron microscopy (Figure 2.1B).

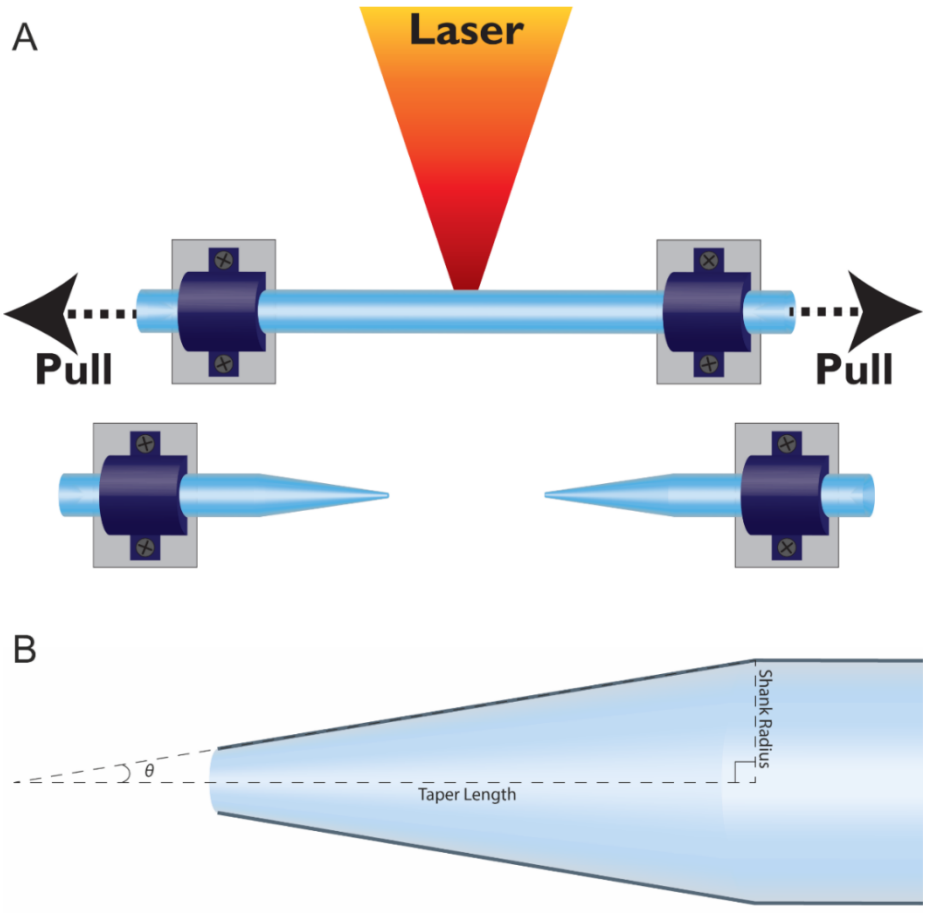

Figure 2.1. Schematic illustration of the fabrication process for a pair of nanopipettes and the geometry of a nanopipette. *(A) The glass capillary was inserted into the SU-P2000 micropipette puller, a laser heat source was applied onto the centre of the capillary, simultaneously, the capillary was pulled by force in the opposite direction. The whole process is controlled by specified pulling parameters. Each glass capillary will generate a pair of nanopipette. (B) The schematic illustration of the geometry of a nanopipette tip end. To characterise the nanopipette, the taper length and the shank radius are often used.*

2.3.3 Scanning Electron Microscopy

The nanopores of the nanopipettes were imaged by scanning electron microscopy (SEM) (Leo 1530 FEG-SEM; Zeiss). The nanopipette was first coated with a gold layer of few nanometer thicknesses via sputter coating. The nanopipettes were then mounted onto the sample holder and tilted to an angle of 60 and above for imaging. The nanopipettes were imaged at between 2 and 3 kV at a working distance of 5 mm and below at an aperture size of 30.00 m using an InLens detector. The SEM images used in the thesis were performed by Dr Mukhil Raveendran, Dr Mark Rosamond and Samuel Confederat.

2.3.4 Nanopipette pore size estimation

Besides using the SEM to image the nanopore of the nanopipette, the pore diameter can also be estimated by theoretical approach based on an equation from Perry et al (Perry et al., 2016a) will be used, this equation does not consider the surface charge contributed by the quartz surface.

Equation 1

$$R_{Nanopipette} \approx \frac{1}{\kappa \pi r_i \frac{shank\ radius}{taper\ length}} + \frac{1}{4\pi r_i}$$

Where the $R_{Nanopipette}$ is the resistance of the pore in Ω, κ is the solution conductivity in S/m, r_i is the inner nanopipette radius in m, the shank radius is in m and taper length is in m.

The Perry *et al.* model does not consider surface conductivity contribution to the nanopore conductance (Perry et al., 2016a). A better approximation should consider the surface charge on the quartz wall which induces an electroosmotic flow (EOF) that contributes to the ion concentration distribution within the nanopore and influences the current response (EOF will be further discussed in Chapter 4). In particular, a positive voltage will cause a EOF directed out of the pore and a negative voltage will cause an EOF in the opposite direction. The result of this flow is an increase in the ion-current rectification induced by the charge at the quartz wall (ICR will be further discussed in Chapter 4). Also, Perry model does not include the stray capacitances acting at the interface of the nanopipette and the electrolyte. The resistive behaviour introduced by Perry *et al.* has to be summed to the capacitive effect of the dielectric (quartz) between the inner and outer solution, thus, a total impedance has to be considered. However, when working with direct current voltages throughout this thesis, the capacitance has a negligible effect and it is common practice not to include it in the impedance calculation which will then involve only a series of resistors, as Perry introduced (Perry et al., 2016a). Furthermore, as the aim is not to generate an accurate model that describes the relationship between resistance and pore's dimension, but rather the purpose of the equation is only to check whether the pore's dimensions are significantly different between each fabrication. Additionally, the actual size of the nanopore will be characterised through scanning electron microscopy (Section 2.3.3).

The following parameters were used: 1.2 S/m (0.1 M KCl conductivity), the resistance value of the of the nanopipette when 0.1 M KCl is used inside the nanopipette and also as the bath, 4 mm taper length and 250 µm shank radius. The output of the equation will then be the pore radius in m.

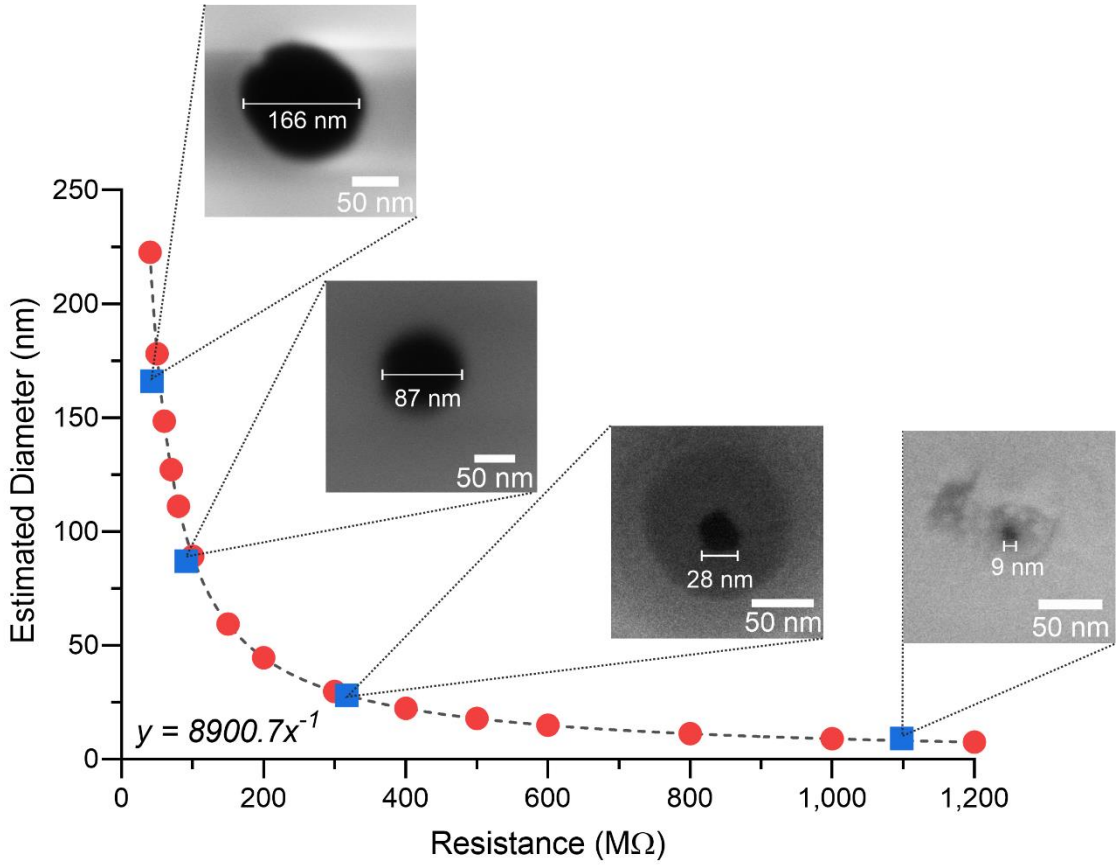

Figure 2.2. Nanopore diameter estimation curve based on equation 1. *Assuming the electrolyte conductivity and minimum variations on the geometry of the nanopipette, a simpler equation $y = 8900.7\ x^{-1}$ can then be used to approximate the diameter of the nanopore instead. Red dots indicate the estimated diameters when different resistance values are used in the equation. Blue squares indicate the measured nanopores' sizes (scanning electron microscopy image inserts) and the corresponding resistance value.*

The values of the taper length and the shank radius were obtained by SEM imaging are further refined by Dimitrios Soulias and Fabio Marcuccio through the combination of current-voltage curve and COMSOL Multiphysics modelling.

Multiple values of resistance ranging from 1200 to 50 MΩ were input into the equation, under the assumption that the geometry (taper length and shank radius) of the nanopipette remains the same, the pore radius and diameter can then be approximated. These values were used to construct a calibration curve with a simplified equation to estimate the nanopore diameter (Figure 2.2). The accuracy

of the estimation curve is cross checked through nanopore imaging via the scanning electron microscopy.

2.3.5 Single molecule detection set-up

For the translocation experiments, the nanopipettes were filled with analyte of interest diluted into 1× PBS, the nanopipette was fitted with a Ag/AgCl working electrode. The tip of the nanopipette was then immersed into the electrolyte bath of choice with a grounded Ag/AgCl reference electrode, thus establishing a complete electric circuit between the inside of the nanopipette to the outer bath solution. Depending on the polarity of the analyte, the application of a voltage to the working electrode caused molecules from inside of the nanopipette to translocate through the nanopore and into the bath solution. The ionic current was measured using a MultiClamp 700B (Molecular Devices) patch-clamp amplifier in voltage-clamp mode. Unless specified, the signal was filtered using Bessel filter at 10 kHz and digitized with a Digidata 1550B (Molecular Devices) at a 100 kHz sampling rate (every 10 μs) and recorded using the software pClamp 10 (Molecular Devices).

2.3.6 Current Trace analysis and data output

Event current analysis was carried out with a custom MATLAB script (provided by Prof Joshua B. Edel, Imperial College, London, UK). The MATLAB script is capable of picking out individual events in given ion current trace using defined thresholds, at least 5 standard deviations above baseline noise. The baseline is tracked via asymmetric least square smoothing algorithm and fit determined by Poisson probability distribution function. The first and last data point above the calculated baseline for each event is taken as the start and the end of the event, the event current peak maxima is measured away from the baseline, then the event dwell time is measured by full width at half maximum of the full translocation event. Figure 2.3 depicts the analysis process.

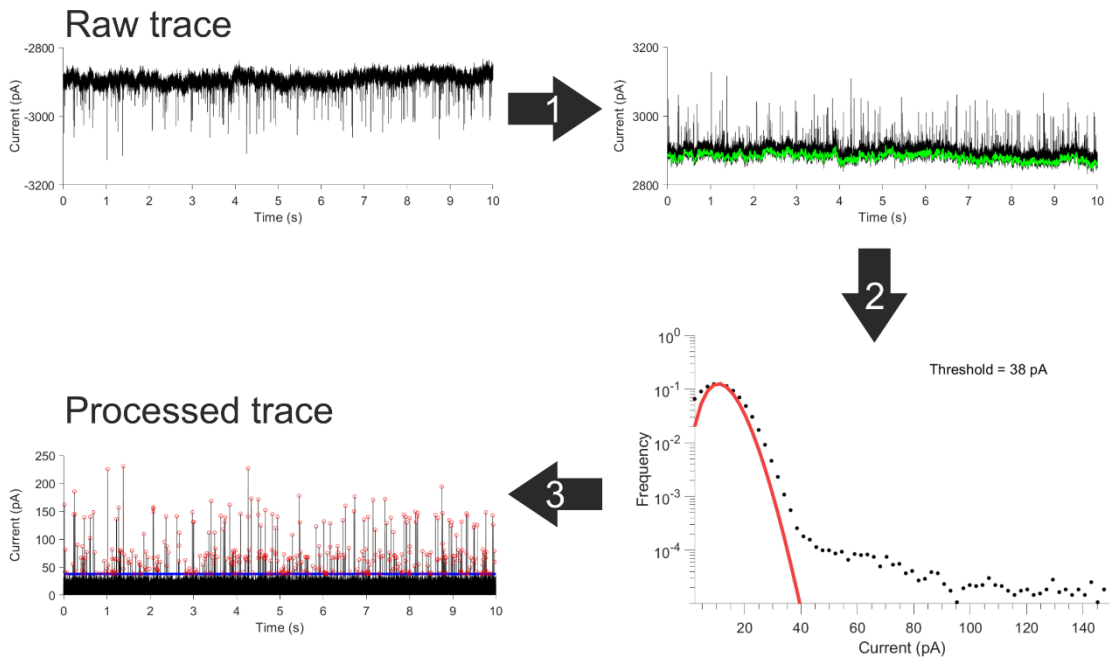

Figure 2.3. An example workflow of the MATLAB script analysis on trace. *The raw current trace is loaded into the custom written MATLAB script. (1) The MATLAB script first inverted the raw trace as the event peaks go downward (the translocation caused an increase in the conductance), then the baseline is tracked via an asymmetric least square smoothing algorithm. (2) The threshold is then determined by Poisson probability distribution function at a minimum of 5 standard deviations above baseline noise. (3) Translocation events that are above the threshold are collected for analysis.*

The script calculated data outputs were plotted with different statistical software. The main output of the trace data included the current peak maxima and dwell time. For the calculation of the average and error of the overall dwell time value, the standard error of the mean (S.E.M.) were reported as the S.E.M. calculation indicated, not according to the hardware limitation.

2.4 Cell Culture and Nanoinjection

2.4.1 Cell culture and maintenance

All cells were cultured in cell culture flasks (83.3911.302; Sarstedt) or 35 mm glass bottom dishes (FD35-100; World Precision Instrument Ltd) inside an incubator at 37°C with 5% CO_2. Table 2.2 lists the cells used in this thesis and the culture medium used.

Table 2.2. Cell lines used in this thesis and the culture medium composition.

Cell Line	Origin	Culture medium
HeLa	CVCL_0030, Verified by ECACC	Dulbecco's Modified Eagle's Medium (D5671; Sigma Aldrich) supplemented with 1× GlutaMax™ (35050038; Thermo Fisher), 1× Penicillin Streptomycin (15140122; Fisher Scientific) and 10% (v/v) foetal bovine serum (F7524; Sigma Aldrich)
HeLa RNuc	Established by expressing pmCherry-NLS in the original HeLa CVCL_0030. Followed by FACS sorting	Dulbecco's Modified Eagle's Medium (D5671; Sigma Aldrich) supplemented with 1× GlutaMax™ (35050038; Thermo Fisher), 1× Penicillin Streptomycin (15140122; Fisher Scientific) and 10% (v/v) foetal bovine serum (F7524; Sigma Aldrich)
Normal Human Epidermal Keratinocytes (NHEK)	C-12005; PromoCell	Keratinocyte Growth Medium 2 (C-20011; PromoCell), 1× Penicillin Streptomycin (15140122; Fisher Scientific)
Human Umbilical Vein Endothelial Cell (HUVEC)	C-12253; Promocell	Endothelial Cell Growth Medium (C-22010; PromoCell), 1× Penicillin Streptomycin (15140122; Fisher Scientific)
Primary Rat Cortical Neurons	A36511; Gibco	Neurobasal medium (21103049; Gibco), 1× GlutaMax™ (35050038; Thermo Fisher), 1× B-27 supplement (17504044), 1× Penicillin Streptomycin (15140122; Fisher Scientific)
Primary Mouse Dorsal Root Ganglion (DRG) Neurons	Provided by Prof Nikita Gamper's research group in University of Leeds	Neurobasal medium (21103049; Gibco), 1× GlutaMax™ (35050038; Thermo Fisher), 1× B-27 supplement (17504044), 1× Penicillin Streptomycin (15140122; Fisher Scientific)

For dividing cells (HeLa, HeLa RNuc, NHEK and HUVEC), the cells were passaged when they were confluent. The cells were washed with 1× Dulbecco's PBS (D8537; Sigma Aldrich), followed by the addition of a pre-warmed 1× trypsin-EDTA (T3924; Sigma Aldrich), the cells were then left inside the incubator for 3 minutes, the detached cells were collected by centrifugation at 500×rcf to remove the trypsin-EDTA, the pellet was immediately resuspended in culture medium, then plated into a cell culture flask or onto the 35 mm glass bottom dish. To cryopreserve the cells for long term storage, after the removal of the trypsin-EDTA solution, cells were resuspended in Synth-a-Freeze™ Cyropreservation medium (A1254201; Gibco) at minimum of 1×10^6 cells/ml. A minimum of 100 µl of the resuspended cell mixture was dispensed into a 1.8 ml cryovial (E3090-6222; Starlab). The cryovial was immediately sealed inside a polystyrene box and frozen down overnight at -80°C, and then transferred to a liquid nitrogen canister for long term storage.

For neuronal cell-culture, the glass bottom dish was pre-coated with synthetic laminin peptide (SCR127; Sigma Alrich) according to the manufacturer's instructions. After treatment, all solutions were removed from the inside of the

dish and rinsed with ddH_2O, then the dishes were dried inside the flow hood and wrapped with parafilm and stored at 4°C. Prior to use, the dishes were rinsed two times with pre-warmed culture medium. For the primary rat cortical neurons, the 1 ml thawed cell vial (1×10^6 cells) was mixed with 11 ml of the pre-warmed culture medium , and plated equally onto six laminin coated dishes. For the primary mouse DRG neurons, the cells were obtained by dissection carried out by Dr Vincenzo Prato of Prof Nikita Gamper's research group in University of Leeds, the neurons were deposited onto the laminin coated 35 mm glass bottom dishes. The day of either thawing or dissection was dated as day 0 and all neurons were used between 3 to 10 days counting from day 0.

2.4.2 Cell transfection and Cell line establishment

Three plasmids were used to transfect cells in this thesis: pMaxGFP, pmCherry-NLS and the pSV-β-Galactosidase Control Vector (E1081; Promega). To transfect cells, Lipofectamine® 2000 (11668030; Thermo Fisher) was used. The cells were plated at 50% confluency inside a 35 mm dish prior to the day of transfection in standard culture medium. 4 μg of the plasmid was diluted into 125 μl of serum-free culture medium in one Eppendorf tube, then 4 μl of lipofectamine reagent was diluted in 125 μl of serum-free culture medium in another Eppendorf tube, the two tubes were allowed to sit on bench for 5 minutes. Then the plasmid containing culture medium was dispensed drop by drop into the lipofectamine serum-free culture medium containing tube and incubate at room temperature for another 15 minutes. The mixture was then dispensed onto the culture dish and incubated overnight, the culture medium was exchanged the next day. Transfection was confirmed by microscopic imaging using a Zeiss LSM880 with Airyscan (Zeiss) or with an EVOS microscope with an appropriate fluorescent wavelength light cube.

The establishment of the HeLa RNuc stable cell line involved the transfection of the pmCherry-NLS into the HeLa (CVCL_0030) cell line. Upon transfection, the cells were cultured in standard culture medium with an additional G418 sulfate (10131035; Gibco) at 1 mg/ml concentration to apply selective pressure for 2 weeks. Then the cells were sorted by fluorescence-based flow cytometry (FACS) and only selected for the high brightness cells. The FACS sorting was done by Dr Ruth Hughes at the University of Leeds Bio-imaging and Flow Cytometry facility.

2.4.3 Scanning Ion Conductance Microscopy

The SICM scan head consisted of a Z-piezo motor with the range of 25 µm for the vertical positioning of the nanopipette and a 100 µm XY-piezo motor for lateral positioning of the sample (Ionscope). The SICM set-up utilises the AxoPatch 200B (Molecular Devices) patch-clamp amplifier in voltage-clamp mode. The signal was filtered using Bessel filter at 10 kHz and digitized with a Digidata 1440A (Molecular Devices) at a 100 kHz (interval 10 µs) sampling rate and recorded using the software pClamp 10 (Molecular Devices). A custom written software by Dr Pavel Novak of ICAPPIC Ltd was used to control the SICM set-up (Novak et al., 2009). A nanopipette filled with analyte was used to approach the cell surface via the hopping mode where the nanopipette is vertically approached to the cell surface until the ion current drops below 99.5% of the baseline ion current, thereby defining the height of the surface at this position (Novak et al., 2009). Repeating this procedure for many positions on the cell surface generates an image of cell topography. The SICM image data was processed by custom written software provided by Dr Pavel Novak of ICAPPIC Ltd. All SICM experiments required the use of 35 mm glass bottom culture dish.

The SICM experiments on cells were performed in CO_2-independent Leibovitz's L-15 medium (21083-027; Gibco). The SICM set-up is placed directly on top of a Yokogawa Spinning Disk confocal system coupled with ANDOR iQ3 live cell imaging system (Oxford Instrument), allowing fluorescence and brightfield imaging. The confocal microscope was fitted with a 455, 488 and 561 nm laser and emission filter set that enables the visualisation of a wide range of fluorescent dye. The nanopipette tip was aligned with the microscope and positioned next to a cell of interest for scanning or nanoinjection.

2.4.4 Nanoinjection

For all nanoinjection procedures, the ion current trace was recorded by pClamp 10 (Molecular Devices). All fluorescent images were captured by the ANDOR iQ3 live cell imaging system with appropriate excitation laser and emission filter combinations. The nanopipette was lowered down at 10 µm/s during cell penetration.

Different biomolecules were injected in the work described in this thesis and their solution preparation is outlined below.

For fluorescein-conjugated dextran 70,000 g/mol (11520226; Fisher Scientific), the dextran was dissolved and diluted in 0.22 μm filtered 1× PBS, aliquoted and then stored at the concentration of 140 μM at -20°C. To perform injection, the dextran was further diluted down to 140 nM in 1× PBS prior to use, the solution of dextran was then used to fill up the nanopipette.

For pMaxGFP, the cells were plated onto a 35 mm glass bottom gridded dish (81148; Ibidi). The grid had lettered and numbered 4×400 squares with a 50×50 μm dimension for each square. The pMaxGFP plasmids were diluted to 1.3 nM in 1× PBS and used to fill the nanopipette. The duration of the nanoinjection part of the experiments all lasted less than 2 hours, after which the L-15 medium was replaced with the culture medium before returning to the incubator.

For β-galactosidase nanoinjection, in addition to the standard L-15 medium, a final concentration of 2 μM SPiDER-βGal (SG02-10; DOJINDO) was added. SPiDER-βGal was the fluorescent substrate for β-galactosidase. The size excluded chromatography purified β-galactosidase was diluted to 1 μM with 1× PBS and used to fill the nanopipette. As an injection control, a 100 nM 1× PBS diluted Alexa Fluor 594 Maleimide was also used to perform nanoinjection in the nucleus.

For the α-synuclein fibril seeds nanoinjection, A90C Alexa Fluor 594 labelled α-synuclein fibril seeds were generated and provided by Dr Michael Davies. The processes were described in Section 2.2.3, 2.2.4 and 2.2.6. The 200 μM monomeric equivalent fibril seeds were diluted to 1 μM monomeric equivalent with 1× PBS. The solution was then used to fill up the nanopipette for nanoinjection.

Chapter 3

Quantitative Nanoinjection of Biomolecules into Cells Via Nanopipette

3.1 Scanning Probe Microscopy

The Scanning probe microscopies (SPM) are a family of techniques employing a scanning probe to map the topography of surfaces and interfaces (Bottomley, 1998). The most widely used SPM is the atomic force microscopy (AFM) which was developed in 1986 (Binnig et al., 1986) and utilises a nanoscale tip placed at the tip of a cantilever as the scanning probe. In a standard AFM set-up, a laser beam is focused on the cantilever and a position sensitive photo detector monitors the position of the laser while the probe is scanned over the surface in the lateral direction. The physical interaction between the cantilever tip and the surface of the sample displaces the cantilever in the vertical direction, *i.e.* the Z plane. Since the Z plane is monitored while the scanner moves in the lateral directions, a surface topography map can be generated (Jalili and Laxminarayana, 2004). The AFM has been used to obtain the topography of molecules such as water networks (Shiotari and Sugimoto, 2017; Cao, D. et al., 2019) and it is also frequently used to characterise nanoparticles and protein structures including amyloid fibrils (Lutter et al., 2019; Aubrey et al., 2020; Nirmalraj et al., 2020; Heath et al., 2021). However, the force applied to the surface is not ideal for the topography mapping of "soft" eukaryotic cells as it may distort the cells during the scan. An alternative SPM to map the topography of cells is scanning ion conductance microscopy (SICM). The SICM is a non-contact SPM that relies on the ion current through a nanopipette to monitor the probe-surface distance rather than a force interaction (Chen, C.C. et al., 2012; Page et al., 2017; Zhu, C. et al., 2020).

3.1.1 The Scanning Ion Conductance Microscopy

The SICM was developed in the 1989 (Hansma et al., 1989) and unlike the AFM, the SICM uses a glass nanopipette as the scanning probe (Chen, C.C. et al., 2012; Stanley and Pourmand, 2020; Zhu, C. et al., 2020). The SICM operates in a conductive liquid environment, *i.e.* in electrolytes, and it utilises the ion current through a nanopipette as the feedback mechanism (Figure 3.1A).

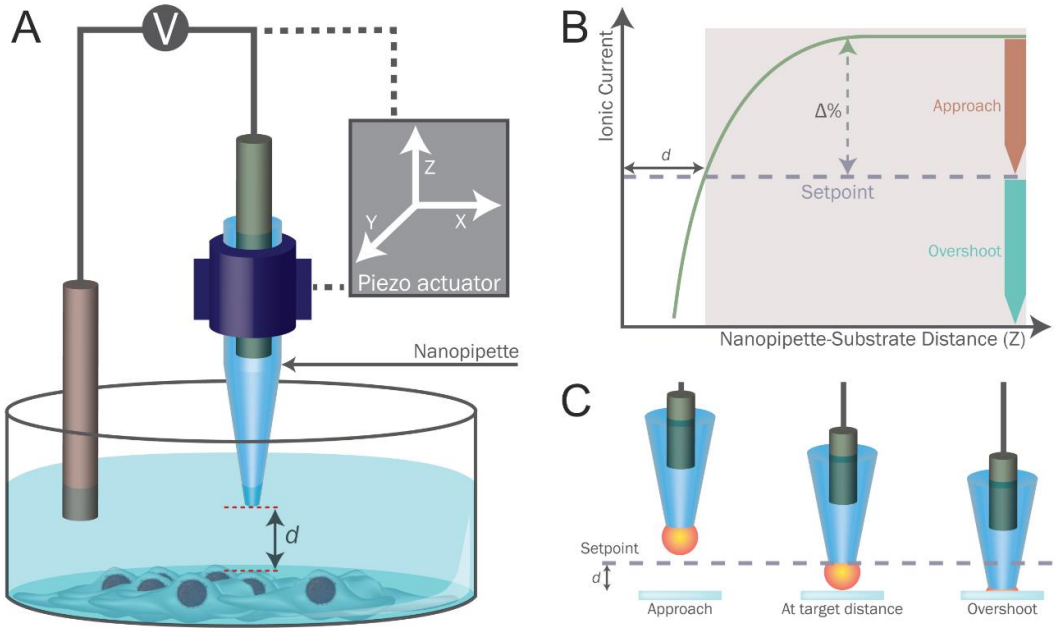

Figure 3.1. The principles of Scanning Ion Conductance Microscopy (SICM). *(A) illustrates the set-up of the SICM. The core components of the SICM are: a nanopipette probe inserted with an electrode, an additional electrode in the bath and electrolytes between the two electrodes. The position of the nanopipette is controlled by the vertical Z-piezo actuator and the lateral X- and Y-piezo actuator. When the nanopipette has reached a vertical distance that is less than the diameter of the nanopipette, it causes the ionic current to substantially drop as illustrated in (B). By predefining the setpoint (Δ% of the change in the current baseline), the nanopipette stops approaching the surface once the setpoint is reached. Thus the setpoint controls the distance d between the nanopipette probe and the substrate. The nanopipette can overshoot and contact the surface if it approaches the surface too fast (C).*

The operation of the SICM relies on the application of constant voltage to the nanopipette leading to a constant ionic current through the nanopore. The Z-piezo actuator lowers the nanopipette to approach the substrate and when the distance between the nanopipette tip and the substrate is smaller than the diameter of the pore of the nanopipette, the ionic current starts to drop (Figure 3.1B). The ionic current drop is due to the flow of ions at the nanopipette tip being hindered by the substrate, and this additional resistance due to the surface is termed the access resistance (Chen, C.C. et al., 2012; Page et al., 2017; Zhu, C. et al., 2020). The magnitude of the ion current drop is measured as the percentage of drop (Δ%), and this is known as the setpoint setting in SICM, because of the relationship between the access resistance and the setpoint. The distance *d* between the nanopipette tip and the substrate can then be controlled (Figure 3.1B), as the higher the setpoint is, the shorter the distance *d* would be. The setpoint is used as the input in a feedback loop, and it maintains a constant nanopipette-substrate distance *d* as the nanopipette is scanned across the sample (Figure 3.1B) (Chen, C.C. et al., 2012; Page et al., 2017; Zhu, C. et al., 2020). However, the nanopipette

can overshoot and crash the tip into the substrate if the approach speed is too fast (Figure 3.1C). It is important to point out that under certain conditions, for example, using a narrow nanopipette, and/or approaching a charged substrate in a low ionic strength electrolyte, the ionic current may increase instead of decrease (McKelvey et al., 2014; Perry et al., 2015; Perry et al., 2016b).

The setpoint setting is important in obtaining the correct topography when scanning a substrate that contains rapid changes in height, *e.g.* steep slopes, as unsuitable setpoint settings often led to a distorted topography. To demonstrate this effect, Del Linz *et al.* used the SICM to scan a red blood cell with increasing setpoints from Δ0.3% to Δ0.8%. They showed that at high setpoint setting of Δ0.8%, the SICM topography was distorted (Figure 3.2Ai), and the cell appeared to be more rigid than the topography obtained with the Δ0.3% setpoint. (Del Linz et al., 2014).

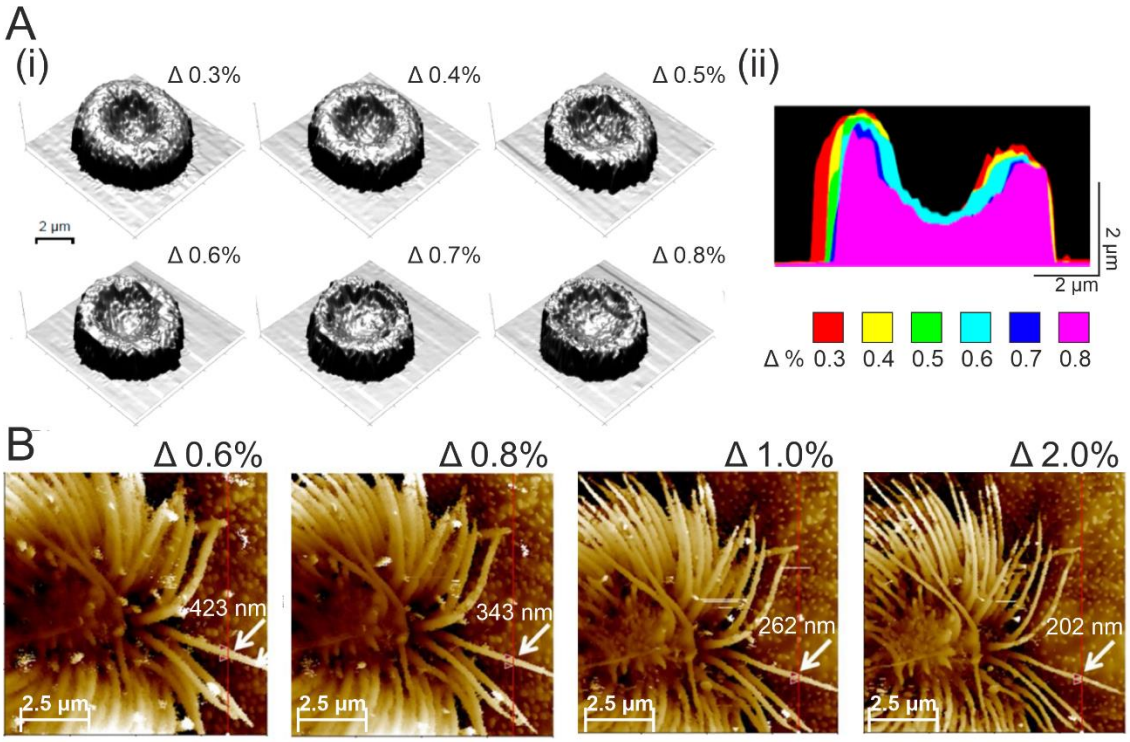

Figure 3.2. The influence of the setpoint on the generation of topography. *The topography of a red blood cell obtained by SICM (A). Higher setpoint leads to the deformation and rigid topography of the red blood cell (A(i)), and the cross-section analysis of the topologies from (i). The cross-section area of the topography is smaller when higher setpoint is used. The SICM image of the fixed rat trachea ciliated cell (B). The SICM measured width of the cilia (the red vertical line and arrow indicated the location) is reduced by almost 2 fold when changing the setpoint for Δ0.6% to Δ2.0%. This suggested deformation due to the scanning parameter. (A) is adapted and reannotated from (Del Linz et al., 2014). (B) is adapted and reannotated from (Nakajima et al., 2018).*

The cross-sectional profile of the topography of a red blood cell showed that the overall area of the high setpoint topography was smaller than that of a lower setpoint scan (Figure 3.2Aii) (Del Linz et al., 2014). Nakajima *et al.* also demonstrated similar topography distortion effects caused by the changing the setpoint from Δ0.6% to Δ2.0% on the topography of a fixed rat trachea ciliated cell (Figure 3.2B) (Nakajima et al., 2018). The study showed that the thickness of the cilia decreased from 423 nm at Δ0.6% to 202 nm at Δ2%. One of the reasons for the distortion of the topography is that the nanopipette-substrate distance is shorter when a higher setpoint is used. When a voltage is applied, the electrolyte inside the nanopipette flows out of the nanopipette and generates a nanoscale fluid flow at the tip end (Clarke, R.W. et al., 2012; Babakinejad et al., 2013). As a result, when the nanopipette is placed near the cell surface, the fluid force pushes on the cell membrane, and consequently distorts its topography. In fact, since the distance *d* and the setpoint setting modulate the magnitude of the fluidic force exerted on the cell surface, a number of studies have characterised and utilised this relationship to probe the mechanical properties of cells with SICM (Clarke, R.W. et al., 2016; Chen, Y. et al., 2018).

3.1.2 Hopping Scanning Mode

Similar to AFM, the SICM can also be operated with different scanning modes. There are three main scanning modes: the non-modulated distance constant feedback mode (DC mode), the constant distance-modulated feedback mode (AC mode), and the hopping mode. The DC scanning mode is simple, as the nanopipette is held at the setpoint value and scans the entire area, whereas the AC mode operates similarly to DC mode, but with additional controls over the tip-substrate distance (Chen, C.C. et al., 2012; Page et al., 2017; Zhu, C. et al., 2020).

Hopping mode, used in this thesis, (Novak et al., 2009) (also known as the backstep (Happel et al., 2003), standing approach (Takahashi et al., 2010) or approach-retract scanning mode (Jung et al., 2015)) was developed to reduce the scanning time while obtaining high quality topography scans. The hopping scanning mode relies on numerous repeats of approaches and the retraction of the nanopipette tip (Figure 3.3A). In hopping mode, the nanopipette approaches the surface substrate until it reaches the setpoint setting, then the height of the substrate is recorded. Unlike DC and AC mode, where the probe will start to move laterally to scan the

area, the hopping mode retracts the nanopipette back to a defined distance far away from the substrate (this distance is not controlled by the setpoint). When the nanopipette is retracted to the defined position, the nanopipette is moved laterally, then it approaches the surface again, records the height position data. Then the SICM retracts the nanopipette and moves laterally again. The approach, retract and move steps are repeated numerous times to generate the topography image, and thus the name hopping mode (Figure 3.3A) (Novak et al., 2009).

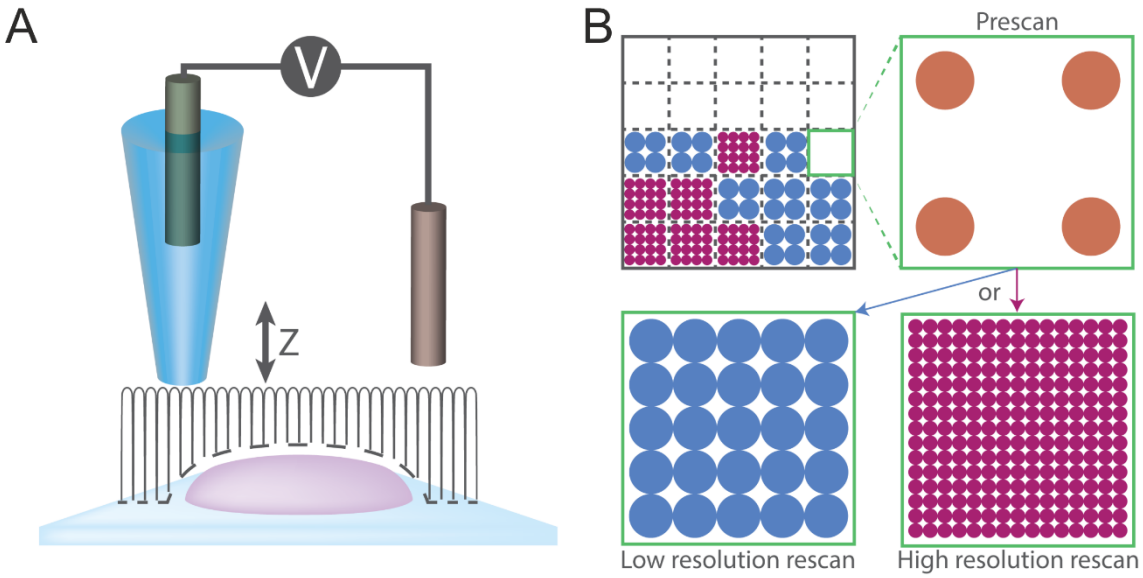

Figure 3.3. The hopping scanning mode of SICM. *The hopping scanning mode is depicted here in (A). The hopping scanning mode is composed of several steps. The nanopipette will approach the surface substrate until the setpoint is reached, then it will retract back to a predefined distance, then the probe will move laterally by a defined distance and the process will repeat, thus hopping mode. (B) Illustrates the multiple steps utilised by the hopping mode to generate the substrate topography image. 1. The scan area is divided into numerous squares ranging from 2 × 2 up to 512 × 512 squares. The number of these squares define the overall resolution of the topography, which is similar to the number of pixels in an image. A 5 × 5 square division is illustrated here. 2. In each of these squares, a prescan is performed. The prescan will take 4 vertical position data at the corner of each square and the measured position data is used to determine the overall roughness of the substrate in that square. 3. Depending on the overall roughness of the square determined by the prescan, the hopping mode will either perform a low-resolution level rescan or high resolution level rescan of the exact same square. The difference between a low resolution rescan and high resolution rescan is that there are more vertical position data in the high resolution rescan, and thus higher lateral resolution. This is depicted by more dots in the high-resolution scan compared to the low resolution rescan. Typically, a low-resolution scan is used when the prescan indicates an overall smooth substrate surface and vice versa. The final topography image generated will contain at least two levels of rescan. (A) and (B) are redrawn from (Chen, C.C. et al., 2012).*

The generation of the SICM topography image also takes multiple steps (Figure 3.3B) (Novak et al., 2009). While it can look rather complicated, the image construction is similar to how pixels are used to construct a digital image. Multiple steps are performed by the SICM: 1. A scan area is defined, for example a 25 × 25

μm scan area; 2. This 25 × 25 μm scan area is divided into numerous squares, for example, a 25 squares division, similar to how a digital image can be divided into numerous pixels. Under this division, each square/pixel will have a scan area of 5 ×5 μm. 3. A prescan is performed by using the nanopipette to approach the four corners of the square and the height position data from these four approaches is recorded. 4. The recorded height position data is processed and is used to determine the average roughness *i.e.* the overall height of the substrate. If the average substrate roughness is higher than the user defined value, a more detailed high lateral resolution rescan of the same square will be carried out while a low lateral resolution rescan of the square will be carried out if the average roughness is below the user defined value (Figure 3.3B). The high lateral resolution rescan means that there will be more hops in that square compared to the low lateral resolution rescan. For example, the high lateral resolution rescan sets the probe to laterally move 100 nm after each hop, then the 5 × 5 μm scan area of the divided square will be composed of 2500 hops. Whereas for the low lateral resolution rescan, a lateral move of 200 nm will only have 625 hops, which is 4 times less data than the high resolution rescan. Thus, despite that 25 squares/pixels are used to generate the topography of the cell, the image is composed of at least two resolution levels (Figure 3.3B) (Novak et al., 2009). This method is implemented as it can be used to provide a detailed high resolution scan on substrate like the cell, and saves valuable time from over probing the surface of the glass instead (Novak et al., 2009).

The majority of the imaging methods use the term high resolution to describe the number of pixels in a digital image. In hopping mode SICM, the term high resolution is usually used to indicate that the lateral move distance between each hop is small and narrow, and thus more of the cell surface detail is probed, and a high resolution lateral resolution scan is obtained (Novak et al., 2009). Although the hopping mode can laterally hop the probe at a very short distance, even down to <10 nm depending on the piezo actuator, it does not mean that the lateral resolution is higher than a 100 nm hop setting. Several studies have investigated how the size of the nanopore of the nanopipette determines the lateral resolution of the SICM topography in addition to the the lateral hopping distance (Rheinlaender and Schäffer, 2009; Del Linz et al., 2014; Rheinlaender and Schäffer, 2015). These studies demonstrate that the lateral resolution of a nanopipette is

three times the nanopore radius, *i.e.*, a 50 nm radius nanopipette will have a lateral resolution of 150 nm (3 × 50 nm). This means that the nanopipette can only resolve structures that are at least 150 nm apart from each other (Rheinlaender and Schäffer, 2015). Thus, if the lateral hop distance is 75 nm and the nanopipette has a 50 nm radius, then the nanopipette is only able to differentiate the height difference every 2 hops, subsequently leading to oversampling and doubling the scanning time. However, it has also been reported that the SICM scan can reach a higher than predicted resolution using the above estimation, as demonstrated by Shevchuk *et al*., who used a 12.5 nm diameter nanopipette (18.75 nm resolution estimation) to resolve structures that are 3-6 nm (Shevchuk, A. I. et al., 2006) and 15-17 nm structures with the 30 nm diameter nanopipette (45 nm resolution estimation) (Novak et al., 2009). The difference could potentially be due to the geometry of the nanopipette.

One of the advantages of the hopping mode is that it minimises the substrate-nanopipette tip collisions. As demonstrated during the development of the hopping mode (Novak et al., 2009), when fixed neurons were first scanned with the hopping scanning mode and then followed by the DC scanning mode, the obtained topography was different (Figure 3.4). In the DC mode, the fine neurites at the edge of the cell body disappeared, and the overall topography was distorted as evidenced by the horizontal line artefacts throughout the imaging process. This was due to the collisions between the neuron and the nanopipette, and potentially detached the neurites from the plate (Figure 3.4B). In contrast, the hopping mode provided a high resolution image of the neuron, with neither line artefacts nor distortion, and fine details such as the neurite were retained (Figure 3.4A) (Novak et al., 2009). Similar observations have been made when the hopping mode was used to successfully probe the topography of collagen fibers, whereas the AC scanning mode had multiple collision issues and the overall quality of the topography generated was low (Ushiki et al., 2012).

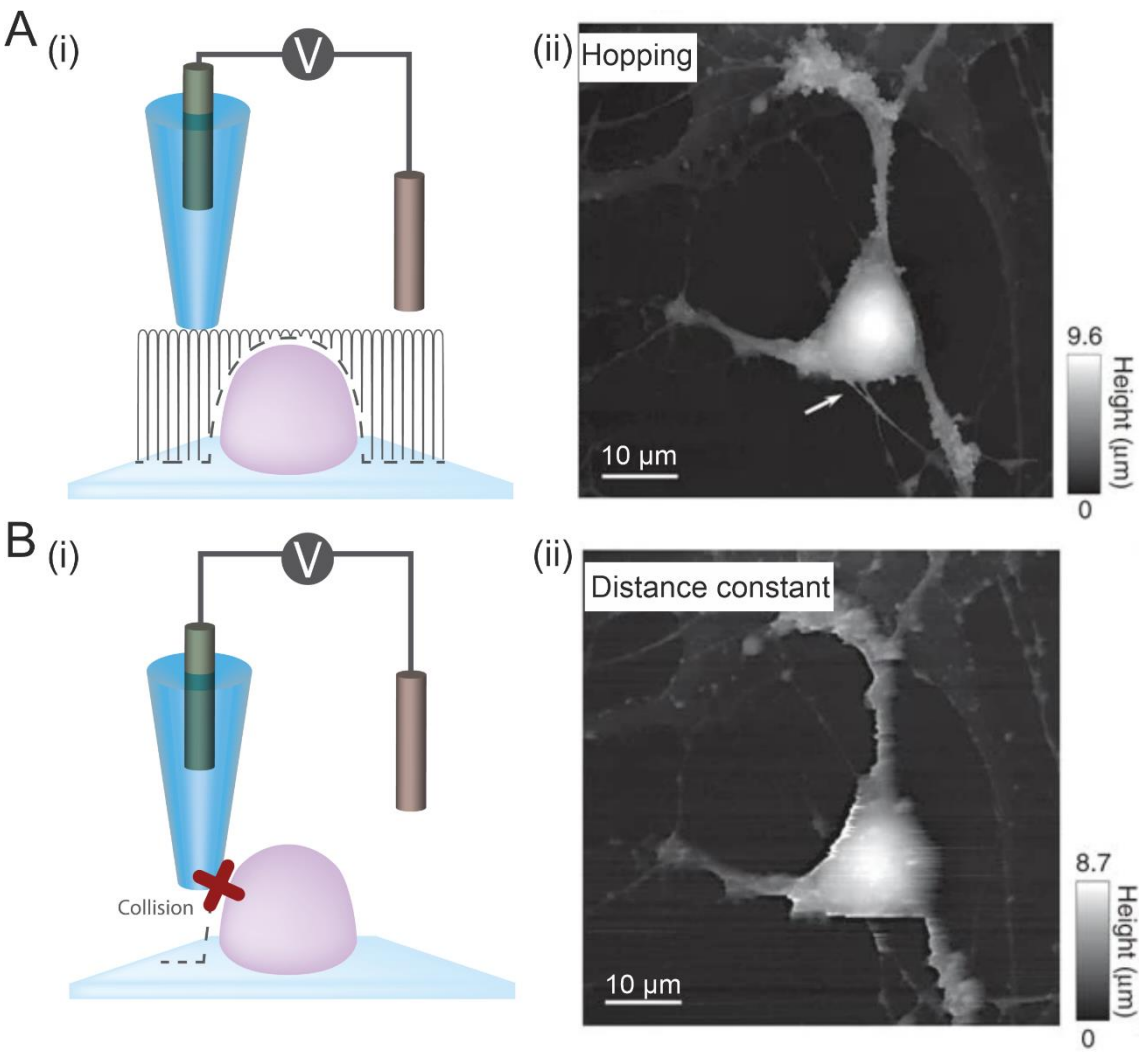

Figure 3.4. Scanning of the fixed neurons using different scanning modes. *Hopping mode enables non-contact topography scanning by the SICM on a steep substrate like a neuron (A). The schematic illustration depicts the hopping mode with a steep substrate (A(i)), and the topography scan of the neurons using the hopping mode (A(ii)), arrow pointing to a fine neurite. The distance constant mode distorts the topography (B). The schematic-illustration depicts the issue using the distance constant mode to scan steep substrates. Collisions happen between the nanopipette and the substrate due to the steep change in the angle and the height (B(i)). The distorted topography of the neuron and the fine neurite disappears when using the distance constant mode (B(ii)). This figure is redrawn (i) and adapted (ii) from (Novak et al., 2009)*

3.1.3 The SICM as a single-cell surgical tool

In a typical SICM set-up, the scanning unit is placed directly on top of an inverted optical fluorescence microscope, so that correlated optical images and SICM topography can be obtained and can facilitate the positioning of the nanopipette over the cell of interest (Shevchuk, A. I. et al., 2006; Actis et al., 2013; Novak et al., 2014; Hennig et al., 2015; Simonis et al., 2017; Zhou, Y. et al., 2018; Simonis et al., 2019).

The primary function of the SICM is to provide topography of the substrate through a non-contact way of imaging. Numerous applications of the SICM have been summarised and discussed in a recent review (Zhu, C. et al., 2020). The majority of these applications are topography based, such as: the development of Macro-SICM which has a maximum scan area of 25 × 25 mm to study the wound healing process (Schierbaum et al., 2018); the morphological difference between healthy and the failing cardiac muscles (Lyon et al., 2009); the time-lapse generation of neurites from the neurons with a high-speed SICM (Takahashi et al., 2019); the investigation of the endocytosis of extracellular material (Shevchuk, Andrew I. et al., 2012; Klenerman et al., 2013; Novak et al., 2014; Chen, Y. et al., 2018); cell mechanical properties investigation (Rheinlaender and Schäffer, 2013; Clarke, R.W. et al., 2016); cell surface charge mapping (Page et al., 2016; Perry et al., 2016b; Perry et al., 2017); cell surface conductivity mapping via potentiometric-SICM (Chen, C.C. et al., 2013; Zhou, L. et al., 2016; Zhou, L. et al., 2017) and cell surface pH mapping (Zhang, Y. et al., 2019). Finally it has been used as a high spatial resolution patch clamp as the electronics for SICM are identical to the standard electrophysiology electronics (Miragoli et al., 2011; Novak et al., 2013; Leo-Macias et al., 2016; Vivekananda et al., 2017; Torres-Perez et al., 2020). Additionally, the SICM together with the nanopipette have been used as a "surgical" tool to perform single cell analysis, for example, the extraction of cellular materials for downstream analysis as well as the injection of materials into the cell, with the aid of the fluorescence microscopy.

Extracting materials out of cells for downstream analysis such as sequencing can be used to track fundamental cellular processes, such as differentiation, cellular senescence, cellular pathology, and drug effectiveness (Hasin et al., 2017; Wörheide et al., 2021). Typically, a large number of cells will be lysed and analysed as an average across the entire population. However, this approach only provides information about the population average and neglects the inherent heterogeneity between each cell, indeed a multi-omics approach demonstrated that each single cell can vary despite being the same cell line (Macaulay et al., 2017; Goldman et al., 2019; Stuart and Satija, 2019; Carter, B. and Zhao, 2020). Analysis on a single cell level often relies on processes such as fluorescence activated cell sorting (FACS) and microfluidic droplet cell isolation in order to isolate cells from a heterogenous mixture (Hwang et al., 2018; Mincarelli et al., 2018).

Alternatively, SICM can be used to extract materials out of a single cell once the probe has penetrated into the intracellular space of the cell (Higgins, S.G. and Stevens, 2017; Actis, 2018). The nanopipette extracts intracellular materials via the electrowetting process and this method is called nanobiopsy (Actis et al., 2013). The electrowetting is based on the electrochemical properties of the liquid-liquid interface, where an application of a voltage across such an interface changes the surface tension, and the resulting force is sufficient to cause the liquid from the outside to flow into the nanopipette (Mugele and Baret, 2005; Laforge et al., 2007). The original concept of the nanobiopsy was based on a study by Laforge *et al.* In the study, the group filled the nanopipette with organic 1,2-dichloroethane solution, then a negative voltage was applied from the nanopipette side. The inorganic solution such as water outside the nanopipette ingressed into the nanopipette but no solution movement was observed when a positive voltage was applied (Figure 3.5A) (Laforge et al., 2007). Based on this concept, Actis *et al.* filled a nanopipette with 1,2-dichloroethane, 10 mM tetrahexylammonium tetrakis(4-chlorophenyl) borate organic solution, approached and penetrated a fibroblast cell and extracted the intracellular mitochondria to perform genomic analysis of the mitochondria (Figure 3.5B) (Actis et al., 2013). Based on the same methodology, in 2016, Nashimoto *et al.* extracted mRNAs from different locations of the MFC-7 cells and performed a quantitative polymerase chain reaction (PCR) on the level of expression of *Gapdh* and the *Pou5f1* before or after cell differentiation and showed that the level of *Pou5f1* increased after the differentiation (Nashimoto et al., 2016). Then Tóth *et al.* extracted messenger RNAs (mRNAs) from the nucleus, cell body and axon of a single neuron and revealed that different mRNAs can be found localised to different compartments of the neuron (Tóth et al., 2018).

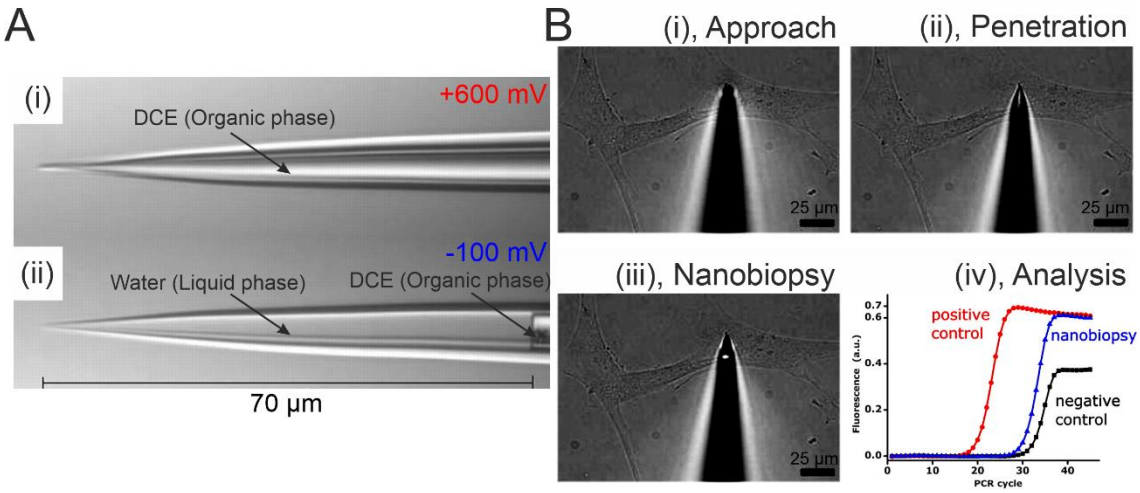

Figure 3.5. Extraction of intracellular materials via the nanobiopsy. *The electrowetting inside the nanopipette (A). The brightfield microscope image of a nanopipette filled with the organic 1,2-dichloroethane solution immersed into a water while maintaining a positive potential difference at +600 mV (A(i)). Reversing the polarity of the potential difference to -100 mV caused the water in the bath to ingress (A(ii)). Single cell nanobiopsy performed on a human fibroblast cell (B). The 1,2-dichloroethane containing 10 mM tetrahexylammonium tetrakis was used to fill the nanopipette, then a silver wire coated with silver tetrakis (4-chlorophenyl) borate was inserted into the nanopipette with a typical Ag/AgCl wire in the bath as the reference electrode. The SICM allows the nanopipette to approach (B(i)), penetrate (B(ii)) and perform nanobiopsy (B(iii)). The GFP plasmid transfected HeLa cell was nanobiopsied and the amount of transcripts inside the nanobiopsied content was analysed via quantitative PCR targeting the GFP mRNAs comparing to the cell lysate GFP mRNA content (positive control) and water (negative control), showing that the nanobiopsy removed contents from the cytoplasm (B(iv)). (A) is adapted from (Laforge et al., 2007), (B) is adapted from (Actis et al., 2013).*

As discussed in Chapter 1 Section 1.4, the term nanoinjection describes the process where a nanoscale probe like the nanopipette is used to perform the injection of extracellular materials into the intracellular space of a cell via electrophoretic forces. Although the use of SICM is not necessary for nanoinjection as the same process can be performed with a micromanipulator as in microinjection, the SICM provides high spatial positioning which is ideal for a precise location injection. Hennig *et al.* demonstrated the positioning ability of the SICM and the nanopipette by injecting a fluorescent DNA dye into the cytoplasm of the cell showing that the dye diffused into the nucleus within 300 seconds (Figure 3.6Ai-ii) (Hennig et al., 2015).

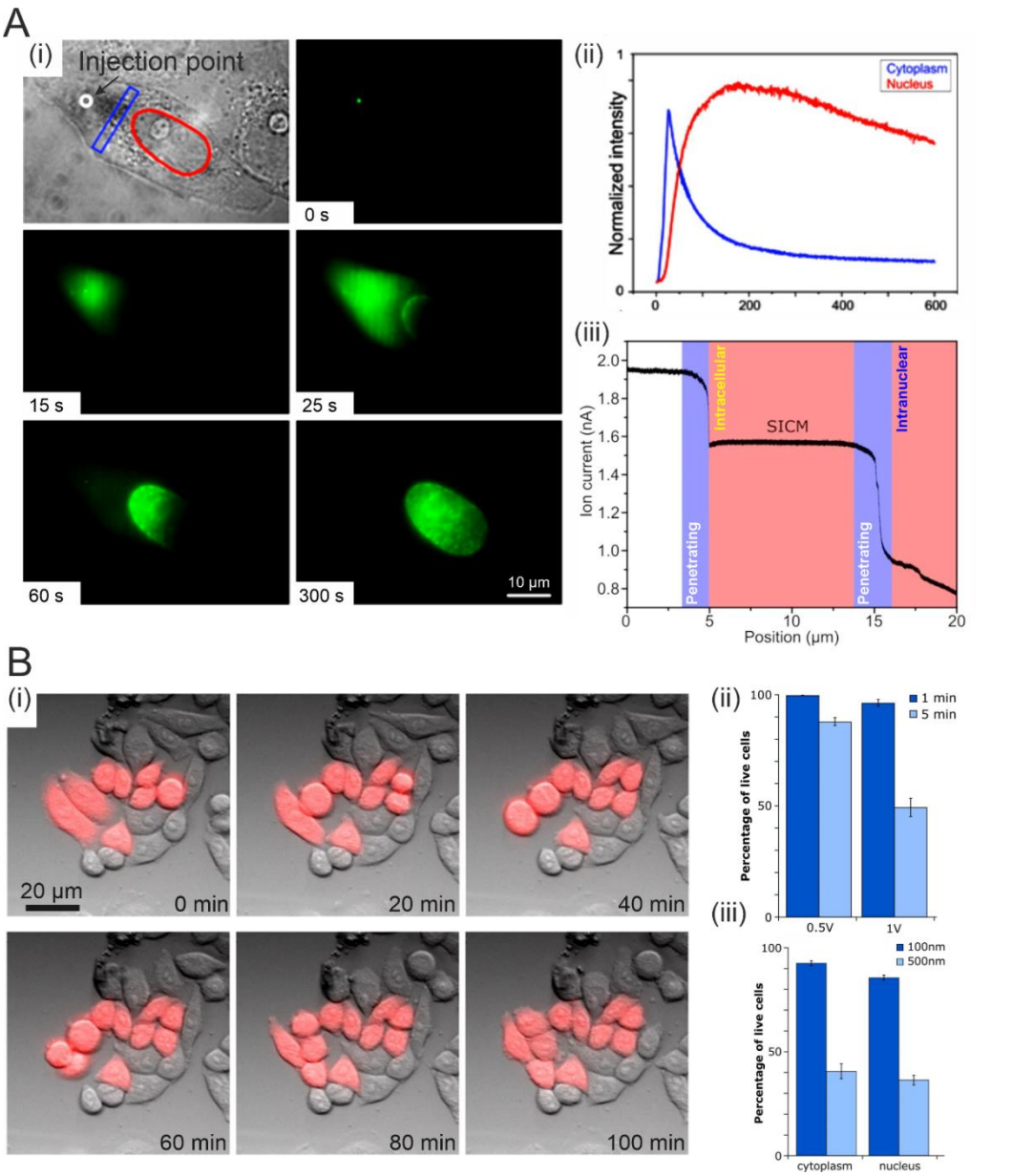

Figure 3.6. Noninvasive nanoinjection to deliver fluorescent labels and dyes into the cell. *The nanoinjection of Sytox Green DNA dye into the cytoplasm of a single epithelial U2OS cell (A). The nanoinjection site is shown as a white dot, showing that the diffusion of the DNA dye into the nucleus is complete within 300 seconds (A(i)). The fluorescent intensities of the cytoplasmic region (blue box in A(i)) and the nucleus region (Red circle in A(i)) were quantified (A(ii)). The electrical component of the SICM allows real-live time monitoring of the nanoinjection process. The ionic current baseline dropped when the nanopipette was penetrating the cell and entered the intracellular space. The ionic current dropped again when the nanopipette was penetrating the nucleus into the intranuclear space (A(iii)). The nanoinjection of multiple U2OS cells with fluorescently red labelled dextran (B). The time-lapse image of the colony of the cell showed that the nanoinjected cells survived and divided 100 mins post injection (B(i)). However, using a higher voltage and a prolonged nanoinjection time resulted in the lower survival rate of the cells (B(ii)). Moreover, using a large nanopore (500 nm) caused more deaths than the 100 nm nanopore during injection, irrespective of the location of injection. (A(i-ii)) are adapted from (Hennig et al., 2015), (A(iii) is adapted from (Simonis et al., 2019), (B) is adapted from (Simonis et al., 2017).*

Additionally, it was also noted that the ionic current baseline dropped when the nanopipette penetrated into the inside of the cell, and penetration into the nucleus caused the ionic current baseline to be further reduced (Figure 3.6Aiii) (Hennig et

al., 2015; Simonis et al., 2019). This reduction was attributed to the cell plasma membrane and the nuclear membrane which acted as additional resistors and consequently a reduction in conductivity (Hennig et al., 2015; Simonis et al., 2019). Simonis *et al*. demonstrated that the post-nanoinjection survival rate of the cell depended on the size of the nanopipette, the injection time and the strength of the applied voltage. It showed that nanoinjection using a small nanopipette (*c.a.* 100 nm in diameter) over a shorter injection time, allowed the propagation of a colony of injected U2OS cells. In contrast, there was a lower survival rate with a micropipette of *c.a.* 500 nm in diameter or when a larger voltage was applied for a longer period of time (Figure 3.6B) (Simonis et al., 2017). Additionally, a double injection approach can also be carried out with a double barrel nanopipette (a type of nanopipette that contains two capillaries with the resulting nanopipette contains two nanopores side by side at the nanopipette tip). The double barrel nanopipette can be filled with two different fluorophores in the two separate barrels, and used to penetrate the cell. The fluorophores were then delivered one barrel at a time by applying a suitable voltage (Adam Seger et al., 2012; Hennig et al., 2015).

3.1.4 Developing a Quantitative nanoinjection platform

The injection of extracellular material into a cell is a relatively easy process, but quantifying the number of molecules injected has been difficult to achieve. Two methods have been used to estimate the quantity of the extracellular materials delivered into the cell. For example, the microinjection volume can be measured by timing the injection duration, and the micropipette is filled with a known concentration of biomolecules, together the amount of molecules can be approximated. Alternatively, the fluorescence intensity of the molecules delivered into the cell can also be used to assess the number of molecules injected (Drews et al., 2016; Cao et al., 2018). A key challenge that still remains, however, is the absolute quantification of the material delivered, *i.e.* how many molecules have been delivered? This concept has been explored before with nanopillars (Huang, J.A. et al., 2019) and an optical tweezer combined nanopore approach (Kurz et al., 2014), however, the first approach lacks the spatial control and the second approach has a relatively complicated set-up and cannot be used with adherent cells respectively. The set-up of the SICM and nanopore single molecule sensors share similar electronics, and thus the nanoinjection can in theory be performed at

single molecule resolution by detecting the translocation of the molecule one at a time during the nanoinjection procedure. However, this means that the 100 nm nanopipette used in previous nanoinjection studies would not be suitable for this purpose (Hennig et al., 2015; Simonis et al., 2017; Simonis et al., 2019), and instead a more narrow nanopipette with a nanopore diameter ranging from 10 to 30 nm would have to be used in order to detect single molecule translocations (Li, W. et al., 2013; Ivanov et al., 2015; Martyushenko et al., 2015; Chen, K. et al., 2017; Sze et al., 2017; Wang, V. et al., 2019; Chen, K. et al., 2020; Wang, X. et al., 2020).

3.2 Aims

The aim of this chapter is to develop a quantitative nanoinjection platform for the delivery of biomolecules into cells. This platform will couple the nanoscale resolution of the SICM and the single molecule sensitivity of the nanopipette. This chapter will present its implementation for both cell lines and primary cells and test the delivery of a of variety biomolecules including: DNA plasmids, the enzyme β-galactosidase, and amyloid fibrils. These biomolecules are of biological interest and additionally, they are also used to demonstrate several concepts of the quantitative single-molecule nanoinjection platform:

1. Voltage triggers the delivery of these biomolecules.

2. SICM can inject biomolecules into cellular compartments.

3. The nanoinjection procedure has negligible effect to cell viability and function.

4. The nanoinjection process does not disrupt the structure of the biomolecules.

5. The number of biomolecules delivered can be quantified with single molecule resolution by counting the number of the translocation events.

3.3 Results

3.3.1 SICM cell topography scan and stability

Cells were plated onto a 35 mm diameter glass bottom dish one day prior to the experiment and the culture medium was replaced with the Leibovitz's phenol red free L-15 medium before the scan (Figure 3.7). The 35 mm dish was set at the position indicated in Figure 3.7, and the position of the nanopipette was in alignment with the microscope objective. A Ag/AgCl electrode was inserted into the nanopipette and another reference Ag/AgCl electrode was immersed inside the 35 mm dish to establish a complete electric circuit.

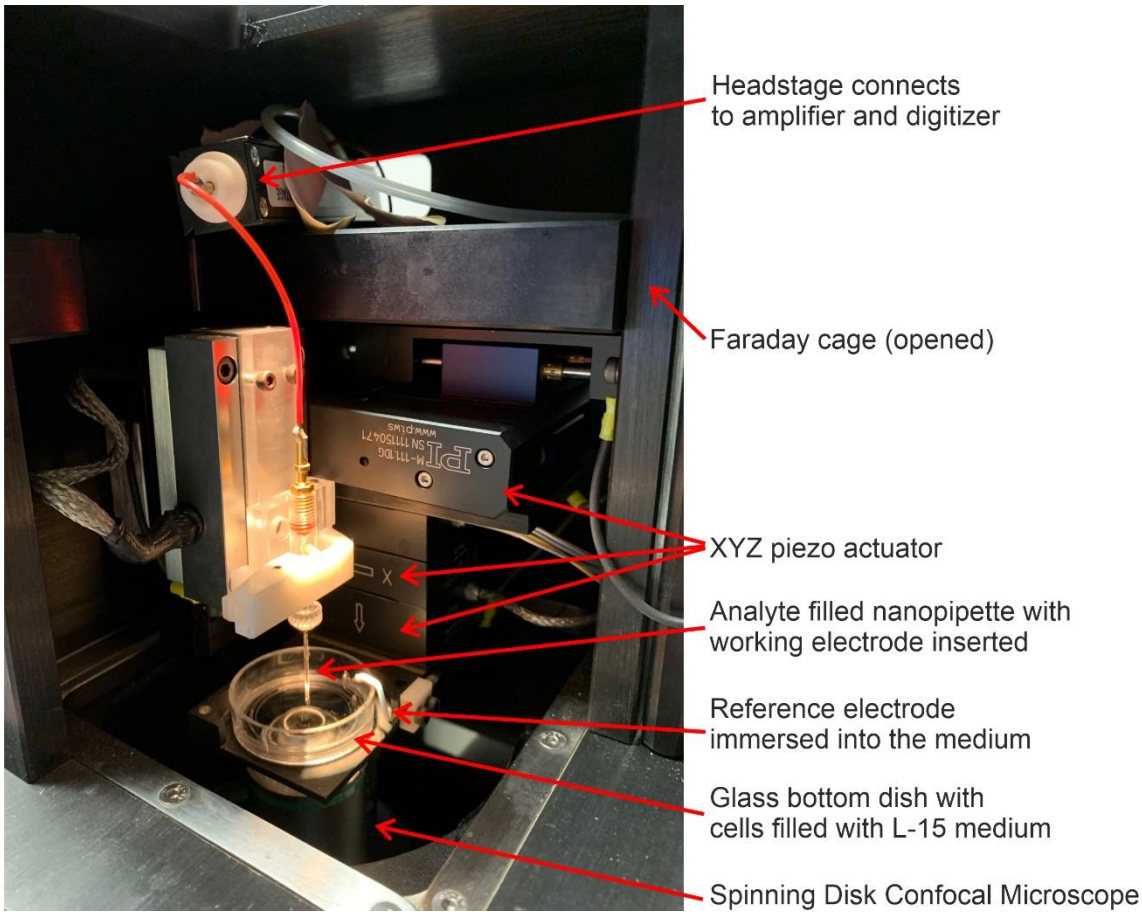

Figure 3.7.The set-up of the Scanning Ion Conductance Microscopy (SICM). *Set-up of the SICM used throughout this chapter, beside the necessary standard electronics and components e.g. the headstage and the Faraday cage. The SICM is composed of piezo actuators that control the X, Y and Z position during scans and sits directly on top of a spinning disk laser confocal microscope to provide high resolution fluorescent microscopy.*

When a direct current voltage is applied between the two Ag/AgCl electrodes inside electrolyte, an ionic current is formed. Using a NaCl electrolyte as an

example, when a sufficiently high voltage is applied, the freely moving Na^+ and Cl^- ions in the electrolyte migrate to electrodes depending on their polarities. At the anode, the Cl^- in the electrolyte losses an electron and undergoes oxidation reaction with the silver wire and precipitate as salt on top of the electrode. The electron migrates through the wire to the cathode side and the AgCl taken up the electron and undergoes oxidation to release a free Cl^- back to the electrolyte solution.

To show that the SICM set-up here is capable to control the position of the nanopipette and scanning by the hopping mode, a nanopipette with a nanopore of a 88 nm diameter was filled with PBS and approached the glass surface substrate with a setpoint at maximum Δ0.7%. The nanopipette reached the defined nanopipette-substrate distance and started hopping (Figure 3.8).

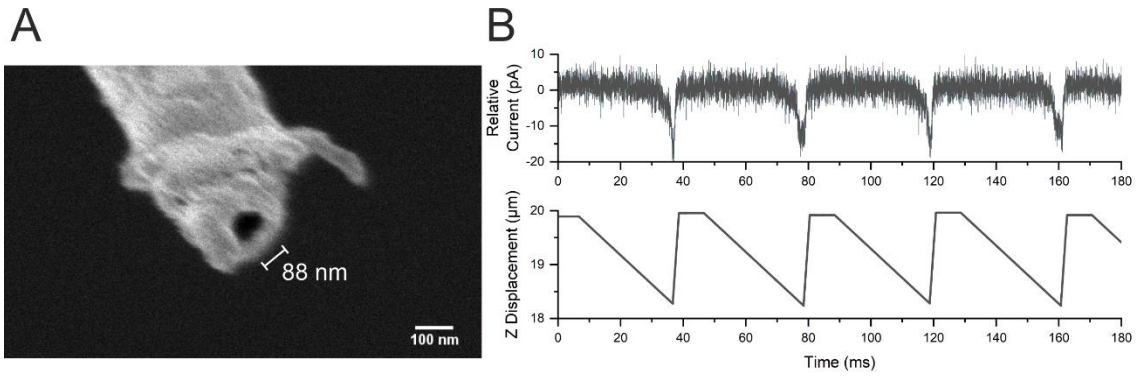

Figure 3.8. SEM micrograph of the nanopipette and ion current approach curves and Z-piezo displacement. *(A) The SEM micrograph of the nanopipette used as a scanning probe was approximately 88 nm in diameter. (B) A typical hopping trace of the SICM on top of the glass substrate. The sudden drop in the current occurred when the Z-piezo moved further downward. The current returned to baseline when the nanopipette was retracted back to the starting position. Each hop takes approximately 40 ms in this case. The nanopipette was imaged by Samuel Confederat.*

The current baseline remained stable until *c.a.* 40 ms, it dropped 20 pA and immediately returned back to 0 pA. At the same time, the Z-piezo moved from *c.a.* 20 µm down to *c.a.* 18 µm at *c.a.* 40 ms mark and then returned to *c.a.* 20 µm again (Figure 3.8B). As previously described in Section 3.1.2, the sudden drop in the current baseline was due to access resistance, which indicated that the nanopipette was near the surface substrate. Once the hopping scanning mode detected this drop in the current baseline, it immediately retracted the nanopipette back to a set distance and the entire process was repeated (Figure 3.8B). This process would repeat itself indefinitely unless stopped by the user.

To demonstrate the SICM here is stable and can perform high resolution cell scanning, multiple cell types were imaged/scanned by the SICM with the same parameters, which included the cancerous cell line HeLa cells, primary cells including the normal human epidermal keratinocytes (NHEK), human umbilical vein endothelial cells (HUVEC), primary rat cortical neurons and mouse dorsal root ganglion (DRG) neurons (Figure 3.9). All the scanning was performed in hopping mode with a set-point between Δ0.3 to Δ0.7%. For a typical large area scan (96 × 96 μm), the final image resolution of 480×480 was used and an area of 1×1 μm prescan was used to determine the surface roughness. Then, for any substrates that were 1 μm above the glass bottom, a lateral hop of 200 nm was used, and for anything below 1 μm, a lateral hop of 400 nm was used. The nanopipette here had a lateral scanning resolution of *c.a.* 132 nm (Rheinlaender and Schäffer, 2015).

The topography image of the HeLa cells showed fuzzy cell surfaces, this was due to the existence of surface cilia as previously shown by the SEM (Porter et al., 1974). In contrast, the SEM images of the NHEK, HUVEC cells, rat cortical and mouse DRG neurons were all flatter. Similarly, the SEM images of these cells have been shown to have relatively smoother surfaces (Smith, R.A. and McInnes, 1986; Rosdy et al., 1991; García-Pérez et al., 2011; Qiu et al., 2012), these suggested that the SICM used here was capable of obtaining high quality and resolution topographies that agreed with the SEM images.

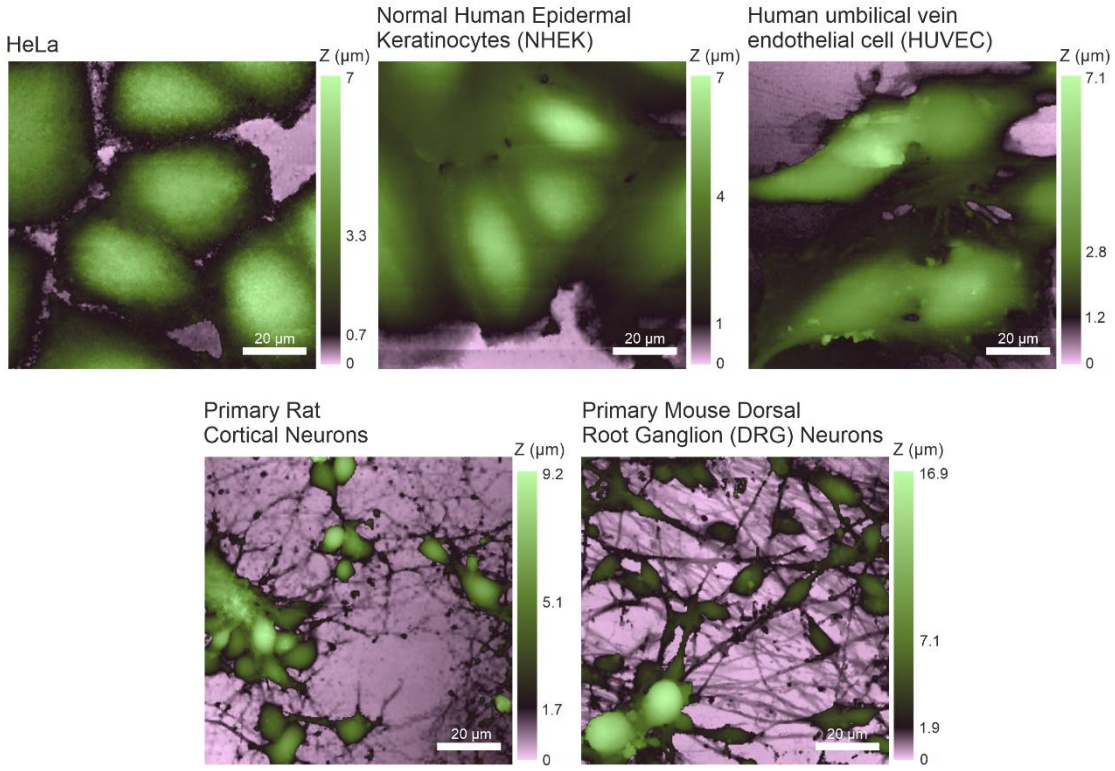

Figure 3.9. Scanning Ion-Conductance Microscopy (SICM) imaging of live cells. *Five different types of cells were imaged with the SICM. The cells were the HeLa cells, NHEK, HUVEC, primary rat cortical and primary mouse DRG neurons. Colour scales were adjusted so there would be a clear difference between the background glass substrate and the cell.*

3.3.2 The quantitative nanoinjection workflow and methodology

The quantitative nanoinjection platform and the workflow of the injection is illustrated in Figure 3.10. The SICM is mounted on top of an inverted confocal fluorescent microscope. Similar to topography scanning mode, the biomolecule loaded nanopipette will be used to approach the cell substrate, until it reaches the predefined setpoint, then the nanopipette will be repositioned to the cell of interest by using the bright field image and will approach the cell surface again (Figure 3.10B). Hopping is then stopped and the nanopipette is moved downward by a predefined distance at high speed to penetrate the cell membrane and access the intracellular space. A suitable voltage will then be applied to trigger the delivery of the cargoes. Simultaneously, the ion-current trace is recorded for further analysis to identify the translocation events.

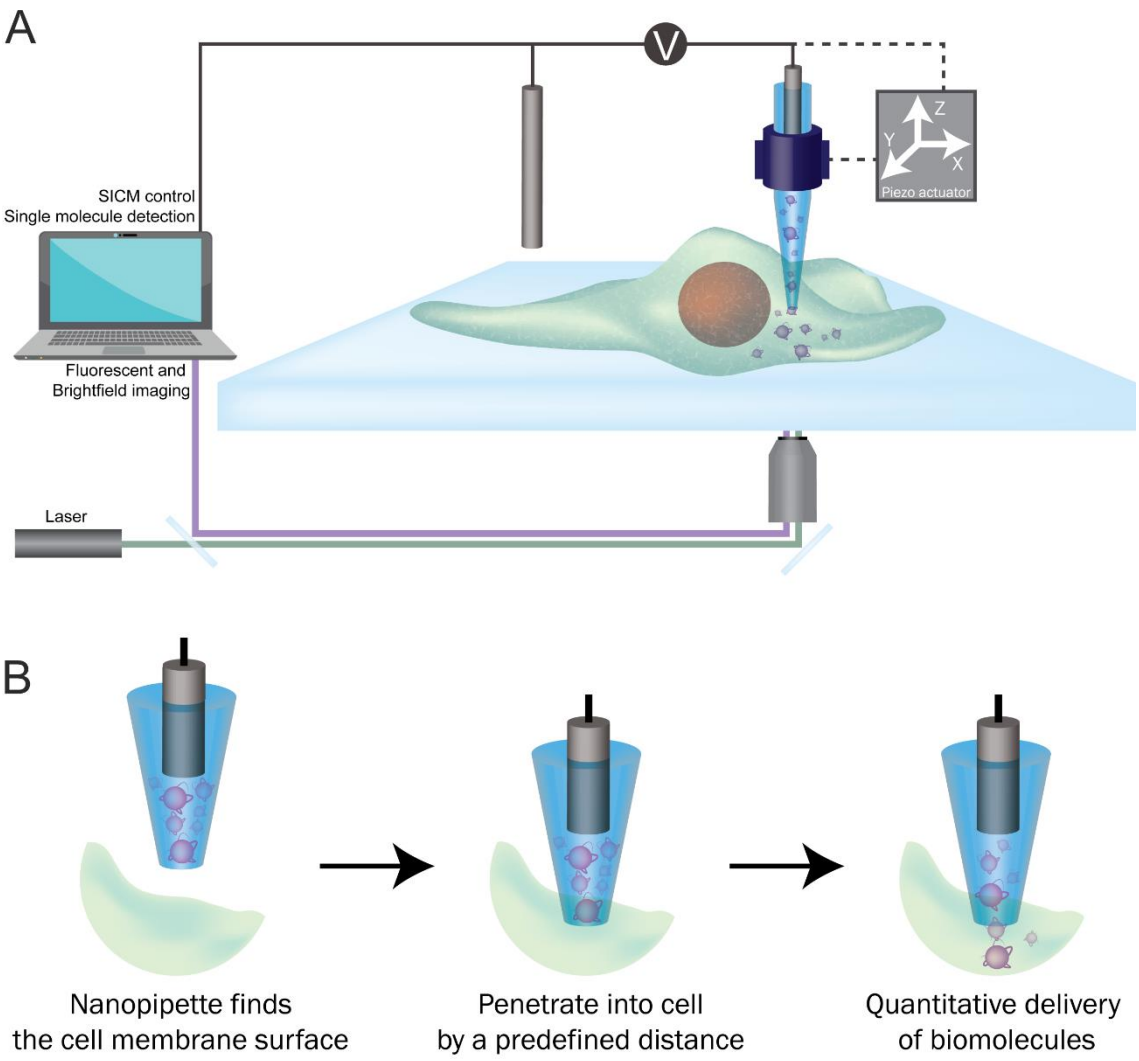

Figure 3.10. Schematic illustration of the nanoinjection platform and the nanoinjection procedure. *The SICM is placed directly on top of a fluorescent microscope which allows the fluorescent and bright field imaging of the cell during nanoinjection (A). The SICM allows accurate positioning of the nanopipette to any X-Y spatial location of the cell. Then, the nanopipette of the SICM finds the surface of the cell membrane by hopping mode. The nanopipette penetrates the cell membrane into the intracellular environment by controlling the Z-piezo actuator to lower down a predefined distance (B). Finally, the biomolecules are delivered into the cell by electrophoretic forces and the ionic-current trace is recorded and processed to identify molecule translocation signals.*

The recorded ion-current trace during the nanoinjection process will be further processed by using a custom written MATLAB script as described in Chapter 2 Section 2.3.6. The script adjusts the baseline using algorithms and the adjusted current baseline will be shown throughout this work (Figure 3.11A). Each upward peak is associated with the translocation of a molecule, and thus the number of molecules translocated through the nanopipette into the cell can then be quantified. Figure 3.11B depicts a translocation event and the associated terminology that will be used throughout. The dotted horizontal line indicates the script calculated current baseline and the event current peak maxima describes

how far the current has moved away from the script calculated current baseline, *e.g.* 0.3 nA current peak maxima means that the peak has a highest point of 0.3 nA away from the current baseline. The full width at half maximum is used to calculate the event dwell time (Figure 3.11B). These two parameters correlate with the size, shape and translocation dynamics of the molecules (Muthukumar et al., 2015; Yusko, E. C. et al., 2017; Varongchayakul et al., 2018). Lastly, all the detected data will be processed and presented on a population scatter plot by plotting the current peak maxima against the dwell time (Figure 3.11C).

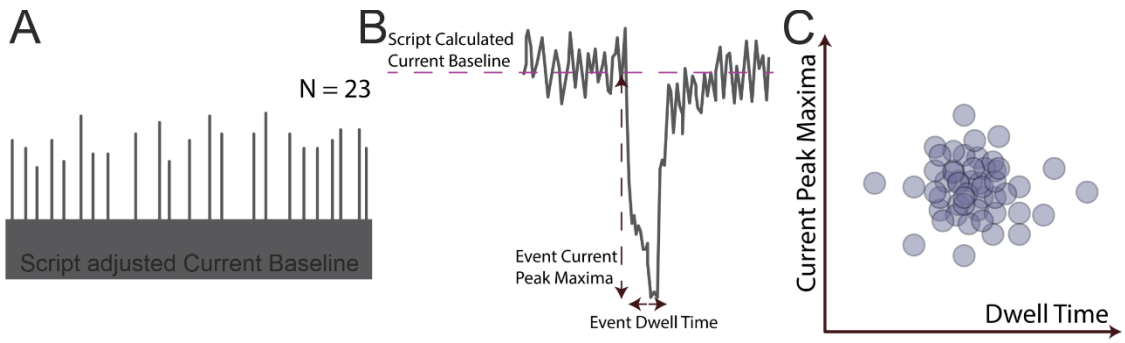

Figure 3.11. Schematic illustration of the types of data associated with the current trace analysis. *The obtained current trace data is processed by the custom written MATLAB script. (A) Illustrates a baseline adjusted current trace with multiple upward peaks. Each peak is the event translocation signal and the total number of these peaks is counted and indicated with 23 events counted here. The MATLAB script event calling threshold determination method can be found in Chapter 2. (B) Illustrates an example of a translocation event and two important parameters are measured for each translocation event: the current peak maxima and the dwell time. These parameters are determined by the shape, size and orientation of the translocated molecule. (C) Illustrates a population scatter plot generated by collecting the current peak maxima and the dwell time data of each detected translocation event.*

The nanopipette used for the nanoinjection has a diameter of *c.a.* 24 nm (Figure 3.12). The estimated volume of injection can be estimated according to a study by Babakinejad *et al.* via calculating the flow rate (Babakinejad et al., 2013). To calculate the flow rate, the following Equation 2 will be used (Babakinejad et al., 2013):

Equation 2

$$Q_{tot,\Delta\Psi} = (\mu_{EP} + \mu_{EO})\pi R_0 \tan(\theta)\Delta\Psi$$

where $Q_{tot,\Delta\Psi}$ is the estimated flow rate due to a potential difference (voltage), μ_{EP} and μ_{EO} are the electrophoretic and electroosmotic mobilities of the analyte, R_0 is the radius of the nanopore, θ is the inner half cone angle and $\Delta\Psi$ is the voltage difference. Due to the electrophoretic and electroosmotic mobilities of the analytes

in this thesis will not be measured, the model values from Babakinejad *et al.* will be used instead (Babakinejad et al., 2013). To estimate the total flow rate of a *c.a.* 24 nm wide nanopipette, the following values were used as the input: $\mu_{EP} = \mu_{EO} = 1.4\times10^{-8}$ m^2 V^{-1} s^{-1}, R_0 = 12 nm (1.2×10^{-8} m), $\theta = 3.6°$ (calculated from Section 2.3.4), assuming a potential difference of 500 mV, thus $\Delta\Psi = 0.5$V. The resultant estimated flow rate would be 33 fl s^{-1}, thus approximately 2 pl of solution will be delivered per minute. However, it is important to state that equation was derived and based on a standard 1×PBS environment in the original study (Babakinejad et al., 2013), the actual flow rate inside the cell can be different inside the cell.

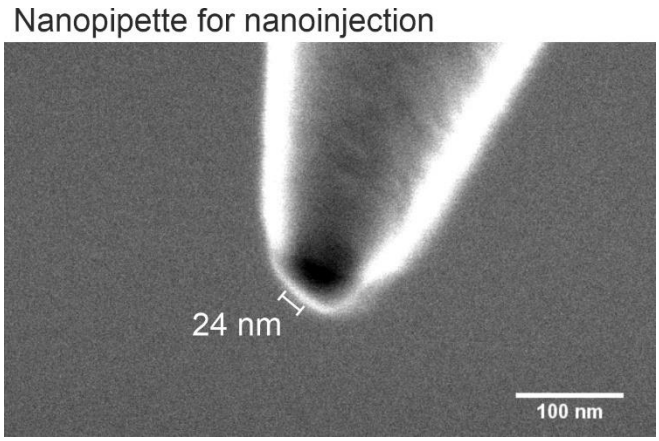

Figure 3.12. The SEM image of a narrow pore nanopipette. *The nanopipette showed here has a pore size of roughly 24 nm at the tip. The nanopipette was imaged by Samuel Confederat.*

3.3.3 Intracellular delivery into the cytoplasm and nucleus

This section shows that the delivery process can be triggered by applying voltage and that the delivery can be carried out in either the nucleus or the cytoplasm. To achieve these two objectives, charged fluorescent dye conjugates were delivered into the cytoplasm or the nucleus.

To aid the visualisation of the nucleus, stably transfected HeLa cells expressing a fluorescent protein mCherry conjugated with a nuclear localisation signal (NLS) were generated. The NLS sequence caused the conjugated protein to be actively imported into the nucleus by the nuclear import machinery (Stewart, M., 2007). The plasmid pmCherry-NLS was transfected to the HeLa cells through lipofection. Successfully transfected HeLa cells expressed the mCherry-NLS, and the mCherry-NLS fluorescent signals co-localised with the nucleus DNA stain Hoechst (Figure

3.13A), this co-localisation confirmed that the mCherry-NLS was localised to the nucleus. The untransfected HeLa cells did not express the mCherry-NLS (Figure 3.13B).

To select for stable transfectants, the HeLa cells were grown under selective pressure by adding G418 sulfate to the culture medium. FACS was used to isolate HeLa cells expressing mCherry-NLS. This population of the HeLa cells stably expressed the mCherry-NLS and this cell line was named HeLa RNuc.

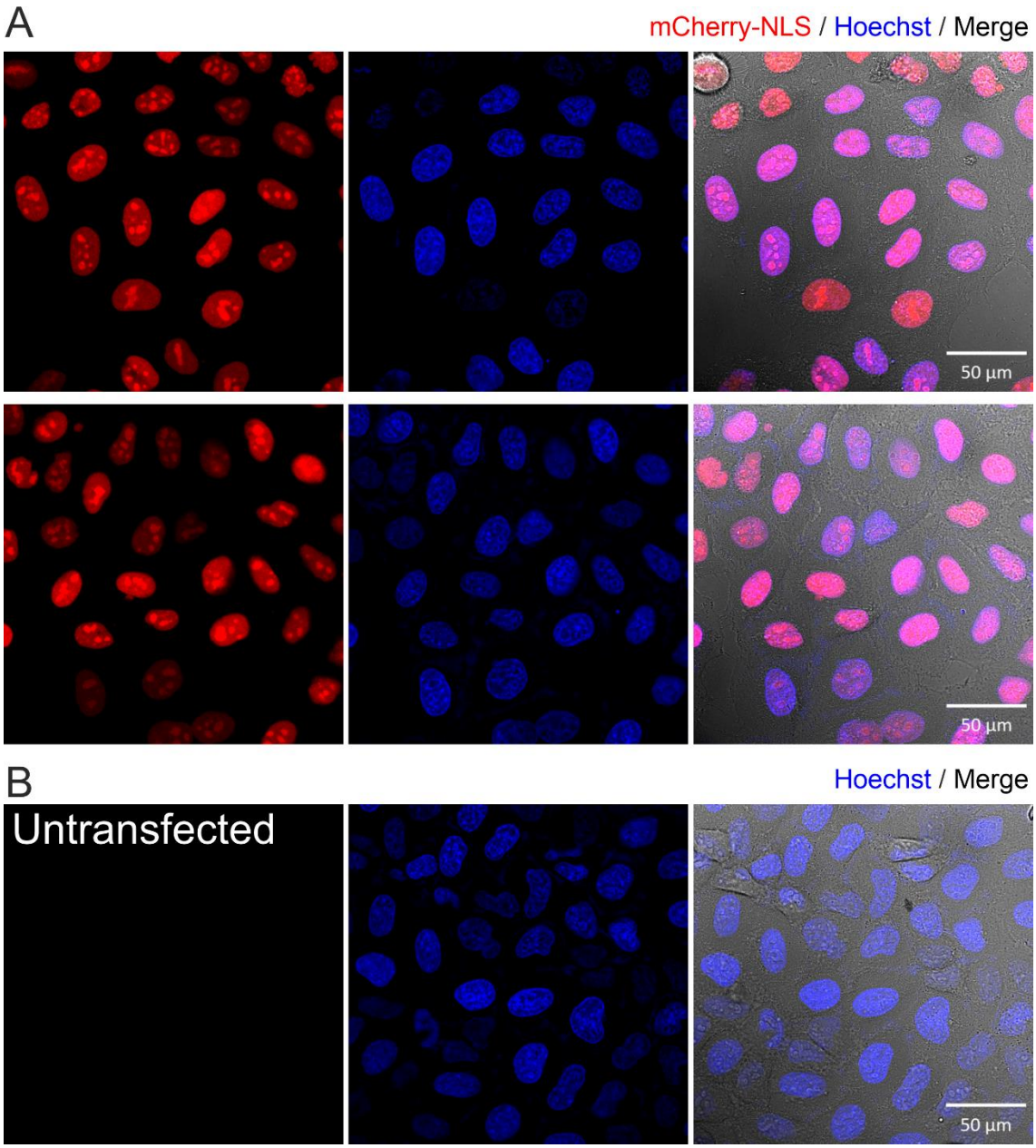

Figure 3.13. The generation of the mCherry-NLS expressing HeLa cell line. *The pmCherry-NLS plasmid was transfected to the HeLa cells via lipofection and the HeLa cells were FACS sorted and imaged with a fluorescent confocal microscope. The pmCherry-NLS transfected cells showed red nuclei co-localized with the Hoechst nuclei staining (A). The untransfected control showed no mCherry-NLS signal (B). Red, mCherry-NLS; Blue, Hoechst 33342; Grey, brightfield image.*

Before the nanoinjection procedure, the vertical position of the nucleus in HeLa RNuc cells would be determined so that the distance required to move the nanopipette down to perform nucleus nanoinjection was known. The distance was determined via the Z-stack imaging technique with a laser scanning confocal microscope by moving the focal plane of the confocal microscope. The plasma membrane was labelled with the Cell Mask™ Green Plasma Membrane stain (Figure 3.14A) and was used to determine the highest and the lowest point of the cell. The stack thickness was 955 nm and Z-stack imaging was performed from the lowest point of the cell to the highest point of the cell. The X-Z and Y-Z plane were used to determine the highest point of the nucleus and the highest point of the cell membrane (Figure 3.14B). The distance between the highest point of the nucleus and the highest point of the cell membrane was calculated for 29 different cells. The data were collected and summarised, and the average distance from the top of the cell membrane to the top of the nucleus was calculated to be 3.1 ± 0.1 μm (Figure 3.14C). This information would be used for the nucleus nanoinjection.

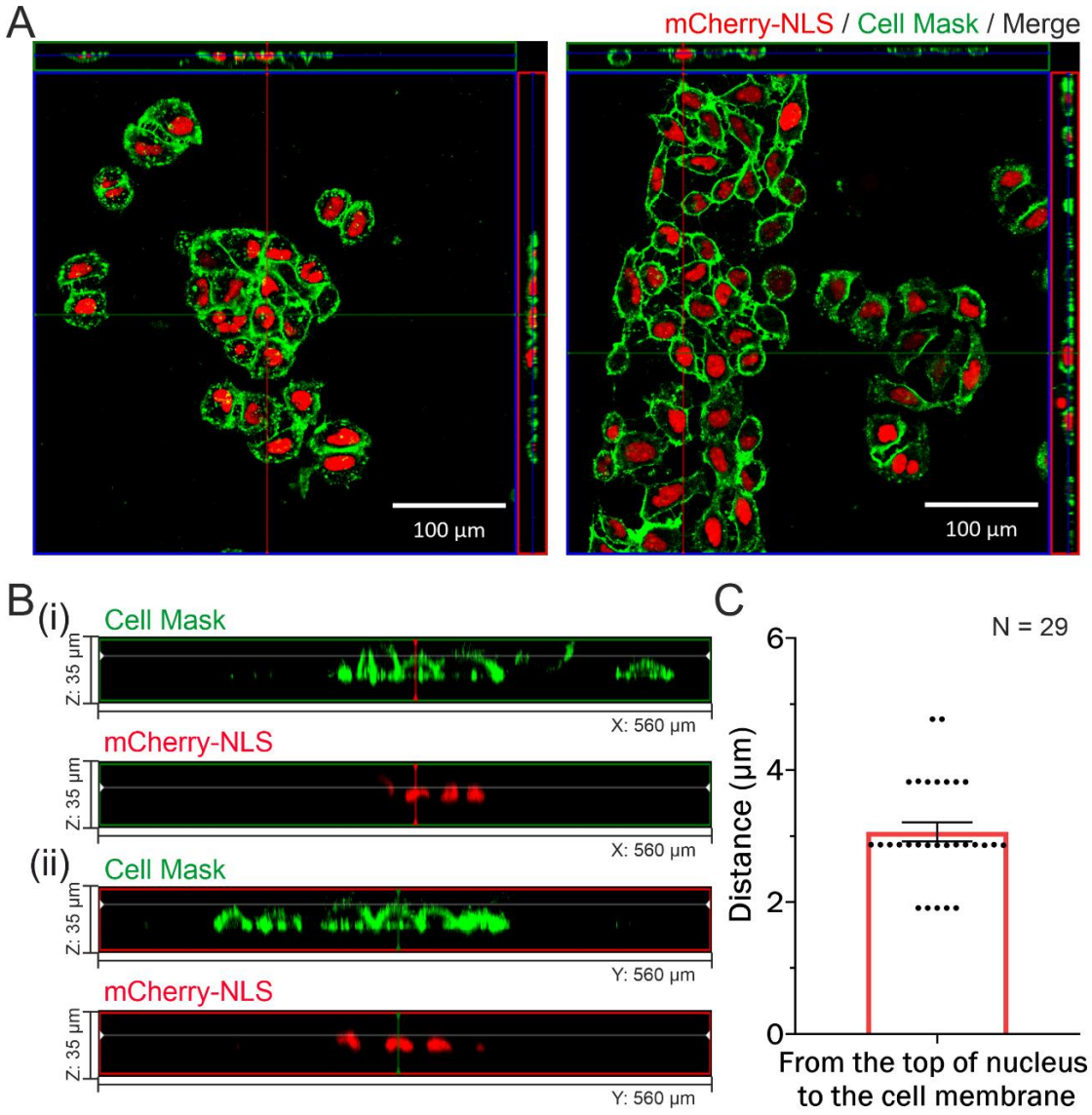

Figure 3.14. The depth location of the nuclei of the HeLa RNuc was imaged by fluorescent Z-stack imaging. *The orthogonal projection image of the HeLa RNuc cells stained with the Cell Mask™ plasma membrane stains and Hoechst nuclei stain (A). Fluorescent Z-stack imaging was used, 25 stacks were generated for each image at 955.4 nm thickness. The X-Z and X-Y planes were used to calculate the distance between the top of the cell membrane (Green) and the top of the nucleus (Red) (B). The distance between the top of the cell membrane and the top of the nucleus had an average of 3.1±0.1 µm (N=29 cells). Red, mCherry-NLS; Green, Cell Mask™ green plasma stain.*

The nucleus is separated from the cytoplasm by the nuclear envelope and this barrier allows biomolecules to move between the two compartments either by active transport machinery or passive diffusion (Stewart, M., 2007; Cautain et al., 2015; Graumann and Evans, 2017). In general, the passive diffusion has a size limitation such that most biomolecules with a molecular weight less than 60 kDa can diffuse into and out of the nucleus (Rout et al., 2016). Here, to demonstrate that the quantitative nanoinjection set-up was capable of compartment specific injection, charged fluorescent dextran conjugates were used, similar to other

nanoinjection studies (Simonis et al., 2017; Simonis et al., 2019). The 70 kDa fluorescein dextran conjugate was chosen to be injected into either the nucleus or the cytoplasm of the HeLa RNuc cells. The rationale was that the 70 kDa dextran was not able to passively diffuse into the nucleus (D'Angelo et al., 2009) and has been delivered to the nucleus before (Guillaume-Gentil et al., 2013) Therefore by nanoinjecting the 70 kDa fluorescein dextran to either the cytoplasm or the nucleus, it would demonstrate this platform could perform intracellular compartmental delivery, as immediately after the nanoinjection, the dextran should either be found inside the nucleus or the cytoplasm but not in both compartments.

The 70 kDa fluorescein dextran was diluted to 140 nM in PBS and used to fill the 24 nm nanopipette for nanoinjection. The nanopipette approached the cell and then was positioned directly above the nucleus with the aid of the mCherry-NLS fluorescent signals. Then the nanopipette was moved downward by 4 µm to penetrate the nucleus and the measured distance between the membrane and the nucleus was approximately 3 µm (Figure 3.14). An additional 1 µm was added to ensure the nanopipette penetrated the nucleus envelope. A negative voltage was applied for 2 minutes to electrophoretically deliver the anionic fluorescein dextran conjugates into the intracellular space. The 70 kDa fluorescein dextran conjugates co-localised with the mCherry-NLS (Figure 3.15). This showed that the fluorescein dextran conjugates were delivered into the nucleus. This also demonstrated that the 24 nm wide nanopipette and its geometry profile used here could be used to electrophoretically deliver materials into the intracellular space.

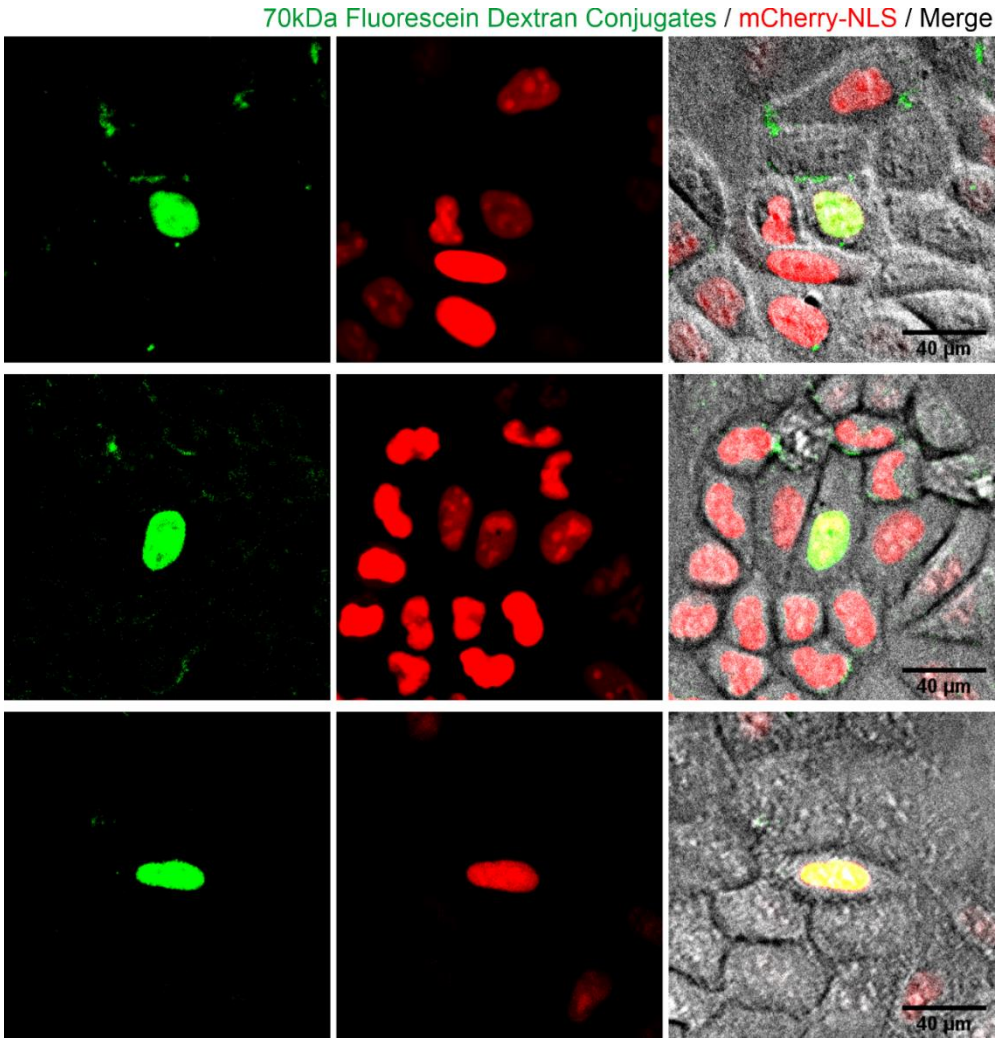

Figure 3.15. The delivery of 70 kDa Fluorescein dextran conjugates into the nuclei of the HeLa RNuc cells. *The 70 kDa fluorescein dextran conjugates were delivered into the nuclei of the HeLa RNuc cells. The dimension of the conjugates prevented them from diffusing into the cytoplasm and were retained inside the nuclei after nuclei nanoinjection. Red, mCherry-NLS; Green, 70 kDa Fluorescein dextran conjugates; Grey, Brightfield image.*

Next the ability to deliver molecules into the cytoplasm by nanoinjection was tested (Figure 3.16). The nanopipette was positioned on top of the cytoplasm with the aid of the mCherry-NLS and the brightfield view. The nanopipette was moved down 2 µm to reach the cytoplasm from the cell membrane, followed by the application of negative voltage to trigger the delivery of the fluorescent dextran conjugates. Because of the size of the dextran, the fluorescein dextran conjugates were excluded from diffusing into the nucleus and remained in the cytoplasm. These experiments demonstrated that the platform was capable to carry out nanoinjection in different compartments, and the delivery could be triggered by the application of a suitable voltage.

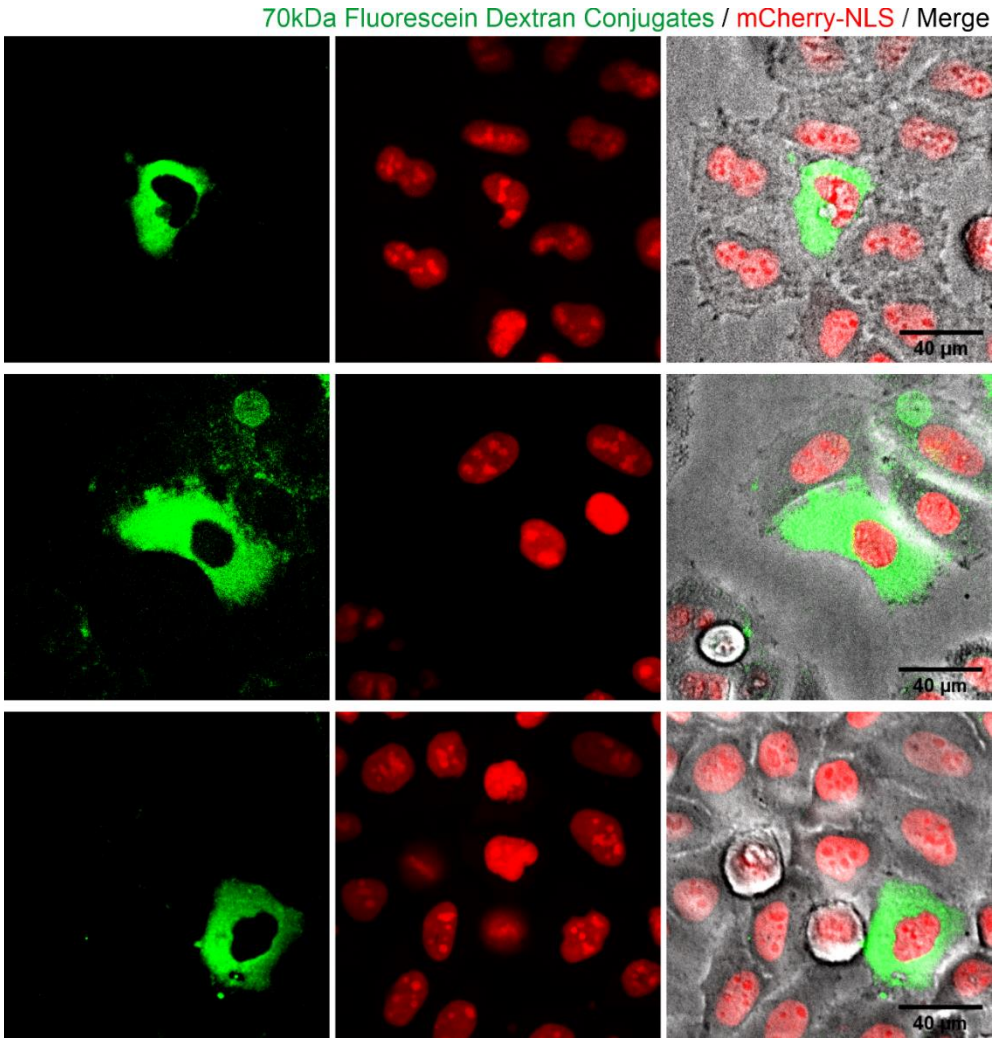

Figure 3.16. The delivery of 70 kDa Fluorescein dextran conjugates into the cytoplasm of the HeLa RNuc cells. *The 70 kDa fluorescein dextran conjugates were delivered into the cytoplasm of the HeLa RNuc cells, the dimension of the conjugates prevented them from diffusing into the nuclei and excluded from the nuclei. Red, mCherry-NLS; Green, 70 kDa Fluorescein dextran conjugates; Grey, Brightfield image.*

As mentioned in Section 3.1.3, several nanoinjection studies have shown that that the current baseline dropped when the nanopipette had successfully penetrated the cell membrane, due to the cell membranes acting as additional resistors (Adam Seger et al., 2012; Simonis et al., 2017; Simonis et al., 2019). Here, moving the Z-piezo actuator down by 2 µm to penetrate the cell membrane into the cytoplasm led to an initial drop from the ionic current baseline and shortly afterwards, the current baseline raised and stabilised (Figure 3.17A). However, the current baseline never recovered to the value prior to the penetration. In contrast, there was no drop in the current baseline when moving the nanopipette downward in the solution away from the surface (Figure 3.17B).

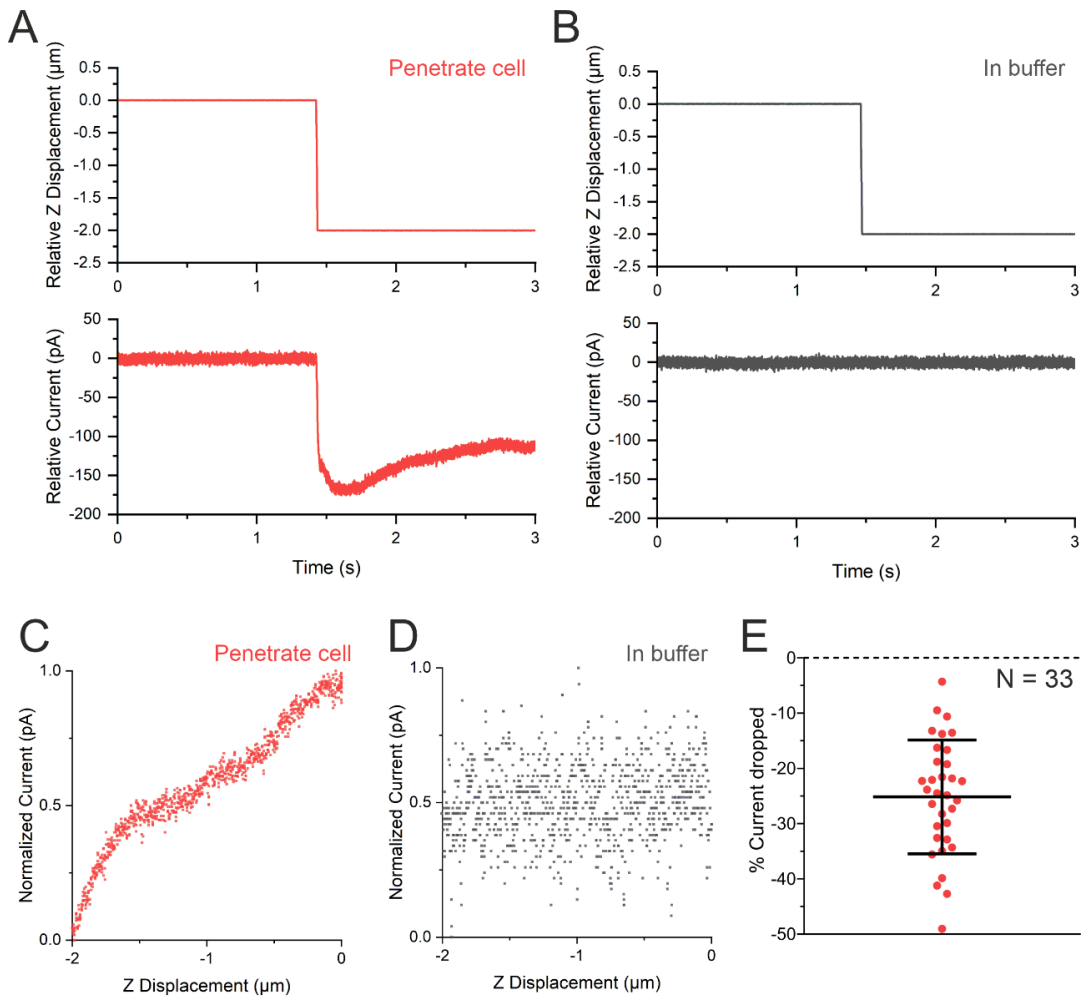

Figure 3.17. Characterising the changes in the ionic current during the penetration of the cell membrane. *The Z-piezo actuator was moved down by 2 µm from the cell membrane to penetrate the cell into the cytoplasm (A), moving down in pure electrolyte (B). The ionic current initially dropped to about 150 pA when the nanopipette was lowered to penetrate the cell membrane, then the ionic current raised by c.a. 50 pA and stabilised as the new baseline. A scatter plot was generated by plotting the distance moved against the normalised current for the cell penetration (C) and in pure electrolyte (D). A steady decline can be seen for the cell penetration unlike in the air control. The percentage of the drop in ionic current between the pre-penetration baseline and the post-penetration baseline showed an average of 25.2 ± 1.8% drop (N=33) (E).*

By plotting the normalised current value against the Z displacement, it idenified a clear correlation between these two factors for the cell penetration profile (Figure 3.17C), but no clear correlation when the nanopipette was not in close proximity to the cell membrane (Figure 3.17D). Altogether 33 cell penetration associated current drop traces were analysed and summarised, the average percentage of drop in the current baseline was 25.2 ± 1.8%.

Although, in principle, the cell membrane capacitance can be used to determine whether the nanopipette has made contact with the cell membrane via whole-cell patch clamp, this is carried out by deliver a small voltage-clamp step that is long enough for the clamp current to come to steady state (Gentet et al., 2000;

Golowasch et al., 2009), if the pipette has made contact with the cell, then the membrane capacitance of the membrane can be recorded. However, due to the small nanopore dimension (*c.a*. 25 nm wide), it is difficult to perform the whole-cell patch clamp as the narrow nanopipette cannot break the patched membrane by suction force. Similar issue had been encountered before when Novak *et al.* attempted to study the channel activities of individual synaptic boutons (Novak et al., 2013). To position the nanopipette near the synaptic boutons, cell topography of the neurons was scanned by the SICM first, this required the use of a narrow nanopipette of 100 nm wide. However, to perform patch clamp on the synaptic bouton, the nanopipette had to be controlled widened to obtain a micropipette as the 100 nm nanopipette was not able to rupture the patched cell membrane (Novak et al., 2013). Similar widening procedure can be used here to measure the cell capacitance, but by widening the nanopipette to a micropipette, it loses the single molecule sensitivity, and thus this approach was not pursued.

Apart from the noticeable drop in the current baseline during cell membrane penetration, in some nanoinjected cells, there were black dots at the site of injections when imaged by confocal microscopy (Figure 3.15 and Figure 3.16). Similar observations have been reported by Hennig *et al.*, when cell cytoplasm nanoinjection was performed. With the use of super-resolution imaging, it was shown that the cytoskeleton was disrupted at the point of injection (Hennig et al., 2015). Another possibility is that the black dot was due to membrane hole caused by the penetration and retraction of the nanopipette.

To investigate this, the nucleus of the HeLa RNuc was nanoinjected with fluorescent 70 kDa dextran conjugates (Figure 3.18A). Prior to the membrane penetration, a 3 × 3 μm topography of the cell membrane just below the nanopipette tip was recorded (Figure 3.18Bi). Then immediately after the retraction of the nanopipette from the cell, the same 3 × 3 μm scan area would be probed again (Figure 3.18Bii). A black dot could be seen in the mCherry-NLS fluorescent channel after the nucleus nanoinjection (Figure 3.18A). The SICM topography showed that there was no hole in the cell membrane, although the line profile analysis showed that the cell membrane was lifted after the nanoinjection (Figure 3.18C), potentially due to the nanopipette retraction.

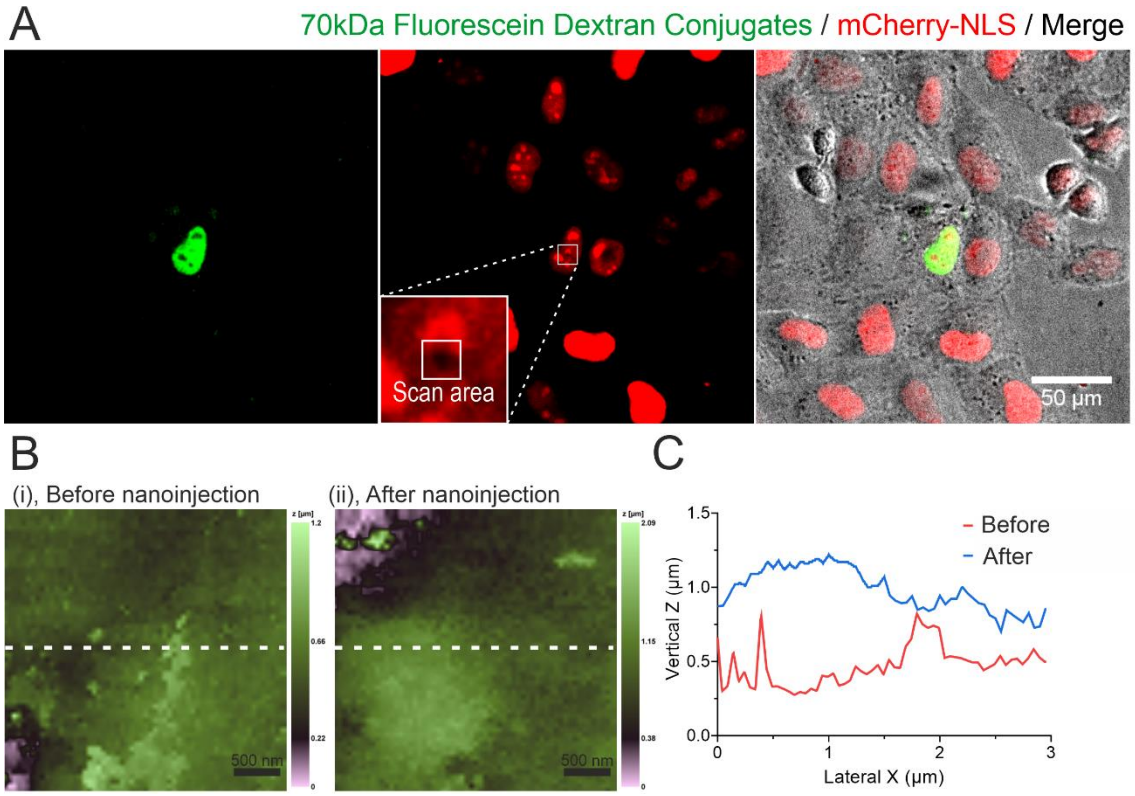

Figure 3.18. The investigation of the nanoinjection artefact. *The nanoinjection procedure generated a black dot artefact as shown in (A). The indicated area was scanned by SICM (B) before nanoinjection (i) and after nanoinjection (ii) and there were no visible membrane disruptions. (C) The line profiles of the topography scan obtained from B and the dotted lines in (B) indicated the line of the measurement. It showed that the cell was lifted by approxiamtely 0.5 µm after the nanoinjection.*

According to previous studies, depending on the cell type, membrane holes resulting from mechanical disruption should be sealed within 90 to 300 seconds (Moe et al., 2015). For HeLa cells, it would require roughly 120 to 240 seconds to seal the membrane hole (Jimenez et al., 2014). The overall time required to scan that area was approximately 10 mins which means that the membrane hole would have been sealed by the time the SICM finished the scan.

3.3.4 Nanoinjection of DNA plasmids

After the demonstration of compartmental specific delivery of charged fluorescent molecules, it was then tested if DNA plasmids could be delivered into the nuclei of cells through nanoinjection and consequently transfect the nanoinjected cell. In these experiments the current trace was monitored, and molecules would also be counted for the first time during the development of the nanoinjection platform.

To show that the nanoinjection procedure could be used to deliver biomolecules for functional readout, the pMaxGFP plasmids would be nanoinjected into the cell by nucleus nanoinjection (Figure 3.19). However, a key factor in these experiments was to minimise the effect on cell viability in the injection process. As Simonis *et al.* showed, the survival rate of the cell depends on the dimension of the nanopipette pore, the voltage applied and the duration of the injection (Simonis et al., 2017), and proposed that the smaller the pore, the higher the chance for the cell to survive. The size of the nanopipette used in that study was of approximately 100 nm wide in diameter, but the pore size of the nanopipettes used herein was *c.a.* 24 nm, a quarter of the size used by Simonis *et al.* and should reduce the harm caused on the cell (Simonis et al., 2017). Additionally, the injected cell would only be able to express GFP if its intracellular machinery was not damaged by the process of nanoinjection and thus provides additional readout on the viability of the injection procedure.

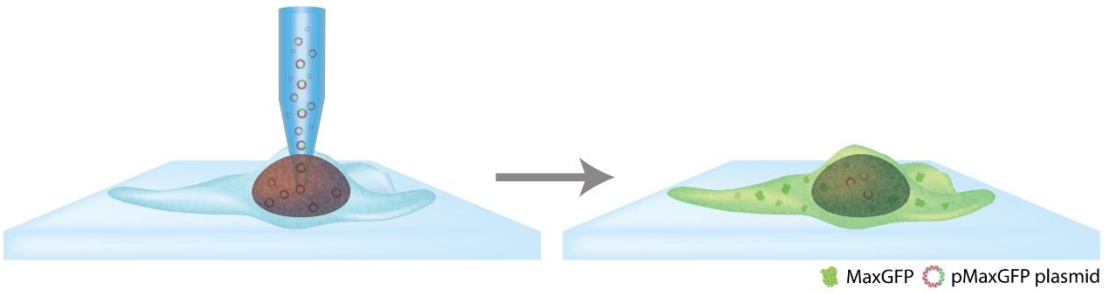

Figure 3.19. The quantitative nanoinjection of the pMaxGFP plasmid into single cell. *The schematic illustration for the single cell transfection by quantitative nanoinjection (A). The nanopipette is first filled with PBS containing 1.3 nM pMaxGFP and the same nanopipette was used to approach the cell surface. After accurate positioning of the nanopipette on top of the cell via SICM, the nanopipette penetrates the cell membrane to reach into the cell nucleus by moving the Z-piezo actuator down to a predefined distance. Then the pMaxGFP plasmid is delivered to the nucleus by electrophoresis, and the ion-current trace is recorded for RPS signal analysis. The injected cell became green after successful transfection of the pMaxGFP.*

The pMaxGFP plasmids encoded for a GFP variant – MaxGFP (also known as the TurboGFP) and this plasmid was used for nanoinjection, as this GFP variant has a faster maturation rate and is in general brighter than the other GFP variants (Evdokimov et al., 2006). The site of nanoinjection was the nucleus, as studies have shown that direct microinjection into the nucleus was the most efficient way to transfect the cell (Lu et al., 2009; Kirton et al., 2013; Rossi et al., 2017). Approximately 20 copies of the plasmids would be sufficient to transfect the cell, in

sharp contrast to almost 20,000 copies of plasmids needed in the cytoplasm (Lechardeur et al., 1999; Bai et al., 2017). The HeLa RNuc cell line was used since the nucleus could be easily identified. In control experiments, HeLa RNuc cells were transfected with pMaxGFP via lipofection. The HeLa RNuc was capable to generate the MaxGFP proteins after the transfection of the pMaxGFP plasmids (Figure 3.20A). The untransfected control showed no MaxGFP fluorescent signals upon excitation with an appropriate laser (Figure 3.20B).

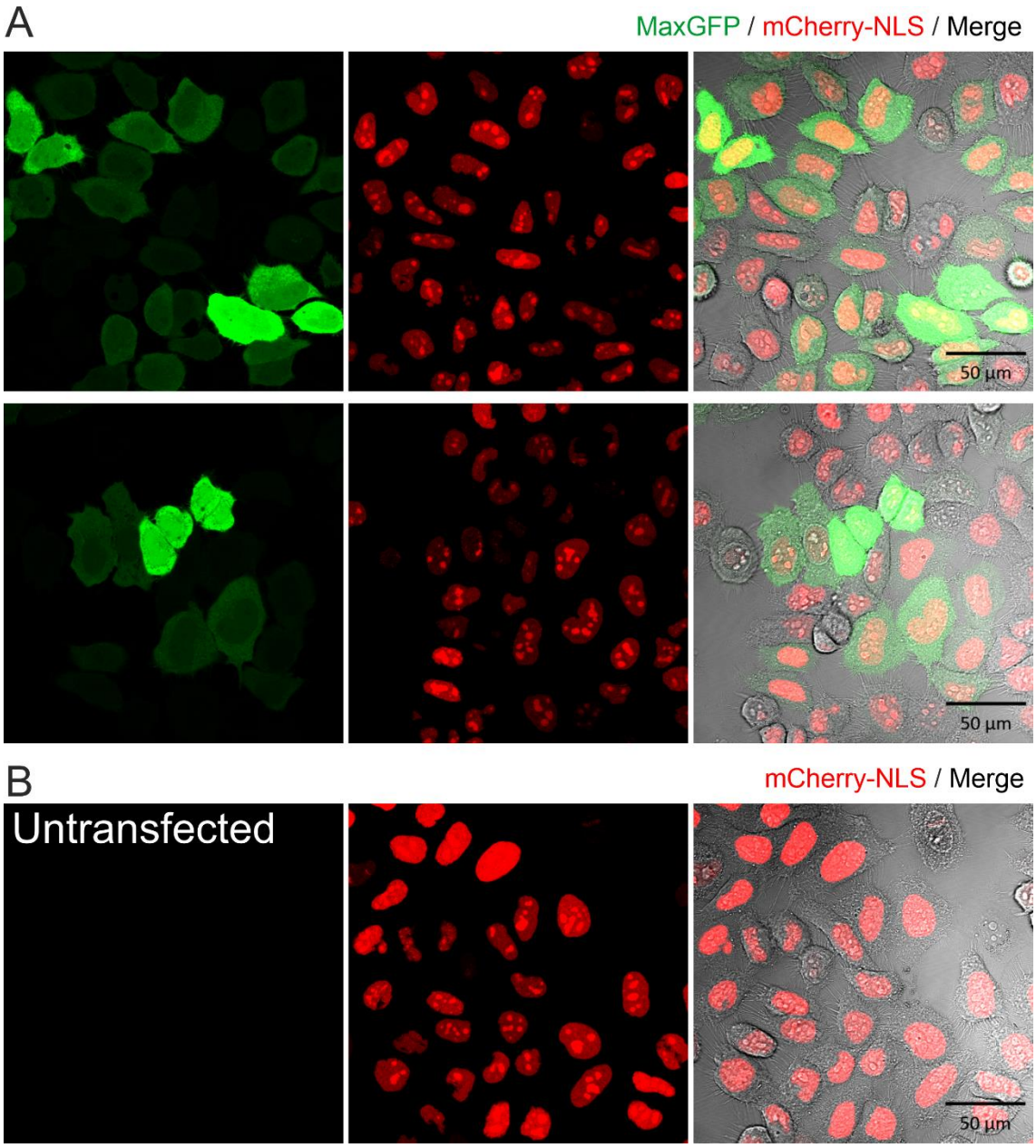

Figure 3.20. The transfection of the HeLa RNuc cells with the pMaxGFP plasmids. *The pMaxGFP plasmid was transfected to the HeLa RNuc cells via the lipofection and imaged with a confocal microscope (A). The pMaxGFP transfected cells became green throughout the whole cell when excited with the appropriate laser. The untransfected control showed no MaxGFP expression (B). Red, mCherry-NLS; Green, MaxGFP; Grey, brightfield image.*

After determining that the HeLa RNuc cells were capable to co-express MaxGFP, pMaxGFP plasmids were then nanoinjected into the nuclei of cells. The plasmids transfected cells would require incubation at 37°C for at least 16 to 24 hours after transfection to allow time for the cells to express the proteins. Thus, to identify the nanoinjected cell 24 hours later, a grid imprinted glass bottom dish was used. The gridded dish contained 4 main squares, and each of these squares was further divided into 400 50 × 50 μm squares and all the squares were numbered and lettered to allow tracking. The HeLa RNuc cells were seeded onto the grid one day prior to SICM injection.

To demonstrate that the nanopipette is capable to detect the translocation of the pMaxGFP plasmid, the nanopipette was filled with 1.3 nM pMaxGFP plasmid diluted in 1×PBS, immersed into the L-15 medium, and -500 mV was used to trigger the delivery of the negatively charged plasmid through electrophoresis (Figure 3.21). The translocations of plasmid were detectable with the nanopipette.

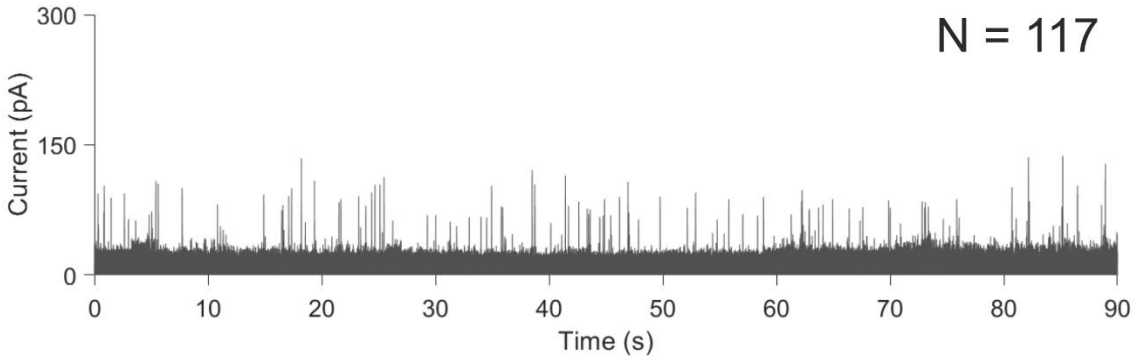

Figure 3.21. The detection of pMaxGFP plasmids translocation inside the L-15 medium. *The 1.3 nM pMaxGFP diluted in 1×PBS filled nanopipette was immersed into the L-15 medium and -500 mV was applied to trigger the delivery of the pMaxGFP plasmids. 117 events were recorded.*

On the day of the injection, similar to the nucleus injection of the dextran conjugates, the nucleus of the cell was penetrated with the nanopipette filled with 1.3 nM pMaxGFP plasmid diluted in 1×PBS and a voltage of -500 mV was applied for *c.a.* 2 minutes to trigger the delivery of the negatively charged DNA plasmids. There was no expression of the MaxGFP fluorescent proteins immediately after the nanoinjection, similarly a black dot at the site of the nanoinjection was observed (Figure 3.22A). 24 hours later, the MaxGFP expression was confirmed by confocal microscopy. Instead of the original nanoinjected single cell, two cells were observed that expressed MaxGFP (Figure 3.22A). The doubling time of a HeLa cell

is *c.a.* 16.2 hours (Kumei et al., 1989), thus the nanoinjected cell divided into two cells during the 24 hours incubation period, both of which expressed MaxGFP.

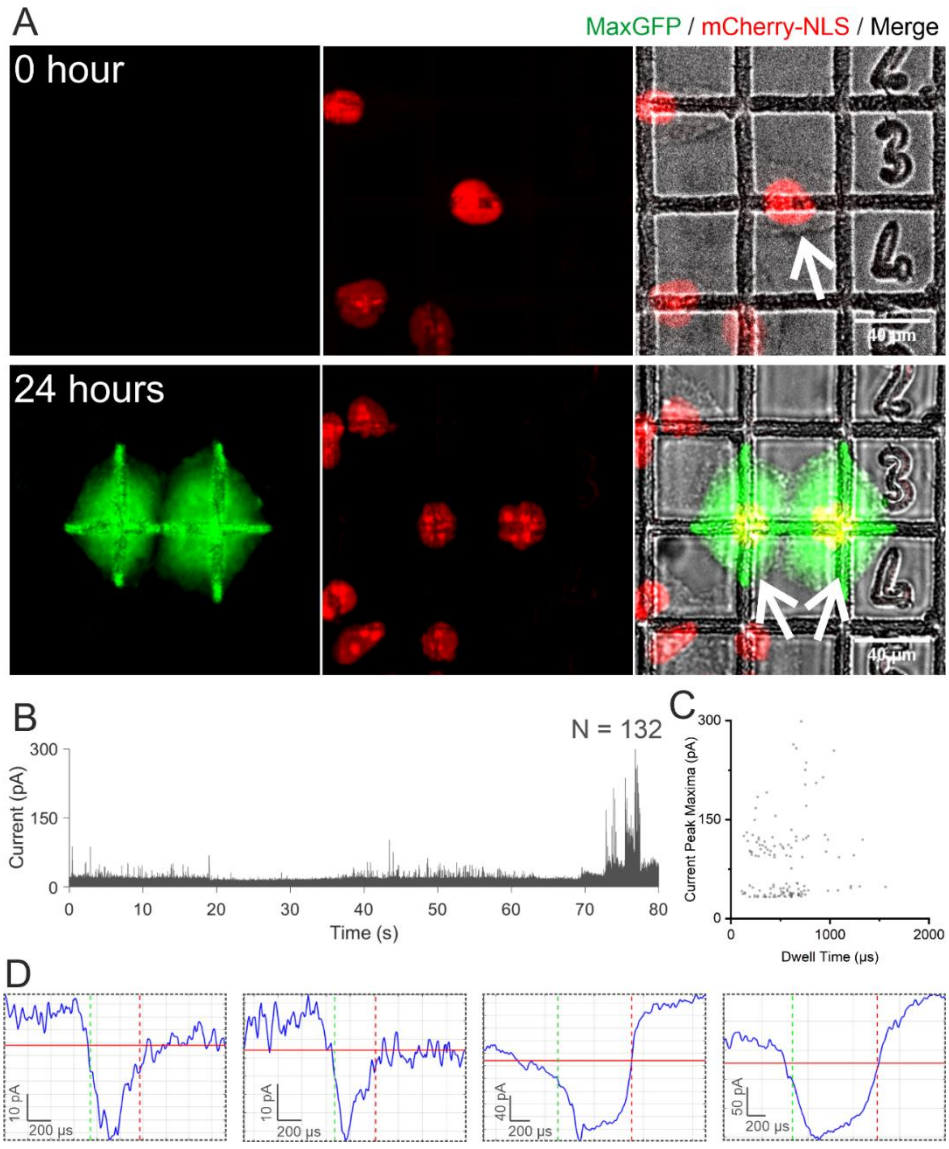

Figure 3.22. Single cell transfection of the HeLa RNuc cells with the pMaxGFP via quantitative nanoinjection – 1. *HeLa RNuc cells were plated onto a gridded glass dish of 50 × 50 µm per square. On the day of the nanoinjection (0 hours), a cell was nanoinjected with the pMaxGFP (arrow) and the same cell was located 24 hours later with the aid of the grid, the cell expressed MaxGFP and had divided (arrows) (A). The baseline adjusted ionic current trace during the nanoinjection was recorded and analysed, and a total of 132 translocation events were detected during nanoinjection (B). The population scatter of the detected translocation event signals (C). Four translocation event signals were shown from the ionic current trace which were randomly sampled (D).*

The current trace during the injection was analysed and showed that 132 translocation events were detected (Figure 3.22B-D). The scatter showed at least two populations separated with one under 75 pA and the other above 75 pA (Figure 3.22C). The trace showed at least 3 bursts of translocation signals at around 0-20 seconds, then around 40-60 seconds and lastly around 70-80 seconds

(Figure 3.22B). The average dwell time and the current peak maxima of the recorded event translocation signals was at 565 ± 30 μs and 84 ± 5 pA respectively.

Two further HeLa RNuc cells were transfected in their nuclei by the quantitative nanoinjection approach (Figure 3.23 and Figure 3.24). The same injection procedures as outlined before was used. Similarly, the nucleus nanoinjected HeLa RNuc cells expressed the MaxGFP proteins 24 hours later (Figure 3.23A and Figure 3.24A) and had divided.

For the cell in Figure 3.23, a total of 44 translocation events were recorded during the nanoinjection, and the average dwell time and current peak maxima of these events were 1200 ± 90 μs and 130 ± 16 pA respectively (Figure 3.23B-D). There were three burst regions at the region from 0 to 2, 6 to 10 and 30 to 40 seconds (Figure 3.23B). The blank regions of the ionic current trace were electronic noise and were removed manually as it interfered with the calculation of the baseline. The population scatter showed a broad distribution (Figure 3.23C) and potentially two populations of molecules with one under 1000 μs and one above 1000 μs.

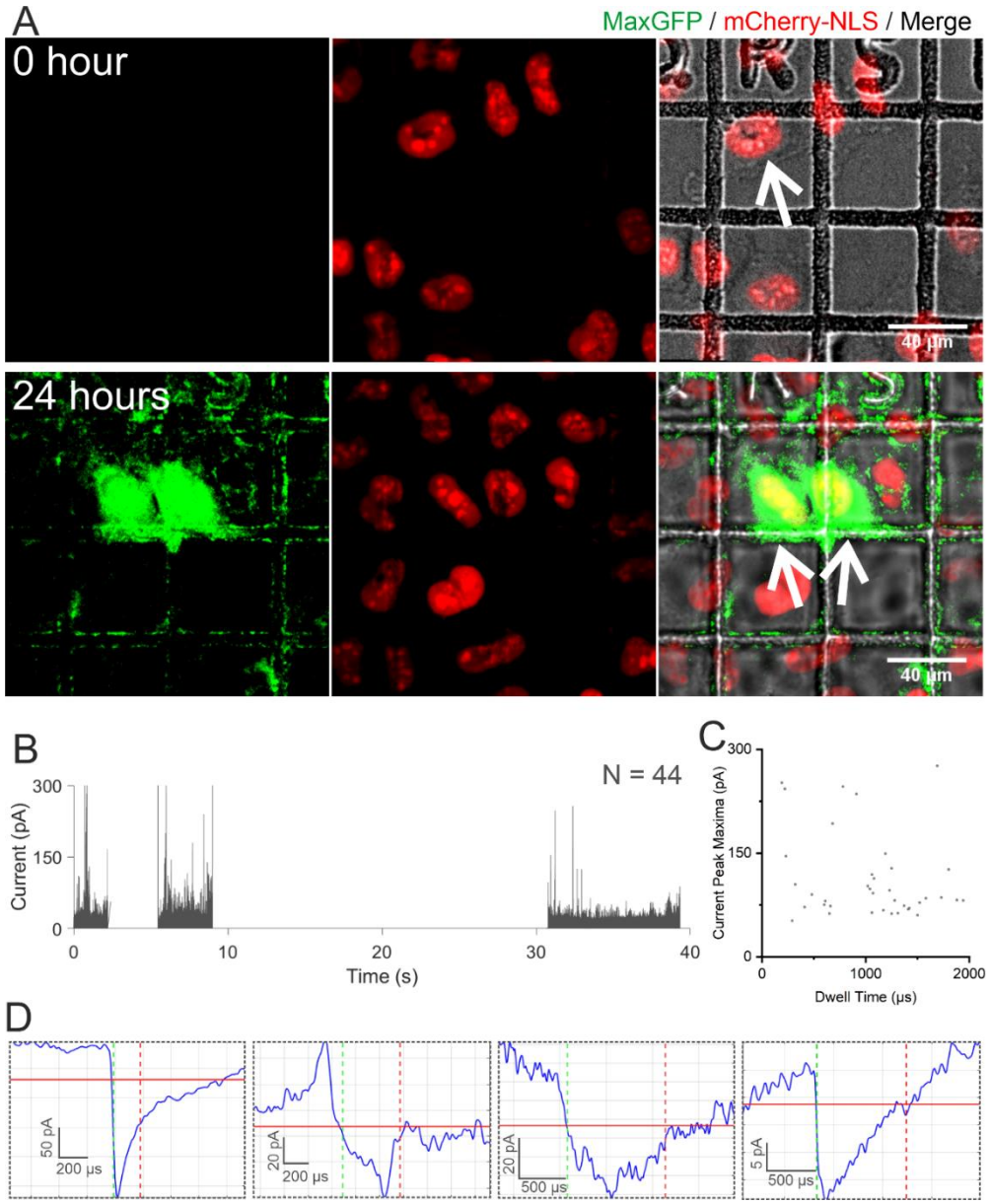

Figure 3.23. Single cell transfection of the HeLa RNuc cells with the pMaxGFP via quantitative nanoinjection – 2. *HeLa RNuc cells were plated onto a gridded glass dish of 50 × 50 µm per square. On the day of the nanoinjection (0 hours), a cell was nanoinjected with the pMaxGFP (arrow) and the same cell was located 24 hours later with the aid of the grid, the cell expressed MaxGFP and had divided (arrows) (A). The baseline adjusted ionic current trace during the nanoinjection was recorded and analysed, and a total of 44 translocation events were detected during nanoinjection (B). The population scatter of the detected translocation event signals (C). Four translocation event signals were shown from the ionic current trace which were randomly sampled (D).*

For the cell in Figure 3.24, 37 translocation events were detected with the average dwell time and the current peak maxima at 987 ± 120 µs and 43 ± 5 pA respectively (Figure 3.24B-D). There was no clear burst region for this nanoinjection. The population scatter showed an emerging single population with a broad distribution on the dwell time (Figure 3.24C).

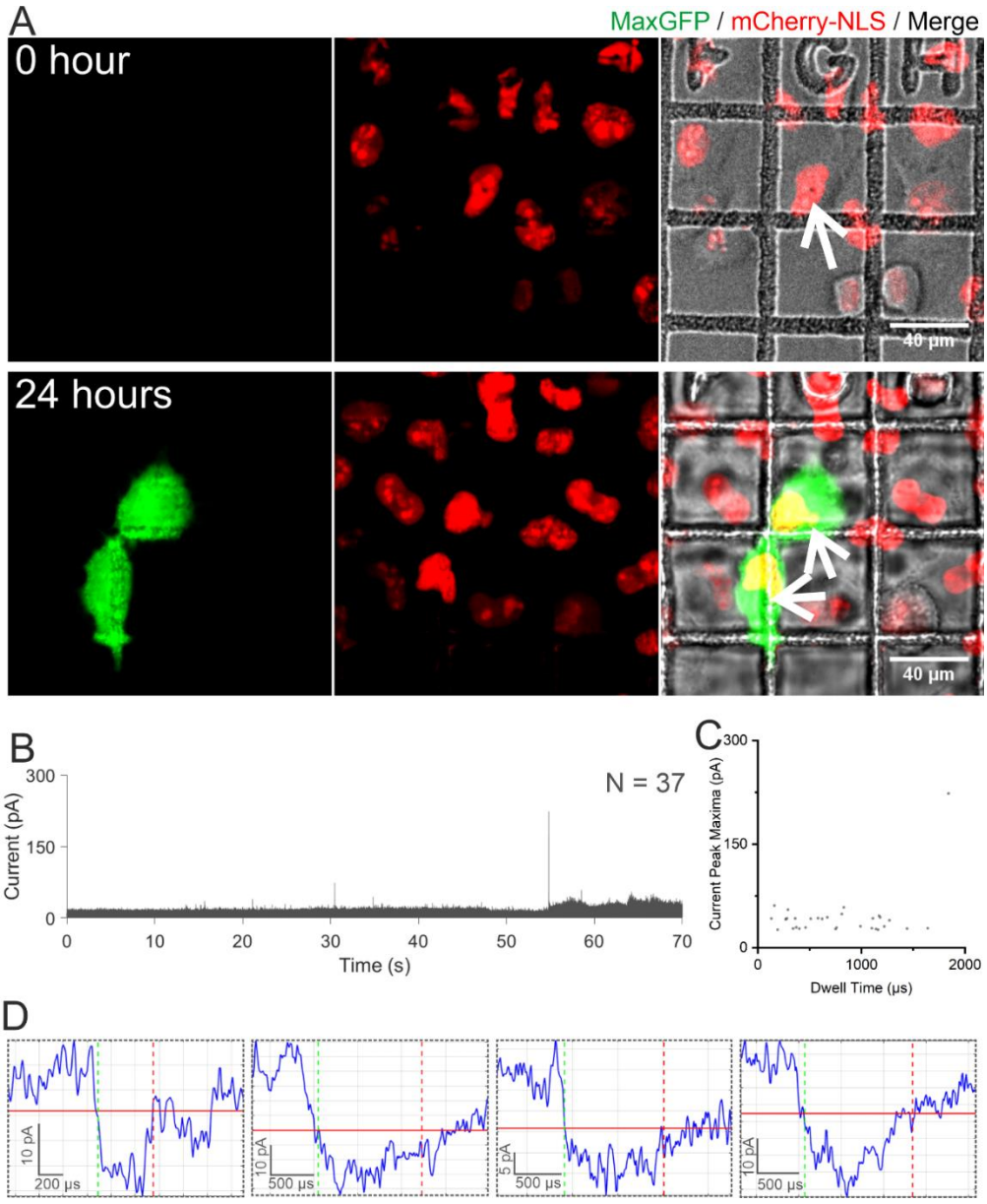

Figure 3.24. Single cell transfection of the HeLa RNuc cells with the pMaxGFP via quantitative nanoinjection – 3. *HeLa RNuc cells were plated onto a gridded glass dish of 50 × 50 µm per square. On the day of the nanoinjection (0 hours), a cell was nanoinjected with the pMaxGFP (arrow) and the same cell was located 24 hours later with the aid of the grid, the cell expressed MaxGFP and had divided (arrows) (A). The baseline adjusted ionic current trace during the nanoinjection was recorded and analysed, and a total of 37 translocation events were detected during nanoinjection (B). The population scatter of the detected translocation event signals (C). Four translocation event signals were shown from the ionic current trace which were randomly sampled (D).*

These 3 nanoinjection experiments demonstrate that the nanoinjection procedure results in the expression of a protein encoded by the plasmid and does not affect the viability or cell division of the injected HeLa cells.

The transfection of immortalised cell lines such as the HeLa cells are routine in cell biology, but the plasmid transfection of primary cells such as neurons is more challenging. Whether performing a nanoinjection using a nanopipette with a < 30 nm nanopore can deliver a DNA plasmid into primary cells without affecting their

viability was examined next. Primary mouse dorsal root ganglion (DRG) neurons were used as a model primary cell, as they are difficult to transfect using a common transfection routine (Kirton et al., 2013).

The primary DRG neurons were plated onto a gridded dish and cultured for 4 days prior to nanoinjection. To visualise the nucleus, membrane permeable nucleic acid binding fluorescent dyes such as Hoechst 33342 and DRAQ5 were considered, but several studies pointed out that these dyes could cause DNA damage and affect the viabilities of the cell (Singh et al., 2004; Zhao, H. et al., 2009; Sen et al., 2018). This led to the decision that the primary neurons would not be labelled with fluorescent dyes. Since the transfection would be most effective with direct nucleus injection, the rough position of the nucleus was assumed to be in the centre of the cell and would also be the highest point of the entire cell. The SICM and bright field imaging together were used to identify the highest point of the cell, and the nanopipette would then be moved downwards to perform nanoinjection.

Two DRG neurons were successfully transfected by using this approach (Figure 3.25 and Figure 3.26). The DRG primary neurons expressed the MaxGFP fluorescent proteins 24 hours after nanoinjection (Figure 3.25A and Figure 3.26A). The morphology of the first cell suggested that it could be a glial-like cell contaminant in the DRG neuron during the surgical preparation (Figure 3.25), whereas the other had a neuronal-like morophology (Figure 3.26). Nonetheless, for the first cell, 13 translocation events were detected with the majority of the events located between 10 to 20 seconds, and there was no clear single population in the scatter plot (Figure 3.25B-C). The average dwell time and the current peak maxima were 1121 ± 210 μs and 97 ± 23 pA respectively. Moreover, 24 hours after the nanoinjection the cell expressed MaxGFP.

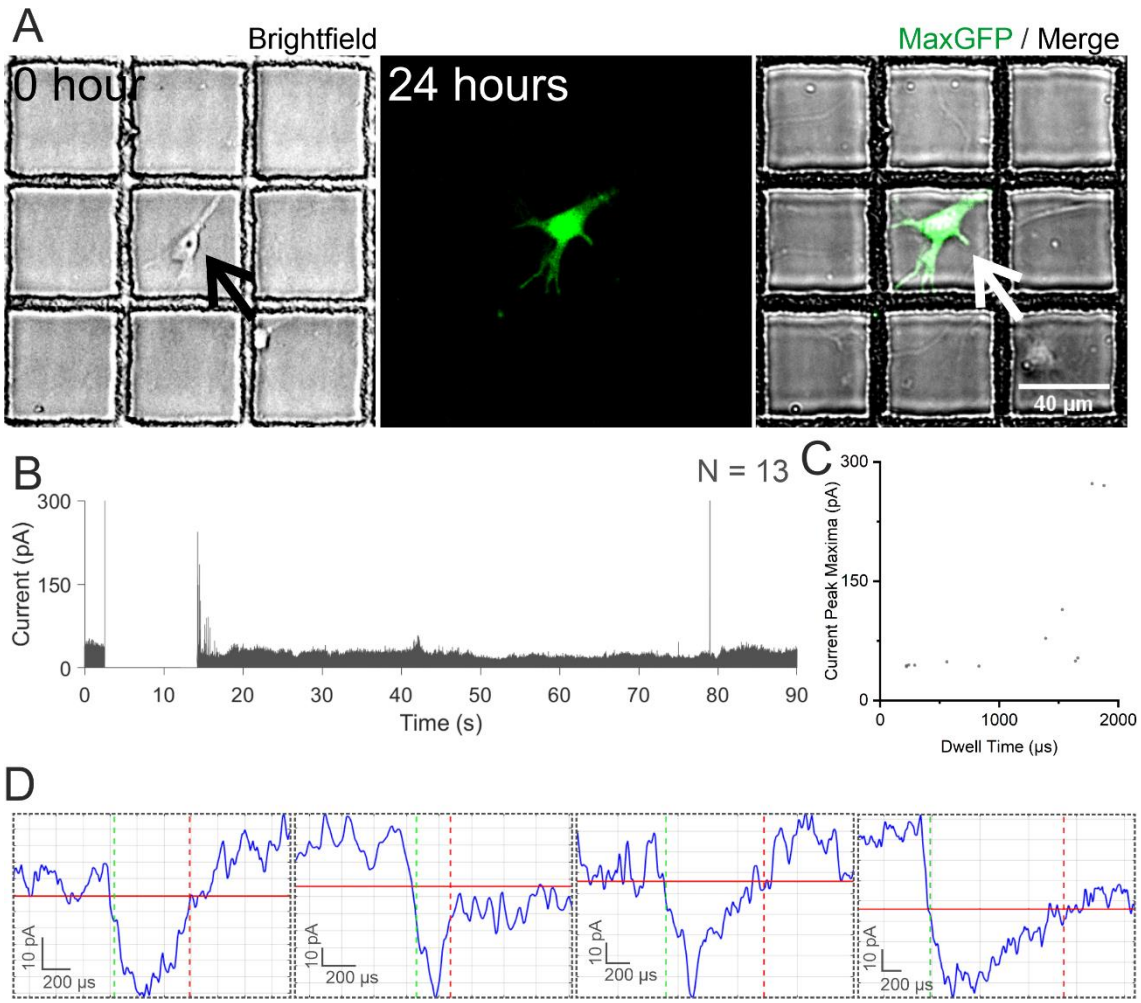

Figure 3.25. Single cell transfection of a primary DRG neuron with the pMaxGFP via quantitative nanoinjection – 1. *Primary DRG neurons cells were plated onto a gridded glass dish of 50 × 50 µm per square. On the day of the nanoinjection (0 hours), a cell was nanoinjected with the pMaxGFP (arrow), and the same cell was located 24 hours later with the aid of the grid. The cell expressed MaxGFP (A). The baseline adjusted ionic current trace during the nanoinjection was recorded and analysed, and a total of 13 translocation events were detected during nanoinjection (B). The population scatter of the detected translocation event signals (C). Four translocation event signals were shown from the ionic current trace, which were randomly sampled (D).*

For the second cell, there were 41 translocation events detected with an average dwell time of 800 ± 120 µs and current peak maxima of 31 ± 2 pA, and the scatter showed a broad distribution along the dwell time (Figure 3.26B-C). This cell also expressed MaxGFP 24 hours after nanoinjection.

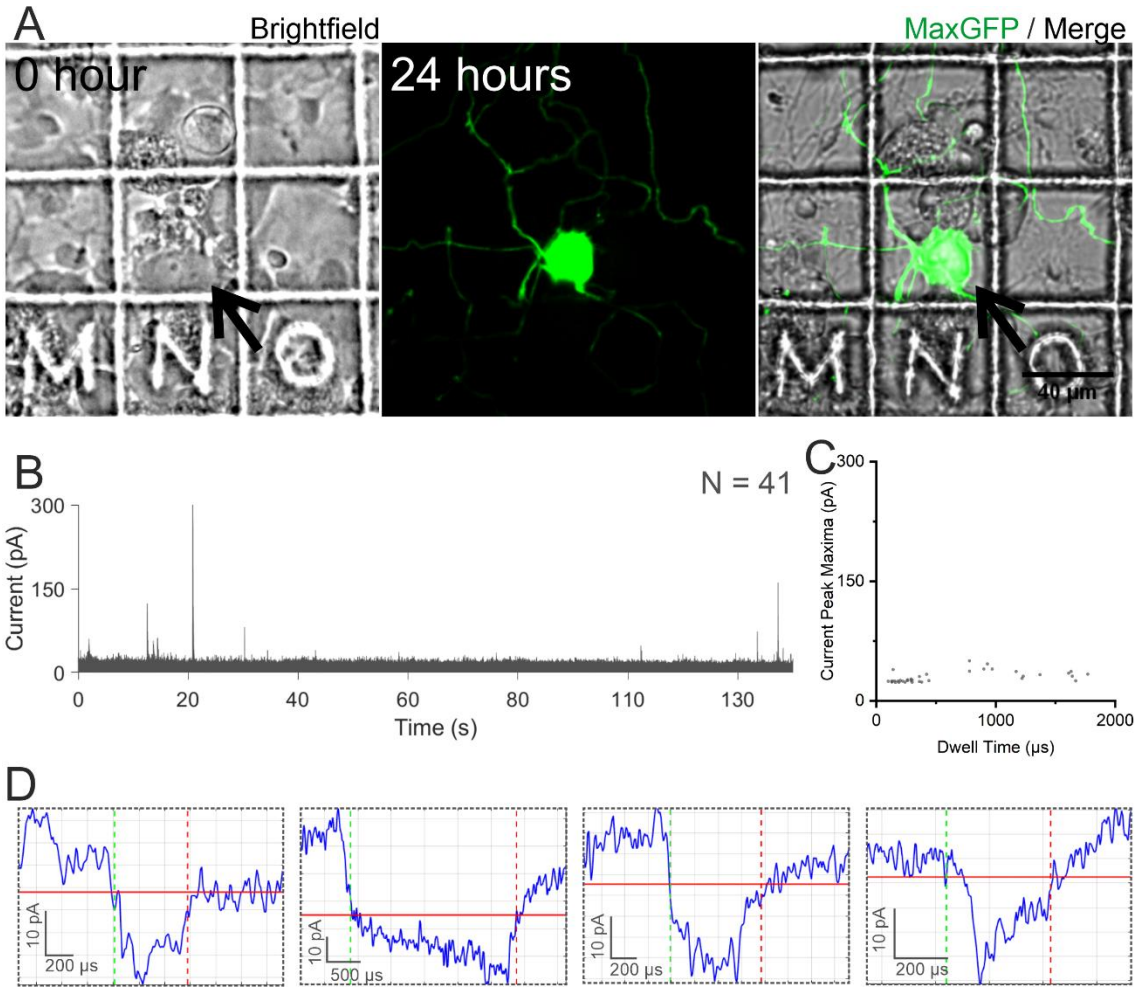

Figure 3.26. Single cell transfection of the primary DRG neurons with the pMaxGFP via quantitative nanoinjection – 2. *Primary DRG neurons cells were plated onto a gridded glass dish of 50 × 50 µm per square. On the day of the nanoinjection (0 hours), a cell was nanoinjected with the pMaxGFP (arrow), and the same cell was located 24 hours later with the aid of the grid. The cell expressed MaxGFP (A). The baseline adjusted ionic current trace during the nanoinjection was recorded and analysed, and a total of 41 translocation events were detected during nanoinjection (B). The population scatter of the detected translocation event signals (C). Four translocation event signals were shown from the ionic current trace, which were randomly sampled (D).*

Whether the translocation events observed so far associated with the tranloscations of the DNA plasmid were tested. The nanopipette was filled with 1×PBS and penetrated HUVEC cells, negative voltages of -500 mV were used, similar to the delivery of the plasmid (Figure 3.27). Less than 10 events were recorded in 2 attempts, these events could be due to random ionic flux in the set-up and also random interactions between the intracellular materials and the nanopipette pore. Pan *et al.* recently demonstrated that resistive pulse can be generated inside the intracellular environment when the cell engulfed nanoparticles translocated from inside the cell to the nanopipette through the nanopore (Pan et al., 2020). Yu *et al.* also showed that resistive pulse signal can be generated by molecules interacting with the nanopipette tip. In that study, a

resistive pulse signal was generated when a *c.a.* 100 nm amorphous amyloid aggregates in the electrolyte bath temporarily interacted with the 30 nm wide nanopore of the nanopipette tip (Yu et al., 2019), due to the size of the aggregates, it was not possible for the aggregates to be translocated through the nanopore. These studies demonstrated that temporarily interaction between the nanopipette tip and the intracellular macromolecules can lead to formation of the resistive pulse signal. To ensure that the translocation events were due to the biomolecules inside the nanopipette, a higher concentration of the analyte can be used to fill the nanopipette.

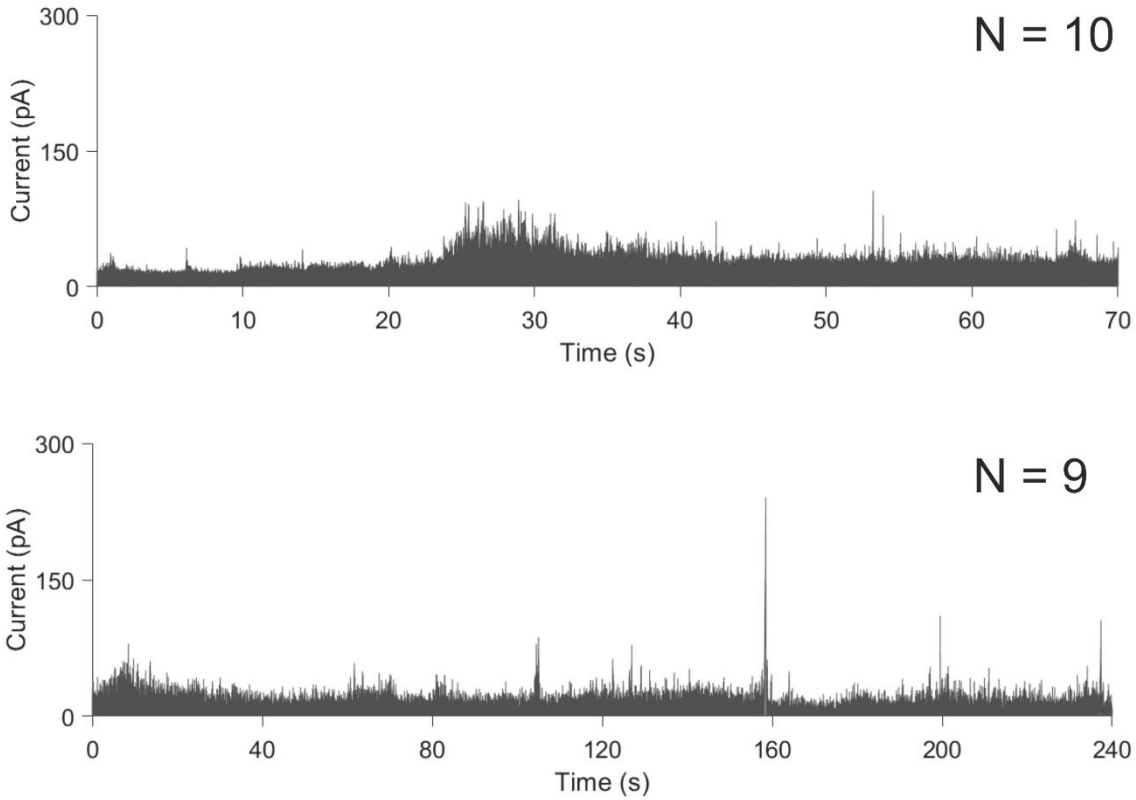

Figure 3.27. Event translocation testing with a bare pore nanopipette. *The nanopipette was filled with 1×PBS and penetrated into two primary HUVEC cells, -500 mV were applied, the traces were analysed. There were some events, however this could be due to random ionic flux and/or intracellular materials temporarily interacted with the nanopore.*

3.3.5 Nanoinjection of enzymes

The next objective was to test whether nanoinjection can perform quantitative delivery of functionally active enzyme into the cell, as the reaction catalysed by the enzyme provides a way to confirm the successful delivery.

The tetrameric enzyme β-galactosidase was chosen to be nanoinjected, it has a molecular weight of 465 kDa, with a dimension of 18 × 14 × 8.7 nm as resolved by cryo-electron microscopy (Bartesaghi et al., 2014) which would fit the size of the nanopipette pore. Additionally, this enzyme is only functional when the tetrameric structure of the β-galactosidase is retained (Juers et al., 2012; Li, X. et al., 2018), and thus posed as a good candidate to also test whether nanoinjection could deliver biomolecules into cell without disrupting the structures. The endogenous level of β-galactosidase is typically used as the senescence marker in mammalian cells, as the cell ages, the β-galactosidase increases in lysosomes (Lee, B.Y. et al., 2006; Jakhria et al., 2014; Cai et al., 2020). As a result, different colorimetric and fluorescent substrates are commercially available to measure the enzyme activity. These substrates include the commonly used colorimetric X-gal substrate (Itahana et al., 2013), and fluorescent substrates such as the 5-dodecanoylaminofluorescein di-β-D-galactopyranoside and SPiDER-βGal can also be used (Jakhria et al., 2014; Doura et al., 2016).

The nanopipette was filled with β-galactosidase and was nanoinjected into cell, the activity of the β-galactosidase was monitored using the fluorescent substrate SPiDER-βGal. The SPiDER-βGal was chosen because it has several good properties: 1. it is cell membrane permeable; 2. it has the highest quantum yield amongst all fluorescent β-galactosidase substrates; 3. the substrate itself is not fluorescent, it is only fluorescent after reacting with β-galactosidase; 4. the cleaved substrate is not cell membrane permeable, thus the fluorescence signal can build up inside the cell over time (Doura et al., 2016). 2 μM of the SPiDER-βGal was added to the cell culture medium throughout the entire nanoinjection process. To avoid the nanoinjected β-galactosidase localisation overlapping with the endogenous lysosomal β-galactosidase, the protein was nanoinjected into the nucleus instead (Figure 3.28).

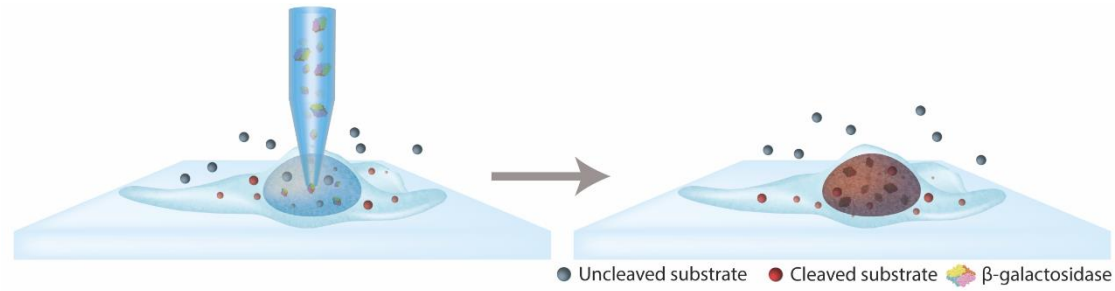

Figure 3.28. The schematic illustration of the quantitative nanoinjection of functional enzyme into mammalian cells. *The nanopipette is filled with 1 μM β-galactosidase in PBS and the same nanopipette is used to approach the cell surface. After accurate positioning of the nanopipette on top of the cell, the nanopipette penetrates the cell membrane to reach into the cell nucleus by moving the Z-piezo actuator down to a predefined distance. Then the β-galactosidase is delivered to the nucleus by applying voltage. During this entire process, 2 μM of SPiDER-βGal substrate is added to the SICM imaging medium. The substrate reacts with both the endogenous lysosomal localised β-galactosidase and the nucleus injected β-galactosidase, which can be detected by fluorescent microscopy.*

To validate that the β-galactosidase could cleave the SPiDER-βGal substrate into its fluorescent excitable form, HeLa cells were transfected with the commercially available pSV-β-Galactosidase plasmid. The SPiDER-βGal was added to the medium at 2 μM and incubated for 5 minutes before imaging with a fluorescence microscope (Figure 3.29A).

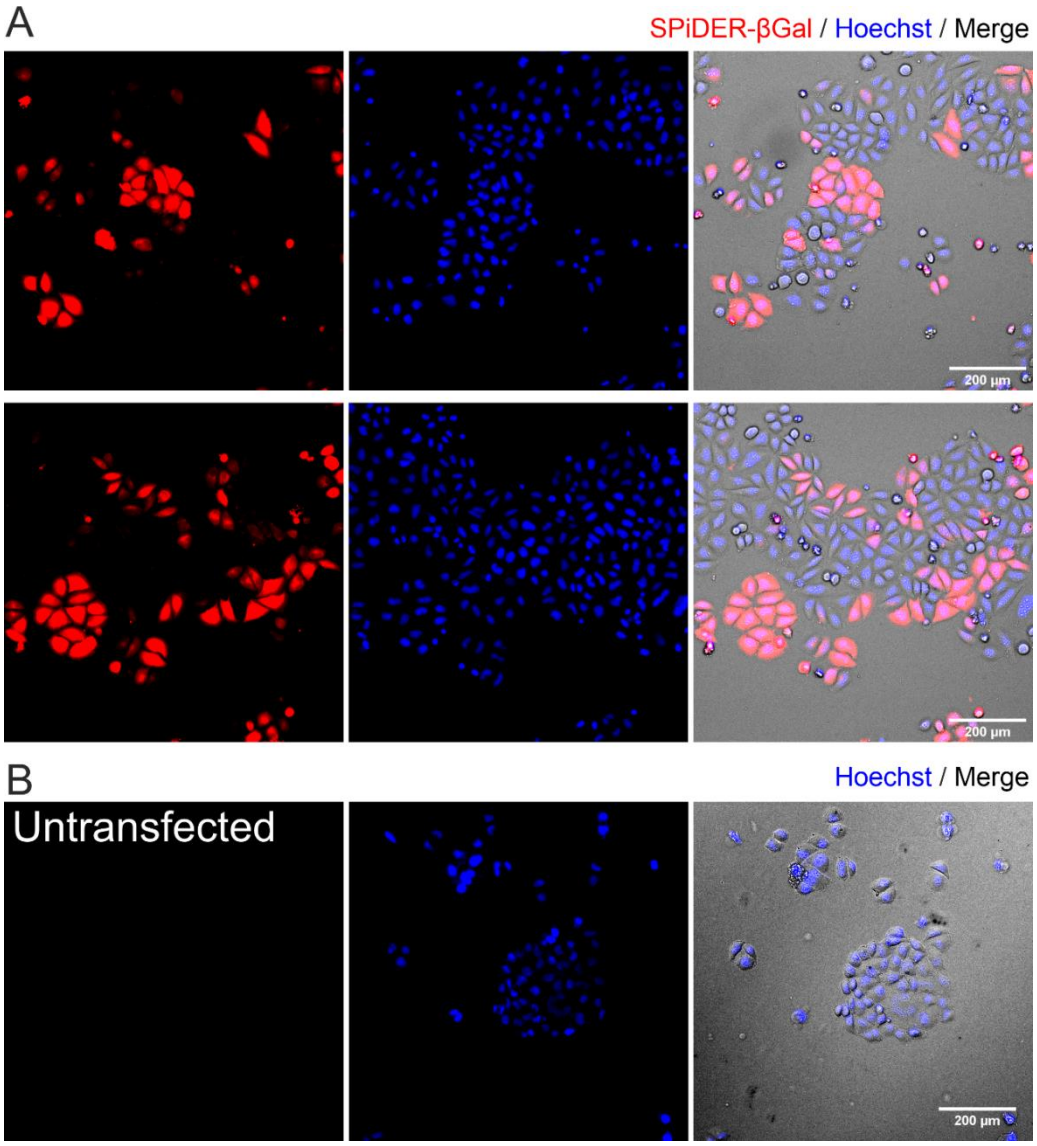

Figure 3.29. The characterisation of the β-galactosidase and SPiDER-βGal reaction inside cells. *The HeLa cells were transfected with the commercially available pSV-β-galactosidase plasmid via the lipofectamine 2000 system. After the transfection, the cells were incubated with 2 µM of SPiDER-βGal for 15 minutes and then imaged by a widefield fluorescence microscope. The pSV-β-galactosidase transfected cells became red overall after the incubation with the SPiDER-βGal after excitation with suitable wavelength (A). The untransfected control showed no fluorescent signals (B). Red, SPiDER-βGal; Blue, Hoechst 33342; Grey, brightfield image.*

The cells successfully transfected with the pSV-β-Galactosidase plasmid became more fluorescent when excited with an appropriate wavelength, in contrast to the untransfected cells (Figure 3.29B).

The *E. coli* β-galactosidase used for nanoinjection was commercially available, the protein was further purified and analysed by size exclusion chromatography (SEC), a chromatography technique that separates molecules based on their hydrodynamic radii (Hong et al., 2012). Proteins and molecules with different molecular weights were used to calibrate the size exclusion column (Figure 3.30A).

Then the β-galatosidase was further purified using the calibrated column and only the higher molecular weight eluate was retained (Figure 3.30A). The calculated molecular mass was 491 kDa, and the calculation was based on the elution volume and column calibration curve (Figure 3.30B). This molecular weight is consistent with the purified β-galactosidase retaining its tetrameric structure (Bartesaghi et al., 2014).

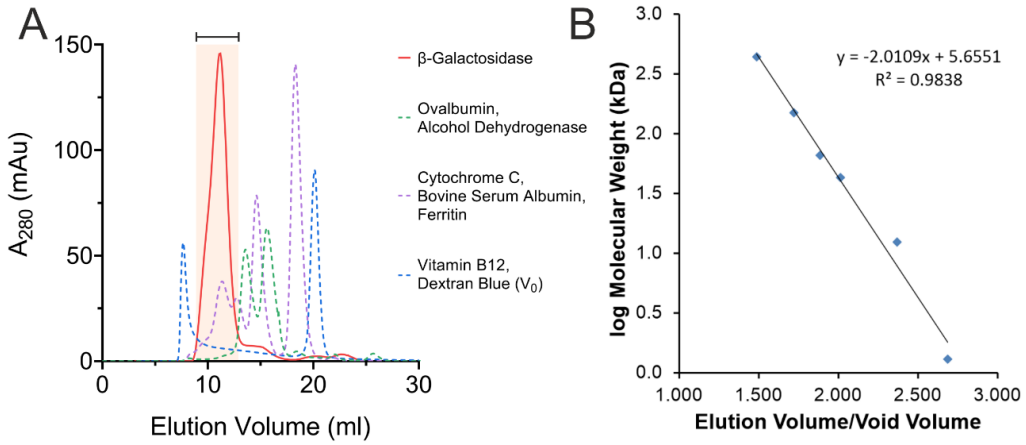

Figure 3.30. Characterisation of β-galactosidase via size-exclusion chromatography. *(A) The purchased β-galactosidase is further purified using a Superdex 200 10/300 GL column. The left panel shows the elution profile of the β-galactosidase. The bracket indicates the volume (4 ml) collected for use. The β-galatosidase elution profile (red) is overlaid on top of the elution profiles of the calibrants. The β-galatosidase eluted at the expected elution volume for a tetramer. The molecular weight of the calibrants are: ovalbumin (43 kDa), alcohol dehydrogenase (150 kDa), cytochrome C (12 kDa), bovine serum albumin (66 kDa) and ferritin (440 kDa). The calibration curve for the Superdex 200 10/300 GL column is shown on the right. The void volume is at 7.6 ml. The calculated molecular weight for β-galactosidase is 491 kDa based on the calibration graph (B), whereas the molecular weight of the tetramer is 465 kDa.*

The enzyme activity of the purified 1 μM *E. coli* K-12 β-galactosidase was also analysed using 2 μM SPiDER-βGal substrate and a fluorescent plate reader (Figure 3.31A). The excitation spectrum was measured from 442 to 590 nm with a 0.5 nm step and the emission spectrum was measured from 504 to 695 nm with a 1 nm step inside a fluorescence plate reader (Figure 3.31A). The cleaved SPiDER-βGal excitation and emission maxima wavelength was determined to be at 530 and 550 nm respectively, in line with the original study (Doura et al., 2016).

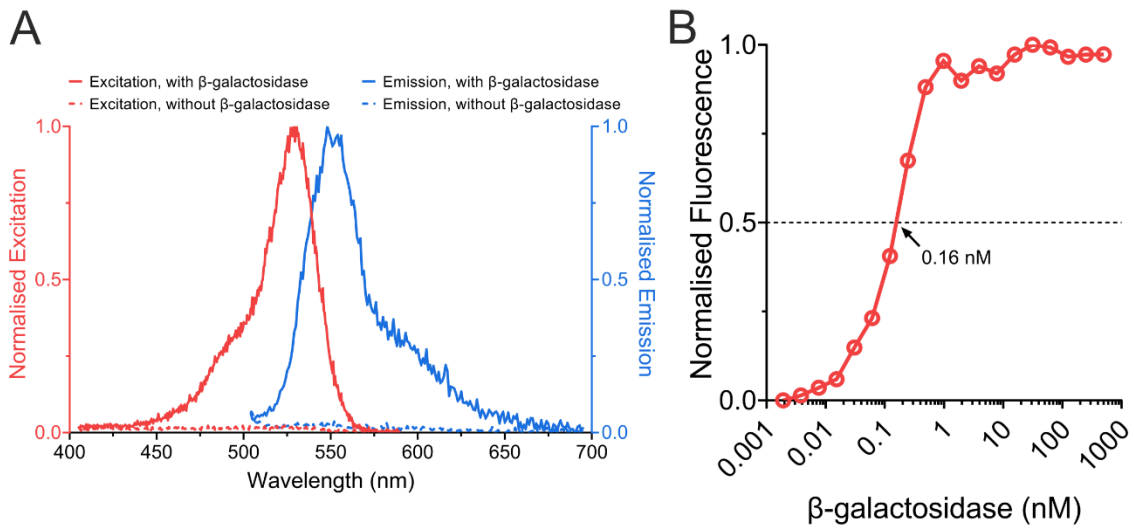

Figure 3.31. The fluorescence excitation/emission properties of the cleaved SPiDER-βGal and the determination of the concentration of β-galactosidase needed to react with the SPiDER-βGal substrate. *1 μM β-galactosidase is incubated with 2 μM SPiDER-βGal and the emission/excitation spectra is analysed. The excitation maxima is at 530 nm and emission maxima is at 550 nm. Without the addition of the SPiDER-βGal substrate, there is no fluorescent signal (A). The sensitivity of the fluorescent substrate is checked by performing a serial dilution of the β-galactosidase from 1 μM down to 1 pM. 2 μM of SPiDER-βGal substrate is added to the β-galactosidase and allowed to incubate for 5 minutes at room temperature prior to reading. 0.16 nM of β-galactosidase is required to reach half of the maximum fluorescent signals (B).*

Then, a serial dilution of β-galactosidase was performed from 1 μM down to 1 pM. It was important to determine the minimum effective concentration of β-galactosidase, as this informed the minimum number of molecules that would need to be delivered to the cell to produce a detectable fluorescent signal. The minimum concentration of β-galactosidase required to excite half of the maximum fluorescent signal from 2 μM cleaved SPiDER-βGal was at 0.16 nM (Figure 3.31D). Since the delivery of the β-galactosidase would be quantified and counted, thus the number of molecules needed to be delivered to reach 0.16 nM inside the cell could then be calculated. Using the HeLa cells as the model cell, the nucleus volume was reported to be around 0.7 pL (Guillaume-Gentil et al., 2016), and using this value, approximately 67 molecules would be needed to reach 0.16 nM inside a 0.7 pL volume.

Similar to the pMaxGFP plasmid detection control, the nanopipette was filled with 1 μM β-galactosidase enzyme diluted in 1×PBS, immersed into the L-15 medium, and -500 mV was used to trigger the delivery of the negatively charged proteins through electrophoresis (Figure 3.32). Unlike the plasmid, the translocation of the protein β-galactosidase was not readily detectable, due to proteins translocate through the nanopore at high velocity (Plesa et al., 2013).

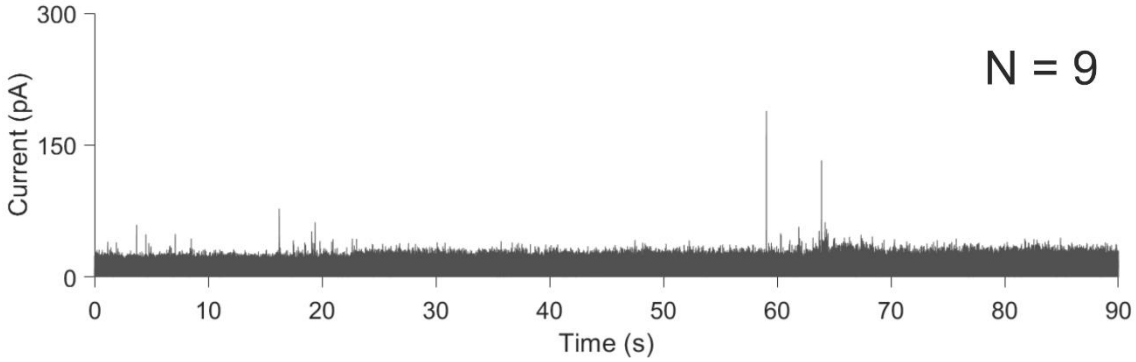

Figure 3.32. The detection of β-galactosidase translocation inside the L-15 medium. *The 1 μM β-galactosidase diluted in 1×PBS filled nanopipette was immersed into the L-15 medium and -500 mV was applied to trigger the delivery of the β-galactosidase. 9 events were recorded.*

The primary human umbilical vein endothelial cell (HUVEC) was chosen as the cell for nanoinjection with β-galactosidase. This was because the nuclei of the HUVEC cells were readily identifiable through bright field microscopy, without the need of fluorescent labelling. The nanopipette was loaded with 1 μM β-galactosidase diluted in PBS containing 0.1 ng/μl Alexa Fluor 594 maleimide. The concentration of the β-galactosidase was chosen to be sufficiently high to ensure that the translocation events detected were due to the β-galactosidase. Then the nanopipette was moved downward by 4000 nm to penetrate the cell membrane to reach the nucleus, and the negatively charged β-galactosidase (pI = 4.61, (Boyer et al., 1970)) would be delivered to the cell electrophoretically by applying a voltage of -700 mV. The Alexa Fluor 594 Maleimide dye was used as a co-injector to confirm the injection location.

The successful nucleus nanoinjection of the functional β-galactosidase into the nucleus of a single HUVEC cell could be observed as an increase in nuclear fluorescence after the injection, while the neighbour cell had a lower level of nuclear fluorescence (Figure 3.33A).

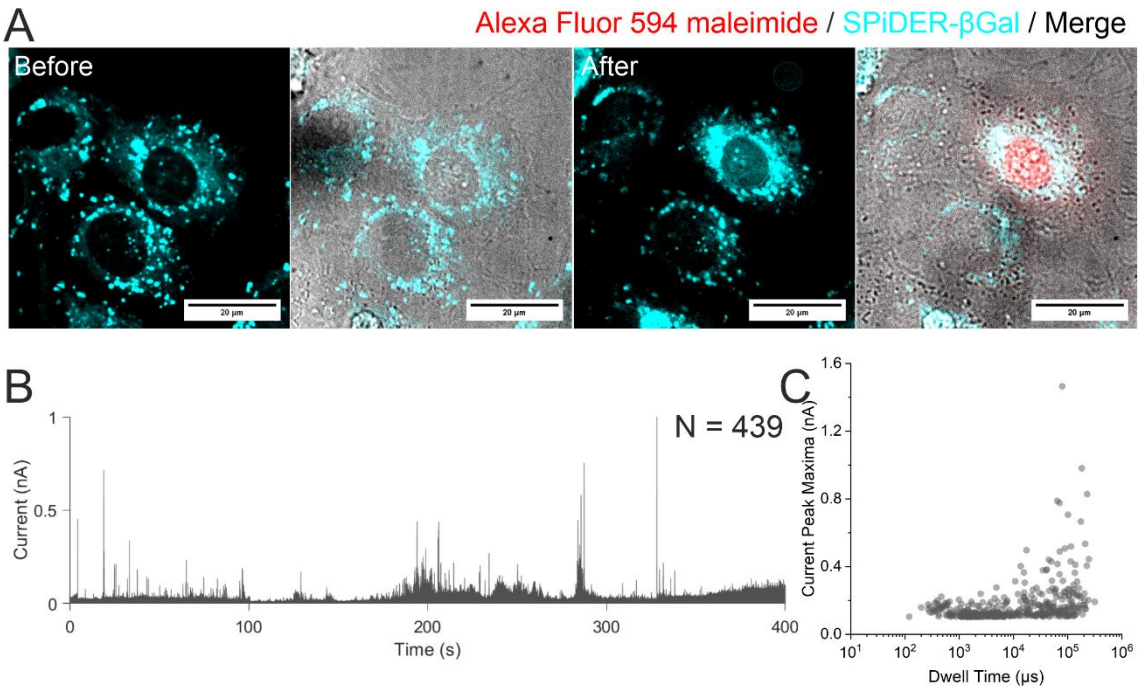

Figure 3.33. Intracellular quantitative nanoinjection of the enzyme β-galactosidase. *The primary cell HUVEC was used as the cell model. The purified β-galatosidase was diluted to 1 µM with PBS containing 0.1 ng/µl Alexa Fluor 594 maleimide and was used to fill the nanopipette. The SPiDER-βGal was added to the SICM imaging buffer at a final concentration of 2 µM. (A) Fluorescent and brightfield images of the SPiDER-βGal channel and brightfield were taken before the nanoinjection. Once inside the cell, a voltage of -700 mV was used to deliver the β-galactosidase into the nucleus. The fluorescent and brightfield images were taken after the nanoinjection. (B) 439 molecules were recorded from the current trace during the injection and (C) the population scatter produced from the trace.*

The custom written MATLAB script processed current trace indicated that 439 β-galactosidase molecules were translocated (Figure 3.33B). The average dwell time recorded was 41761±2707 µs and 0.288±0.014 nA. The Alexa Fluor 594 signal was only observed after the nanoinjection demonstrated that the intracellular injection was successful and importantly, that the fluorescent signal was inside the nucleus indicating that the injection had taken place in the target cellular compartment (Figure 3.33A).

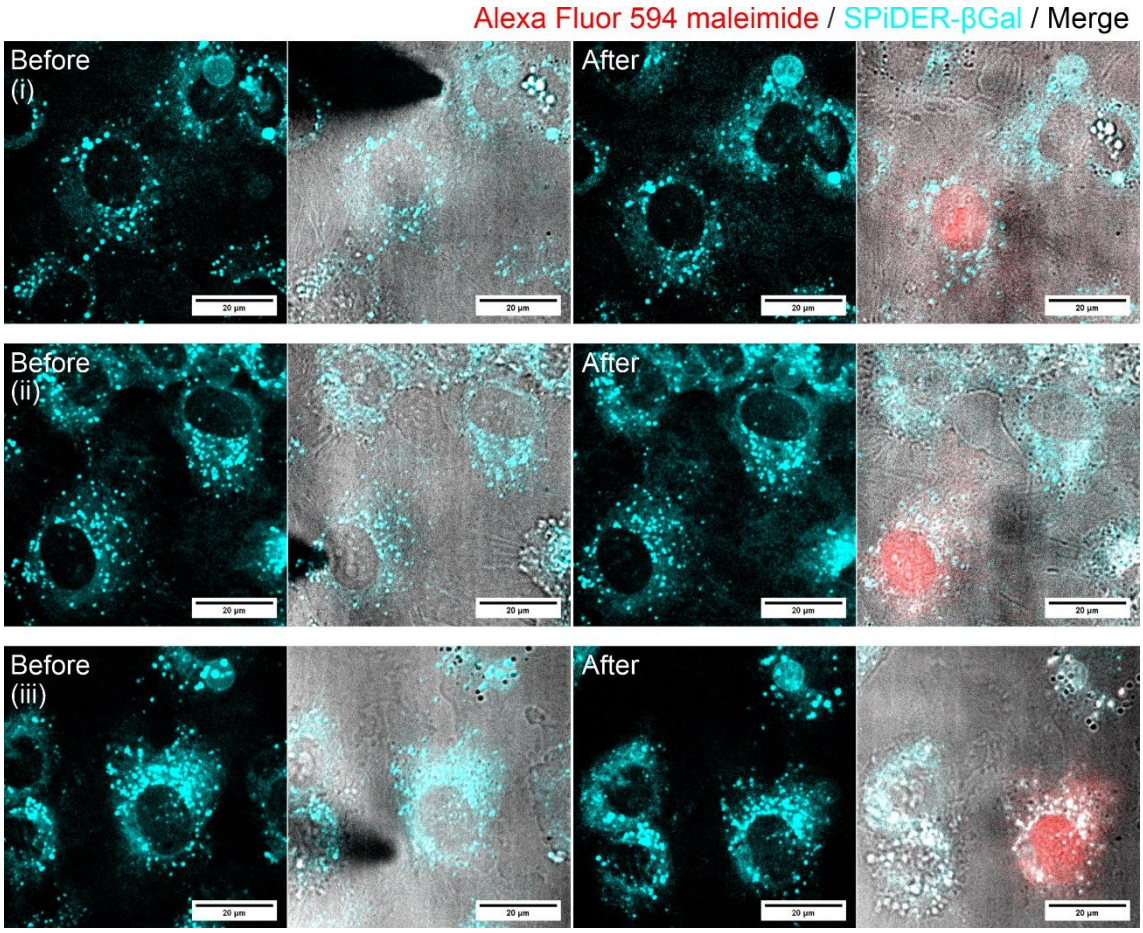

Figure 3.34. The injection of the Alexa Fluor 594 Maleimide dye to the nucleus of the HUVEC cell. *Three examples were shown. The nanopipette was filled with 0.1 ng/µl Alexa Fluor 594 Maleimide and delivered to the nucleus with a voltage of -700 mV. The before and after nanoinjection showed that the cell fluorescent signals were similar when the SPiDER-βGal channel was used. The Alexa Fluor 594 confirmed that the injection had carried out and that injection did not interfere with signals from the SPiDER-βGal channel.*

To confirm that the increase in fluorescent signals in the SPiDER-βGal channel was due to the injection of β-galactosidase, mock injections were carried out by using the PBS solution containing 0.1 ng/µl Alexa Fluor 594 Maleimide (Figure 3.34). The Alexa Fluor 594 Maleimide injected cells were fluorescent positive, in contrast, the cells lacked any visual changes when the SPiDER-βGal fluorescent channel was used. The current trace was also recorded during the injection, and the script analysis showed there were some translocation events (data not shown). However, these event signals could be due to a random flux of the ion current, and interferences from intracellular macromolecules with the nanopipette (Pan et al., 2020), which would require further study in the future.

Similar to the nanoinjection of plasmids, additional 8 HUVEC cells were injected with the β-galactosidase. The molecules injected vary from 44 to 1061 molecules

(Figure 3.35). The number of molecules delivered was close to or above the previously approximated minimum number of molecules required to cause at least 50% of the fluorescent signal generated by the reaction between β-galatosidase and the SPiDER-βGal. The population scatter varies between each injection, potentially due to the intracellular environment varying slightly between cells. The injected cells and the traces can be found in the Appendix – A.

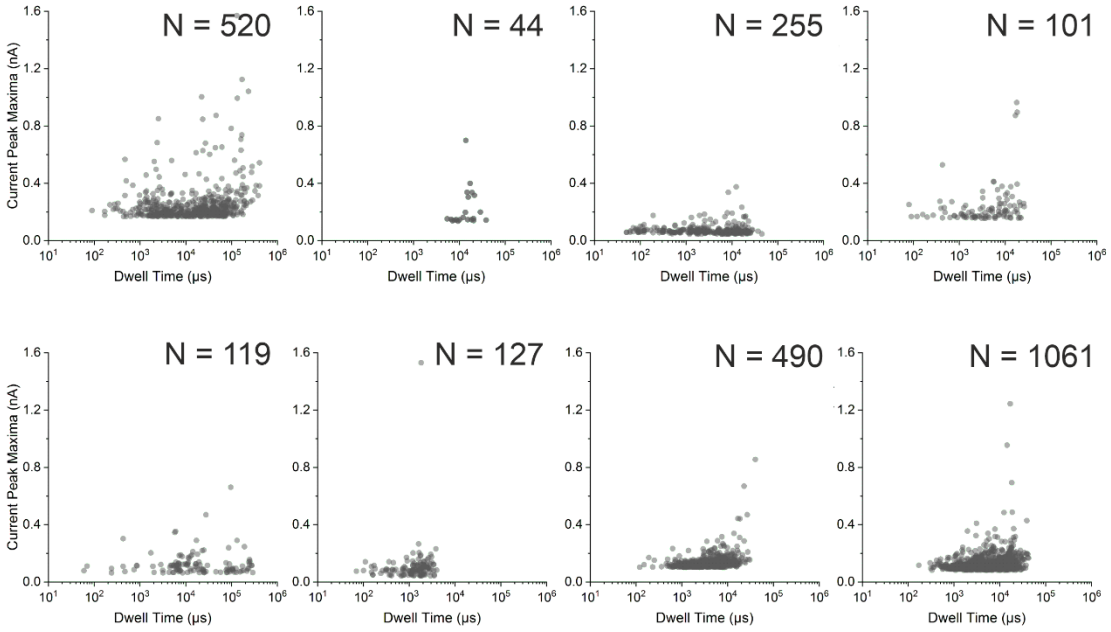

Figure 3.35. The summarised scatter plots of the additional eight nanoinjections. *Each scatter plot represents a single nanoinjection of β-galactosidase into the nucleus of the HUVEC cells. Each scatter was produced by analysing the associated injection current trace. The population scatters showed the different distributions of the molecules between each nanoinjection experiment.*

Altogether 9 HUVEC cells were injected with β-galactosidase, and to quantitatively demonstrated the results, the corrected total cell fluorescence (CTCF) fold change was calculated. During the nanoinjection experiment, the SPiDER-βGal channel was used to take fluorescent images before and after nanoinjection, alongside the bright field image of the same cell (Figure 3.36A). These images were analysed with ImageJ to obtain the fluorescent signal data for the calculation of CTCF. First, three background fluorescent levels were measured by selecting three spots where there were no cells with three numbered dotted circles (Figure 3.36A), which were used to calculate the average background fluorescent levels. The nanoinjected cell, denoted as the target cell here, only the fluorescent signal of the centre of the nucleus was measured, as indicated with a red dotted circle (Figure 3.36A). The

same measurement was performed on a cell that was not injected, denoted as neighbour cell, as shown in Figure 3.36A with a blue dotted circle. This entire process was used in both before and after SPiDER-βGal channels fluorescent images and repeated for all the image sets.

The CTCF for 9 sets of images were calculated, and then the fold difference was calculated by comparing the CTCF values before nanoinjection to after nanoinjection, *i.e.* a positive fold change indicated that the CTCF value was higher after the nanoinjection. It showed that the target cell had a higher CTCF fold change than the neighbour cell, indicating that the β-galactosidase injection had caused the SPiDER-βGal fluorescent signals in the nucleus to become brighter than the control neighbour cell (Figure 3.36B). Indeed, the majority of the target cells had a higher CTCF fold change than the neighbour cells within the same image set (Figure 3.36C). Finally, the relationship between the number of β-galactosidase molecules delivered and the CTCF fold change was investigated by using a scatter plot (Figure 3.36D). However, neither population nor correlation could be identified, which could be due to variations in the cell shape and the volume of the nucleus could be slightly different between each cell.

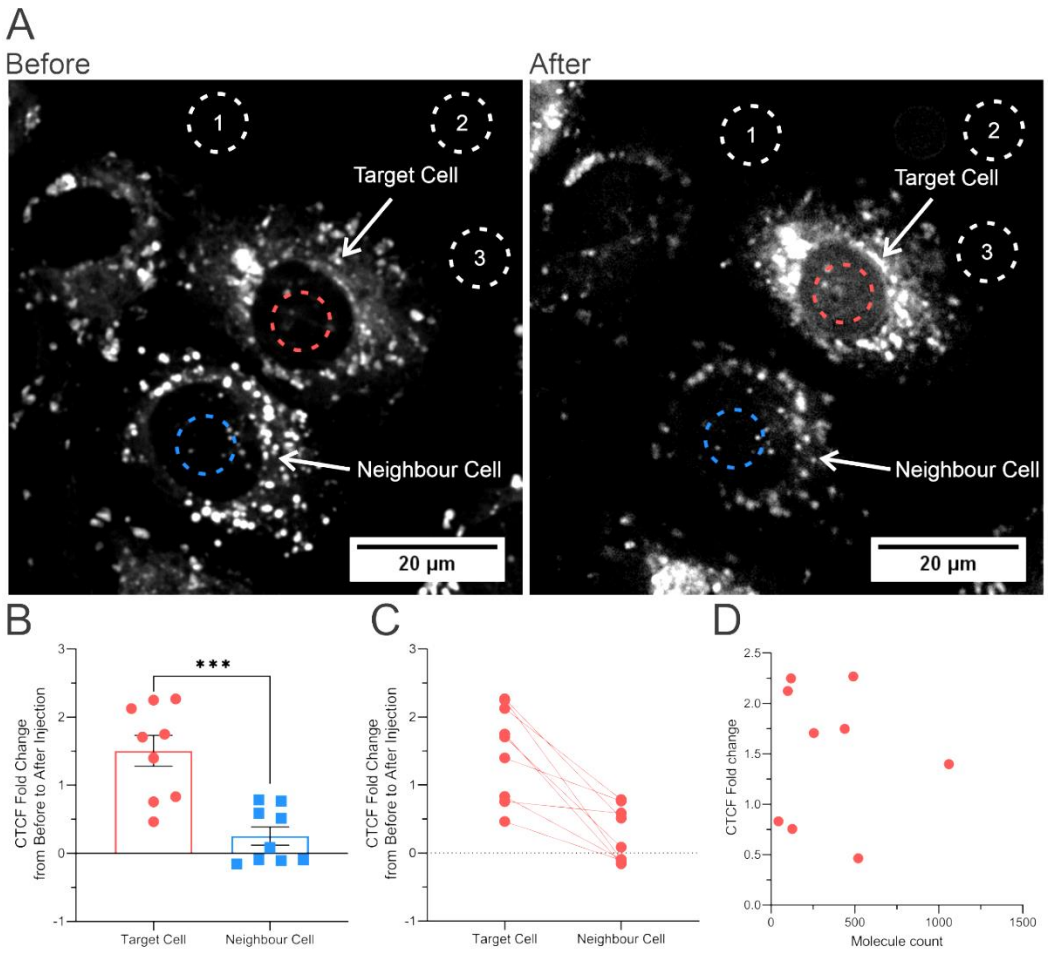

Figure 3.36. Quantification of fluorescent signals before and after nanoinjection with β-galactosidase . *(A) A set of representative SPiDER-βGal fluorescent images are shown. The numbered dotted circles were used to measure the fluorescent level of the background, red and blue dotted circles indicated the fluorescent measurements taken for either the nucleus of the target nanoinjected or the neighbour control cells. The CTCF values were calculated for both before and after nanoinjection images, and the same procedure was repeated for the remaining 8 sets of experiment images. (B) The CTCF fold change was calculated by comparing the CTCF values of the cell after nanoinjection to before nanoinjection. The CTCF fold change showed that nanoinjected cells had a higher CTCF value, i.e. a brighter nucleus compared to the neighbour cell. The pairing correlation plot showed that the nanoinjected cell usually had a higher CTCF fold change compared to its own neighbour cell. (D) Showed the scatter plot of molecule count against CTCF fold change of the target cell, no clear correlation could be identified between the molecule count and the CTCF fold change.*

3.3.6 Quantitative Nanoinjection of amyloid fibrils

As discussed in Chapter 1, the quantitative nanoinjection platform has the potential to be used to study amyloid diseases, here this concept will be tested. Alexa Fluor 594 fluorescently labelled A90C α-synuclein fibrils were generated as outlined in Chapter 2 Section 2.4.4. The fibrils were thawed and pelleted by centrifugation at 16,000×rcf for an hour. The supernatant was removed, and then the pellet was resuspended and diluted to 1 µM monomeric equivalent in 1× PBS and the resultant suspension was used to fill the nanopipette for nanoinjection.

The primary rat cortical neurons had been used to study Parkinson's disease as a cell model (Íñigo-Marco et al., 2017; Kahle et al., 2018; Ganjam et al., 2019; Cascella et al., 2021), and thus were used here. The neurons were seeded and cultured for an additional 4 days prior to usage (Figure 3.37).

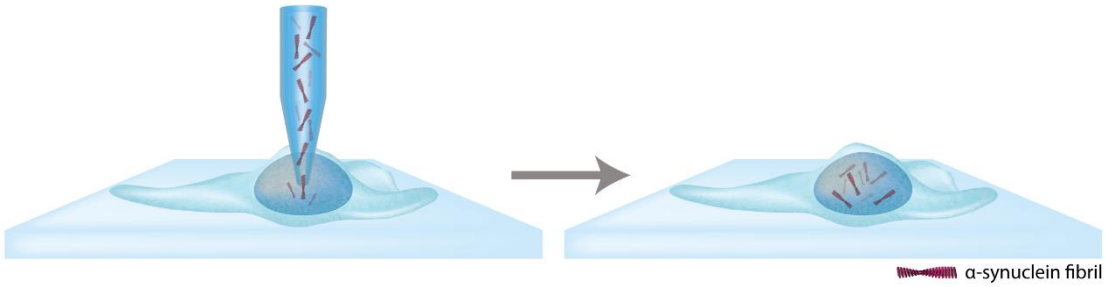

Figure 3.37. Schematic illustration of the injection of the α-synuclein fibrils. *The A90C fluorescently labelled α-synuclein fibrils were injected into the cell by nanoinjection, then the cell was imaged immediately after the nanoinjection.*

The centre of the neuronal body was chosen as the location of the injection and the nanopipette was moved downward by 4 μm to reach the intracellular cell space. The depth decision was made based on the SICM topography data. After the penetration, a negative voltage of -700 mV was used to deliver the negatively charged fibril seeds into the cell. The assumption was made based on the resolved α-synuclein fibril model, that the C-terminal region of the monomeric α-synuclein was not packed into the fibril core (Tuttle et al., 2016) and would be negatively charged at neutral pH. To test whether the nanopipette can detect the translocation of the α-synculein fibril, the nanopipette was filled with 1 μM fluorescently labelled α-synuclein fibril diluted in 1×PBS, immersed into the L-15 medium, and -500 mV was used to trigger the delivery of the negatively charged fibrils through electrophoresis (Figure 3.38). Similar to the translocation of β-galactosidase, the translocation of the fibril was not readily detectable, due to proteins translocate through the nanopore at high velocity (Plesa et al., 2013).

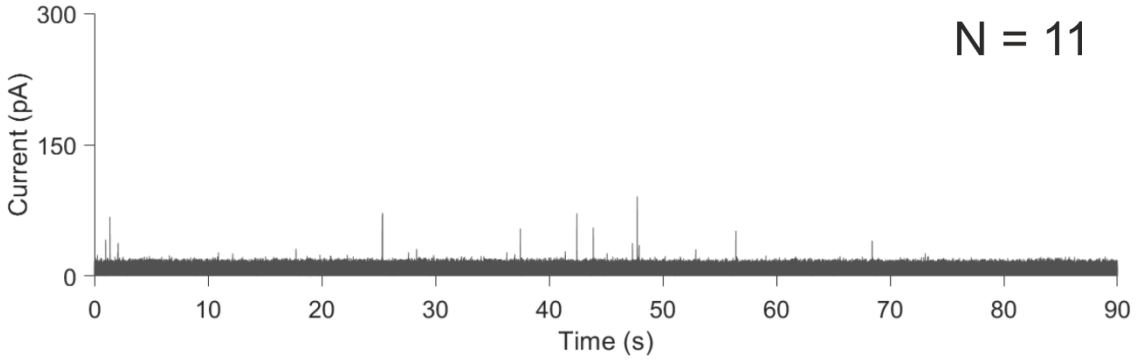

Figure 3.38. The detection of α-synuclein fluorescently labelled fibrils translocation inside the L-15 medium. *The 1 μM monomeric equivalent α-synuclein fluorescently labelled fibrils diluted in 1×PBS filled nanopipette was immersed into the L-15 medium and -500 mV was applied to trigger the delivery of the α-synuclein fluorescently labelled fibrils. 9 events were recorded.*

The fluorescent images showed that after the injection of Alexa Fluor 594 labelled fibril seeds, there was an increase in fluorescent signal inside the cell (Figure 3.39A), since the architecture of fibrils were fluorescent labelled, and these together indicate the successful delivery of α-synuclein fibrils into the cell. A total of 153 translocation events were detected during this injection (Figure 3.39B). The average dwell time μs and the current for these events were 9246±722 and 0.197±0.011 nA respectively.

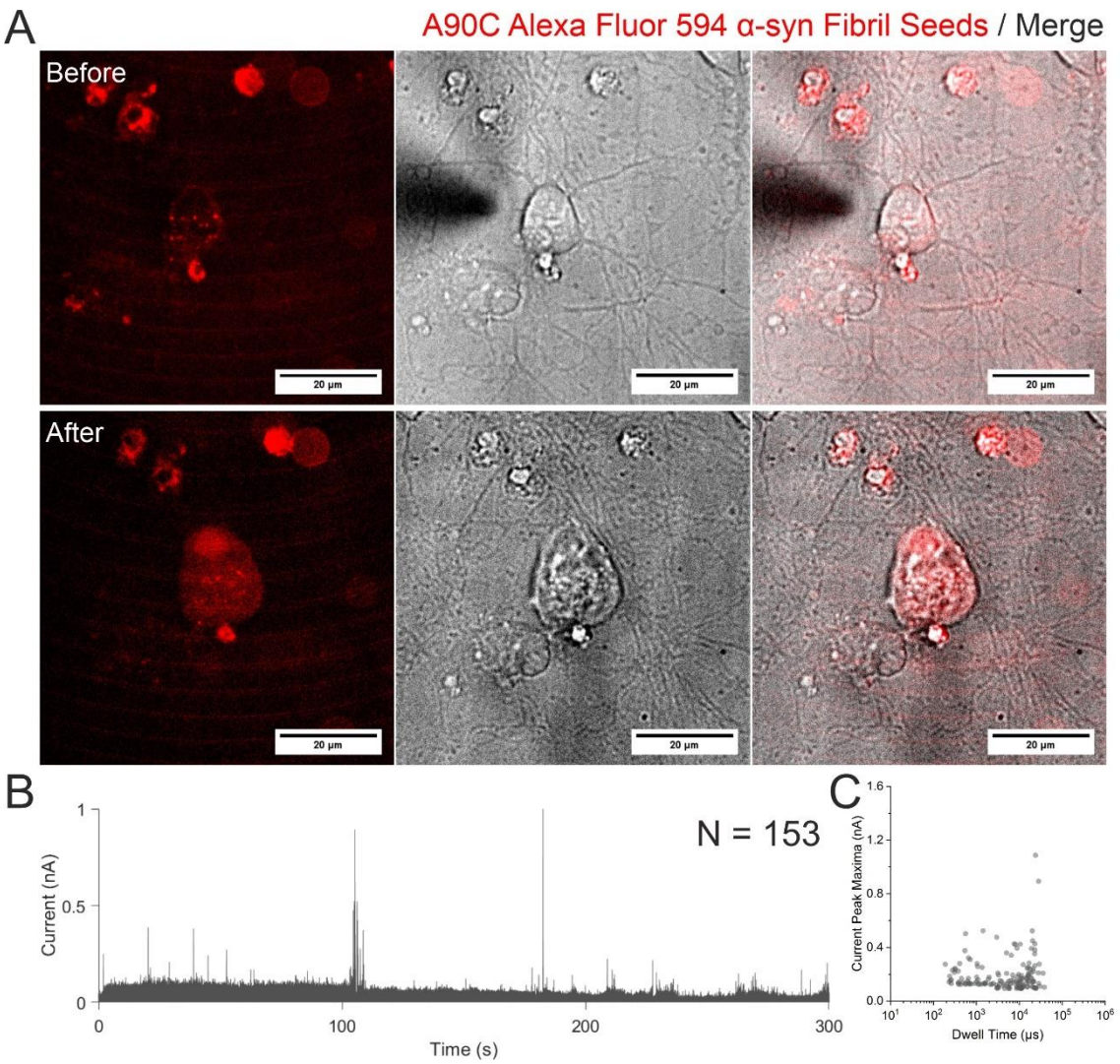

Figure 3.39. Quantitative nanoinjection of fluorescently labelled α-synuclein fibrils into primary rat cortical neurons - 1. *The nanopipette was filled with 1 µM monomeric equivalent A90C Alexa Fluor 594 labelled α-synuclein fibrils diluted in PBS. The before and after nanoinjection of the neurons, showed that the neurons became fluorescently positive after the nanoinjection of the fluorescently labelled fibrils (A). The molecule count and the trace showed 153 molecules were detected (B) and a scatter plot was generated from the trace.*

Then, two more rat cortical neurons were injected with the fluorescent labelled fibril seeds and both cells became more fluorescent after the nanoinjection (Figure 3.40 and Figure 3.41). For Figure 3.40, 305 translocation events were recorded, and the average dwell time and the current were 4962±322 µs and 0.416±0.014 respectively.

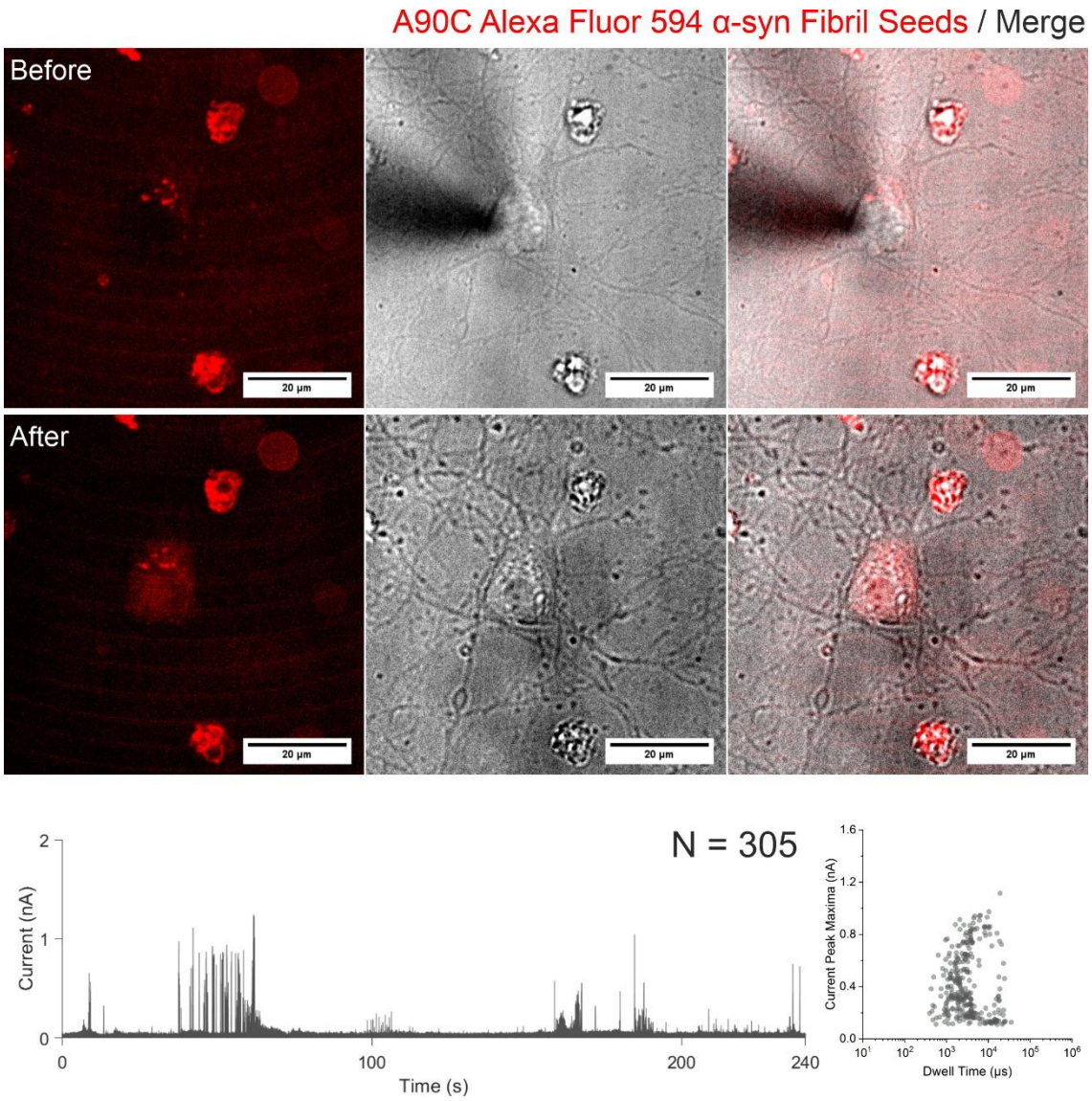

Figure 3.40. Quantitative nanoinjection of fluorescently labelled α-synuclein fibrils into primary rat cortical neurons - 2. *The nanopipette was filled with 1 µM monomeric equivalent A90C Alexa Fluor 594 labelled α-synuclein fibrils diluted in PBS. The before and after nanoinjection of the neurons, showed that the neurons became fluorescently positive after the nanoinjection of the fluorescently labelled fibrils (A). The molecule count and the trace showed 305 molecules were detected (B) and a scatter plot was generated from the trace.*

For Figure 3.41, 426 events were recorded, the average dwell time and the current were 2001±157 µs and 0.212±0.002 nA respectively.

In all three fibril nanoinjections, the morphologies of the cells suggested that they were slightly swollen. This was expected as the size of the cell was a lot smaller compared to the HUVECs based on observation from the confocal microscope. Injection of even femtoliters of liquid could change the morphology of the cell. After the nanoinjection of the fibrils, the neuronal cells were swollen from approximately 10 µm wide to 20 µm wide.

The increased in the cell volume triggers an adaptive response where the cell volume will be regulated by ion release and uptake through the membrane ion channels and active pumps (Hoffmann et al., 2009; Ginzberg et al., 2015). However, dysregulation of the cell volume can be problematic as it can lead to cell death (Bortner and Cidlowski, 2020). Thus, strategies to minimise the volume of fluid injected into the cell should be further explored. The injection fluid volume can be reduced if a higher particle concentration of amyloid fibrils was used to fill the nanopipette, as this reduces the injection time and subsequently the fluid volume and thus reduce the morphology deformation without comprising on the number of molecules delivered.

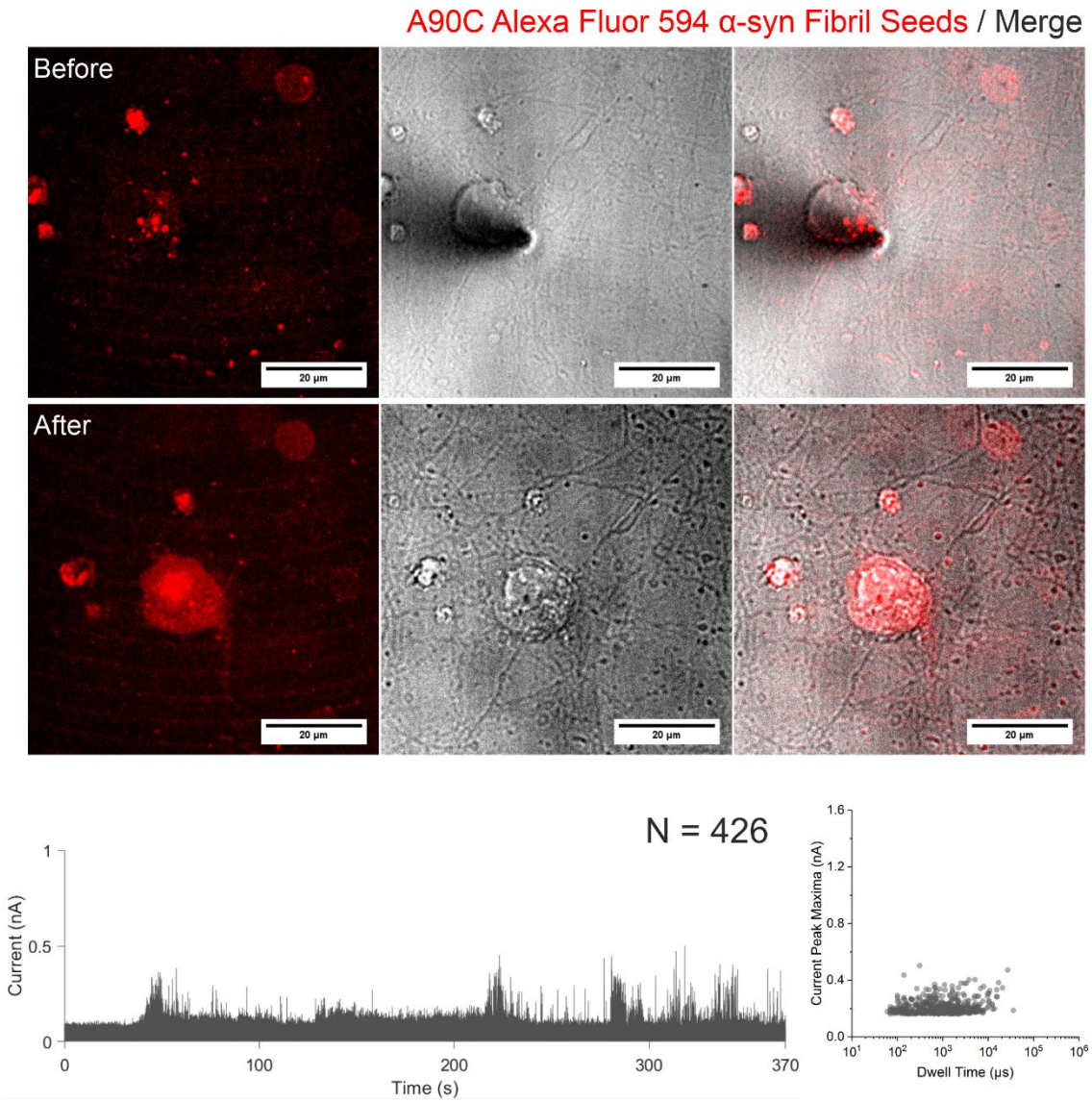

Figure 3.41. Quantitative nanoinjection of fluorescently labelled α-synuclein fibrils into primary rat cortical neurons - 3. *The nanopipette was filled with 1 µM monomeric equivalent A90C Alexa Fluor 594 labelled α-synuclein fibrils diluted in PBS. The before and after nanoinjection of the neurons, showed that the neurons became fluorescently positive after the nanoinjection of the fluorescently labelled fibrils (A). The molecule count and the trace showed 426 molecules were detected (B) and a scatter plot was generated from the trace.*

There were random fluorescent signals coming from cells before the nanoinjection (Figure 3.39 to Figure 3.41), and these random fluorescent signals of the cell were attributed to cell autofluorescence of both living and dead neurons.

In summary, these demonstrations of the quantitative nanoinjection of the fluorescent amyloid fibrils showed that this platform can be used to quantitatively nanoinject amyloid fibrils in a relevant disease model, and thus in future work enable the study of their biological effects.

3.4 Discussion

3.4.1 Summary and highlights

This chapter described the development of a quantitative nanoinjection platform. The platform combined the use of the SICM, which has a high spatial resolution control, with a nanopipette acting as both a SICM probe and a single molecule detector. This was used for the delivery of biomolecules (DNA plasmids, enzyme β-galactosidase and α-synuclein amyloid fibrils) into the cell at high spatial resolution with single molecule resolution sensitivity.

Five different objectives related to the concept of the quantitative nanoinjection were outlined in the beginning of the chapter and each was achieved:

1. Voltage triggers the delivery of these biomolecules.

2. SICM can inject biomolecules into cellular compartments.

3. The nanoinjection procedure has negligible effect to cell viability and function.

4. The nanoinjection process does not disrupt the structure of the biomolecules.

5. The number of biomolecules delivered can be quantified with single molecule resolution by counting the number of the translocation events.

In this chapter, different biomolecules were delivered into cells including DNA and proteins. These molecules were delivered by applying a suitable voltage, this subsequently demonstrated that the nanoinjection can be triggered by the application of a suitable polarity of the voltage (Objective 1). The compartmental delivery of molecules into cells was demonstrated by delivering the 70 kDa fluorescein dextran conjugates into either the cytoplasm or the nucleus, and the nuclear injection of DNA plasmids and β-galactosidase (Objective 2). The delivery of pMaxGFP into both HeLa and primary DRG cells resulted in the expression of the MaxGFP fluorescent protein, demonstrating that the process of the delivery did not harm the cell and the viability of the injected cell was retained (Objective 3). The delivery of the enzyme β-galactosidase and the demonstration of enzymatic activity inside the nucleus indicated that the structure of the enzymes was not disrupted (Objective 4)(Juers et al., 2012; Li, X. et al., 2018). Finally, the ionic

currents of the nanoinjection of DNA plasmids, β-galactosidase and the α-synuclein amyloid fibrils were monitored and the number of molecules translocated were quantified (Objective 5). The detected number of pMaxGFP plasmids delivered into the nuclei were up to 150 copies and led the cell to express the MaxGFP. This number is in agreement with previous studies that showed only 20 copies of plasmids inside the nucleus are needed to transfect the cell (Lechardeur et al., 1999; Bai et al., 2017). The number of β-galactosidase needed to cause 50% of the maximum fluorescent signal generated by cleavage of the substrate SPiDER-βGal in the volume of the nucleus was estimated herein to be 67. The number of β-galactosidase molecules injected into the nuclei resulting in detectable enzyme activity ranged from 44 to 1061, which was in agreement with this calculation. Finally, ≥150 α-synuclein amyloid fibrils were injected into neurons, and this number of molecules could potentially affect the cell function.

3.4.2 Molecule delivery mechanism

Throughout this chapter, negative voltage was used to trigger the delivery of the biomolecules through electrophoresis, this was decided based on the properties of the biomolecules. The 70 kDa fluorescein dextran conjugate is anionic, and the pMaxGFP DNA plasmid is negatively charged, the enzyme β-galactosidase diluted in 1×PBS is negatively charged due to its isoelectric point of 4.61 (Boyer et al., 1970), and the α-synuclein fibril seed is assumed to be negatively charged based on a resolved fibril model where the negatively charged C-terminal of the α-synuclein monomer is not packed into the fibril core (Tuttle et al., 2016). However, electrophoresis is not the only force that can drive the biomolecules from the inside of the nanopipette to the outside environment. The electroosmotic flow (EOF) also contributes to the movement of molecules and it has been used to deliver fluorescent dye to the cell (Qian, R.-C. et al., 2018).

The EOF is a viscous fluid flow either towards or away from the nanopipette tip, and the direction of the flow depends on the surface charge of the nanopipette, the nanopore size and the thickness of the electrical double layer (EDL) (Laohakunakorn and Keyser, 2015). The formation of EOF and EDL will be further discussed in detail in Chapter 4. In general, due to the surface charge of the quartz and the geometry of the nanopipette, a positive voltage will induce a flow towards

the nanopipette tip, a negative voltage will induce a flow away from the nanopipette tip, and the magnitude of the flow depends on the concentration of the ions inside electrolyte (Yusko, Erik C. et al., 2009; Laohakunakorn and Keyser, 2015). Consequently, the successful delivery of biomolecules depends on the dominant force in the system which can be electrophoresis or EOF.

Since negative voltage was used to electrophoretically deliver the analytes throughout this chapter, the EOF acts against the movement of the molecules as a result. According to a simulation study by Calander *et al.*, the EOF is as strong as electrophoresis when 10 mM salt electrolyte are used, and this subsequently leads to the accumulation of analytes 200 nm away from the nanopipette tip (Calander, 2009). However, the nanoinjections of all the tested biomolecules through electrophoresis have led to expected intracellular responses, *e.g.* the nanoinjection of pMaxGFP plasmids has led to the production of MaxGFP 24 hours later. These results showed that all tested biomolecules can be delivered into the cell, and electrophoresis was the dominant driving force during the nanoinjection. Since 1×PBS contains *c.a.* 140 mM of salt, the EOF may not be strong enough to completely counteract the electrophoresis and halt the movement of biomolecules, and it only acts to slow down the translocation velocity.

In the future, further testing can be carried out to understand the role of EOF during the nanoinjection, since the intracellular environment is different from the typical electrolyte bath environment which may alters the EOF. Alternatively, biomolecules can be delivered into the cell via EOF by diluting the biomolecules in lower salt condition, in order to generate a stronger EOF to overcome the electrophoresis (Qian, R.-C. et al., 2018).

3.4.3 Further optimisation of the Nanoinjection

Although the capabilities of the platform have been demonstrated for different biomolecules, the overall success rate for penetrating the cell while retaining single molecule sensitivity remains low. In the majority of attempts, the nanopipette either failed to penetrate the cell membrane or the pore was widened during cell penetration, as evidenced from a sudden increase in the current baseline.

The success rate of cell penetration is associated with the geometrical profile of the nanopipette. Shen *et al.* showed that pipette of 300 nm in diameter fabricated from quartz had a higher flexural rigidity compared to the borosilicate fabricated nanopipette, and a high flexural rigidity led to successful penetration of a yeast cell (Shen et al., 2015). Similarly, the profile of a <50 nm nanopipette was studied and showed that the highly flexible profile correlated with a high success rate at gaining access into intracellular space, and demonstrated that the size of the pore was not the determinant issues in cell membrane penetration, but rather the profile and the geometry of the nanopipette (Jayant et al., 2019). As the nanopipettes used throughout were also quartz, further geometrical profile optimisation could be carried out in the future to increase the success rate of cell penetration.

Another issue of nanoinjection is that without the use of the fluorescent molecules or fluorescent labelled molecules, it is never certain that the probe has reached the intracellular space. Chen *et al.* used the nanopipette to probe the membrane vibration and showed that when the nanopipette was brought to proximity of the membrane by the SICM, the current baseline started to oscillate at a defined frequency, due the fluid flow of the nanopipette alone (Chen, B.B. et al., 2019). A similar current oscillation pattern has been observed before when the nanopipette approached the cell membrane, suggested that similarly, the sub 30 nm nanopipette also induced vibration on the membrane. This information could be used to estimate the position of the nanopipette relative to the cell membrane more accurately. Further optimisation of the injection parameters could also help minimise impacts on the nanopipette during penetration and the associated pore widening damage. Pore damage means the loss of single molecule sensitivity and consequently affects the data acquired and its interpretation. In the future, the nanopipette after injection could be imaged by the SEM to ensure that the penetration process did not substantially alter the pore dimensions.

Rahman *et al.* recently developed a system that allowed on demand delivery of single molecules via a nanopore, when a defined number of translocation events were observed through a nanopore, the system stopped applying voltage immediately (Rahman et al., 2019). This is relatively simple to implement into the current platform. In the future, a semi-automatic control system with robotic aid can be implemented into the platform, and this approach has been adopted for

large scale microinjection (Chow et al., 2016a; Nan et al., 2019). This increases the scalability of the platform and can be used to acquire more data in shorter time frame.

3.4.4 Using the platform to investigate biological questions

The main attraction of the quantitative nanoinjection platform is its ability to quantitatively deliver extracellular characterised materials directly into the intracellular space. The quantitative approach provides control over the number of molecules delivered and subsequently enables the manoeuvre of the cell response more precisely. For example, higher order DNA nanostructures can be intracellularly delivered at a defined number, each of this nanostructure contains a strand of siRNA that can be released upon triggering via strand displacement, the released siRNA can be used to regulate gene expression level (Douglas et al., 2012; Bujold et al., 2016; Bujold et al., 2018). The quantitative nanoinjection approach allows the user to precisely control the gene expression level by controlling the number of siRNAs released from the DNA nanostructures.

As described before, having the single molecule sensitivity during injection could improve our understanding of amyloid diseases. It has been shown repeatedly that intracellular α-synuclein amyloid aggregation can be seeded by introducing *in vitro* generated fragmented α-synuclein amyloid fibrils into cells and animals (Danzer et al., 2009; Freundt et al., 2012; Luk et al., 2012; Rey et al., 2013; Witt et al., 2016; Gribaudo et al., 2019; Rey et al., 2019; Hijaz and Volpicelli-Daley, 2020; Mahul-Mellier et al., 2020; Sang et al., 2021). However, the concentration required to seed the aggregation in a single cell is not known. Recently, super resolution imaging was used to determine that α-synuclein fibrils seeded aggregation kinetics inside the SH-SY5Y neuroblastoma cell line (Sang et al., 2021). The study showed that an average of 75 α-synuclein protein aggregates with a size estimation of 82±11 nm could be found inside the cell when fed with 35±2 nm fibril seeds. Additional α-synuclein aggregates were formed at a rate of 0.22 aggregates/hour inside the cell, and each cell secreted approximately 10^6 α-synuclein aggregates with a size distribution of 35±1 nm per cell per day (Sang et al., 2021). Based on the study by Sang et al, sufficient fragmented α-synuclein fibrils were nanoinjected into cortical neurons to seed the aggregation of the endogenous α-synuclein. Furthermore it

has been shown that 0.25 nM particles concentration of α-synuclein aggregates would be sufficient to cause significant cytotoxicity by cell feeding, this correlate to approximately 200 molecules, this suggested that the number of molecules injected should also elicit cell response (Pieri et al., 2012). However, these studies relied on cell feeding to deliver the aggregates to the cell, the number of aggregates required to elicit any effects inside a particular cellular compartment could be different when they are delivered directly into the cell.

My approach developed here allows the direct quantitative delivery of the α-synuclein fibrils into the cytoplasm. This is important as this approach bypasses the cell uptake route and delivers the α-synuclein amyloid to the cytoplasm directly, and it has been shown that endogenous α-synuclein aggregates inside the cytoplasm and eventually led to the formation of the inclusion bodies (Spillantini et al., 1997). Various studies have showed that α-synuclein aggregates into different oligomeric and fibril structures under different conditions, and subsequently showed that cell response differently to the different α-synuclein aggregates (Cremades, Nunilo et al., 2012; Bousset, Luc et al., 2013; Paslawski et al., 2014a; Paslawski et al., 2014b; Chen, S.W. et al., 2015; Peelaerts et al., 2015b; Fusco et al., 2017; Alam et al., 2019; Guerrero-Ferreira et al., 2019; Chakroun et al., 2020; Guerrero-Ferreira et al., 2020; Schweighauser et al., 2020; Chou et al., 2021). In the future, these aggregates can be extensively characterised via biophysical and biochemical techniques prior to the quantitative nanoinjection. The nanoinjected neurons should be tracked for long term viability and different fluorescent-based viability assay can be implemented to study the effects of the nanoinjected aggregates.

Furthermore, different compartments of the neuron can be nanoinjected with amyloid fibrils, *e.g.* the nucleus, the neuron soma and even the synpatic bouton. These approach can be used to study the different compartmental intracellular response towards the nanoinjected amyloid aggregates, as the cell may respond differently to the aggregates based on its location, *e.g.* nucleus vs cytoplasm (Iadanza, M. G. et al., 2018). Positioning the nanopipette on top of a small cellular surface like the synaptic bouton will require the use of the SICM to probe the topography of that region before injection, as demonstrated by Vivekananda *et al.*, where the nanopipette was positioned to the bouton by scanning at high lateral resolution prior to patch clamp recording (Vivekananda et al., 2017).

3.4.5 The intracellular environment and translocation signals

Usually, the detection of single molecules translocating through a nanopore is carried out inside a simple electrolyte bath condition, for example 0.1 M KCl. These solution conditions are all vastly different from the intracellular environment, and subsequently the translocation signal should deviate from measurements made in a simple electrolyte bath.

The intracellular environment contains numerous marcomolecules in a small volume and this kind of environment is commonly known as the macromolecular crowded environment (Zimmerman and Trach, 1991; Ellis, 2001; Cheung et al., 2013). This highly crowded environment is known to affect numerous intracellular activities (Spitzer, 2011; Kuznetsova et al., 2014; Mittal et al., 2015; Gnutt and Ebbinghaus, 2016; Rivas and Minton, 2016; van den Berg et al., 2017; Badowski et al., 2018; Lebeaupin et al., 2018; Löwe et al., 2020), including protein dynamics and structure (Duncan et al., 2017; König et al., 2021), channels and intracellular transport (Rowe et al., 2014; Nettesheim et al., 2020), formation of condensates (Sabari et al., 2020; Zinchenko et al., 2020), transcription (Richter et al., 2008; Li, Y. et al., 2021), enzyme kinetics (Mittal et al., 2015) and cell volume (Mourão et al., 2014).

Typically, the quantification of the level of the crowding inside the cell relies on the use of the Förster resonance energy transfer (FRET) technique. The FRET crowding sensor usually has the fluorescent proteins attached to long flexible molecules, such as poly(ethylene) glycol (PEG) (Gnutt et al., 2015), DNA (Murade and Shubeita, 2019) or a disordered polypeptide chain (Boersma et al., 2015) and the flexibilities of these molecules are essential as the molecule shape depends on the environment. A high FRET level is achieved when the intracellular environment is highly crowded and causes the fluorescent proteins to come closer, and *vice versa.* An alternative method to probe the crowding level is to trace the diffusivity of the fluorescent probe inside the cell, but the diffusivity of the probe can also be affected by other factor such as transient interactions with other intracellular macromolecules (Konopka et al., 2006; Mika et al., 2016).

Here, the translocations of different biomolecules into the cell were detected by the nanopipette. Using the β-galactosidase as example, the calculated average

dwell time is exceptionally long *i.e.* approximately 40,000 µs. This is in sharp contrast to previous measurements with a solid-state nanopore which showed that proteins, including β-galactosidase, translocate at a high speed through the nanopore with a short dwell time (Plesa et al., 2013). Some researchers have studied prolonging the translocation time of materials through the nanopore. Aramesh *et al*. showed that the translocation time of both proteins and DNA through a nanopore could be increased by mechanical confinement between the nanopore and a soft surface like the cell membrane (Aramesh et al., 2019). Factors such as viscosity can also prolong the translocation time of DNA in solid-state nanopores (Fologea et al., 2005), and the intracellular environment is extremely viscous and thus the translocation dynamic of the molecule could also be altered during nanoinjection (Caragine et al., 2018). The increase in dwell time from data for nanoinjection of cells in this thesis is greater than previous studies, suggesting that other factors such as macromolecular crowding could play an important role in the characteristics of the translocation events. The role of macromolecular crowding will be further explored in Chapter 4.

Finally, with proper calibration and further optimisation of the quantitative nanoinjection platform, the translocation event signals could potentially be used as a non-fluorescence-based technique to understand the intracellular environment, by delivering molecules into the cell, *i.e.* repurposed the platform as an intracellular environment sensor. This could be tested in future studies by examining whether manipulating and changing intracellular crowding affects the translocation signals detected for biomolecules injected into cells.

Chapter 4

Macromolecular Crowding

Enhanced Detections in Bath by Nanopipette

4.1 Nanopores as single molecule sensors

As discussed in the previous chapters, nanopipettes can be used as a single molecule sensors to detect a variety of DNA structures and proteins (Xue et al., 2020)The nanopipette is considered a solid-state nanopore, and due to the way it is fabricated, it is also a conical nanopore. Since the nanopipette is the main focus throughout the entire thesis, the properties and behaviours of conical nanopores will also be the main focus in this Chapter.

4.1.1 Electrical properties of nanopores

The commonly used material to fabricate the nanopipettes is the quartz glass capillary which is a hard crystalline mineral composed of silicon dioxide (Stanley and Pourmand, 2020). When this material is immersed into a neutral pH electrolyte the deprotonation of the surface oxide groups induce a negative charge in and around the nanopore (Behrens and Grier, 2001; Déjardin et al., 2005). This negative surface will then be immediately screened with cations, inducing the formation of the electrical double layer (EDL). The thickness of the EDL depends on the electrolyte concentration and it varies between 10 nm in 1mM KCl, to 3 nm in 10mM KCl, and to 1 nm in 100 mM KCl (Cohen, 2003). The EDL plays an important role in a phenomenon known as the ion current rectification (ICR). The ICR results in an asymmetric ion current upon the application of a symmetric voltage. The extent of the ICR strongly depends on the geometry and the surface charge of the nanopore (Wang, J. et al., 2014; Tseng et al., 2016). In general terms, a negatively charged conical nanopore will exhibit negative ICR (Figure 4.1) (Experton et al., 2017).

Assuming a conical glass nanopore with a diameter of 20 nm is immersed into a 1 mM KCl solution, the EDL will be 10 nm thick. Under this condition, the ionic current is carried predominantly by the cations in the EDL, and this effect causes the nanopore to be cation permselective (Experton et al., 2017). When a positive voltage is applied at the base of a cation permselective nanopore, the ions migrate to their respective electrodes by electrophoresis. However, due to the permselectivity towards cations, cations can also migrate towards the cathode through the EDL, while anions are excluded and accumulated at the base of the nanopore, this creates an imbalance in the charge across the nanopore. To mitigate

the effect, the ions reorganize and completely migrate away from the region close to the tip end of the pore, *i.e.* depletion of ions, and this subsequently results in a reduction in ion concentration at the tip end. Under this condition, the application of positive voltage at the base of the nanopore depletes the ions and leads to the reduction in conductivity. In contrast, when a negative voltage is used, it causes the ions to accumulate near the tip end and increases the conductivity of the nanopore, thus explaining the observation of ICR (Figure 4.1A) (Experton et al., 2017)

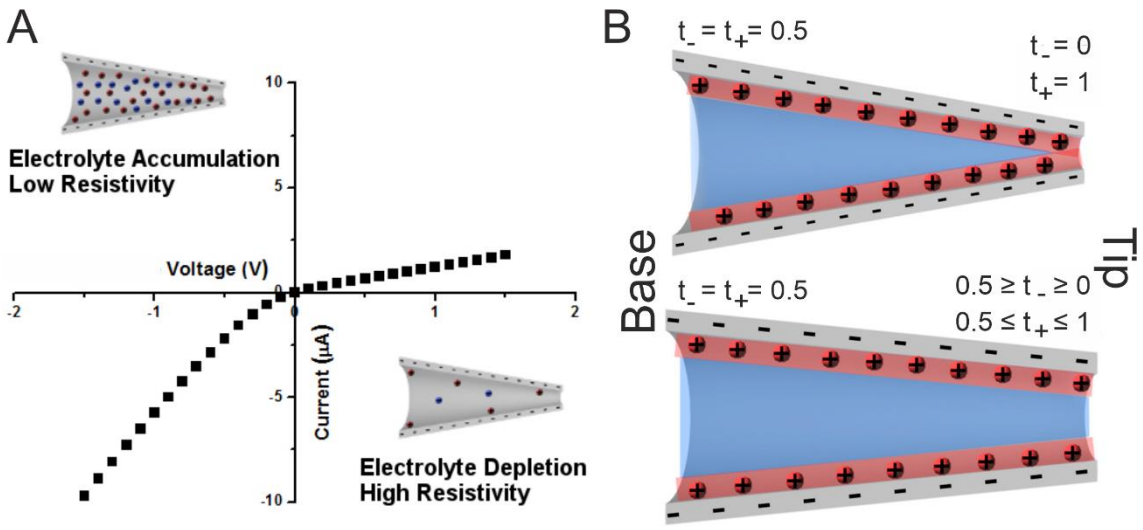

Figure 4.1.Ion current rectification (ICR) and permselectivity of the conical nanopore. *The ICR occurs because of the ion concentration polarization inside the nanopore. The ions are depleted in the nanopore when a positive potential bias is applied at the base of the tip, which leads to the reduction in conductivity. The ions accumulate inside the pore when a negative voltage is applied, and there is a subsequent increase in the conductivity. The current-voltage plot was measured at 0.1 M KCl (A). The formation of EDL in the conical nanopore shields the negatively charged nanopore surface, the EDL completely overlaps at the conical nanopore opening. The transference number - t_+ is at its highest at 1 while t_- is at 0. However, even when the EDL does not overlap at the conical nanopore opening, the conical nanopore still has relatively higher t_+ and lower t_- values at the tip end. The tip base is assumed to have a $t_+ = t_- = 0.5$ as the effect of the EDL is negligible. The t_+ and t_- are the cation transference and the anion transference number respectively (B). Adapted from (Experton et al., 2017).*

However, studies have reported that ICRs also occur in conical nanopore with an opening diameter much larger than the EDL thickness (Siwy et al., 2004; Apel et al., 2011), this is due to the extent of the cation permselectivity at the tip end of the nanopore. The permselectivity is measured by the transference number (the fraction of the total electrical current carried in an electrolyte by a given ionic species) of cations and anions, *i.e.* a measure of the prevalence of cations over anions (Laohakunakorn and Keyser, 2015). For the tip end of a perfect cation permselective nanopore, *i.e.* the EDL is perfectly overlapped at the tip end of the

nanopore, the transference number of the cation t_+ is equal to 1 and conversely, the transference number of the anion t_- is equal to 0. Since the EDL effect is negligible at the base of the nanopore, the transference number is *c.a.* at $t_+=t_-=0.5$, indicating a state of neutrality. Whenever the t_+ at one side of a channel is bigger than the t_+ on the other side, the ionic current will rectify due to the ion concentration polarization (Figure 4.1B) (Experton et al., 2017). Besides the geometry, the extent of the cation permselectivity and subsequently the ICR can be affected by other factors such as the surface charge distribution, electrolyte concentration and properties. The interplay of these factors affect an important fluid flow phenomenon inside the confined nanopore – the electroosmotic flow (Yusko, Erik C. et al., 2009; Wang, J. et al., 2014; Laohakunakorn and Keyser, 2015).

4.1.2 Electroosmotic Flow in the Conical Nanopore

The electroosmotic flow (EOF) describes the movement of the bulk electrolyte against a charged solid surface under the influence of an electric field (Hossan et al., 2018). The cation layer of the EDL can be further separated into two regions, the more rigid fixed layer and the diffuse layer. The rigid layer is immediately adjacent to the negatively charged wall surface and the cations are immobilised owing to the strong electrostatic interactions. In contrast, the diffuse layer is slightly further away from the wall surface where the cations are mobile. The application of a positive voltage causes the cations from the diffuse layer together with their surrounding hydrating water molecules to migrate either towards the tip end or the base of the nanopore, and generates a net flow of fluid across the nanopore (Hossan et al., 2018). The EOF inside a conical nanopore is related to the ion concentration. Any given positive voltage applied from the base of the nanopore results in lower ion concentration throughout the conical nanopore, while the application of negative voltage results in a higher ion concentration inside the nanopore (Figure 4.2A) (Laohakunakorn and Keyser, 2015). The asymmetric distribution of ions between the inside and outside of the nanopore rectifies the EOF (Figure 4.2B) (Laohakunakorn and Keyser, 2015).

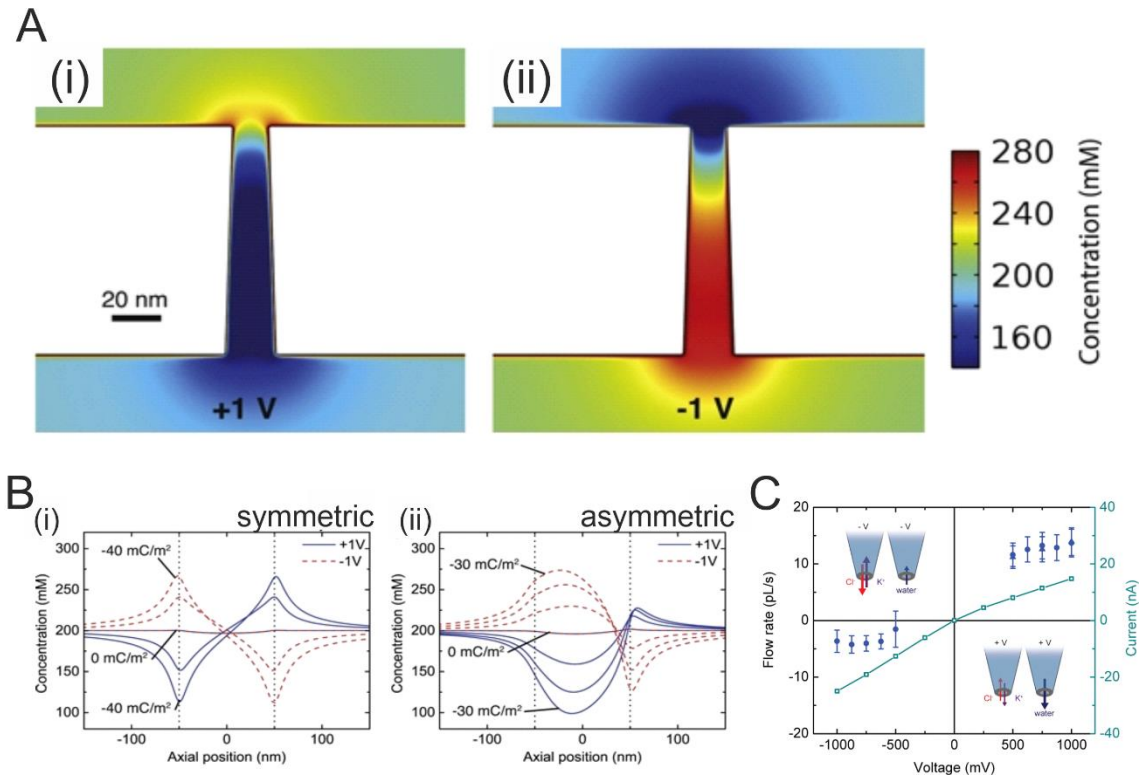

Figure 4.2. The electroosmotic flow (EOF) of the conical nanopore. *The simulated ion concentration profile inside the conical nanopore when ± 1 V was applied from the base of the nanopore (A). The simulation was with a 15 nm wide conical nanopore with a 1.7° taper angle at 200 mM KCl. The ion concentration was lower when a positive voltage was applied indicating the depletion of the ions (A(i)), and a higher ion concentration indicates the ions' accumulation effect at negative voltage (A(ii)). The difference of the ion concentration inside the nanopore between symmetrical (B(i)) and asymmetrical (B(ii)) nanopore. The ion polarization effect is asymmetric with respect to the direction of the current flow. The EOF also rectifies similar to ICR but in an opposite sense. Solid circle is the flow rate, open square is the current (B). The electroosmotic flow is measured by observing the position of a 1.5 µm diameter nanoparticle in front of a 75 nm wide nanopipette under different voltages at 10 mM KCl. Positive flow rate indicates the particle has moved away from the nanopore and vice versa. The EOF is weaker at negative voltage and stronger at positive voltage while ICR is stronger at negative voltage and weaker at positive voltage. (A) and (B) are adapted from (Laohakunakorn and Keyser, 2015), (C) is taken from (Laohakunakorn et al., 2013).*

The strength of the EOF can be calculated as the flow rate, and the flow rate relates to the ion concentration at the tip end via a decreasing function, *i.e.* under positive voltage, the nanopore has a strong EOF towards the tip end and the application of negative voltage causes a weak EOF towards the base of the nanopipette (Figure 4.2C) (Laohakunakorn and Keyser, 2015). This observation is opposite to the ICR and is termed electroosmotic flow rectification (Jin et al., 2010; Laohakunakorn et al., 2013).

4.1.3 Molecule translocation and the characteristic of the event

A resistive pulse sensing (RPS) event is generated when a molecule passes through the nanopore and temporarily disrupts the ionic current flow (Varongchayakul et al., 2018). Although it is intuitive to assume that the translocation of any molecule through the nanopore will always cause a drop in the ionic current by geometrical exclusion, several studies have observed that in certain conditions, the translocation of a molecule can induce an increase in the measured current (Smeets et al., 2006; Aksimentiev, 2010; Kowalczyk and Dekker, 2012; Lan et al., 2014; Ivanov et al., 2015; Raveendran et al., 2018; Raveendran et al., 2020b). This phenomenon has been attributed to the interaction between the cations and negatively charged DNA, such that the cations cover and shield the negatively charged molecules during its translocation (Smeets et al., 2006). The ion shielding was confirmed by the ion counting experiment and showed that dsDNA sequestered cations to form a localised ion cloud (Gebala et al., 2015; Gebala et al., 2016). This ion cloud causes the translocation of the molecule to carry an excess of ions compared to the bulk, leading to an increase in the ionic current flow (Smeets et al., 2006).

Another study further investigated the physics of the ionic current signature of the translocation of the DNA into or out of a glass conical nanopipette at various ion concentrations. This study showed that the increased current is due to ion concentration polarization depending on the direction of the translocation and the geometry of the nanopipette (Figure 4.3) (Chen, K. et al., 2017). As mentioned before, when a positive voltage is applied in a conical nanopore, it causes the concentration of the ions to be depleted around the tip end (Experton et al., 2017), the backward translocation (from bath to the nanopore) of DNA causes a drop in the conductivity of the pore simply due to the geometrical exclusion effects, and is further facilitated by the naturally occurring ion depletion in the conical nanopore (Figure 4.3A). In contrast, the forward translocation (from nanopore to the bath) of the DNA to the outside of the nanopore leads to a biphasic pattern, this is due to the competition between the geometrical exclusion and the ion accumulation effect. As a negative voltage is used to drive the DNA in the forward translocation direction, it accumulates ions at the tip end of the nanopipette due to the geometry of the conical nanopore (Experton et al., 2017). Initially, the geometrical exclusion causes a drop in the ionic current baseline at first, but the closer the DNA reaches

the nanopore, the ion concentration increases substantially at the tip end, and the eventual translocation of the DNA results with an increase in the ionic current (Figure 4.3B). Further reduction of the ion concentration to 20 mM causes the biphasic pattern to disappear and only an increasing current event can be observed, this is attributed to the increase in the strength of the EDL of the nanopipette, which affects the ion concentration polarization and EOF (Figure 4.3C) (Chen, K. et al., 2017). In fact, similar observations have been made in the symmetric nanopore where the ion concentration polarization effect is altered by a salt concentration gradient across the nanopore (Zhang, Yin et al., 2017).

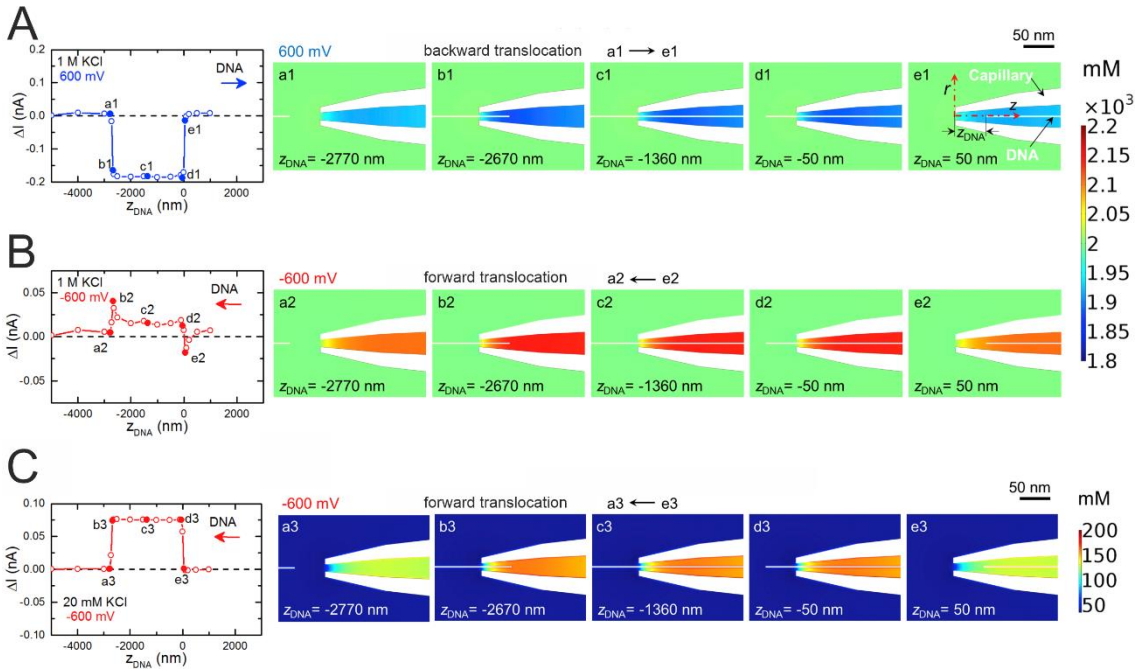

Figure 4.3. How the direction of the translocating molecule affects the RPS signal shape. *The simulation of a DNA rod with a diameter of 2.2 nm and 2720 nm long passing through a 12 nm wide conical nanopore with a taper angle of 5.3° under the potential bias of ± 600 mV, at 1 M KCl. The DNA rod translocates through the conical nanopore in two different directions: backward (outside to inside) under positive voltage (B) and forward (inside to outside) under negative voltage (C). The DNA rod causes the RPS when entering the nanopore in a backward direction, but shows a biphasic pattern when exiting the nanopore in a forward direction. This is due to the combined ion accumulation and geometrical exclusion effects when a negative voltage is used. The RPS is reversed completely when the simulation is done at 20 mM KCl due to stronger EDL and subsequently stronger ion polarization effect. (B-D) Adapted from (Chen, K. et al., 2017).*

4.1.4 Capturing the molecules in solution

Successful detection of the translocation of a molecule depends, amongst many other factors, on having a high signal-to-noise ratio (SNR), *i.e.* the ratio between the observed change in the ionic current to the current baseline noise. Any deviation from the baseline open-pore ionic current measurement without any added

analyte can be regarded as the current baseline noise. The SNR is an important factor to determine whether the nanopore can be used for the detection of the molecule of interest. Both biological and solid-state nanopores have electrical noise caused by an electrical sensing circuit and the physical characteristics of the nanopore and the noise is composed of low-frequency 1/f noise and the high-frequency dielectric and capacitive noise (Fragasso et al., 2020). Generally, a low SNR is undesirable, as the translocation event becomes hard to differentiate from the ionic current noise, and a high SNR is often necessary for single molecule detection (Varongchayakul et al., 2018; Fragasso et al., 2020).

The number of molecules detected by the nanopore in a second is defined as the capture rate. The successful translocation of a single biomolecule through a nanopore requires three separate steps: 1, the molecule moves from the bulk electrolyte toward the pore entrance by diffusion; 2, the molecule is captured by the electric field close to the nanopore; 3, the molecule goes through the nanopore affecting its conductivity by geometrical exclusion and/or ion concentration polarization (Chen, K. et al., 2017). Thus, the first and second steps determine the capture rate of the nanopore, these two steps are termed diffusion-limited and barrier-limited respectively (Grosberg and Rabin, 2010; Charron et al., 2019).

The diffusion-limited capture rate is characterized by the linear voltage dependency and the barrier-limited capture rate is characterized by the exponential voltage dependency (Figure 4.4A). DNA can be either diffusion-limited or barrier-limited depending on the size of the molecule, larger DNA of 10 kbp is usually diffusion-limited and smaller DNA of 50 bp is barrier-limited (Figure 4.4A) (Wanunu et al., 2012; Charron et al., 2019). The capture rate of nanopore translocated proteins have been shown to be barrier-limited when a small solid-state nanopore (<10 nm diameter) is used (Talaga and Li, 2009; Cressiot et al., 2012), and diffusion-limited when a larger nanopore is used (>10 nm diameter) (Plesa et al., 2013; Wu, L. et al., 2014).

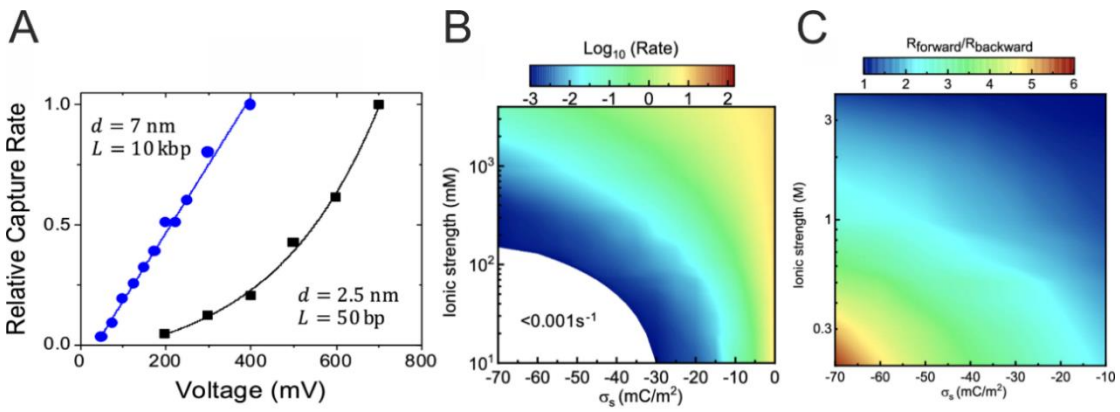

Figure 4.4. The capture rate of molecules in a nanopore. *The relative capture rate of the 10 kbp DNA in a 7 nm wide nanopore in 1.8 M LiCl (blue circle) shows a linear voltage dependence suggesting a diffusion-limited capture process. In contrast, the relative capture rate of 50 bp DNA in a 2.5 nm pore in 3.6 M LiCl shows an exponential voltage dependence suggesting a barrier-limited capture process (black box) (A). The density scatter plot indicates the capture rate of a conical nanopore under the different surface charge density of the nanopore surface and ionic strength of the electrolyte; the capture rate is at its highest when the surface charge is close to neutral and at higher ion concentration. The white area shows that the capture rate is less than 0.001 per second, i.e., 3-4 events per hour. 100 pM of DNA translocating through a 12 nm wide conical nanopore is used for the calculation (B). The density scatter plot compares the capture rate of forward and backward translocation of 100 pM DNA through a 12 nm wide conical nanopore. The capture rate is higher when the DNA passes through the nanopore in the forward direction under most conditions. (A) is taken from (Charron et al., 2019), (B-C) is taken from (Nouri et al., 2019).*

Besides the step limiting factor, there are additional factors to be considered. Using a DNA molecule as the model molecule for nanopore translocation simulation, Nouri *et al.* showed that the geometry, ionic strength, surface charge density and the direction of translocation all played a role in the capture rate of the DNA (Nouri et al., 2019). For instance, increasing the taper angle of the nanopipette nanopore from 15˚ to 80˚ can increase the capture rate of the DNA, but nanopipettes typically have a taper angles between 2˚ to 15˚ and it is difficult to obtain a larger taper-angle (Laohakunakorn and Keyser, 2015; Tseng et al., 2016; Chen, K. et al., 2017; Nouri et al., 2019). The ionic strength and the surface charge density both affect the capture rate, since these parameters also play a role in the formation and the strength of the EDL and consequently the EOF as discussed (Laohakunakorn and Keyser, 2015; Chen, K. et al., 2017; Nouri et al., 2019). For negatively charged molecules such as DNA, since the movement is based on electrophoresis, a negative voltage is usually needed, however, the negative voltage also induces a EOF that is always opposite to the direction of the DNA movement in a glass conical nanopore. Thus, to improve the capture rate of the DNA, the surface charge of the nanopore can be chemically modified to reduce its overall charge as well as increasing the ion concentration in the electrolyte (Figure 4.4B) (Nouri et al.,

2019). Moreover, the translocation direction is also an important factor in the capture rate. The forward translocation of DNA has a relatively higher capture rate than backward translocation with the same surface charge on the nanopore and ion concentration (Figure 4.4C) (Nouri et al., 2019). This can be explained by the strong EOF outflow opposing the motion of the DNA from entering the nanopore (Laohakunakorn et al., 2013; Laohakunakorn et al., 2014; Mc Hugh et al., 2019).

4.1.5 Nanopore detection efficiency and improvement

Nanopore technology has been extremely successful in the detection and analysis of nucleic acids (Muthukumar et al., 2015). Unlike DNA, proteins are small and adopt different conformations based on the solution conditions such as the pH and the ion concentration (Maity et al., 2018). The dimensions of proteins in solutions are smaller than most of the solid-state nanopores and even biological nanopores have difficulties detecting protein translocation due to low SNR (Plesa et al., 2013). The most important factor causing a low SNR is the high translocation velocity of proteins (Plesa et al., 2013). The study by Plesa *et al.* demonstrated that the bulk of proteins translocate on a timescale faster than the tens of microsecond detection limit of the commonly used patch-clamp amplifier (Plesa et al., 2013). To address this low detection efficiency, high bandwidth electronics can be used to improve the amplifier's temporal resolution (Fraccari et al., 2016; Shekar et al., 2016). Alternatively, chemical and biological modification of the surface of the nanopores (Iqbal et al., 2007; Yusko, Erik C. et al., 2011; Wei et al., 2012), or the use of nucleic-acid based carrier molecules can be implemented to enhance the detection efficiency (Bell and Keyser, 2016; Sze et al., 2017).

However, the development of the hardware, surface modification method and procedure can be complex, time consuming and expensive. In contrast, the translocation speed can be slowed down by a careful selection on the types of salt in the electrolyte, the salt concentration across the nanopore, and by increasing the viscosity level of the electrolyte (Fologea et al., 2005; Wanunu et al., 2009; Kowalczyk et al., 2012). These are simple and inexpensive to implement into the detection system. The next section will describe how modifying the electrolyte can improve the detection efficiency. This is illustrated in Figure 4.5 using a salt gradient, a viscogen and macromolecular crowding.

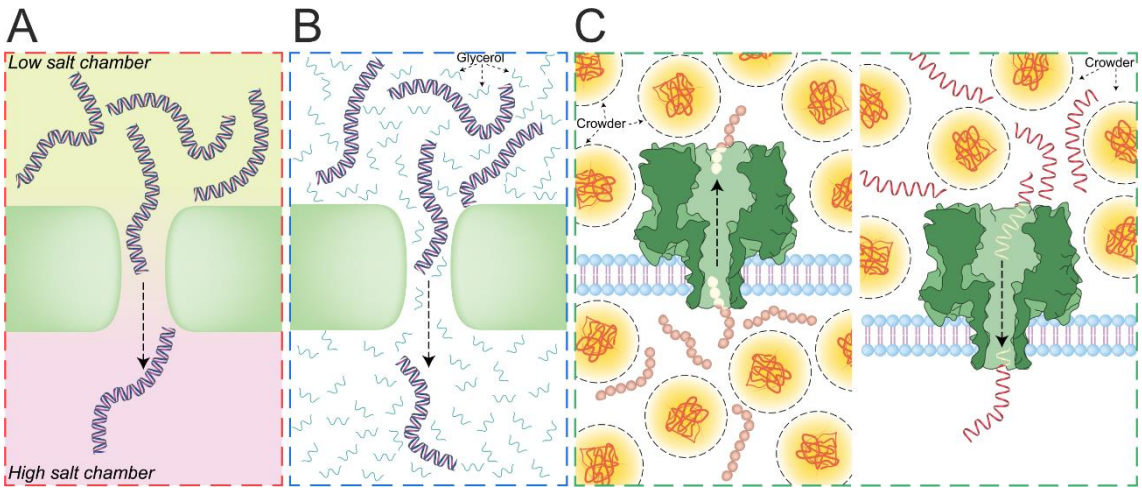

Figure 4.5. Ways to enhance the RPS event signal by modifying the bath electrolyte. *(A) A salt gradient across the nanopore can be established by having a lower salt concentration in one chamber and a higher salt concentration in the other chamber. The RPS event signal and capture rate are improved when the dsDNA is placed in the low salt chamber and migrates into the high salt chamber. (B) Addition of the viscogen agent such as glycerol in both sides of the chamber slows down the translocation of the dsDNA. (C) The RPS event signal and capture rate can be increased by the addition of the macromolecular crowder into the electrolyte. The crowders can be placed in both sides or only one side of the chamber. (A) Redrawn from (Wanunu et al., 2009). (B) Drawn based on (Fologea et al., 2005). (C) Left is redrawn from (Larimi et al., 2019); Right is redrawn from (Yao et al., 2020).*

4.1.5.1 Salt Gradient

In most studies that involve the use of nanopores, the salt concentration is kept the same across the nanopore, *i.e.* both electrolytes chamber have the same ionic strength. In 2009, a study led by Wanunu *et al.* investigated the translocation dynamic of dsDNA in a 3.5 nm solid-state nanopore under an asymmetric salt condition across the nanopore *i.e.* a salt gradient (Figure 4.5A) (Wanunu et al., 2009). The study investigated the effect of a KCl salt gradient by varying the KCl concentration from 0.2 M to 1 M on one side, while the other side of the chamber was kept at 1 M KCl. It showed a pronounced increase in the capture rate when the dsDNA translocated from the low salt chamber to the high salt chamber, but a decreased capture rate when the dsDNA translocated from high to low salt chamber (Wanunu et al., 2009). The salt gradient enhances the capture rate in both the diffusion-limited and barrier-limited regimes due to the build-up of ions in the low salt side, and thus altering the electric field strength and leading to an enhancement in capture rate (Wanunu et al., 2009; He, Y. et al., 2013). The study also showed that the dwell time of the dsDNA RPS signals with the low-to-high salt gradient are longer than those measured in symmetric salt conditions. The

asymmetric salt condition inside the nanopore alters the EOF, the accumulation of ions at the low salt side generates a large EOF acting against the translocation of the DNA and thus prolongs the dwell time (Wanunu et al., 2009; He, Y. et al., 2013).

4.1.5.2 Viscogen

The addition of viscogens like glycerol improves the detection efficiency by increasing the drag force within the nanopore. During the translocation of molecules through the nanopore, several forces such as electrophoresis, EOF and drag force all act on the molecule. Although typically the drag force is often negligible, with the addition of viscogen, the solution viscosity level and consequently the drag force inside the nanopore can be increased. This has been shown to improve the detection efficiency of solid-state nanopores by slowing down the translocation of the dsDNA, and the dwell time of the events are 5 times longer than in pure electrolyte (Figure 4.5B) (Fologea et al., 2005). Moreover, the prolonged translocation time allows the nanopore to distinguish the length of a dsDNA mixture ranging from 2 kbp to 23 kbp (Li, J. and Talaga, 2010). However, glycerol also lowers the conductivity of the electrolyte, which leads to the magnitude of the translocation signal being lower than in the pure electrolyte, and this consequently affects the SNR (Fologea et al., 2005; Li, J. and Talaga, 2010). The increased drag force on the dsDNA molecule, which dramatically slows the motion of the dsDNA, is due to a stronger inter-molecular interaction with glycerol via hydrogen bonds during translocation (Luan et al., 2012).

4.1.5.3 The macromolecular crowding effects

A macromolecular crowded environment is defined as when 20% or more volume of a solution is occupied by macromolecules, leading to a reduced accessible volume to the molecule of interest (Figure 4.6) (Ellis, 2001). The intracellular environment is highly crowded and contains a high concentration of macromolecules. Both prokaryotic (Zimmerman and Trach, 1991) and eukaryotic cells (Cheung et al., 2013) contain on average 300 g/l of macromolecules tightly packed within their intracellular environments. This equates to over 30% of the cellular volume being occupied by macromolecules.

As briefly discussed at the end of last chapter, macromolecular crowding is known to affect numerous intracellular activities (Spitzer, 2011; Kuznetsova et al., 2014; Mittal et al., 2015; Gnutt and Ebbinghaus, 2016; Rivas and Minton, 2016; van den Berg et al., 2017; Badowski et al., 2018; Lebeaupin et al., 2018). One prominent example being the difference in the enzyme reaction kinetics and the substrate association rate observed inside the cell when compared to the measurement in the absence of macromolecular crowding (Mittal et al., 2015). Alteration in the kinetics and association of a single enzyme may not cause any pronounced differences, but small changes in several enzymes can affect the overall metabolic activity of a cell. This is because networks of interconnected enzymes and substrates contribute to the metabolic activity of a cell. It has also been suggested that the cell volume regulation response is a by-product of cytosolic macromolecular crowding, where the cell reduces the liquid volume to modulate cellular physiology such as promoting structural reorganization and reducing protein transport (Mourão et al., 2014).

To recreate the macromolecular environment in the cell, often, inert volume occupying macromolecules are added to the solution. Crowding agents including the flexible polymers such as Ficoll (Stagg et al., 2007; Mardoum et al., 2018), dextran (Goins et al., 2008) and the poly(ethylene) glycol (PEG) (Karbstein and Hancock, 2012; Zhang, D. et al., 2012; Mardoum et al., 2018), more rigid rod-like polymers such as the hydrolyzed polyacrylamide (Babayekhorasani et al., 2016) have also been used to mimic the crowded environment. Alternatively, the macromolecular crowded environment can also be created using a protein crowder such as the bovine serum albumin (BSA) and lysozyme (Mittal et al., 2015; Badowski et al., 2018). However, protein crowding could cause different effects on the biomolecules when compared to chemical crowders, because the protein crowder itself may interact with the biomolecules (Li, C. and Pielak, 2009; Sarkar et al., 2014; Wang, P. et al., 2017).

The effects of macromolecular crowding are simple to appreciate when only steric repulsion is considered. In simple terms, a molecule of interest in a macromolecular crowded environment must avoid steric overlap with other macromolecules, since this would be energetically unfavourable (Sharp, 2015). As a result, the accessible volume for the molecule of interest directly depends on the amount of volume occupied by the macromolecular crowders. This is termed as

the excluded volume effect and it is the first and most important effect caused by the crowders on the molecule of interest (Lebeaupin et al., 2018)(Figure 4.6A).

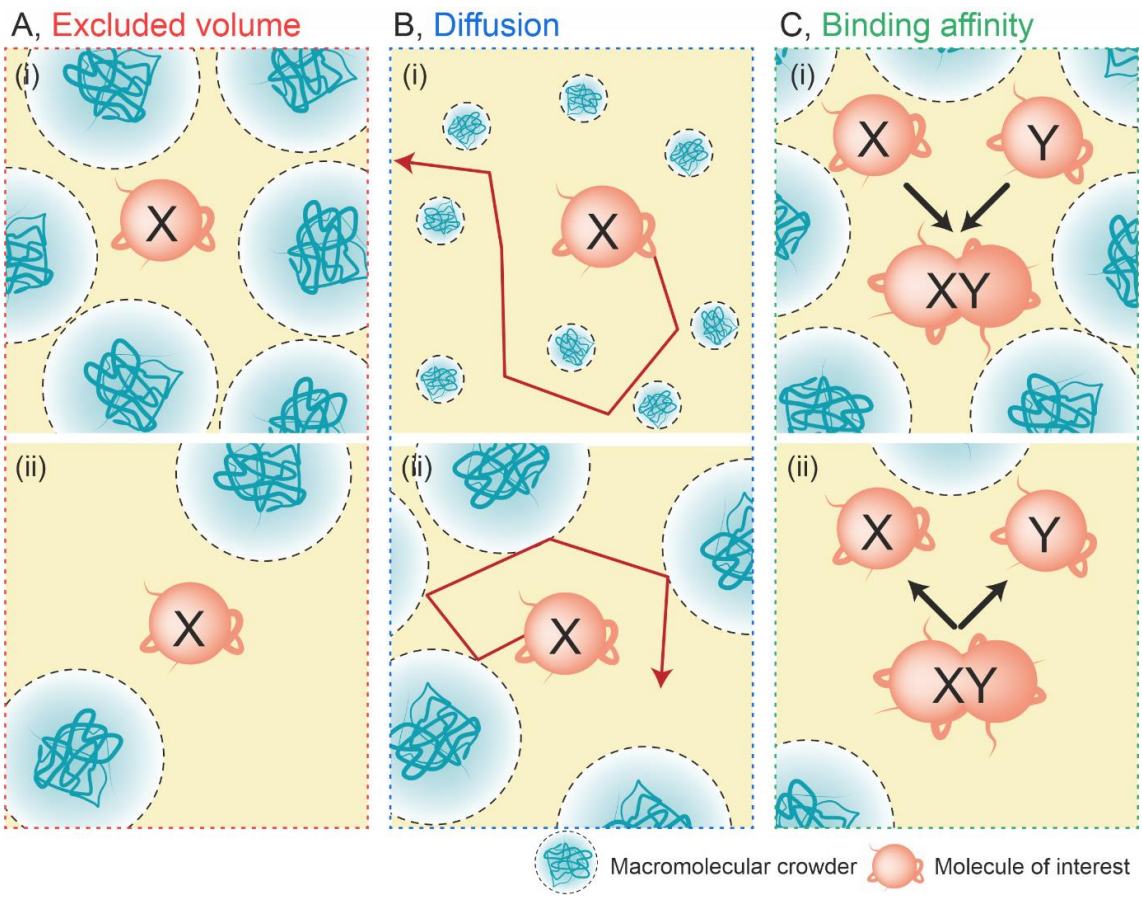

Figure 4.6. The effects of macromolecular crowded environment on the molecule of interest. *(A) The molecule of interest X is placed either in the highly crowded (i) or uncrowded (ii) environment. The access volume (yellow background) is reduced in the highly crowded environment compared to the uncrowded environment. (B) The diffusion of the molecule of interest X is moderated by the size and the properties of the crowders. Smaller mobile crowders do not hinder or constrain the molecule of interest X and it freely diffuses throughout the volume (i). Larger immobile macromolecular crowders hinder and constrain the diffusion of the molecule of interest X, which causes it to undergo anomalous diffusion (ii). (C) The binding affinity of the molecules of interests under the highly macromolecular crowded (i) or the uncrowded (ii) environment. The highly macromolecular crowded environment causes the molecule of interest X to adopt a more compact state and placing another molecule of interest Y in the same space inevitably causes them to interact to form a new complex XY via the depletion interaction. However, when the environment is uncrowded, the molecules of interest are less likely to interact and form a complex. Taken from (Chau, C.C. et al., 2021).*

The second effect on the molecule of interest is its diffusion hindrance. An increase in the crowder concentration affects the diffusion of the molecule of interest with its magnitude depending on the properties and the size of the crowders. When the crowders are smaller and more mobile than the molecule of interest, the molecule of interest can diffuse freely but more slowly due to the increased viscosity of the solution. However, when the crowders are comparable in size or larger to the

molecule of interest and relatively immobile, the molecule of interest is constrained into a limited space, an effect known as the anomalous diffusion (Figure 4.6B) (Dix and Verkman, 2008). Lastly, the molecule of interest always adopts the most compact state to reduce the occupied volume in the highly crowded environment. Placing another molecule of interest in the same space inevitably increases the binding affinity between these molecules, this interaction is termed depletion interaction, and is affected by the strength of the excluded volume effect, and the diffusion hindrance (Figure 4.6C) (Hall and Minton, 2003). These effects could have a strong impact on the electrochemical measurement, for example the diffusion hindrance could affect the interpretation of electrochemical data that often rely on the diffusion coefficient calculated in the uncrowded condition. The sensitivity of the sensor maybe altered via macromolecular crowding, and as a result promotes a stronger interaction between the sensor and the molecule of interest.

PEG is commonly used to generate a crowded environment among the available crowders, and has been used to improve the performance of different techniques including: FRET efficiency (Miyagi et al., 2021), size selective DNA precipitation (He, Z. et al., 2013; Cheng et al., 2015), PCR efficiency (Sasaki et al., 2006) and single-cell RNA sequencing (Bagnoli et al., 2018). Similarly, inspired by the crowded intracellular environment, two studies, each in different ways, have utilised the PEG to enhance the single molecule sensitivity of nanopores (Figure 4.5C) (Larimi et al., 2019; Yao et al., 2020).

Larimi *et al.* utilised a symmetrical macromolecular crowded environment, *i.e.* both sides of the nanopore contained an equal concentration of PEG. Using this, they showed that the detection of the 23 aa long polypeptide Syn-B2 by an α-haemolysin (α-HL) nanopore was greatly enhanced (Larimi et al., 2019). Later, Yao *et al.* utilised an asymmetric macromolecular crowder gradient where the 92 nt ssDNA was mixed with PEG, and translocated through the α-HL into the PEG-free solution (Yao et al., 2020). These two groups both tested PEGs with different molecular weights at various concentrations, and identified that the most pronounced increase in the sensitivity of the α-HL nanopore was with PEG 4000 at ≥ 20% (w/v) (Larimi et al., 2019; Yao et al., 2020). The mechanism behind the enhanced sensitivity for these biological macromolecules was attributed to entropic effects, the alternations in the kinetics of the interactions between the

analyte molecules and the α-HL, due to the highly crowded environment (Lebeaupin et al., 2018; Larimi et al., 2019; Yao et al., 2020).

4.1.6 Investigating the effects of the crowded environment

As mentioned above, the intracellular environment is a highly viscous and crowded environment. In the last chapter, the biomolecule filled nanopipette was used to quantitatively nanoinject molecules into the cell at single molecule resolution, and it was observed that the dwell time of the β-galactosidase and α-synuclein fibrils were significantly broadened. Several possibilities were discussed including nanoscale confinement and viscosity issues. Here, the effects of macromolecular crowding will be further investigated. Larimi *et al.* and Yao *et al.* showed that adding chemical crowder PEG to the electrolyte at high percentage of 20% (w/v) and above enhanced the detection of peptides and ssDNA (Larimi et al., 2019; Yao et al., 2020). Here, the effects of macromolecular crowding will be investigated with the nanopipette. To mimic the quantitative delivery scenario, crowders will only be added to the bath at high concentration, but not inside the nanopipette. The difference between chemical crowders PEG and protein crowders BSA will also be tested here.

4.2 Aims

The aim of this chapter is to investigate the role of macromolecular crowding in the detection of single molecule translocation through a nanopipette. in particular, to mimic the quantitative nanoinjection of molecules from the nanopipette to the intracellular space. The nanopipette will be filled with previously nanoinjected biomolecules: the pMaxGFP DNA plasmids and β-galatosidase in PBS. Then, translocation of these biomolecules will first be carried out in a PBS electrolyte bath by applying different voltages to trigger the translocation of the molecules into the bath to identify whether the translocation of these molecules is readily detectable and if the voltage magnitude triggers their translocation. Then the translocation of the biomolecules will be carried out inside the additive modified PBS bath, the viscogen glycerol added PBS bath and the crowded PEG 8000 PBS bath and the BSA protein crowded bath will be tested. Additional analytes will also be tested in the additives bath including the linearized DNA plasmids, α-synuclein amyloid fibrils and the protein BSA.

4.3 Results

4.3.1 Set-up of the nanopipette detection system

The nanopipette was fabricated by applying heat during the separation of a quartz capillary as outlined in Chapter 2 Section 2.3.2. The fabricated nanopipettes contained a nanopore at the tip end. To perform the single molecule detection with the nanopipette, a patch clamp system containing an amplifier and digitizer was used (Figure 4.7A).

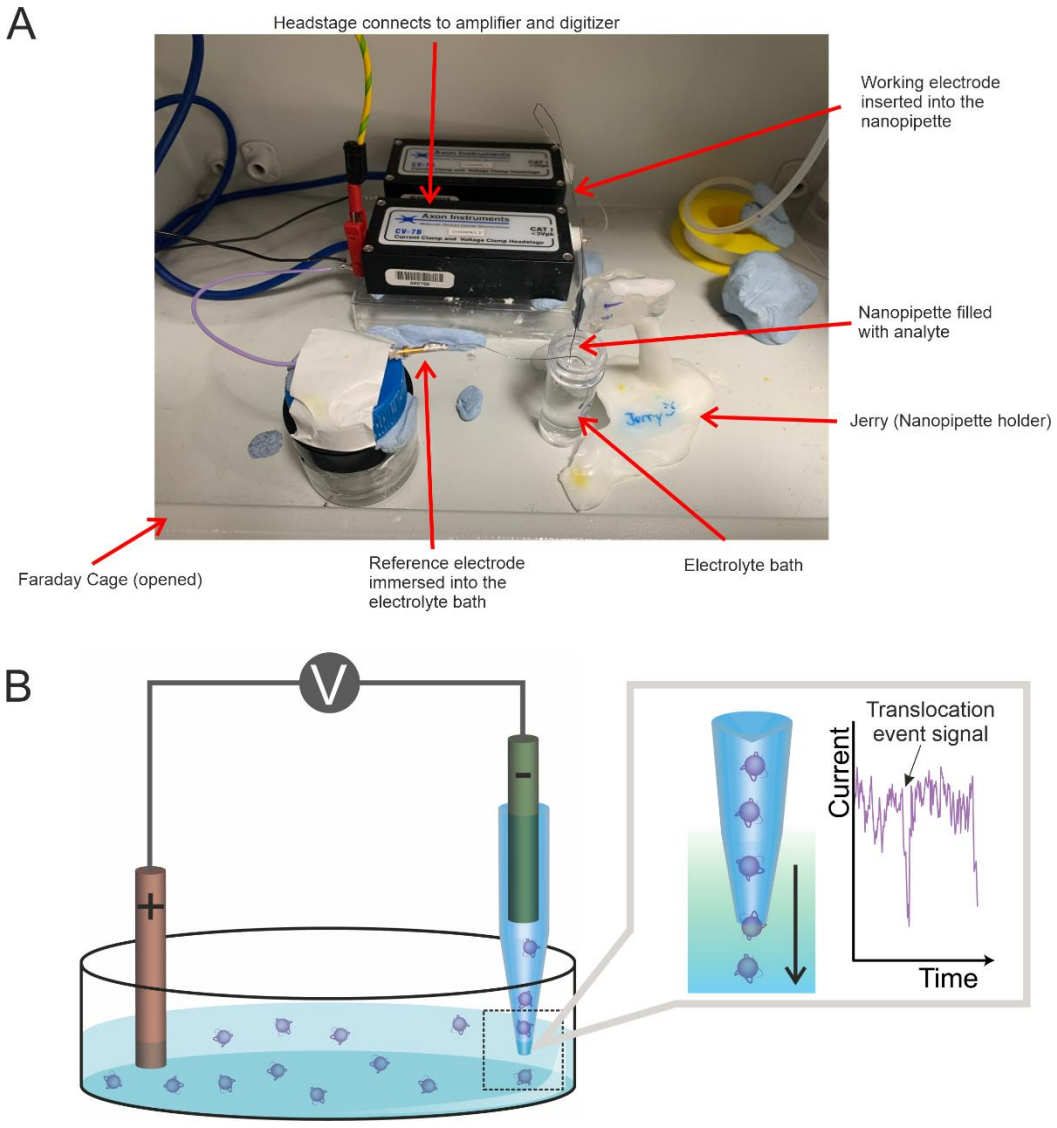

Figure 4.7. Single molecule detection with the nanopipette. *(A) The set-up was placed inside the Faraday cage to protect the device from environmental noise. The nanopipette was connected to the system by inserting the Ag/AgCl electrode inside. The electric circuit was established by placing the reference electrode in the electrolyte bath and immersing the nanopipette in the electrolyte bath simultaneously. (B) The schematic illustration of the set-up. Upon the establishment of an electric field by applying voltage in the working electrode, it led to the translocation of the analyte into the PBS bath from the nanopipette. The translocation of the analyte simultaneously disrupted the current baseline and elicited an observable translocation event signal.*

The headstage of the system was placed inside the Faraday cage to shield the system from electromagnetic noise. Two Ag/AgCl electrodes were connected to the headstage via gold pins. The working electrode was inserted into the analyte filled nanopipette, then the nanopipette was immersed into the electrolyte bath, where the reference electrode was placed to form a complete electric circuit. When a voltage was applied, it triggered the molecules inside the nanopipette to translocate into the bath. Translocation events were identified when the ionic current baseline was temporarily disrupted by geometrical exclusion or ion accumulation effect as illustrated in Figure 4.7B. The size of the nanopores of the nanopipette were imaged and found to have a nanopore ranging from 25 to 28 nm in diameter (Figure 4.8).

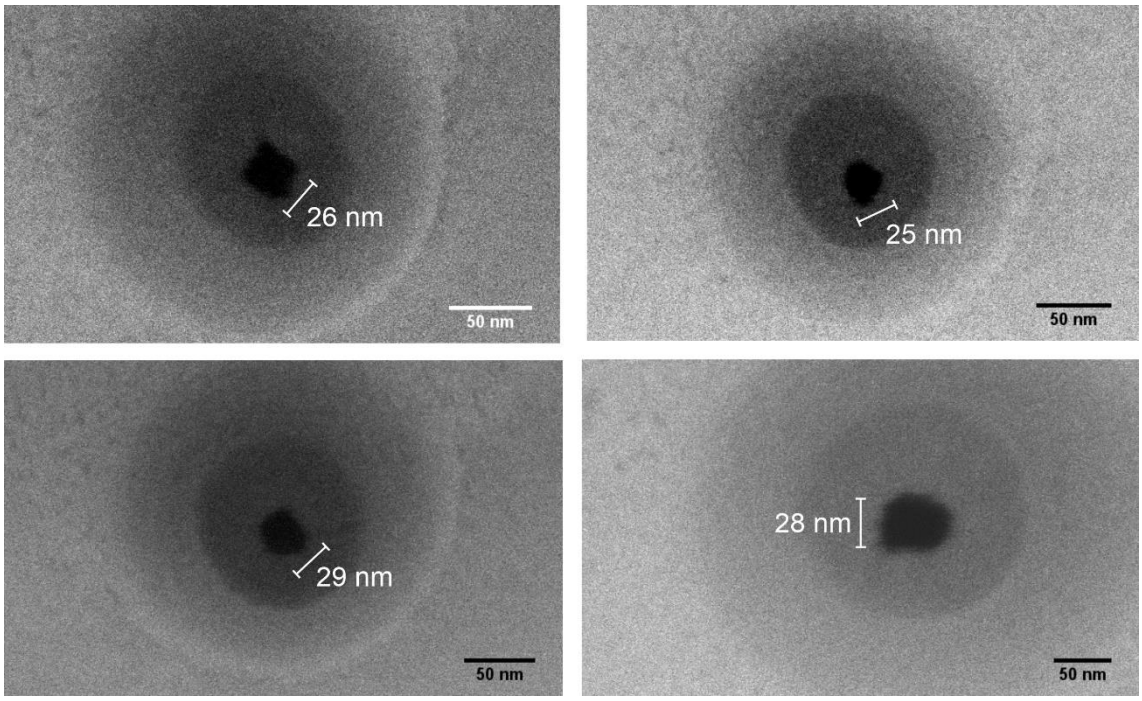

Figure 4.8. The SEM images of the nanopore of the nanopipette. *Four SEM images show the size of the nanopore to be around 27 nm. The nanopipettes were imaged by Dr Mukhil Raveendran and Dr Mark Rosamond.*

4.3.2 Translocation of the molecules under different voltages

The voltage dependent translocation behaviours of the two previously nanoinjected biomolecules: the pMaxGFP DNA plasmids and the protein β-galactosidase will be tested in this section. In Chapter 3, the delivery of these biomolecules was carried out at -500 to -700 mV range, which assumed that a

higher voltage corresponded to higher chance of molecule translocation in the intracellular environment. In this chapter, a more systematic approach will be used to characterise the behaviours of these biomolecules in different electrolyte bath.

In general nanopore translocation experiments, the detection of DNA are standard and relatively easy to perform, but proteins are a lot harder to be detected by the nanopore. DNA molecules are well studied and characterised using nanopores, because of their biochemical properties and result in high SNR during their translocations (Howorka et al., 2001; Smeets et al., 2006; Fologea et al., 2007; Aksimentiev, 2010; Ivanov et al., 2015; Chen, K. et al., 2017; Raveendran et al., 2018). Various proteins have been utilised as the model to study the translocation dynamic of proteins, however, their detection is difficult due to low SNR and fast translocation through the nanopore (Plesa et al., 2013). Here, the DNA pMaxGFP plasmids and protein β-galactosidase represent the opposite ends of this spectrum.

The size of the β-galactoisdase was characterised in Chapter 3, thus would not be shown here. Since the pMaxGFP DNA plasmids would be used as a model analyte to test the nanopipette, additional characterisations were carried out by gel electrophoresis (Figure 4.9). The size of the plasmids was checked by generating the linearized plasmids with restriction enzyme kpn1.

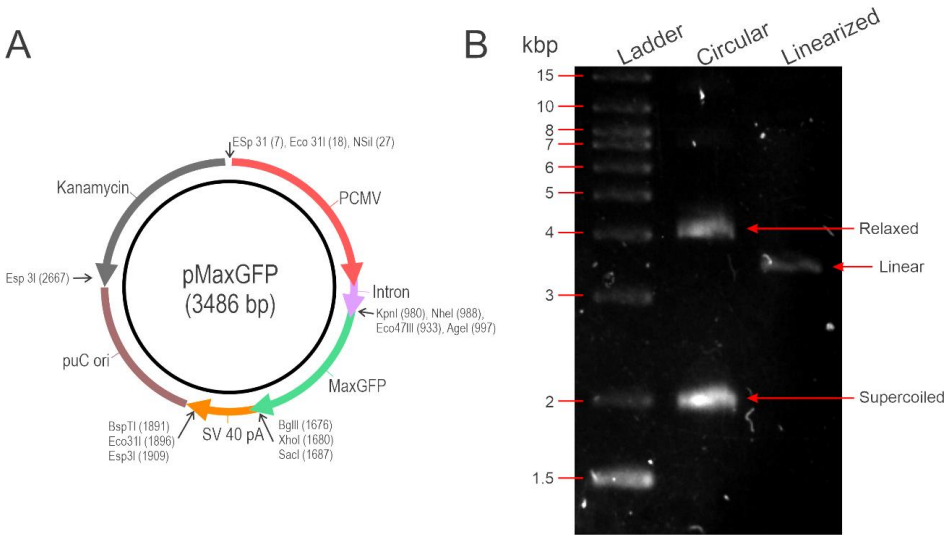

Figure 4.9. The pMaxGFP DNA plasmids and its characterisation by gel electrophoresis. *(A) The plasmid vector map of the pMaxGFP, redrawn from the company provided version. (B) 1 µg of the circular and linearized pMaxGFP was loaded onto a 0.8% agarose gel. The linearized pMaxGFP was generated by restriction digestion using the enzyme Kpn1. The gel electrophoresis showed that there are two topologies in the circular pMaxGFP plasmids, the relaxed and the supercoiled. The linearized pMaxGFP shows a single band with a size of roughly 3.5 kbp, in close approximation with the actual plasmid size of 3.486 kbp.*

Two bands were observed for the undigested circular samples of the pMaxGFP, due to the plasmid existing in either the supercoiled or the relaxed state (Higgins, N.P. and Vologodskii, 2015; Mitchenall et al., 2018). The linearized plasmids migrated at approximately 3.5 kbp, consistent with the 3.486 kbp size of the plasmid (Figure 4.9B). After the characterisation of the pMaxGFPs, the nanopipette was filled with PBS containing 0.13 nM pMaxGFP Four voltages, -900 mV, -700 mV, -500 mV and -300 mV were tested (Figure 4.10 and Figure 4.11).

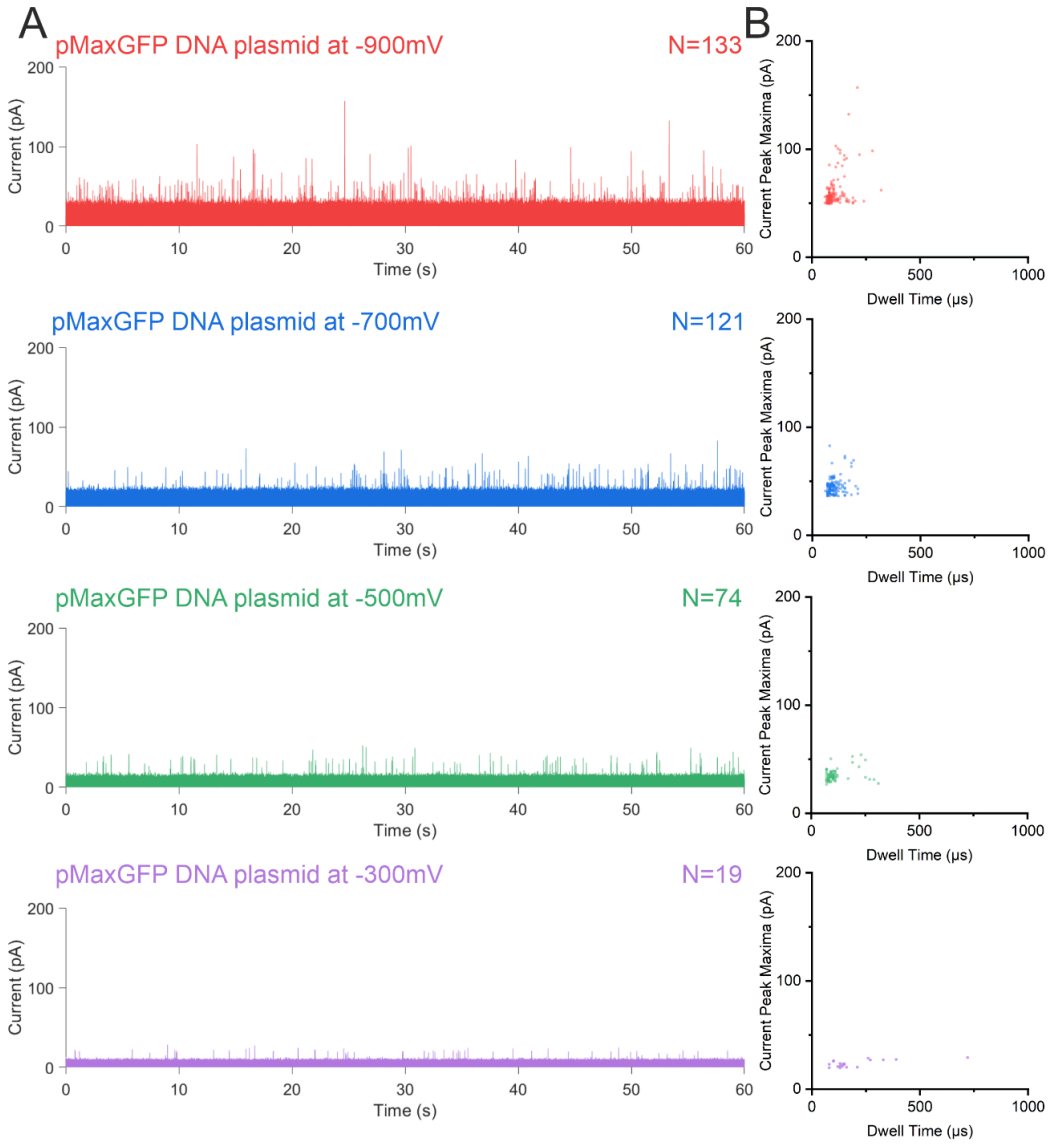

Figure 4.10. The translocation of pMaxGFP plasmid under different voltages. *0.13 nM of the pMaxGFP plasmid was used to fill the nanopipette and then immersed into the PBS bath. Four different voltages were tested with the same nanopipette at -900, -700, -500 and -300 mV. For each tested voltage, on the left is the 60 seconds baseline adjusted current trace of the translocation of the pMaxGFP plasmid (A) and on the right the population scatter of the collected translocation events from the associated trace (B). N refers to the total number of events recorded. This experiment was performed by Fabio Marcuccio and analysed by myself.*

The negative voltage causes the DNA plasmids to migrate towards the electrolyte bath through the nanopore. Their translocations caused an increase in the ionic current, due to the negatively charged DNA plasmids being shielded with clouds of counter ions and their translocation caused an ion accumulation at the tip end of the conical nanopore (Smeets et al., 2006; Kowalczyk and Dekker, 2012; Gebala et al., 2015; Ivanov et al., 2015; Gebala et al., 2016; Chen, K. et al., 2017; Raveendran et al., 2018).

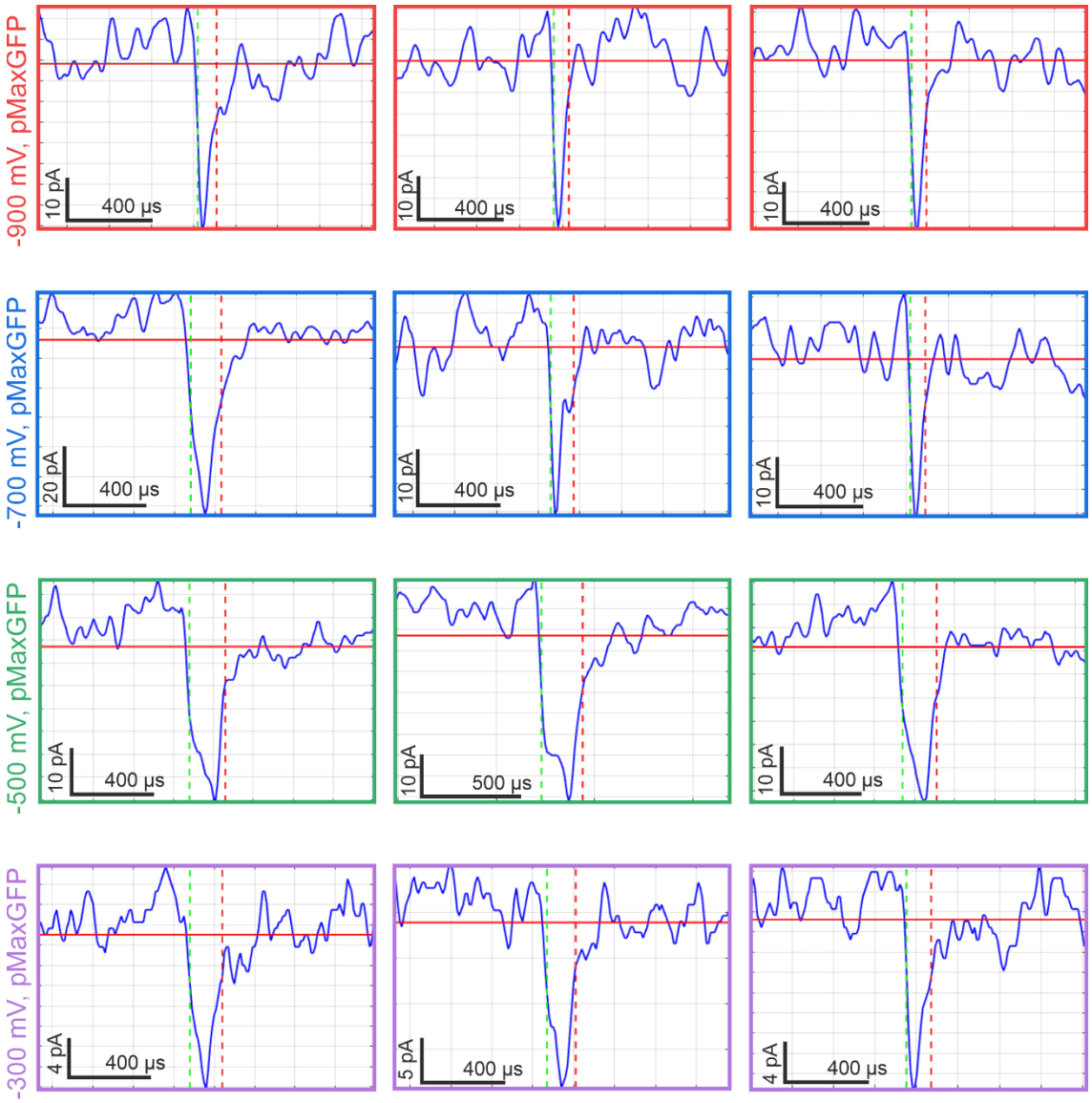

Figure 4.11. The translocation signal events snapshot of the pMaxGFP plasmids. *Three translocation event signal examples are shown for the traces in Figure 4.10. These events were chosen by random sampling.*

The translocations of pMaxGFP were detected with the nanopipette at all tested voltages. The molecule count for the pMaxGFP increased exponentially from 32 ± 8

at -300 mV to 110 ± 18 at -500 mV and plateaued from 136 ± 13 at -700 mV to 127 ± 6 at -900 mV (Figure 4.12). The molecule counts suggested that the capture of the pMaxGFP plasmid had a barrier-limited capture process (Charron et al., 2019). The event current size was largest at -900 mV with the mean current peak maxima at 60.9 ± 1.4 pA, followed by 45.6 ± 0.7 pA at -700 mV, 35.2 ± 0.6 at -500 mV and 23.7 ± 0.7 at -300 mV (Figure 4.12). Lastly, the dwell time was shorter for -900 mV at 107 ± 1 µs, followed by 104 ± 5 µs at -700 mV and 111 ± 4 µs at -500 mV, the dwell time almost doubled at 199 ± 21 µs when -300 mV was used (Figure 4.12).

The electronics used here for the translocation experiments were sampling at 100 kHz (10 µs bandwidth), this means that the current will be recorded every 10 µs. In addition, a low-pass filter was set to 10 kHz (100 µs bandwidth) threshold during all recordings, the low-pass allows signal frequencies that are under 10 kHz to pass through and will remove all frequencies above the threshold value. Under this set-up, translocation events that are on the same time scale or below the low-pass filter bandwidth will be removed, *i.e.* translocation events that are under 100 µs will be removed. Translocation events will include at least 10 points (1 data point per 10 µs). The trace recorded a high event count, indicating that the setting does not significantly affect the detections of the DNA plasmids, but it is highly likely that only the exponential tail of the translocated events were recorded, and that majority of the translocation events were treated as noise, as pointed out by Plesa *et al.* (Plesa et al., 2013).

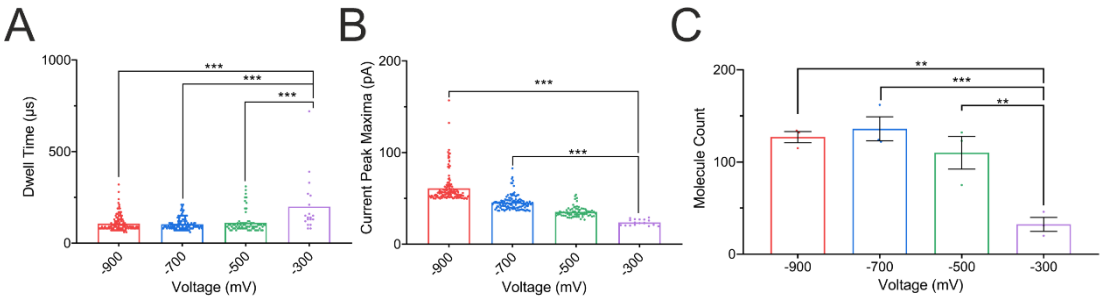

Figure 4.12. The statistical analysis of the pMaxGFP plasmids translocation with the nanopipette under different voltages*. The increase in the applied voltage from -300 to -900 mV led to a decrease in the dwell time (A) but an increase in peak current maxima (B) for the pMaxGFP plasmids translocation. (C) Three 60 second traces were analysed to obtain the average translocation molecule count under different voltages. For the pMaxGFP plasmid, increasing the voltage from -300 to -700 mV resulted in a significant increase in molecule counts and -900 mV had a roughly similar molecule count as -700 mV. Error bars are ± S.E.M. Asterisks indicate P-values (**, P<0.1; ***, P<0.01). The data points in bar chart (A) and (B) correspond to individual events from the current traces presented in Figure 4.10. Kruskal-Wallis tests were used.*

The observation that the translocation of the DNA plasmids through the nanopore at a higher voltage decreases the dwell time is in agreement with previous studies (Harrell et al., 2006; Wanunu et al., 2012).

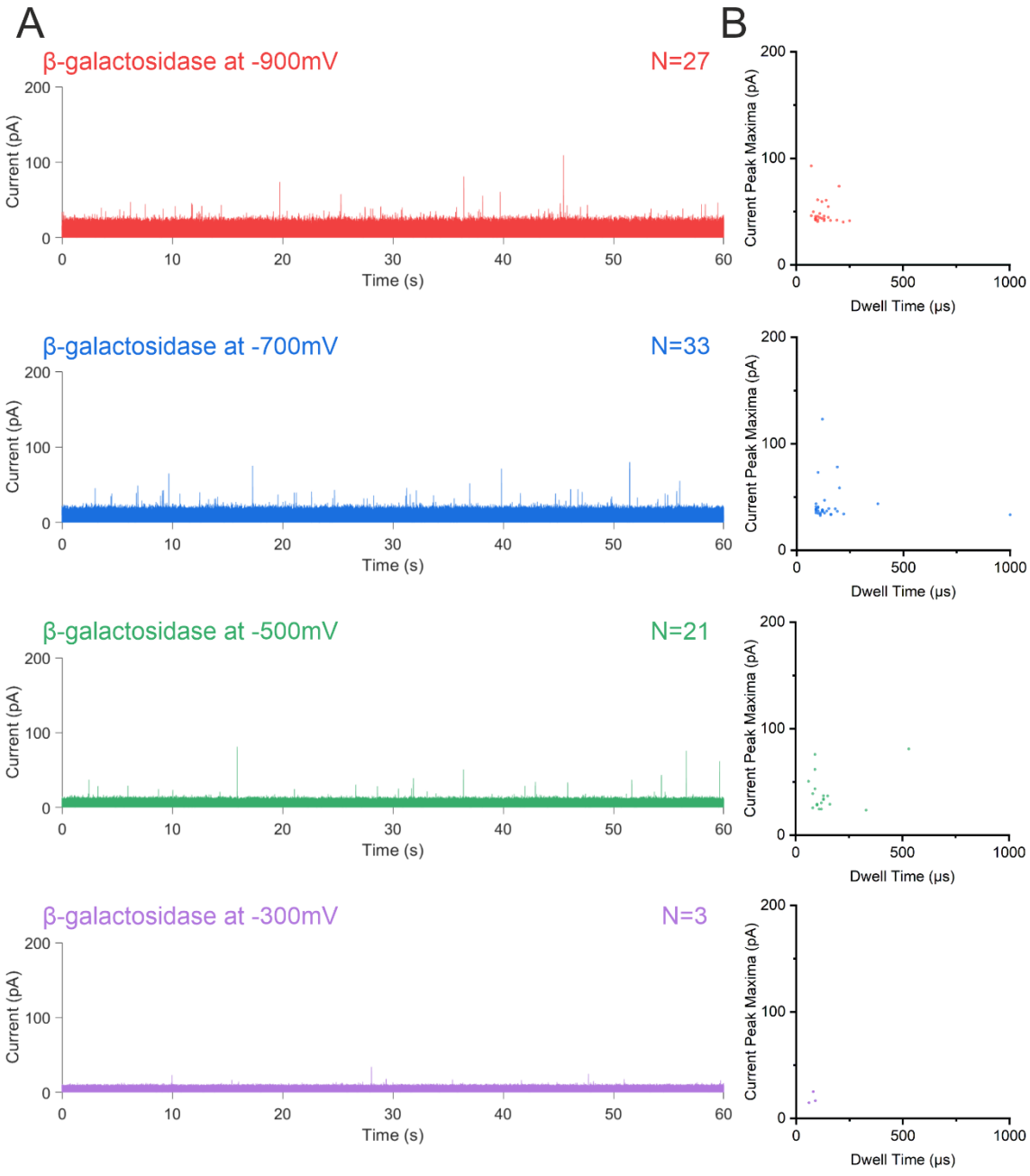

Figure 4.13. The translocation of protein β-galactosidase under different voltages. *1 µM of β-galactosidase was used to fill the nanopipette and then immersed into the PBS bath. Four different voltages were tested with the same nanopipette at -900, -700, -500 and -300 mV. For each tested voltage, on the left is the 60 seconds baseline adjusted current trace of the translocation of the β-galactosidase (A) and on the right the population scatter of the collected translocation events from the associated trace (B). N refers to the total number of events recorded. This experiment was performed by Fabio Marcuccio and analysed by myself.*

After testing the pMaxGFPs, the previously characterised β-galactosidase (Chapter 3 Section 0) was used to fill the nanopipette at 1 µM in PBS (Figure 4.13 and Figure 4.14) and immersed into the PBS bath. Similarly, four voltages, -900 mV, -700 mV, -500 mV and -300 mV were tested.

The negative voltage causes the negatively charged β-galactosidase (pI = 4.61, (Boyer et al., 1970)) to migrate towards the electrolyte bath through the nanopore. Unlike DNA plasmids, the rate of translocations was not as high, however, similar to DNA, the translocation of the β-galactosidase also caused an increase in the ionic current (Chen, K. et al., 2017).

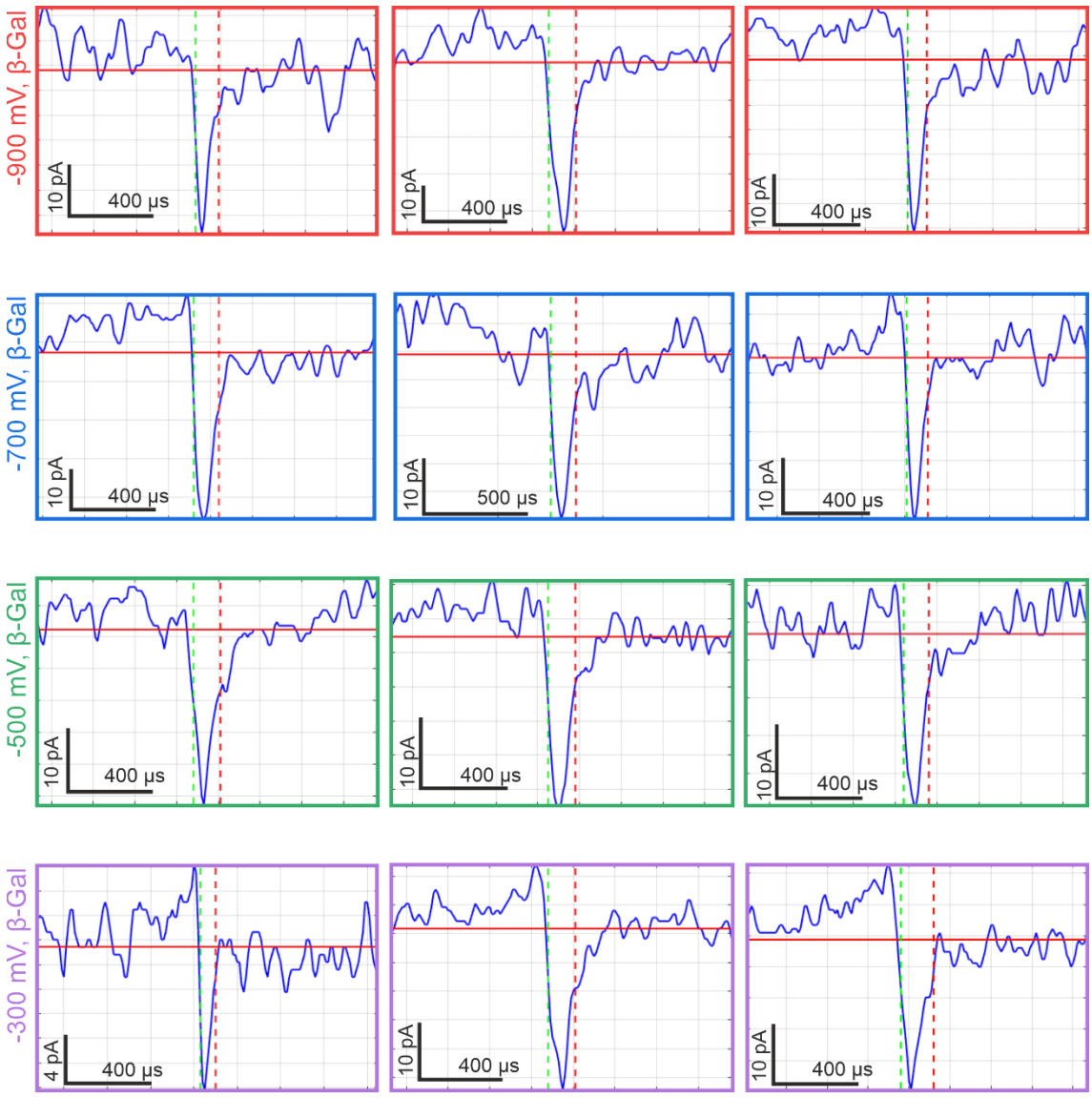

Figure 4.14. The translocation signal events snapshot of the β-galactosidase. *Three translocation event signal examples are shown for the traces in Figure 4.13. These events were chosen by random sampling.*

As Plesa *et al.* described, the translocation of protein is fast and can be difficult to be detected under normal conditions, majority of the proteins translocate through a solid-state nanopore at high velocity of less than 100 μs (Plesa et al., 2013). Consequently, after the application of the low-pass filter of 10 kHz, majority of the true protein translocation events were treated as noise and any detectable translocation signals are likely due to proteins are held long enough inside the nanopore potentially due to protein-surface interaction (Plesa et al., 2013). The nanopipette detected the translocation of the β-galactosidase at all voltages. However, the molecule count remains low, there were 6 ± 3 molecules detected at -300 mV, 26 ± 3 at -500 mV, 43 ± 6 at -700 mV and 28 ± 1 at -900 mV (Figure 4.15). The low molecule count, despite a high concentration of β-galactosidase used to fill the nanopipette, suggested that our system was not able to detect the translocation of proteins effectively. With the hardware setting and experimental set-up used here, the translocations of the β-galactosidase through the nanopipette were likely to be buried in the noise, *i.e.* the SNR ratio is not sufficient for the detection of protein (Plesa et al., 2013). In contrast, the DNA required to be detected was around 0.13 nM, which was approximately 10,000× lower in concentration. Similar to DNA plasmids, the event current size for the all the detectable translocations of the β-galactosidase was largest at -900 mV, with the mean current peak maxima at 48.9 ± 2.3 pA, followed by 43.1 ± 3 pA at -700 mV, 37.7 ± 3.6 at -500 mV and 18.8 ± 3.2 at -300 mV (Figure 4.15) and the differences in magnitude were not as strong as DNA plasmids. Lastly, the dwell time was shorter for -900 mV at 125 ± 9 μs, followed by 160 ± 28 μs at -700 mV and 191 ± 56 μs at -500 mV, and 77 ± 8 μs when -300 mV was used (Figure 4.12). This was different from the DNA plasmids, however, due to the sample size of 3 molecules at -300 mV, there was insufficient data to draw a clear conclusion.

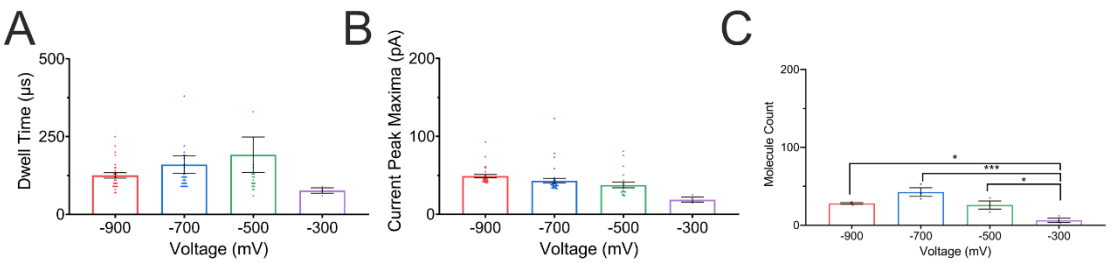

Figure 4.15. The statistical analysis of the pMaxGFP plasmids translocation with the nanopipette under different voltages*. The voltage dependent translocation event analysis for the β-galactosidase translocation, (A) dwell time and (B) current peak maxima. No statistical analysis were performed due to the small sample sizes (under 50 events). (C) Three 60 seconds traces were analysed to obtain the average translocation molecule count under different voltages. For the β-galactosidase, increasing the voltage from -300 to -700 mV resulted in a statistically significant increase in molecule counts and -900 mV had a lower molecule count than -700 mV. Error bars are ± S.E.M. Asterisks indicate P-values (*, P<0.5; ***, P<0.01). The data points in bar chart (A) and (B) correspond to individual events from the current traces presented in Figure 4.13. Kruskal-Wallis tests were used for C.*

4.3.3 Translocation of molecules in the modified electrolyte bath

As discussed earlier in this chapter, the single molecule detection can be improved by changing the nature and concentration of the electrolyte and using a salt gradient (Wanunu et al., 2009; Kowalczyk et al., 2012). However, the high salt condition significantly deviates from the physiological salt condition and this can affect the stability, conformation, and size of proteins (Maity et al., 2018), and therefore will not be investigated here. Additives such as viscogen are used to modify the viscosity of the electrolyte and it has been shown that they significantly slow down the translocation of the DNA molecules through a solid-state nanopore (Fologea et al., 2005; Li, J. and Talaga, 2010). On the other hand, the excluded volume effects of the solution can be modified by macromolecular crowding agents such as the chemical crowder PEG and protein crowder BSA. Indeed, the addition of the PEG has been used to improve the detection efficiency of both synthetic polypeptides and ssDNA in a α-HL nanopore (Larimi et al., 2019; Yao et al., 2020).

Here, the effect of solution properties on the detection of the molecules by the nanopipette was systemically examined by adding additives including glycerol, PEG 8000 and the BSA to the PBS electrolyte bath. Various concentrations of these molecules were added to the PBS electrolyte without modifying its ionic strength. For glycerol, a range from 50% (v/v), 25% (v/v) and 12.5% (v/v) were chosen based on a previous study (Fologea et al., 2005). For the PEG 8000, the concentration of *c.a.* 12.5% (w/v) PEG 8000 has been used to condense chromatin for structural study (Karbstein and Hancock, 2012), thus 12.5% (w/v) was chosen

as the starting point and doubled to 25% (w/v) and finally at 50% (w/v). This concentration was close to the concentration of PEG (40%) utilised before with biological nanopore (Larimi et al., 2019; Yao et al., 2020). The protein crowder BSA was used at 30% (w/v) at first as it is the physiological relevant concentration of proteins inside a mammalian cell (Nishizawa et al., 2017) and the solution was then diluted down to 15% (w/v) and 7.5% (w/v).

The set-up of the system was the same as Figure 4.7A. In addition, the glycerol, PEG 8000 or BSA modified PBS electrolyte bath was used alongside the control PBS electrolyte bath. To begin, the current-voltage relationship was examined. The PBS filled nanopipette was immersed into the electrolyte bath with various concentrations of glycerol (Figure 4.16A), PEG 8000 (Figure 4.16B) or BSA (Figure 4.16C). For each condition, a voltage ranging from -500 mV to 500 mV was applied, then the average I_{-500mV}/I_{500mV} and the average resistance (MΩ) were calculated (Figure 4.16D). Both increasing the concentration of the glycerol or PEG 8000 led to an increase in the nanopore resistance by lowering the solution conductivity (Stojilkovic et al., 2003; Shu et al., 2017). The ionic current of the nanopipette in the standard PBS electrolyte was shown to be rectified and the extent of the rectification is indicated by the I_{-500mV}/I_{500mV} ratio. The increasing concentrations of both glycerol and PEG 8000 minimised the extent of the rectification as observed in the lowering of the I_{-500mV}/I_{500mV} ratio. Interestingly, the ICR in the 50% (w/v) PEG 8000 rectified in the opposite polarity. This was observed in a surface modified nanopipette with the positively charged polyelectrolytes poly-L-lysine (Umehara et al., 2006), and was consistent with a modification of the electroosmotic flow within the nanopore (Yusko, Erik C. et al., 2009; Rabinowitz et al., 2019). Additionally, a similar current-voltage profile has also been reported before with an ultra-short conical nanopore of less than 100 nm in length and a sub-10 nm opening (Ma, L. et al., 2020) or using a gel polymer electrolyte instead of the standard electrolyte with a 200 nm conical nanopore (Plett et al., 2017). In direct contrast to both glycerol and PEG, the protein crowder BSA did not alter the ion current rectification nor did it increase the pore resistance. This could be because the protein BSA was negatively charged at neutral pH (BSA has an isoelectric point of 4.7) in the electrolyte (Medda et al., 2015), and could act as a charge carrier in the established electric circuit.

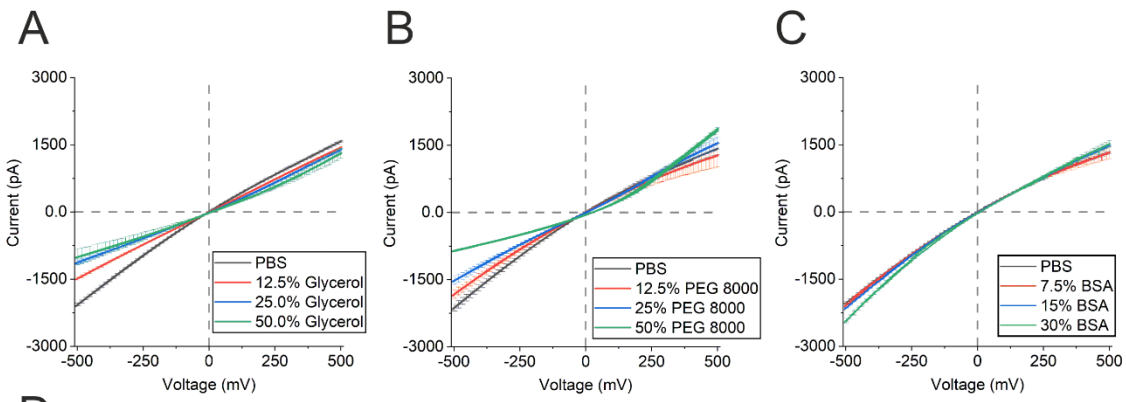

D

Condition	Average I_{-500mV} / I_{500mV}	Average Resistance (MΩ)
PBS	1.49±0.08	288.4±4.2
PBS+12.5% (v/v) Glycerol	1.04±0.01	341.9±5.2
PBS+25% (v/v) Glycerol	0.81±0.02	397.8±10
PBS+50% (v/v) Glycerol	0.76±0.07	445.5±51.1
PBS+12.5% (w/v) PEG 8000	1.39±0.32	298±12.2
PBS+25% (w/v) PEG 8000	1.1±0.23	335.1±3.7
PBS+50% (w/v) PEG 8000	0.47±0.02	369.9±6.4
PBS+7.5% (w/v) BSA	1.62±0.21	293.5±7.8
PBS+15% (w/v) BSA	1.45±0.01	275.9±0.3
PBS+30% (w/v) BSA	1.62±0.07	252.6±6.8

Figure 4.16. The current-voltage properties of the nanopipette in different bath conditions. *PBS was used to fill the nanopipette before immersion into a different PBS containing various concentrations of either (v/v) glycerol (A), (w/v) PEG 8000 (B) and (w/v) BSA (C). Three nanopipettes per condition were tested. The I_{-500mV}/I_{500mV} ratio and the resistance for the nanopipettes measured are calculated and shown in (D).*

To determine whether the modified electrolyte bath solution influenced the molecule translocation dynamic through the nanopore, the DNA plasmid pMaxGFP was used as the model. The PBS solution containing 1.3 nM of pMaxGFP was used to fill the nanopipette. The analyte filled nanopipette was immersed into the PBS bath (Figure 4.17) or PBS bath containing various concentrations of glycerol (Figure 4.18), PEG 8000 (Figure 4.19) or BSA (Figure 4.22). Based on the previous voltage dependent translocation experiments, a voltage of -700 mV was chosen to electrophoretically drive the DNA plasmid out into the bath from the nanopipette. The PBS bath was tested first as the control and the average molecule count for the translocation of pMaxGFP was at 359 ± 5 over the duration of 60 seconds (Figure 4.17A, Figure 4.23A, D). A single population was observed from the population scatter (Figure 4.17B). The average current peak maxima and dwell time for the pMaxGFP in PBS was at 89 ± 1 pA and 111 ± 2 µs (Figure 4.23B-D).

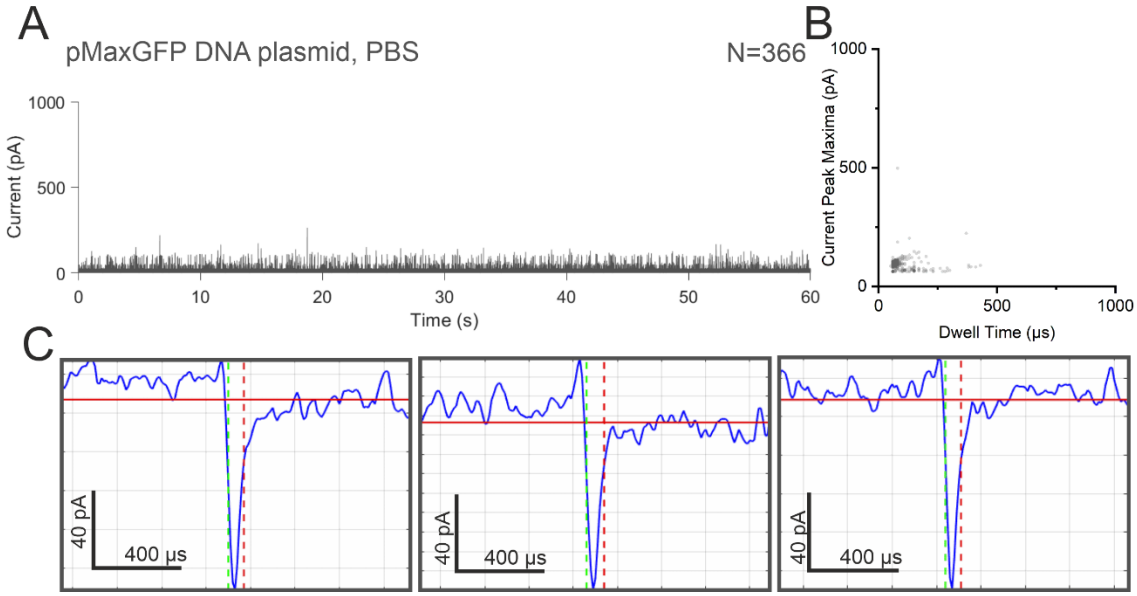

Figure 4.17. The translocation of pMaxGFP plasmid into the PBS bath. *1.3 nM of the pMaxGFP plasmid was used to fill the nanopipette and then immersed into the PBS bath. -700 mV voltage was applied in all conditions. On the left is the 60 seconds baseline adjusted current trace of the translocation of the pMaxGFP plasmid (A) and on the right the population scatter of the collected translocation events from the associated trace (B). Three example translocation signals were shown for each trace which were randomly sampled (C). N refers to the total number of events recorded.*

Increasing concentrations of the glycerol to 12.5% (v/v) caused the molecule count to drop to 255 ± 56, and an increasingly higher concentration of glycerol led to a further reduction in the molecule count to 102 ± 36 and 67 ± 23 molecules per 60 seconds at 25% (v/v) and 50% (v/v) (Figure 4.18A, Figure 4.23A, D). The population scatter showed a major population under 250 µs and 250 pA in all cases (Figure 4.18B). The glycerol had no effect on the dwell time (110 ± 24 µs and 116 ± 12 µs for 25% (v/v) and 50% (v/v) respectively) except at 12.5% (v/v) where the dwell time was statistically significantly lower than the PBS at 88 ± 7 µs (Figure 4.23B-D).

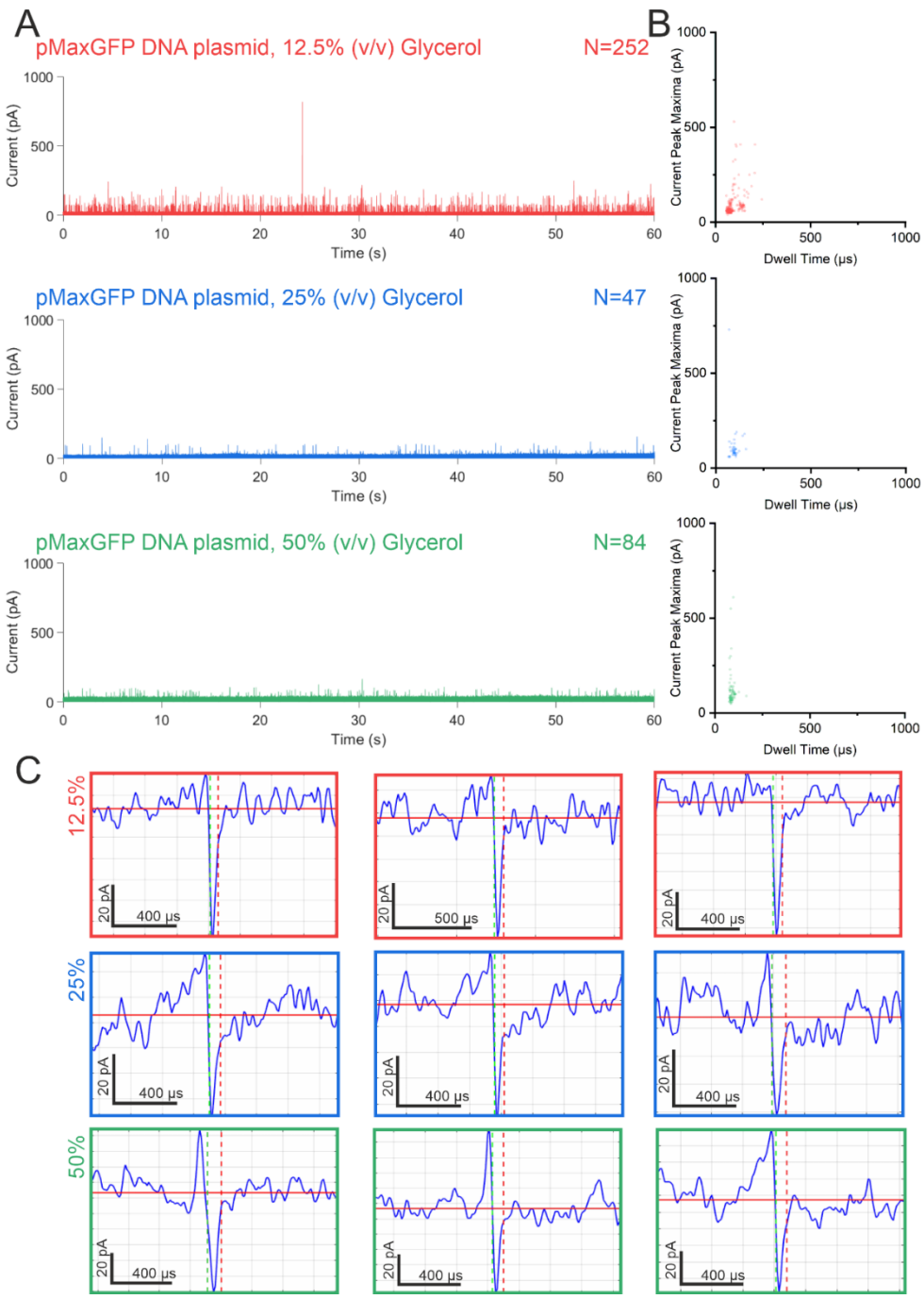

Figure 4.18. The translocation of pMaxGFP plasmid in glycerol PBS bath. *1.3 nM of the pMaxGFP plasmid was used to fill the nanopipette and then immersed into the PBS bath containing 12.5%, 25% or 50% (v/v) glycerol. -700 mV voltage was applied in all conditions. For each condition, on the left is the 60 seconds baseline adjusted current trace of the translocation of the pMaxGFP plasmid (A) and on the right the population scatter of the collected translocation events from the associated trace (B). Example translocation signals were shown for each trace which were randomly sampled (C). N refers to the total number of events recorded.*

The glycerol electrolyte bath had a negligible effect on the average current amplitude similar to PBS regardless of the concentration at 90 ± 2 pA, 96 ± 3 pA, and 89 ± 1 pA for 12.5% (v/v), 25% (v/v) and 50% (v/v) glycerol.

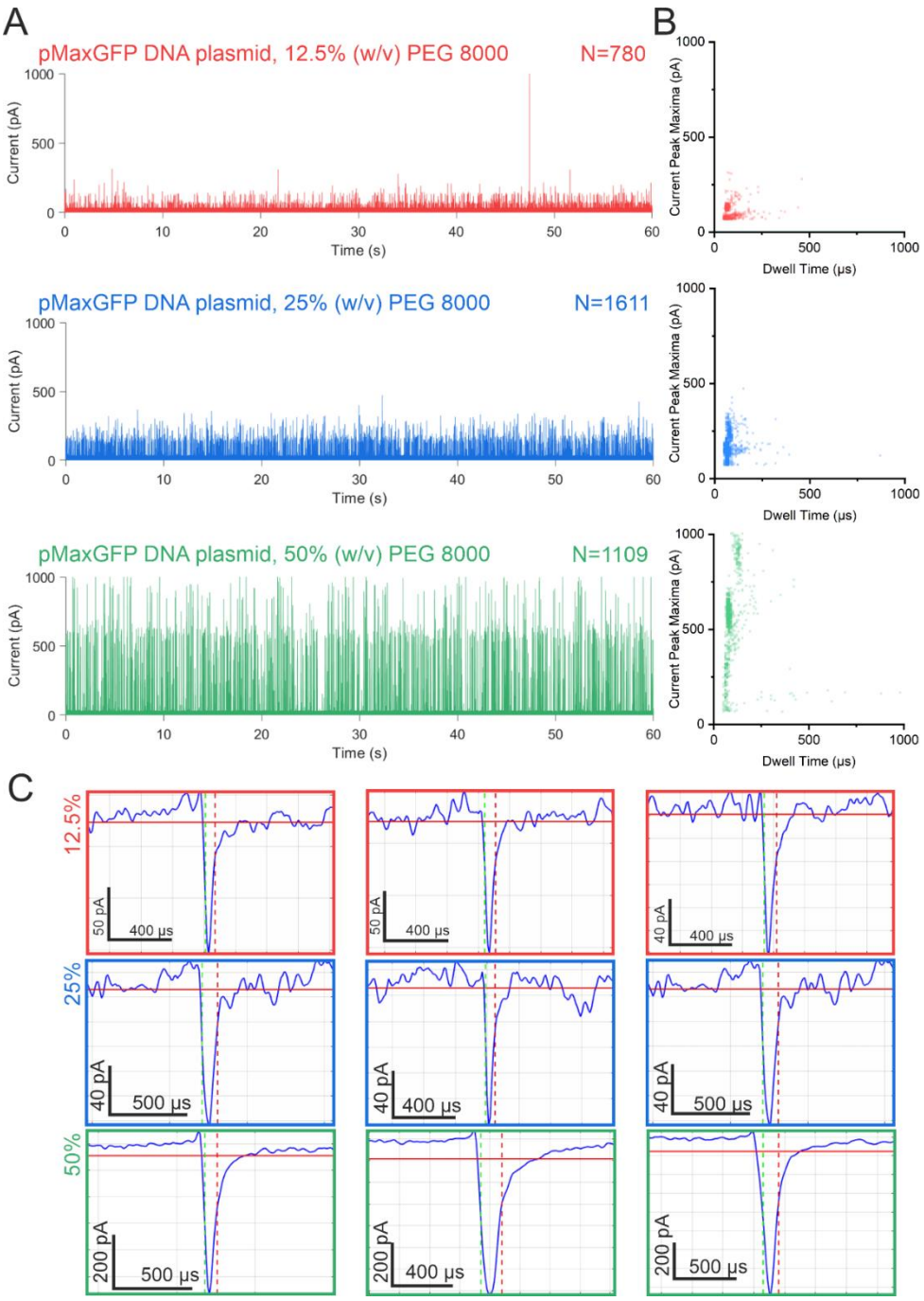

Figure 4.19. The translocation of pMaxGFP plasmid in PEG 8000 PBS bath. *1.3 nM of the pMaxGFP plasmid was used to fill the nanopipette and then immersed into the PBS bath containing 12.5%, 25% or 50% (w/v) PEG 8000. -700 mV voltage was applied in all conditions. For each condition, on the left is the 60 seconds baseline adjusted current trace of the translocation of the pMaxGFP plasmid (A) and on the right the population scatter of the collected translocation events from the associated trace (B). Example translocation signals were shown for each trace which were randomly sampled (C). N refers to the total number of events recorded.*

In sharp contrast, increasing the concentration of the PEG 8000 from 12.5% (w/v) to 50% (w/v) increased the molecule count (Figure 4.19A, Figure 4.23A, D) with the highest molecule count at 25% (w/v) of 1308 ± 156, followed by 50% (w/v) of 1063 ± 24 and finally 743 ± 36 at 12.5% (w/v) over the duration of 60 seconds. As

shown by the population scatter, increasing the concentration of the crowder PEG 8000 to 50% (w/v) clearly showed that there were at least two populations: one located above 750 pA and around 200 µs, and another one under 750 pA and around 100 µs (Figure 4.19B). The average current peak amplitude were all statistically larger than PBS with 102 ± 1 pA, 164 ± 1 pA and 553 ± 8 pA for 12.5% (w/v), 25% (w/v) and 50% (w/v) PEG 8000 respectively (Figure 4.23B, D). The dwell time for 12.5% (w/v) and 25% (w/v) were significantly shorter than PBS alone at 80 ± 6 µs and 72 ± 3 µs. However, the dwell time for 50% (w/v) PEG 8000 was not statistically significantly different from PBS alone at 116 ± 15 µs (Figure 4.23C, D).

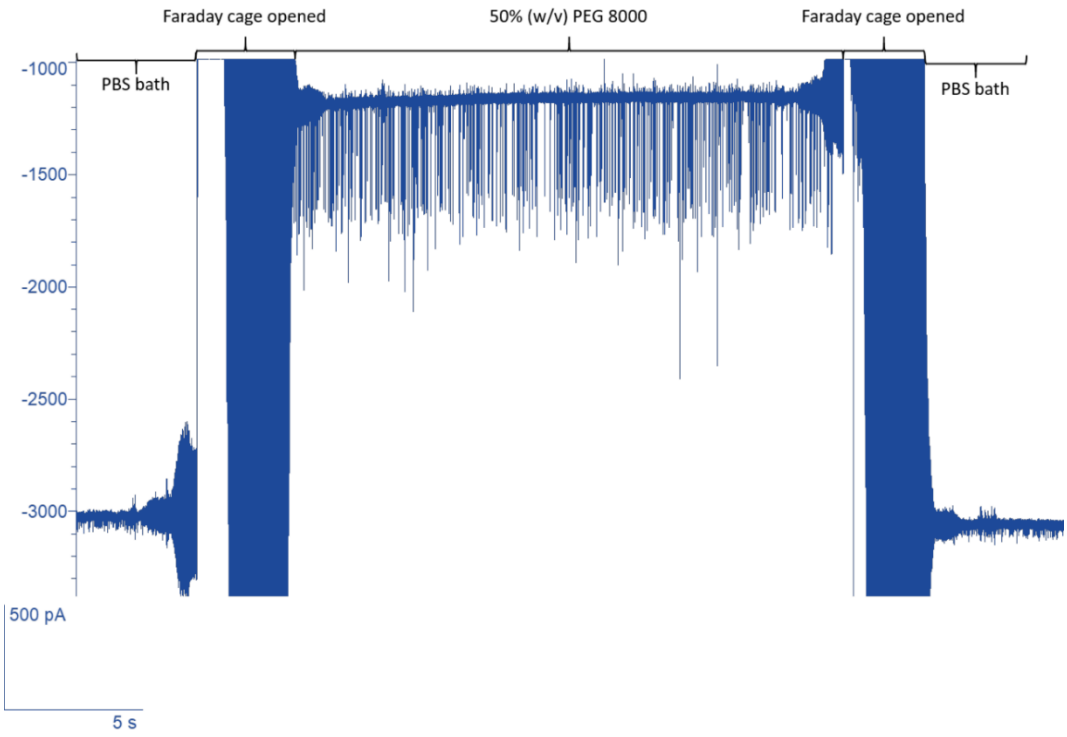

Figure 4.20. The effect of macromolecular crowding on the nanopipette is reversible. *A nanopipette containing 1.3 nM of pMaxGFP plasmid was first immersed into the PBS bath and -700 MV was applied to drive the plasmid into the bath. Without pausing the recording or changing the voltage, the Faraday cage was opened, followed by transferring the nanopipette and the reference electrode into the 50% (w/v) PEG 8000 bath. The Faraday cage was closed for approximately 15 seconds, and then opened again to transfer the nanopipette and the reference electrode back into the PBS bath. The pronounced and reversible change in the current baseline and the peak amplitudes of the plasmid between the PBS and 50% (w/v) PEG 8000 bath can both be observed. The baseline changed from c.a. -3000 pA to c.a. -1300 pA due to the solution properties causing the nanopipette to have a higher resistance as shown in Figure 4.16.*

Furthermore, the dramatic increase of the pMaxGFP event current amplitude observed when placed in the 50% (w/v) PEG 8000 bath was completely bath dependent and could be reversed (Figure 4.20). Here, the pMaxGFP filled

nanopipette was first placed in the PBS bath and -700 mV was applied to drive the plasmid into the bath. Then the nanopipette was moved from the PBS bath into the 50% (w/v) PEG 8000 PBS bath. The current amplitude from the current baseline immediately decreased when placed inside the 50% (w/v) PEG 8000 PBS bath. Finally, the nanopipette was placed back into the PBS bath and the current amplitude increased (Figure 4.20). This experiment demonstrated that the improved current amplitude was due to the presence of the PEG 8000 in the electrolyte bath.

The protein BSA was used to mimic the cellular crowded environment at 30% (w/v) (Nishizawa et al., 2017). However, BSA is also a common analyte for nanopore detection and has been analysed with nanopipettes in the past (Li, W. et al., 2013). Thus, before testing the behaviour of the translocation dynamic in a highly crowded environment created by BSA, it is important to test whether the nanopipette can detect the translocation of BSA from the electrolyte into the nanopipette in the system. The PBS filled nanopipette was immersed into the PBS electrolyte containing 30% (w/v) BSA, and a voltage of -700 mV was applied at the nanopipette (Figure 4.21). Under this condition, the nanopipette was able to pick up *c.a.* 10 molecules over three separate 60 second recordings extremely close to the baseline (Figure 4.21).

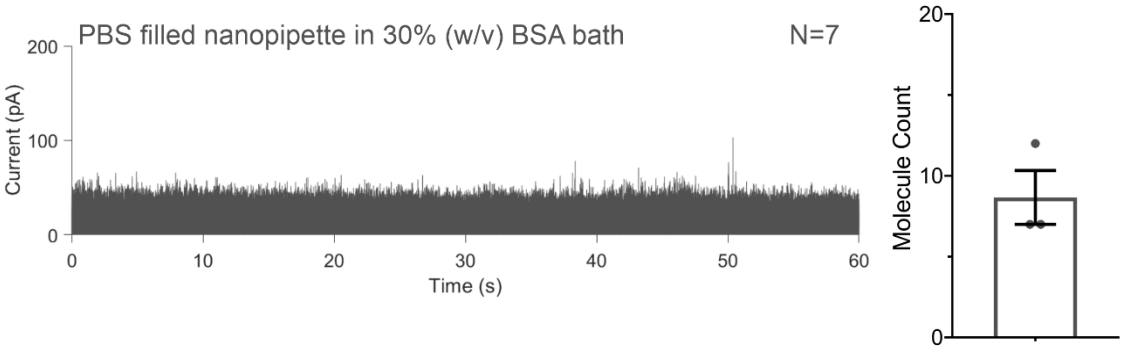

Figure 4.21. PBS filled nanopipette in 30% (w/v) BSA bath. *The PBS was used to fill the nanopipette and was immersed into the 30% (w/v) BSA bath. A potential difference of -700 mV was applied. The 60 seconds trace was shown on the left and three different 60 seconds trace were used for the molecule count analysis. N refers to the total number of events recorded.*

This suggested that although BSA could be detected under the translocation experiment setting, the efficiency was suboptimal with our strigent threshold setting, and had minimum impact on the experiments performed in the BSA crowded bath.

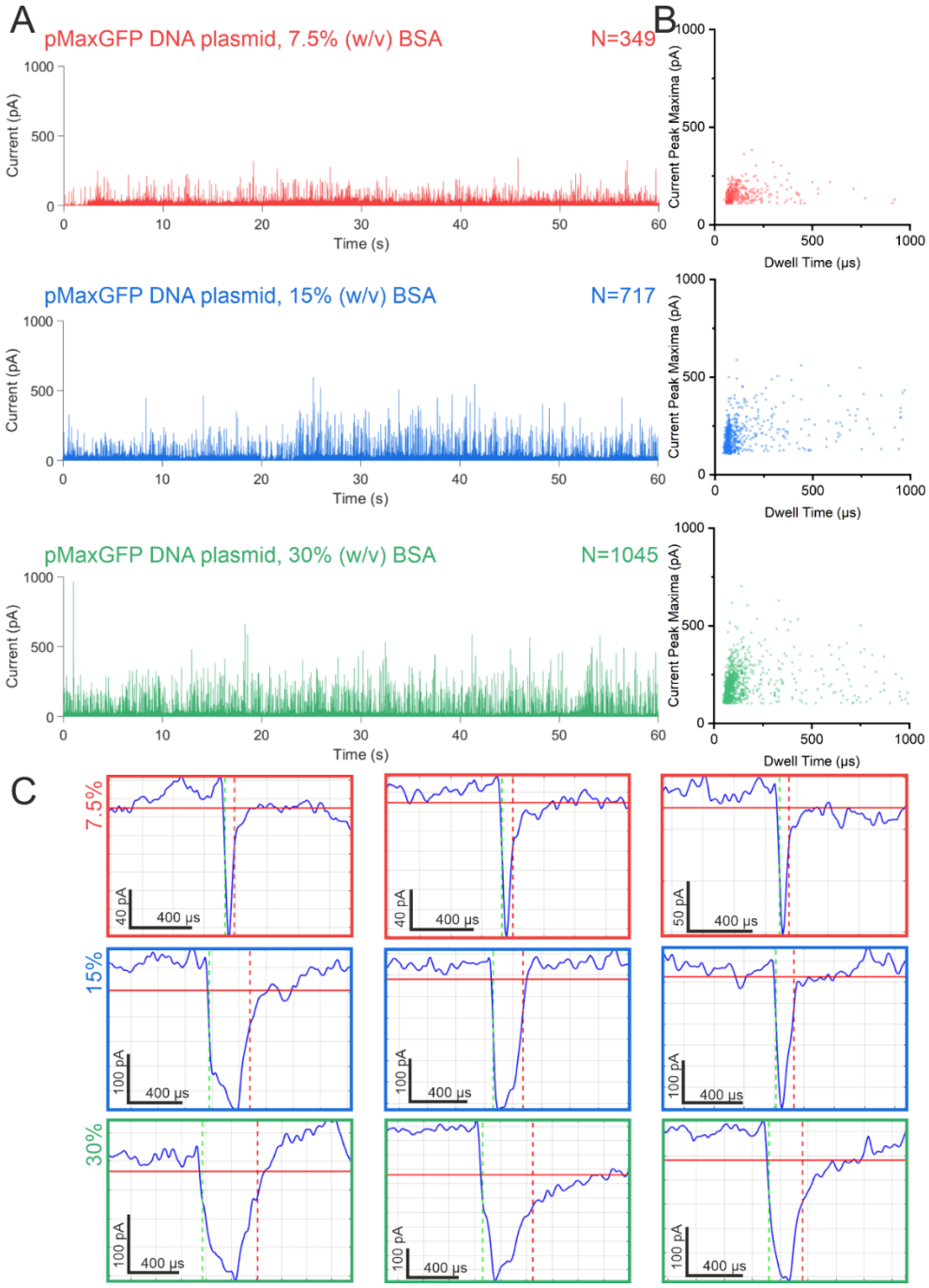

Figure 4.22. The translocation of pMaxGFP plasmid in BSA PBS bath. *1.3 nM of the pMaxGFP plasmid was used to fill the nanopipette and then immersed into the PBS bath containing 7.5%, 15% or 30% (w/v) BSA. -700 mV voltage was applied in all conditions. For each condition, on the left is the 60 seconds baseline adjusted current trace of the translocation of the pMaxGFP plasmid (A) and on the right the population scatter of the collected translocation events from the associated trace (B). Example translocation signals were shown for each trace which were randomly sampled (C). N refers to the total number of events recorded.*

Under the crowded environment formed by dissolving the BSA in PBS at a high concentration, translocation events of the pMaxGFP from the nanopipette into the bath were detected at 7.5% (w/v), 15% (w/v) and 30% (w/v), with a gradual increase in the molecule count from 342 ± 12 to 712 ± 12, and finally at 1073 ± 64

respectively (Figure 4.22A, Figure 4.23A, D). The population scatter of each of the conditions showed a single population and an increasing number of events along the dwell time and current peak maxima axises as the concentration of BSA in the bath increased. The average current peak maxima for all three conditions were statistically significantly larger than PBS with 15% (w/v) at the highest at 217 ± 4 pA followed by 30% (w/v) at 207 ± 3 pA and lastly 7.5% (w/v) 160 ± 2 pA (Figure 4.23B, D). Unlike glycerol and PEG 8000 where the average dwell time of the plasmid was shorter or closer to the PBS, the dwell time in the BSA crowded PBS was statistically significantly longer than PBS in all cases, with 30% (w/v) at the longest with 278 ± 22 μs, then 243 ± 18 μs at 15% (w/v) and finally 167 ± 15 μs at 7.5% (w/v) BSA (Figure 4.23C, D).

The overall comparison of the pMaxGFP translocation dynamic between the three conditions and PBS could be summarised as the following (Figure 4.23): the viscogen glycerol reduced the molecule count and had negligible effects on the current amplitude and dwell time of the single molecule events; the chemical crowder PEG 8000 had the most significant impact in molecule count and current amplitude with the most impact at 50% (w/v); the protein crowder BSA gradually increased the molecule count and affected the current amplitude and dwell time but the current amplification effect was not as pronounced as 50% (w/v) PEG 8000.

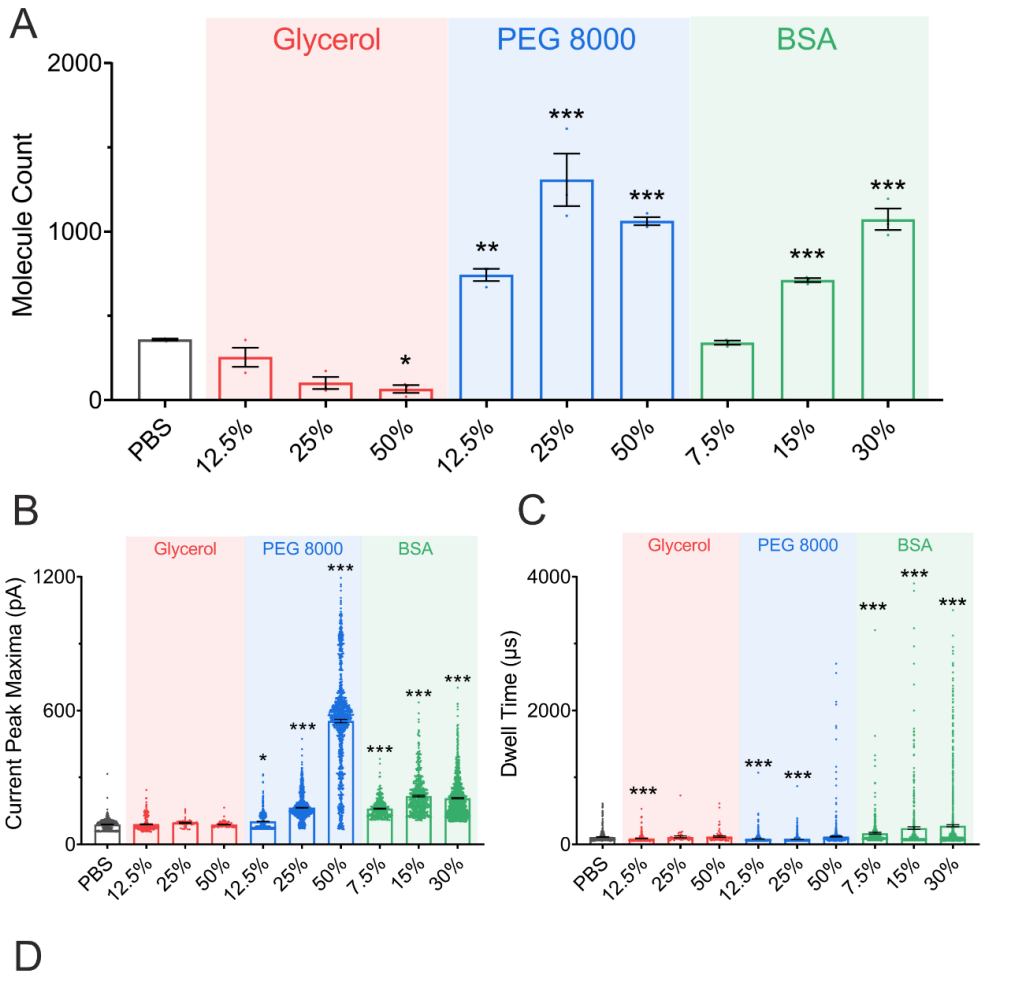

Condition	Molecule Count		Current Peak Maxima (pA)		Dwell Time (µs)	
	Mean ± S.E.M.	Median	Mean ± S.E.M.	Median	Mean ± S.E.M.	Median
PBS	360 ± 5	364	89 ± 1	92	111 ± 10	80
PBS + 12.5% (v/v) Glycerol	255 ± 56	245	90 ± 2	79	88 ± 10	60
PBS + 25% (v/v) Glycerol	102 ± 36	76	96 ± 3	95	110 ± 20	90
PBS + 50% (v/v) Glycerol	102 ± 36	84	89 ± 1	85	116 ± 10	90
PBS + 12.5% (w/v) PEG 8000	743 ± 36	779	102 ± 1	85	80 ± 10	70
PBS + 25% (w/v) PEG 8000	1308 ± 156	1218	164 ± 1	154	72 ± 10	60
PBS + 50% (w/v) PEG 8000	1063 ± 24	1051	553 ± 8	573	116 ± 10	80
PBS + 7.5% (w/v) BSA	342 ± 12	349	160 ± 2	152	167 ± 20	100
PBS + 15% (w/v) BSA	712 ± 12	717	217 ± 4	200	243 ± 20	90
PBS + 30% (w/v) BSA	1073 ± 64	1045	207 ± 3	189	278 ± 20	90

Figure 4.23. The statistical analysis of the pMaxGFP plasmid in different bath conditions. *(A) The molecule count for the pMaxGFP plasmid in different bath conditions. Three 60 seconds traces of each voltage were analysed. The presence of PEG 8000 and BSA in the PBS bath resulted in a pronounced increase in molecule count and current peak maxima (B) when compared to PBS. The BSA caused a significant increase in the dwell time in direct contrast to the addition of PEG 8000 (C) when compared to PBS. The 50% (w/v) PEG 8000 has the strongest effect on the current peak maxima. Asterisks show where the addition of either glycerol, PEG 8000 or BSA resulted in a significant change when compared to PBS alone. Asterisks indicate P-values (*, P<0.5; **, P<0.1; ***, P<0.01). Error bars are ± S.E.M. The data points in bar chart (B) and (C) correspond to individual events from the current traces presented in Figure 4.18, Figure 4.19 and Figure 4.22. One-way ANOVA test was used for (A) and Kruskal-Wallis test were used for (B) and (C).*

The previously characterised 465 kDa tetrameric β-galactosidase was used as the model globular protein to test whether the modified bath conditions improved the detection efficiency of proteins. Firstly, 1 µM β-galactosidase in PBS was used to fill the nanopipette and immersed into the PBS bath and a potential difference of -700

mV was used to electrophoretically deliver the negatively charged β-galactosidase into the bath. The detection efficiency for β-galactosidase in PBS at -700 mV was of 7 ± 5 molecules in three separate 60 second traces (Figure 4.24, Figure 4.30A, D). Then the translocation dynamic of the β-galactosidase was tested in various concentration of glycerol (Figure 4.25), PEG 8000 (Figure 4.26) or BSA (Figure 4.29).

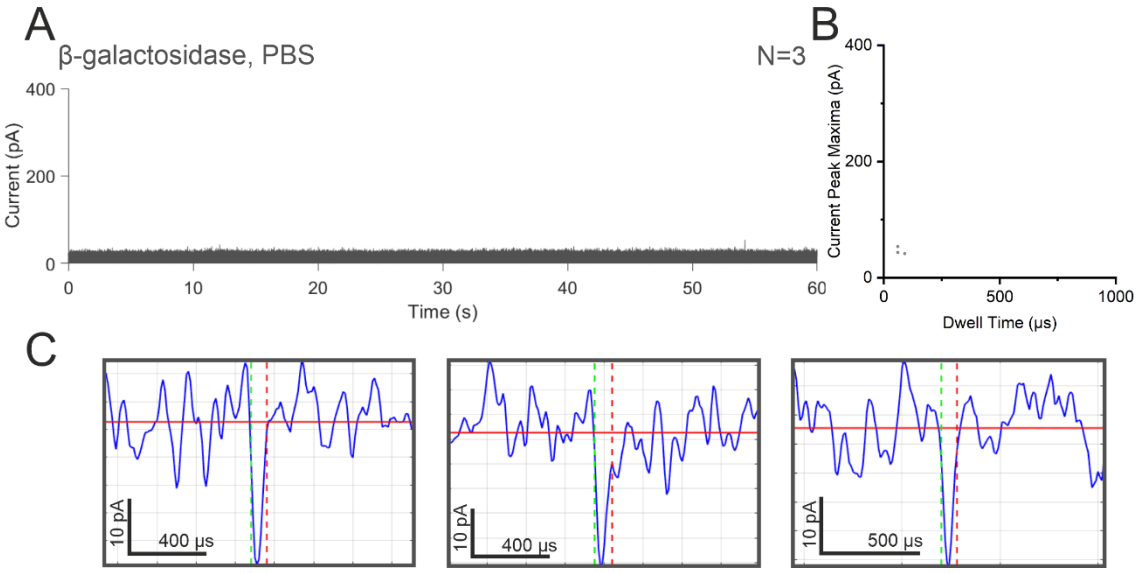

Figure 4.24. The translocation of β-galactosidase into the PBS bath. *1 µM of the β-galactosidase was used to fill the nanopipette and then immersed into the PBS bath. -700 mV voltage was applied in all conditions. On the left is the 60 seconds baseline adjusted current trace of the translocation of the β-galactosidase (A) and the population scatter of the collected translocation events from the associated trace (B). Example translocation signals were shown for each trace which were randomly sampled (C). N refers to the total number of events recorded.*

The detection of β-galactosidase was not improved with the presence of the glycerol even at the highest tested concentration of 50% (v/v). In all cases, the molecule count was 2 ± 1 for 12.5% (v/v), 4 ± 2 for 25% (v/v) and 3 ± 1 for 50% (v/v) glycerol (Figure 4.25, Figure 4.30A, D). No statistical analysis was performed as there were insufficient events recorded.

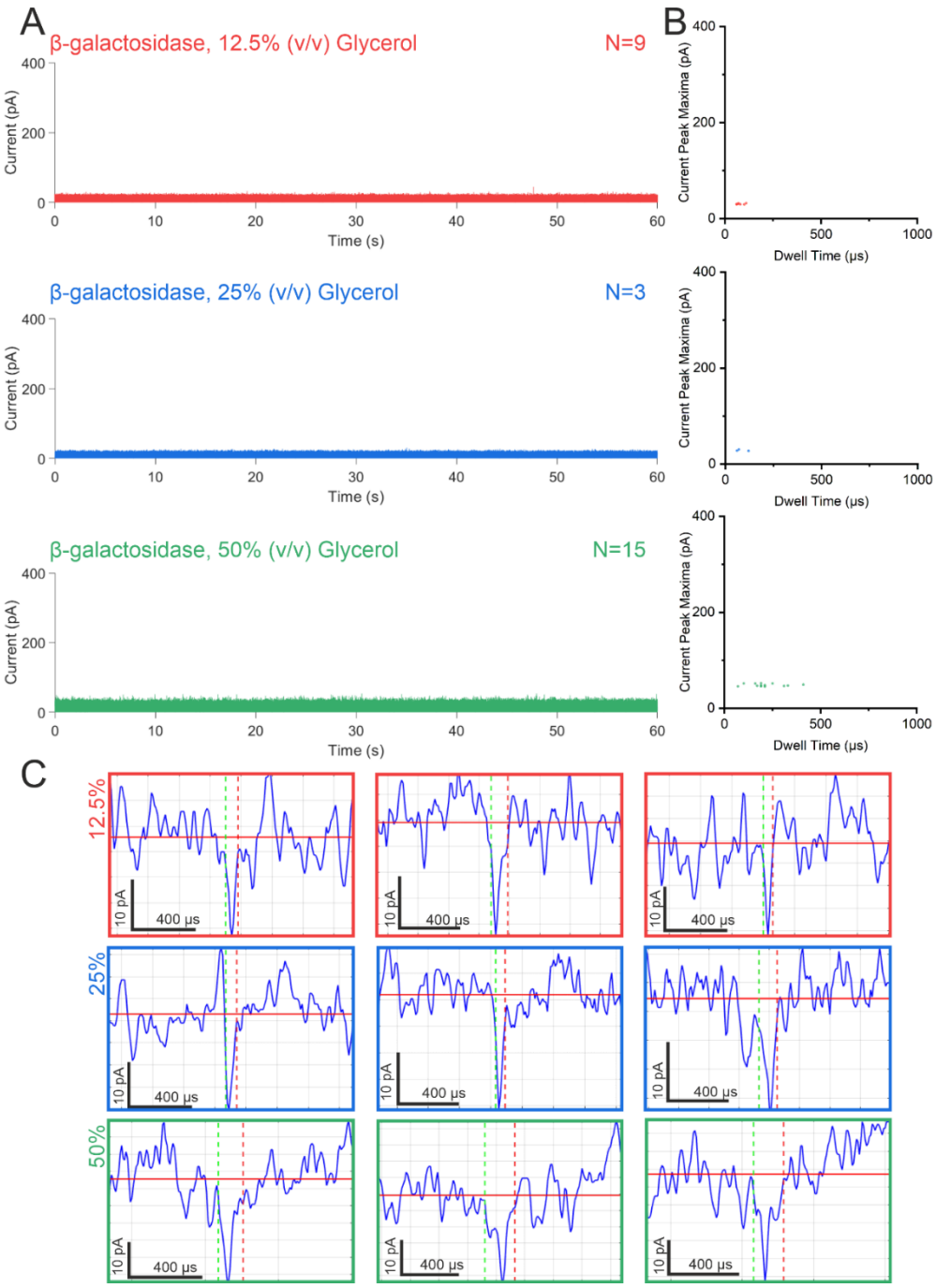

Figure 4.25. The translocation of β-galactosidase in glycerol PBS bath. *1 µM of β-galactosidase was used to fill the nanopipette and then immersed into the PBS bath containing 12.5%, 25% or 50% (v/v) glycerol. -700 mV voltage was applied in all conditions. For each condition, on the left is the 60 seconds baseline adjusted current trace of the translocation of the β-galactosidase (A) and on the right the population scatter of the collected translocation events from the associated trace (B). Example translocation signals were shown for each trace which were randomly sampled (C). N refers to the total number of events recorded.*

Increasing the concentration of the PEG 8000 from 12.5% (w/v) and 25% (w/v) had no significant effect on the molecule count of the translocation of β-galactosidase. However, increasing the concentration to 50% (w/v) significantly increased the molecule count from *c.a.* 10 molecules per 60 seconds into 927 ± 22,

almost a 1000-fold increase in the detection efficiency of the system (Figure 4.26A, Figure 4.30A, D). The average current peak maxima and dwell time for the β-galactosidase in 50% (w/v) PEG 8000 was 70 ± 1 pA and 85 ± 10 µs respectively.

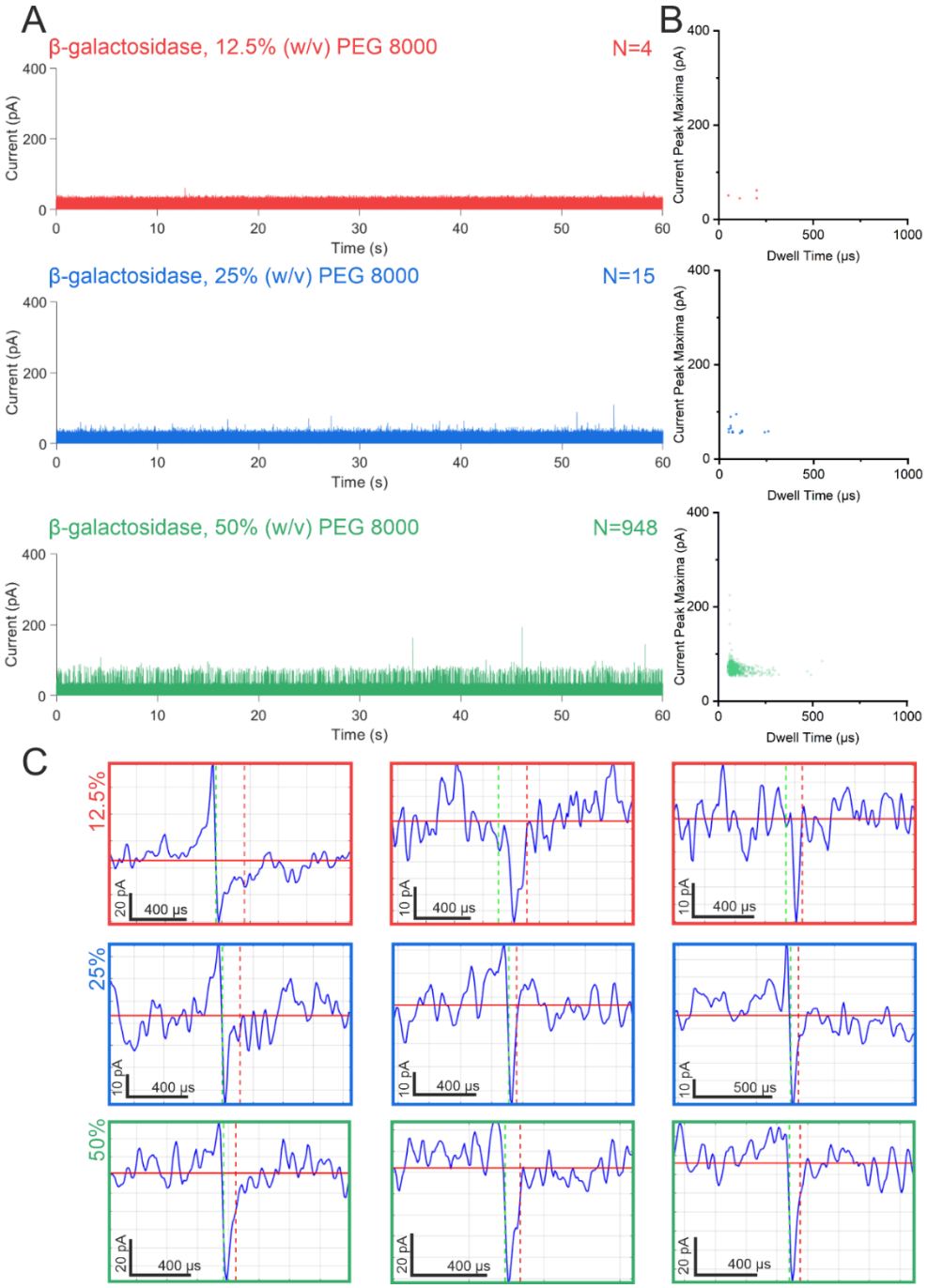

Figure 4.26. The translocation of β-galactosidase in PEG 8000 PBS bath. *1 µM of β-galactosidase was used to fill the nanopipette and then immersed into the PBS bath containing 12.5%, 25% or 50% (w/v) PEG 8000. -700 mV voltage was applied in all conditions. For each condition, on the left is the 60 seconds baseline adjusted current trace of the translocation of the β-galactosidase (A) and on the right the population scatter of the collected translocation events from the associated trace (B). Example translocation signals were shown for each trace which were randomly sampled (C). N refers to the total number of events recorded.*

Since the experimental set-up and the hardware settings were kept the same, higher β-galactosidase molecule translocation count in the 50% (w/v) PEG 8000 PBS bath means that not only the current was enhanced (SNR ratio), but also the translocation of the β-galactosidase have been slowed down, thus the number of translocation signals lost due to hardware settings was reduced (Plesa et al., 2013).

To ensure that the sudden increase of the molecule count at 50% (w/v) PEG 8000 was due to the translocation of β-galactosidase, four nanopipettes were filled with PBS solution and immersed them into the 50% (w/v) PEG 8000 PBS bath (Figure 4.27). No translocation of molecules was detected, which suggested that the nanopipette did not detect the PEG 8000 under this condition.

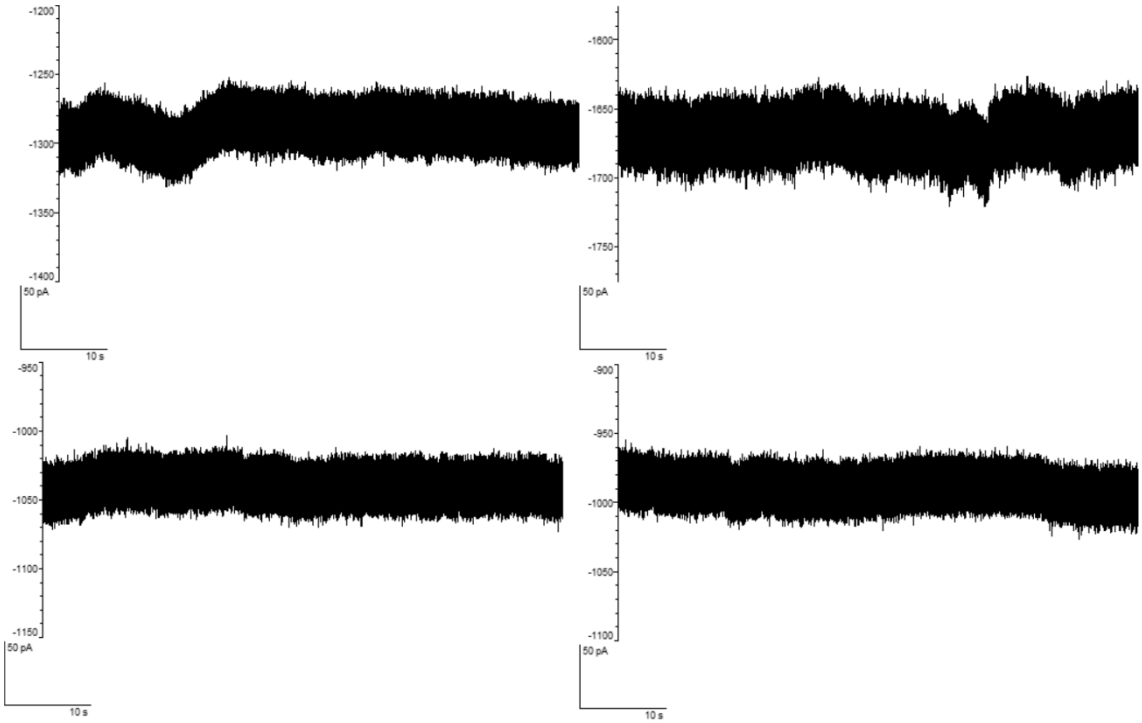

Figure 4.27. PEG 8000 was not detected by the nanopipette. *Nanopipettes were filled with PBS and immersed into the 50% (w/v) PEG 8000 bath with -700 mV potential difference applied. No events peaks were observed throughout the 60 seconds. Each panel shows the current trace from a single nanopipette. Four different nanopipettes were tested.*

Furthermore, different concentrations of β-galactosidase were also tested in the 50% (w/v) PEG 8000 PBS bath, which included the 1 μM, 0.5 μM and 0.1 μM in PBS. This was to determine whether the concentration of the β-galactosidase inside the nanopipette affected the molecule count over 60 seconds duration (Figure 4.28). Indeed, the molecule count reduced when the nanopipette was filled with a lower concentration of β-galactosidase. This suggested that the detection

efficiency of the translocation of the β-galactosidase in the 50% (w/v) PEG 8000 PBS bath was analyte concentration dependent.

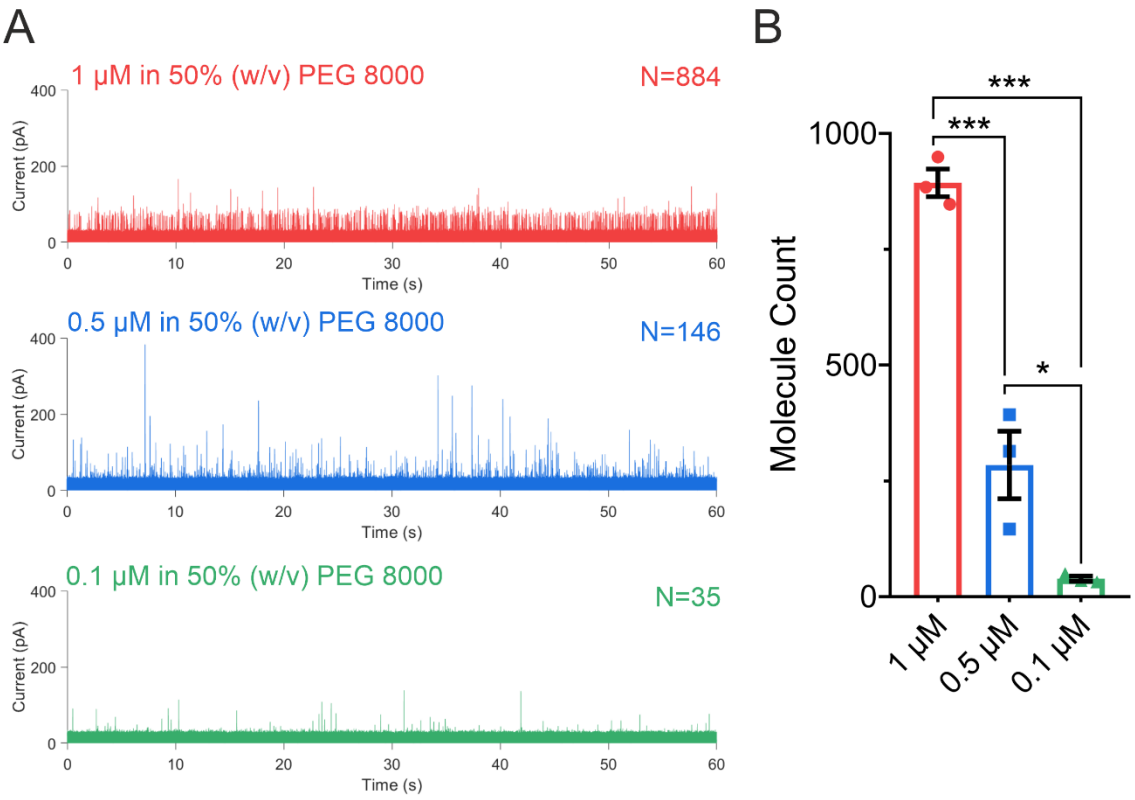

Figure 4.28. The molecule count for β-galactosidase translocation. *Either 1, 0.5 or 0.1 µM of β-galactosidase was used to fill the nanopipette prior to immersion into a 50% (w/v) PEG 8000 bath. A potential difference of -700 mV was used to drive β-galactosidase into the PEG 8000 bath (A). N refers to the total number of events recorded. The number of β-galactosidase events detected was concentration dependent (B). Asterisks indicate P-values (*, P<0.5; ***, P<0.01). Error bars are ± S.E.M. One-way ANOVA test was used for (B).*

Finally, the translocation of the β-galactosidase was tested in the BSA crowded bath. All concentrations of BSA significantly improved the detection of the β-galactosidase compared to PBS. The greatest improvement was at 15% (w/v) at 470 ± 30, then 373 ± 12 for 30% (w/v) and lastly 152 ± 14 for 7.5% (w/v) BSA (Figure 4.29A, Figure 4.30A, D). However, the population scatter obtained for the translocation of β-galactosidase was different for each condition: the population at 7.5% (w/v) spread in both axes a major spread along the dwell time from 100 µs to 500 µs could be identified at 15% (w/v) and a single relatively condensed population could be identified at 30% (w/v) with around 100 pA and under 250 µs (Figure 4.29B). Unlike pMaxGFP translocation in the BSA crowded bath, where the population scatter indicated a single population in all conditions, the translocation of β-galactosidase had more variances in different concentrations of the BSA as

shown in Figure 4.29. The average current peak maxima for the 7.5% (w/v), 15% (w/v) and 30% (w/v) were 129 ± 7 pA, 102 ± 1 pA and 119 ± 2 pA respectively (Figure 4.30B, D). The 15% (w/v) had the longest dwell time at 328 ± 13 μs followed by 30% (w/v) at 274 ± 2 μs and then 244 ± 28 μs for 7.5% (w/v) (Figure 4.30C, D). These differences could be due to the protein-protein interaction in the BSA crowded bath as demonstrated in other studies (Li, C. and Pielak, 2009; Sarkar et al., 2014; Wang, P. et al., 2017).

Overall, for the translocation of β-galactosidase, only the crowded electrolyte bath improved the detection efficiency but not in the environment modified by glycerol. For the chemical crowder PEG 8000, the detection was improved by nearly 1000-fold, but only at the highest tested concentration of 50% (w/v). The protein crowder BSA also improved the detection of the β-galactosidase, and the average current peak maxima and dwell time in all tested concentrations were statistically significantly larger than the 50% (w/v) PEG 8000 PBS bath (Figure 4.30B-D). However, the β-galactosidase event population scatters for different concentrations of BSA were all different and subsequently became less favourable for analyses of a single species molecule compared to the 50% (w/v) PEG 8000 solution.

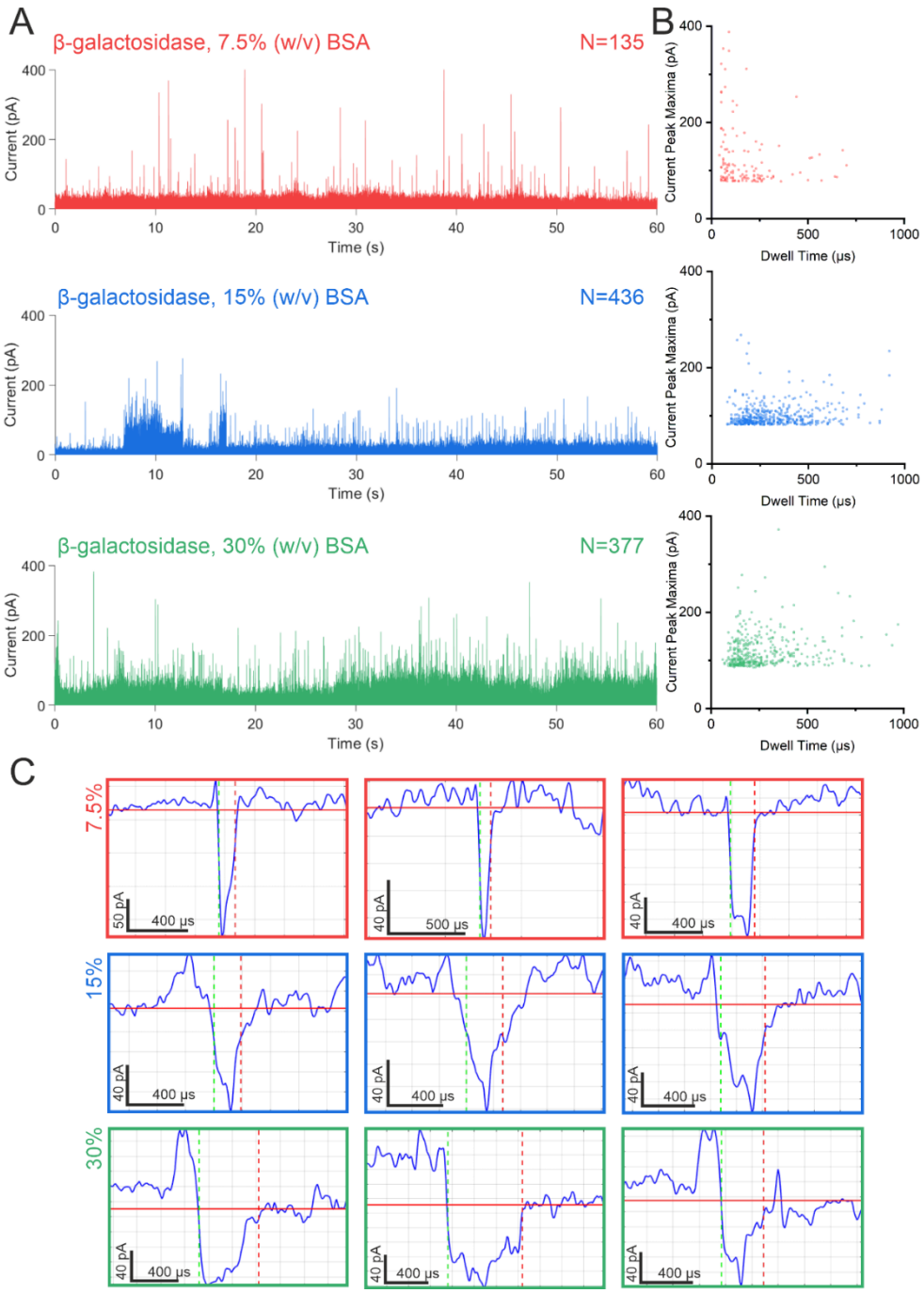

Figure 4.29. The translocation of β-galactosidase in BSA PBS bath. *1 μM of β-galactosidase was used to fill the nanopipette and then immersed into the PBS bath containing 7.5%, 15% or 30% (w/v) BSA. -700 mV voltage was applied in all conditions. For each condition, on the left is the 60 seconds baseline adjusted current trace of the translocation of the β-galactosidase (A) and on the right the population scatter of the collected translocation events from the associated trace (B). Example translocation signals were shown for each trace which were randomly sampled (C). N refers to the total number of events recorded.*

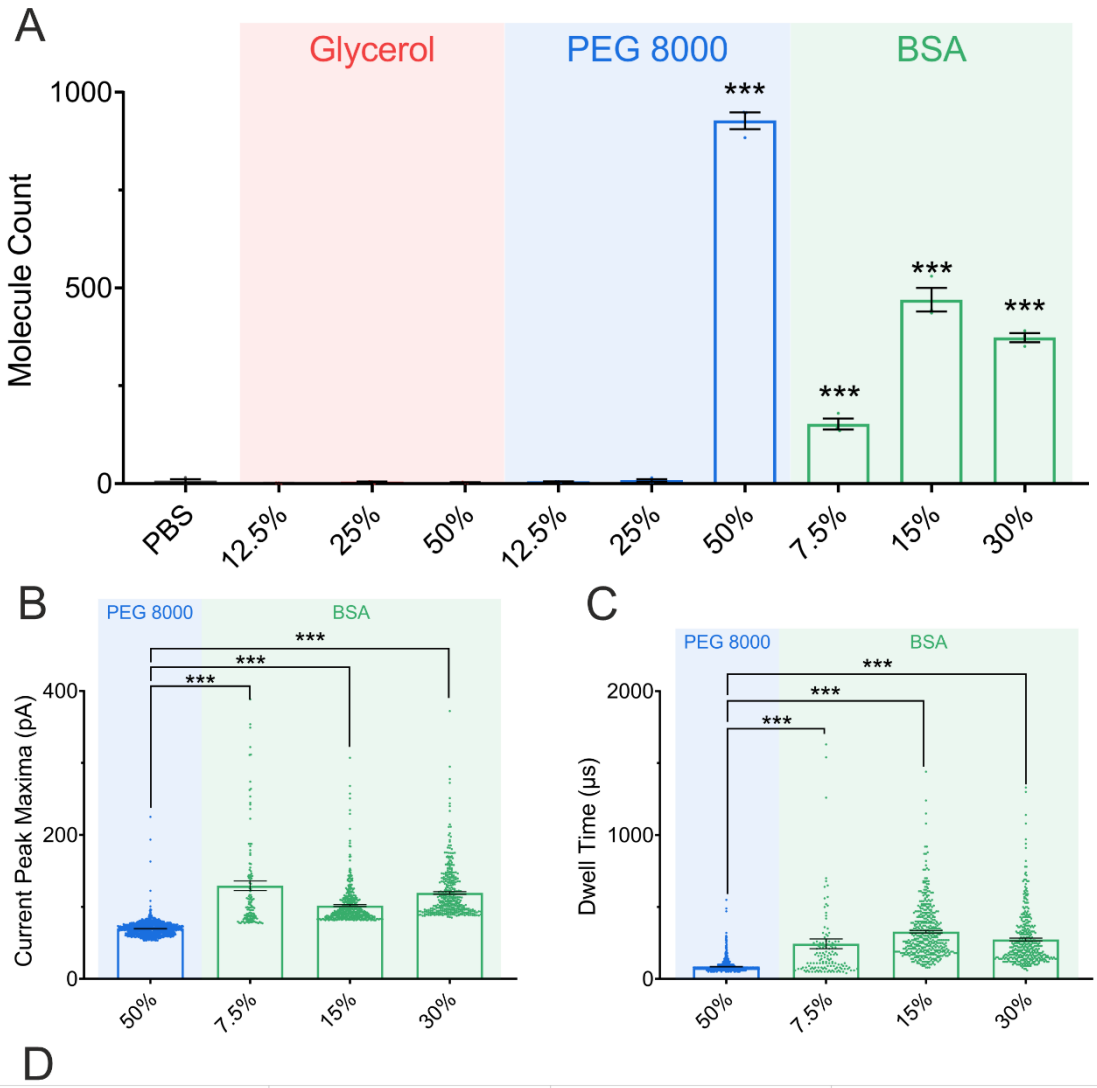

D

Condition	Molecule Count		Current Peak Maxima (pA)		Dwell Time (µs)	
	Mean ± S.E.M.	Median	Mean ± S.E.M.	Median	Mean ± S.E.M.	Median
PBS	7 ± 5	2	N/A#	N/A#	N/A#	N/A#
PBS + 12.5% (v/v) Glycerol	2 ± 1	2	N/A#	N/A#	N/A#	N/A#
PBS + 25% (v/v) Glycerol	4 ± 2	5	N/A#	N/A#	N/A#	N/A#
PBS + 50% (v/v) Glycerol	3 ± 1	3	N/A#	N/A#	N/A#	N/A#
PBS + 12.5% (w/v) PEG 8000	5 ± 1	6	N/A#	N/A#	N/A#	N/A#
PBS + 25% (w/v) PEG 8000	8 ± 3	5	N/A#	N/A#	N/A#	N/A#
PBS + 50% (w/v) PEG 8000	927 ± 22	948	70 ± 1	69	85 ± 10	70
PBS + 7.5% (w/v) BSA	152 ± 14	142	129 ± 7	99	244 ± 30	130
PBS + 15% (w/v) BSA	470 ± 30	444	102 ± 1	93	328 ± 10	270
PBS + 30% (w/v) BSA	373 ± 12	377	119 ± 2	107	274 ± 10	210

#, data not analysed due to suboptimal data collected (<30).

Figure 4.30. The statistical analysis of β-galactosidase in different bath conditions. *(A) The molecule count for β-galactosidase in different bath conditions. Three 60 second traces of each voltage were analysed. The presence of 50% (w/v) PEG 8000 and BSA in the PBS bath resulted in a pronounced increase in molecule count. For (A), asterisks show where the addition of either glycerol, PEG 8000 or BSA resulted in a significant change when compared to PBS alone. The BSA caused a significant increase in both current peak maxima and dwell time when compared to the 50% (w/v) PEG 8000. The data obtained from PBS, glycerol, 12.5% and 25% (w/v) PEG 8000 were not analysed due to suboptimal number of molecules detected (below 30). The 50% (w/v) PEG 8000 has the strongest effect in increasing the molecule count of the β-galactosidase. For (B, C), asterisks show where the addition of BSA resulted in a significant change when compared to 50% (w/v) PEG 8000 (B, C). Asterisks indicate P-values (***, P<0.01). Error bars are ± S.E.M. The data points in bar chart (B) and (C) correspond to individual events from the current traces presented in Figure 4.26 and Figure 4.29. One-way ANOVA test was used for (A), Kruskal-Wallis tests for (B) and (C).*

Different sizes of the crowding polymer alter the excluded volume effects of the solution differently (Knowles et al., 2011). To determine whether the size of the PEG polymer contributes to the enhancement of the current amplitude in pMaxGFP, I used the smaller PEG, a variant that has a molecular weight of 4000 g/mol. PEG 4000 was dissolved in PBS to the concentration of 50% (w/v) to compare with the PEG 8000 at the equivalent concentration. For the translocation of the pMaxGFP, the 1.3 nM DNA plasmid filled nanopipette was immersed into either the 50% (w/v) PEG 4000 or the (w/v) PEG 8000 and -700 mV was applied (Figure 4.31A). There was no statistically significant difference in the molecule count between the PEG 4000 at 1171 ± 46 and the PEG 8000 at 1063 ± 24, but the average current peak maxima for PEG 4000 of 194 ± 2 pA was significantly lower than the PEG 8000 of 586 ± 6 pA (Figure 4.31B, C).

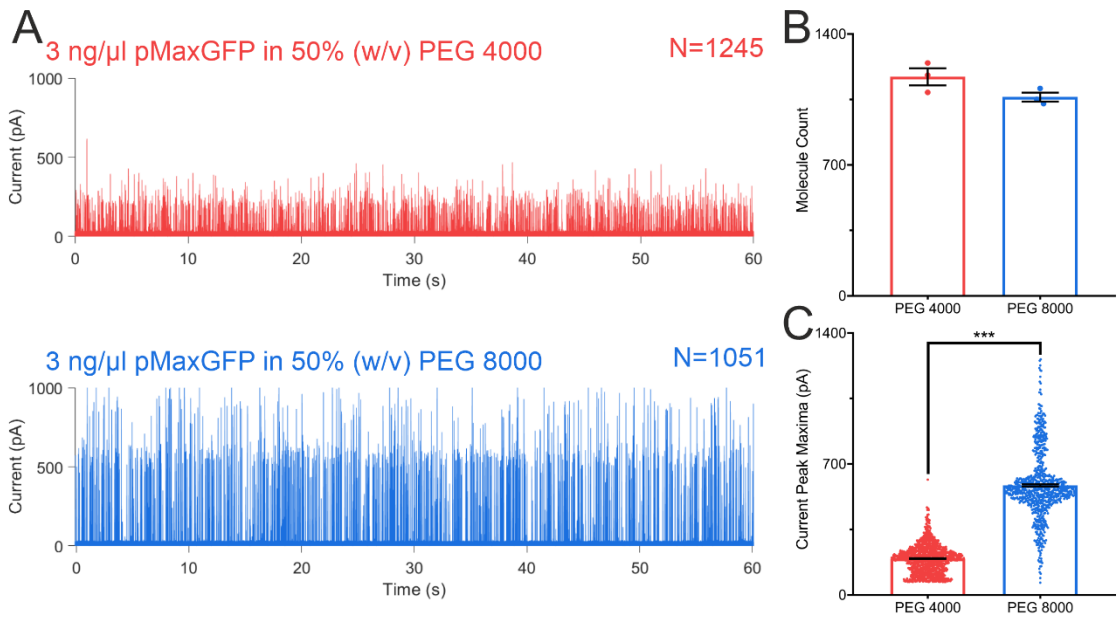

Figure 4.31. The translocation of the pMaxGFP plasmid into either a PEG 4000 or PEG 8000 PBS bath. *1.3 nM of pMaxGFP plasmid was used to fill the nanopipette and then immersed into either a 50% (w/v) PEG 4000 or 50% (w/v) PEG 8000 PBS bath (A). -700 mV voltage was applied in both conditions. Three 60 second traces were used to calculate the molecule count for PEG 4000 and the data-set used for PEG 8000 was the same as 50% (w/v) PEG 8000 from Figure 4.23. There is no significant difference on the molecule count between PEG 4000 and PEG 8000 (B). The current peak maxima in PEG 8000 is significantly larger than PEG 4000 (C). The data points from (C) correspond to the associated trace from (A). N refers to the total number of events recorded. Asterisks indicate P-values (***, P<0.01) Unpaired t-test was used for (B) and a Mann-Whitney test was used for (C).*

Next, to determine whether the PEG 4000 affects the detection efficiency of the β-galactosidase, an experiment was performed in which 1 µM β-galactosidase was used to fill the nanopipette (Figure 4.32A). There was a significantly lower

molecule count for the PEG 4000 (267 ± 63) than PEG 8000 (927 ± 22), and a statistically significant difference on the current peak maxima between PEG 4000 (56 ± 1 pA) and PEG 8000 (66 ± 1 pA) (Figure 4.32B, C). The lower molecule count for the β-galactosidase observed for the PEG 4000 in our system was because the MATLAB script employed a stringent threshold (approximately at 50 pA away from the baseline). Unlike DNA plasmids where their translocation caused a high SNR with or without the addition of PEG, the majority of the translocation events of β-galactosidase were hidden due to the low SNR, and thus the script failed to detect those events. To obtain a better SNR, the current amplitude enhancement by the presence of PEG 8000 at high concentration in the bath electrolyte was essential for the efficient detection of the β-galactosidase.

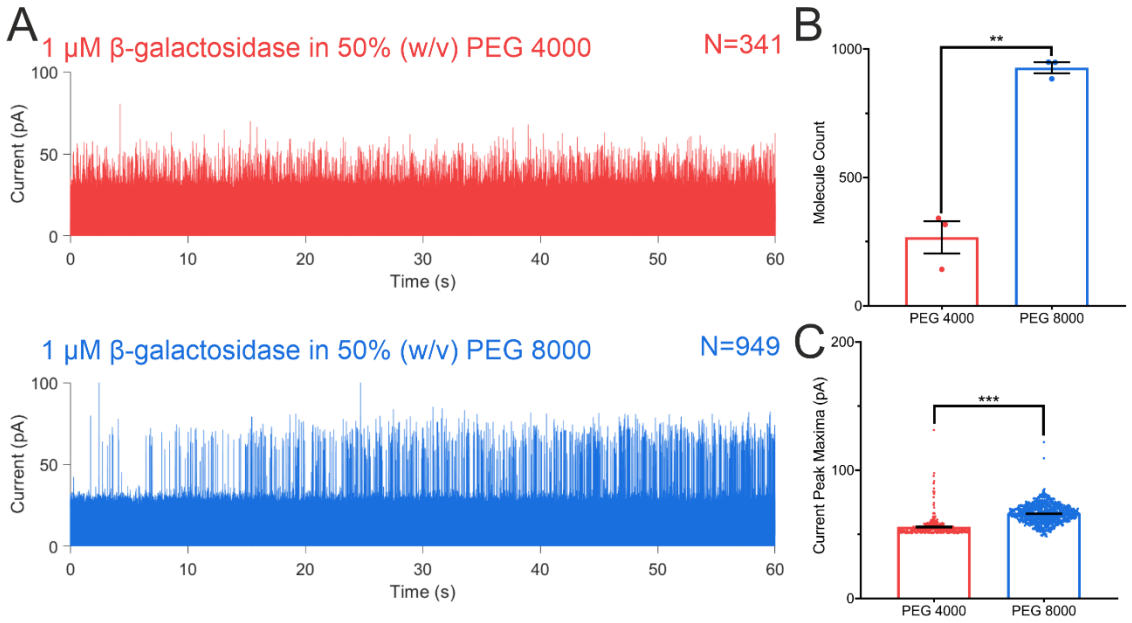

Figure 4.32. The translocation of β-galactosidase into either a PEG 4000 or PEG 8000 PBS bath. *1 µM of β-galactosidase was used to fill the nanopipette and then immersed into either a 50% (w/v) PEG 4000 or 50% (w/v) PEG 8000 PBS bath (A). -700 mV voltage was applied in both conditions. Three 60 seconds traces were used to calculate the molecule count for PEG 4000 and the data-set used for PEG 8000 was the same as 50% (w/v) PEG 8000 from Figure 4.30. The molecule count of β-galactosidase in 50% (w/v) PEG 8000 is significantly higher than in 50% (w/v) PEG 4000 (B). The current peak maxima in PEG 8000 is significantly larger than PEG 4000 (C). The data points from (C) correspond to the associated trace from (A). N refers to the total number of events recorded. Asterisks indicate P-values (**, P<0.1; ***, P<0.01) Unpaired t-test was used for (B) and Mann-Whitney test was used for (C).*

4.3.4 Macromolecular crowding assisted detection

The PEG 8000 polymer at 50% (w/v) in PBS provided the most pronounced enhancement in the current peak amplitude on both the detection of pMaxGFP and β-galactosidase. With the 50% (w/v) PEG 8000 bath, the detection efficiency of the β-galactosidase, a protein that is 465 kDa with a dimension of 18×14×8.7 nm (Bartesaghi et al., 2014), has increased by almost 1000×. Consequently, several more potential applications of using the crowded bath to improve the detection and characterisation of biomolecules were explored.

DNA plasmids exist as circular structures and can be found as either relaxed or supercoiled, and this can be linearized by restriction enzyme digestion (Chandrashekaran, 2004). This is also the case for the pMaxGFP plasmids used here (Figure 4.9). It has been reported that nanopores can distinguish the different topological states of a plasmid and even more complex DNA knots (Fologea et al., 2007; Kumar Sharma et al., 2019). Interestingly, when the circular pMaxGFP plasmids were detected in the 50% (w/v) PEG 8000 PBS bath (Figure 4.19), two populations can be identified in the population scatter, hinting that the crowded bath maybe able to differentiate the topological states of the DNA plasmids.

Either the circular pMaxGFP or the digested pMaxGFP plasmids were used to fill a pair of nanopipette at 1.3 nM in PBS. Then the nanopipette was immersed into either the PBS or the 50% (w/v) PEG 8000 PBS bath and a voltage of -700 mV was used to trigger the translocation. The circular pMaxGFP was measured again to ensure that the difference was not due to nanopore dimension deviation from different pairs of nanopipette.

Differences could be seen for the current amplitudes for the circular and linearized pMaxGFP plasmids in both PBS and PBS with 50% (w/v) PEG 8000, however, there was a more pronounced difference observed in the 50% (w/v) PEG 8000 from the current trace (Figure 4.33 and Figure 4.34). Similar to before in Figure 4.19, under the PEG crowded bath environment, the population scatter of the circular pMaxGFP plasmid showed two populations with one above 750 pA and a second between 500pA to 750 pA. This complex distribution of the population scatter attributed to the presence of both relaxed and supercoiled forms of the pMaxGFP plasmid. In contrast, the population scatter of the linearized pMaxGFP showed a population distribution with the majority of the events located between *c.a.* 300 to

600 pA. Importantly, the population above 750 pA disappeared from the circular pMaxGFP (Figure 4.33B).

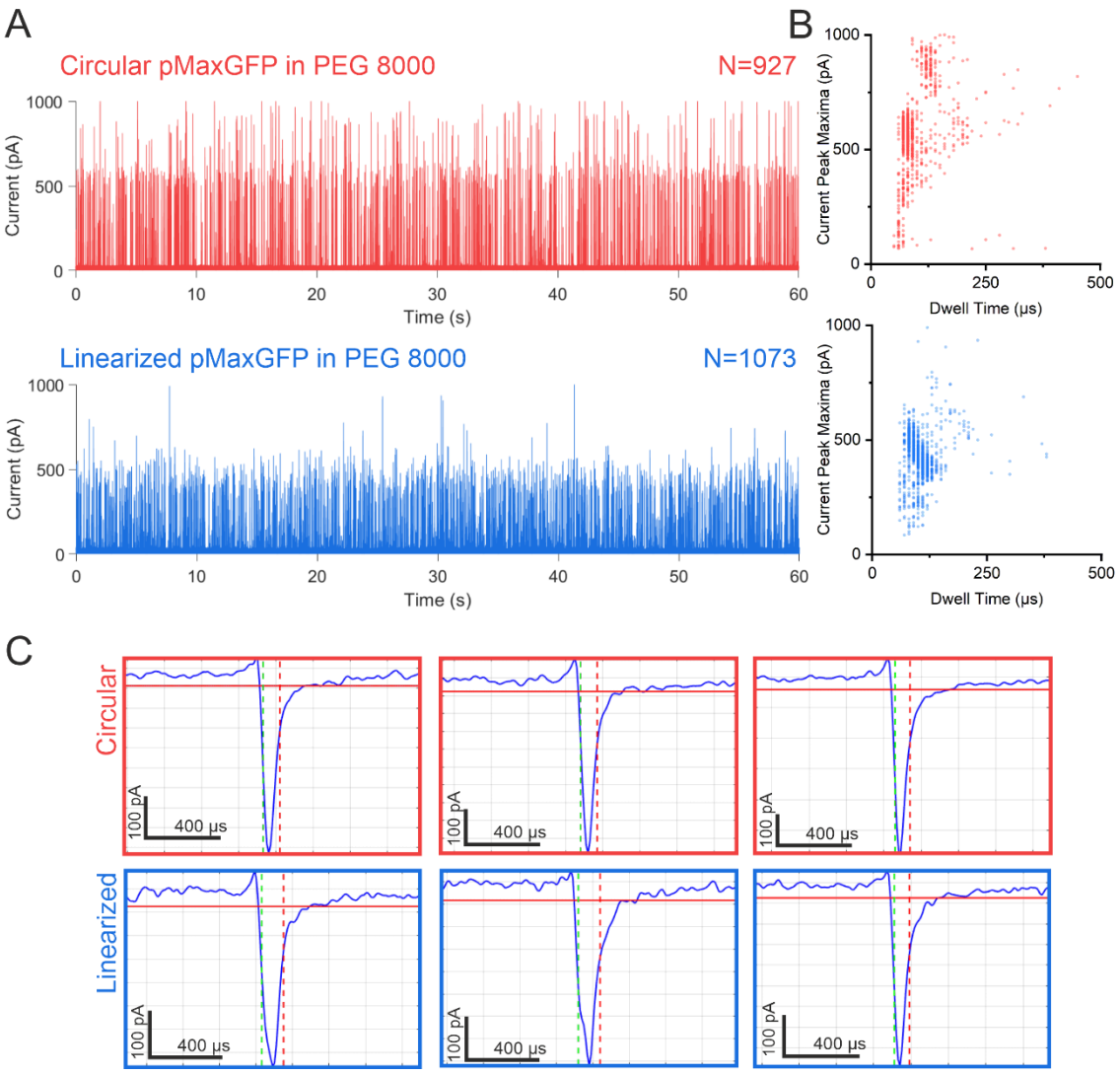

Figure 4.33. Molecular crowding with 50% (w/v) PEG 8000 enables the detection of plasmid DNA topologies. *The baseline adjusted current trace is shown for circular or linearized DNA plasmids in 50% (w/v) PEG 8000 (A) with a scatter plot to show the dwell time as the function of the current peak maxima for each event (B). Example translocation signals were shown for each trace which were randomly sampled (C). Note that only in PEG 8000, the circular DNA has a distinctive population of events with higher peak current maxima than that of linear DNA can be observed. N refers to the total number of events recorded.*

The lack of a second population may reflect that there was only a single topological state after the restriction digestion. The difference between the circular and linearized pMaxGFP was also reflected by their average current peak maxima and dwell time. The circular pMaxGFP plasmid had a statistically significantly larger current amplitude of 544 ± 7 pA and shorter dwell time of 101 ± 10 µs than the linearized pMaxGFP with 287 ± 4 pA and 115 ± 10 µs respectively (Figure 4.35).

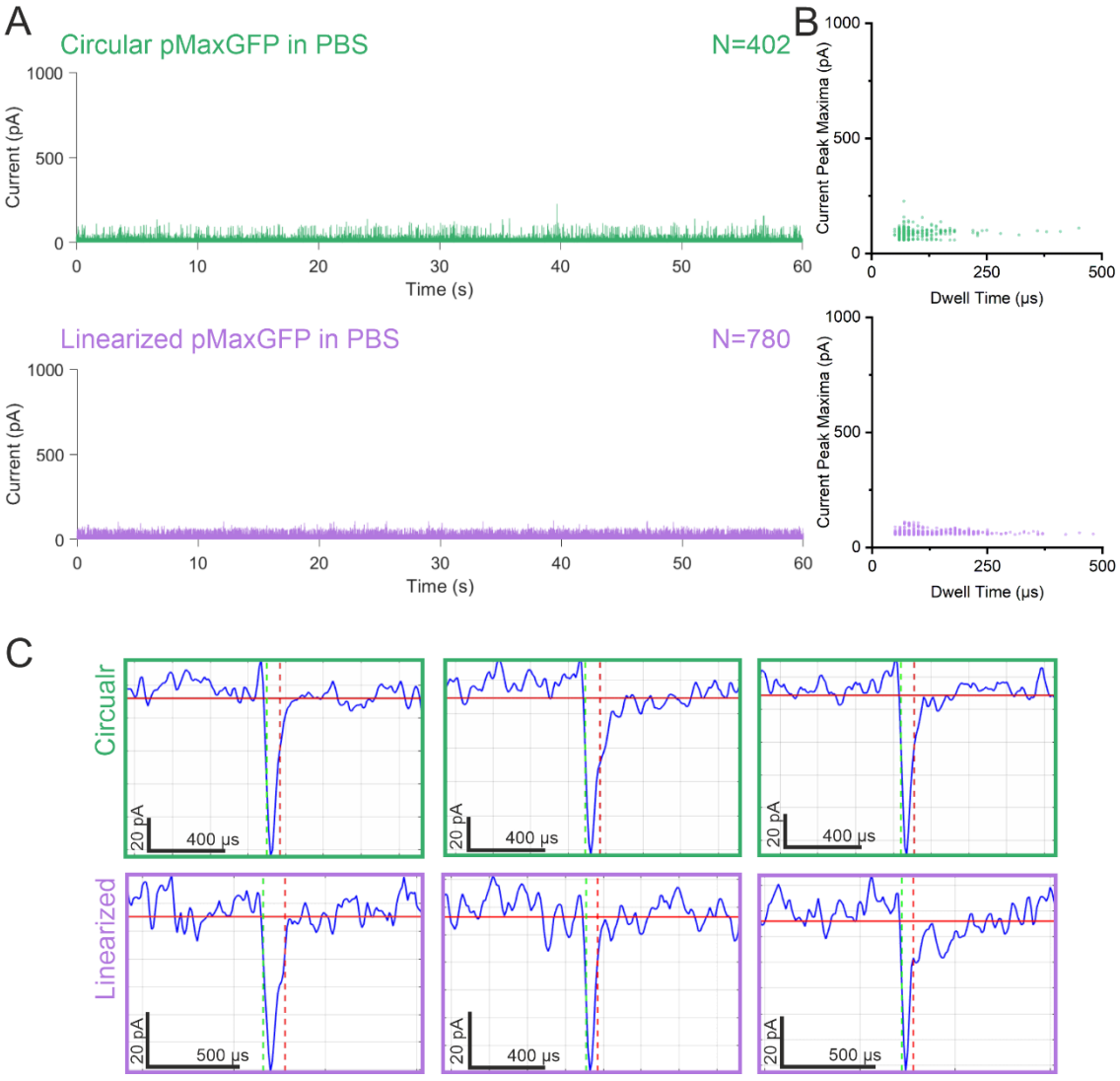

Figure 4.34. The detection of plasmid DNA with different topologies in the PBS bath. *The baseline adjusted current trace is shown for circular or linearized DNA plasmids in PBS bath (A) with a scatter plot to show the dwell time as function of the current peak maxima for each event (B). Example translocation signals were shown for each trace which were randomly sampled (C). N refers to the total number of events recorded.*

On the other hand, both circular and linearized pMaxGFP in the PBS alone produced a single population scatter (Figure 4.34B). Although there was a significantly larger current peak maxima for the circular pMaxGFP plasmid at 89 ± 1 pA compared to linearized counterpart at 63 ± 1 pA, there were no significant differences between their dwell times of 110 ± 13 µs and 108 ± 8 µs respectively (Figure 4.35).

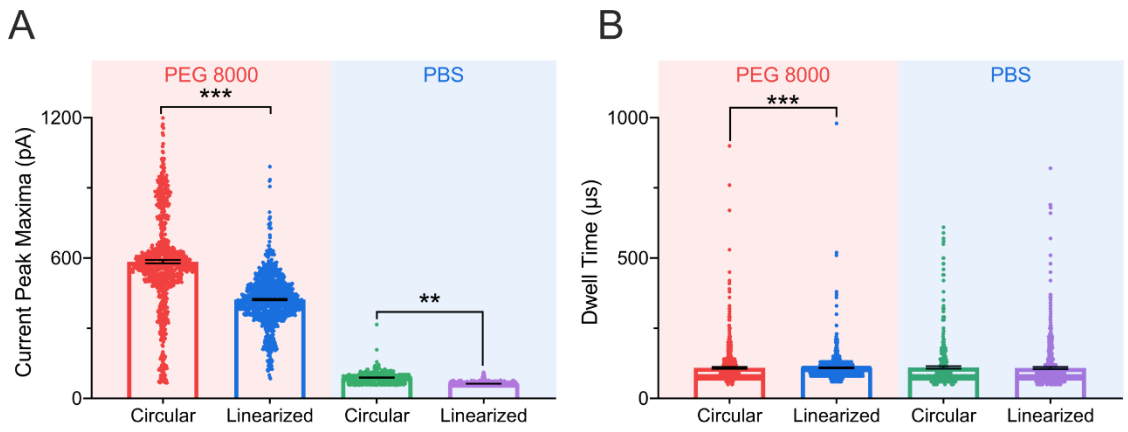

Figure 4.35. Statistical analysis on the translocation events detected for the DNA plasmids in different topological states. *The circular plasmid has a significantly higher average current peak maxima than the linearized plasmid in both PEG 8000 and PBS baths (A). A significantly slower dwell time than the linearized plasmid was recorded when in PEG 8000 (B). The data points in bar chart (A) and (B) correspond to individual events from the current traces in Figure 4.33A and Figure 4.34A. Error bars are ± S.E.M. Asterisks indicate P-values (**, P<0.1; ***, P<0.01). Mann-Whitney test was used for (D) and (E), which tested the difference between the circular and the linearized column in PEG 8000 or PBS subgroup for (D) and (E). The significant of the difference between PEG 8000 and PBS subgroup was not tested.*

To further test whether an even smaller globular protein could be detected with the PEG 8000 crowded bath, the 65 kDa protein BSA was used as the analyte (**not as the electrolyte bath crowder**). The BSA had a dimension of 8.3×5×6.8 nm according to the resolved crystal structure (Majorek et al., 2012). The nanopipette was filled with 1 µM of the BSA in PBS and -700 mV was used to deliver the negatively charged BSA protein into either the PBS or 50% (w/v) PEG 8000 PBS bath. The utilisation of the crowded bath increased the molecule count of the BSA from 10 ± 2 in PBS to 373 ± 27 in the 50% (w/v) PEG 8000 PBS bath (Figure 4.36).

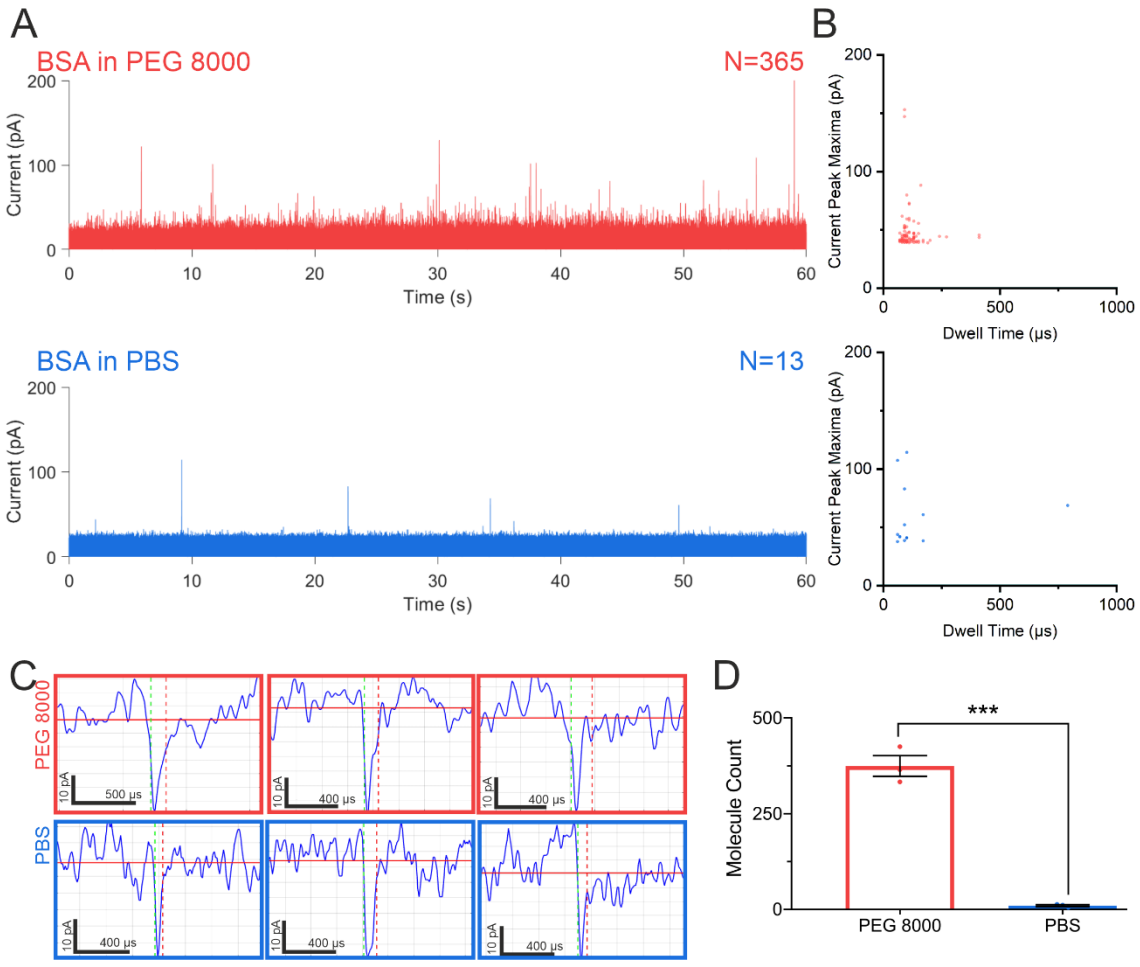

Figure 4.36. BSA can be detected in the 50% (w/v) PEG 8000 PBS bath. *10 µM of BSA was used to fill the nanopipette and then immersed into the PBS bath or PBS containing 50% (w/v) PEG 8000. -700 mV voltage was applied to drive BSA into the bath from the nanopipette. The baseline adjusted current trace is shown for both conditions (A) along with the associated population scatter plot (B). Example translocation signals were shown for each trace which were randomly sampled (C). N refers to the total number of events recorded. Three 60 seconds traces were used to calculate the molecule count. The molecule count for the detection of BSA in 50% (w/v) PEG 8000 is significantly higher than that in PBS (D). No statistical analysis was performed due to the suboptimal number of events that were recorded in PBS (Below 30). Error bars are ± S.E.M. Asterisks indicate P-values (***, P<0.01). Unpaired t test was used for (D).*

Amyloid fibrils are formed when monomeric proteins self-assemble into fibrous protein polymers which have a cross-β molecular architecture (Iadanza, M. G. et al., 2018). The formation of amyloid fibrils and other filamentous proteins has been studied with nanopores, but complex surface modifications of the nanopore are often required to prevent the amyloid fibrils from interacting with the nanopore surface (Yusko, Erik C. et al., 2012; Balme et al., 2016; Giamblanco et al., 2018a). Here, the 50% (w/v) PEG 8000 was tested to investigate whether the utilisation of a crowded bath could improve the detection of amyloid fibrils and by-passing the complex surface modifications, and if varying the length of the amyloid fibrils

would produce a different scatter population distribution similar to the topology differentiation of the DNA plasmids.

To do so, the recombinant human α-synuclein monomer was purified from *E. coli* through multiple steps (Figure 4.37) (The detail processes have been outlined in Chapter 2 Section 2.2.4).

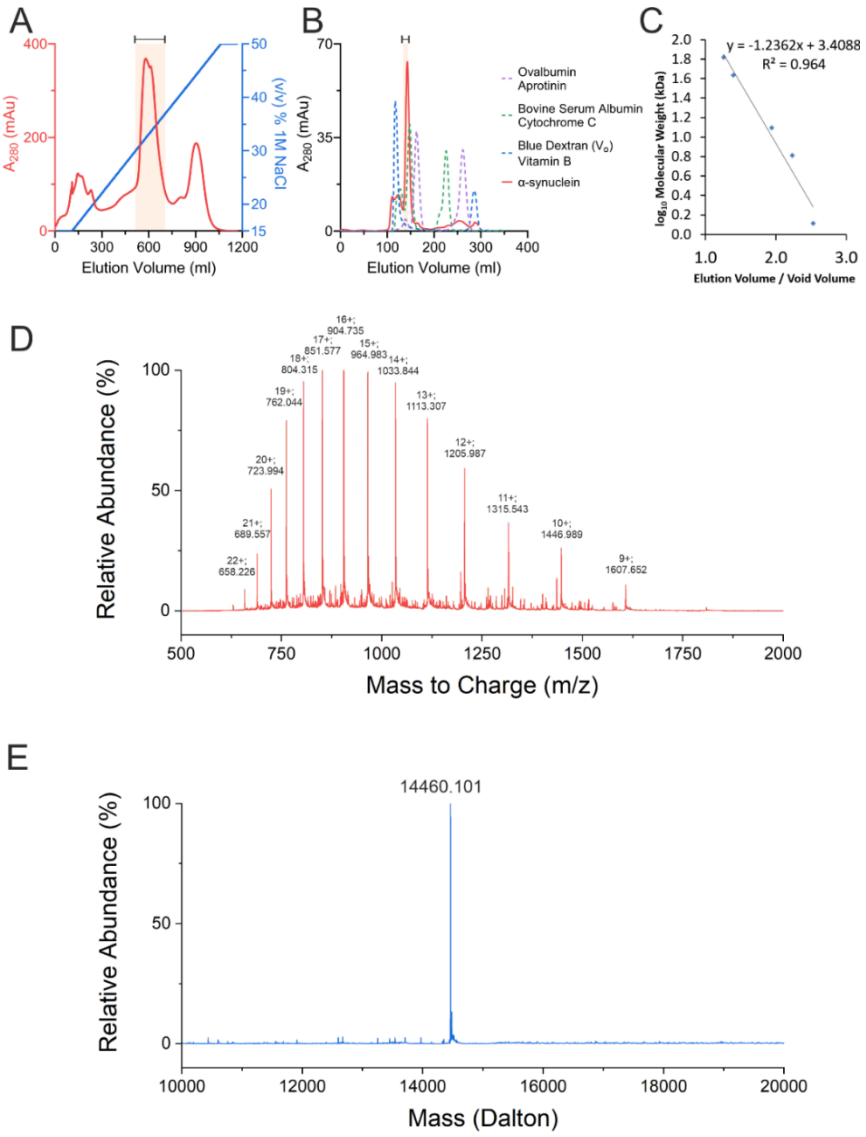

Figure 4.37. Purification and characterisation of the monomeric α-synuclein. *The α-synuclein produced from the E. coli was extracted and purified first using the anion-exchange chromatography (A). 190 ml of the eluate was collected (indicated by the brackets) for further purification using size exclusion chromatography with Supderdex 75 10/300 GL column (B). 10 ml of the eluate from size exclusion chromatography was collected (indicated by the brackets) and lyophilised. The α-synuclein elution profile (red) is overlaid on top of the column calibrants. Using the calibrated curve of the Supderdex 75 10/300 column, the calculated mass of the α-synuclein from the size exclusion chromatography is 65 kDa (Void volume at 116.9 ml) (C). This is potentially due to the increase in hydrodynamic radii of intrinsically disordered proteins during gel filtration as previously shown (Burré et al., 2013). The lyophilised α-synculein was dissolved in PBS and analysis was performed using liquid chromatography electrospray ionisation mass spectrometry. The raw mass to charge (C) and the deconvoluted mass data (D) show that the molecular weight of α-synuclein is 14460 Da, in agreement with the mass of the monomeric α-synuclein.*

The *E. coli* expressed, lysed, and extracted α-synuclein was first purified by anion-exchange chromatography and then further purified by size exclusion chromatography (Figure 4.37A, B, see method chapter for the purification details). The calculated molecular weight of α-synuclein from size exclusion chromatography was to be at 65 kDa indicating a tetrameric structure instead of the monomeric α-synuclein (Figure 4.37C). However, this could be due to the increase in hydrodynamic radii of α-synuclein during gel filtration as previously shown (Burré et al., 2013). The molecular mass of the purified α-synuclein was checked as a monomer of 14,460 Dalton via liquid chromatography electrospray ionisation mass spectrometry (Figure 4.37D, E). The purified monomers were lyophilised for future use. After the production of the α-synuclein monomers, the monomers were used to generate fibril seeds by incubating the monomers at 37°C under constant stirring. These fibril seeds were used to generate the fibrils through elongation reaction by adding monomers to the fibril seeds and incubate at 37°C for 7 days under quiescent conditions (These processes are described in detail in Chapter 2 Section 2.2.6).

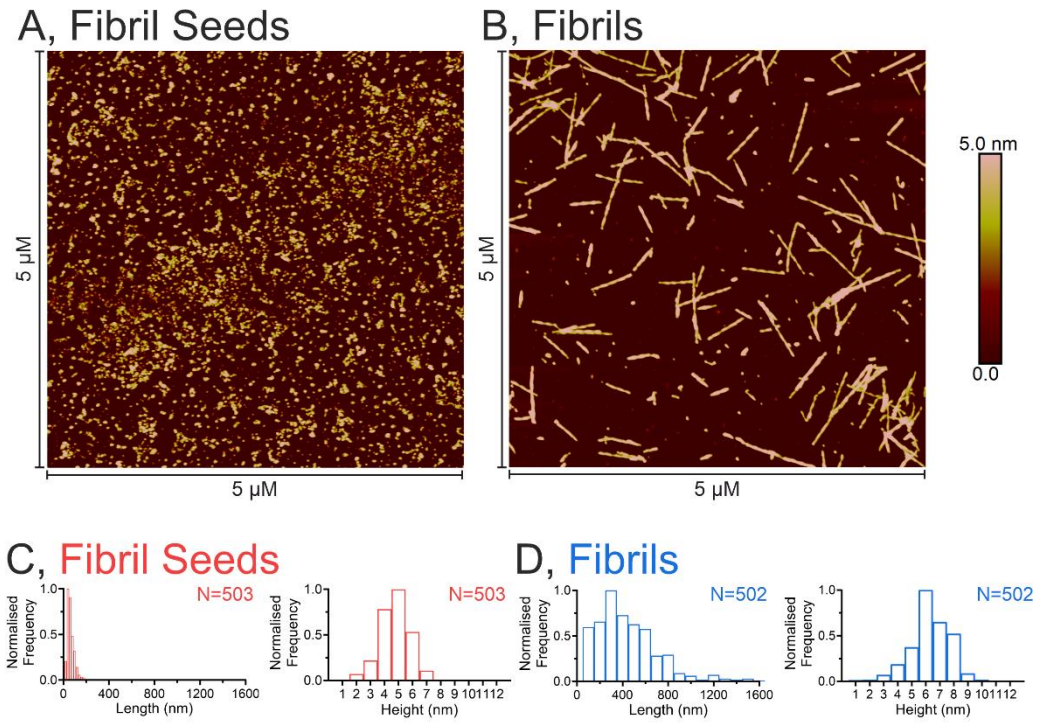

Figure 4.38. Characterisation of the α-synuclein amyloid fibrils. *(A) The representative AFM images of the fibril seeds and fibrils. The fibrils were generated by extending the fibril seeds. The length and height of the fibril seeds (C) and fibrils (D) were measured. The mean length of the fibril seeds was determined to be 66 ± 2 nm with a mode of 40 nm, and a mean height of 5 ± 0.1 nm with a mode of 5 nm. The mean length and height of the fibrils were 442 ± 12 nm with a mode of 300 nm and 6 ± 0.1 nm with mode of 6 nm. N refers to the number of particles traced.*

The height and length distribution of the fibril seeds and fibrils were characterised by atomic force microscopy (AFM) (Figure 4.38A, B). The fibril seeds had a narrow length distribution with a mean length of 66 ± 2 nm and height of 5 ± 0.1 nm. In contrast, the fibrils had a broad length distribution ranging from 100 to 1600 nm with a mean length of 42 ± 12 nm and height of 6 ± 0.1 nm (Figure 4.38C, D).

A nanopipette was filled with a 40 µM monomeric equivalent concentration of either the fibril seed or the fibril, immersed into either the PBS or 50% (w/v) PEG 8000 PBS bath, and -700 mV was used to drive the fibril to the bath.

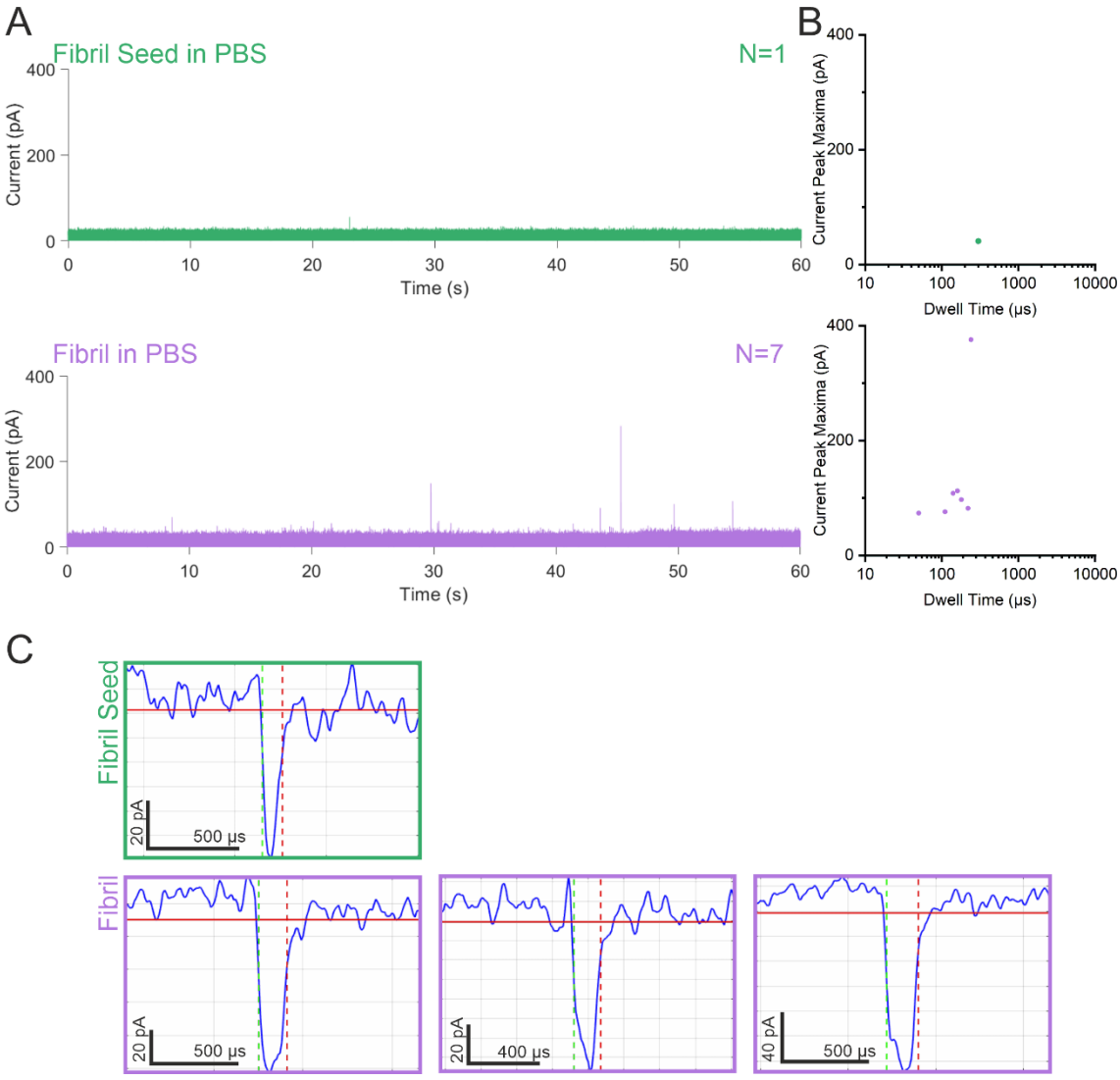

Figure 4.39. The detection of α-synuclein amyloid fibrils in PBS. *The baseline adjusted current trace is shown for the fibril seeds and fibrils in PBS (A) with scatter plots to show the dwell time as a function of the current peak maxima for each event (B). Example translocation signals were shown for each trace which were randomly sampled (C). N refers to the total number of events recorded.*

Although the same monomer concentration had been used to generate the fibril, the particle concentration was not the same between the fibril seed and the fibril

due to the differences in their lengths. The particle concentration could be calculated from the fibril mass per unit length and shown to be 70 kDa per nanometer for the α-synuclein fibril (Iadanza, Matthew G. et al., 2016). By using the average length of the fibrils, the fibril seeds had a 6-fold higher particle concentration at *c.a.* 150 nM compared with the elongated fibril of *c.a.* 25 nM. Similar to what had been observed for β-galactosidase and BSA, both fibril seeds and fibrils were not as readily detectable in the PBS solution with a molecule count of 1 ± 0 and 9 ± 3 respectively (Figure 4.39).

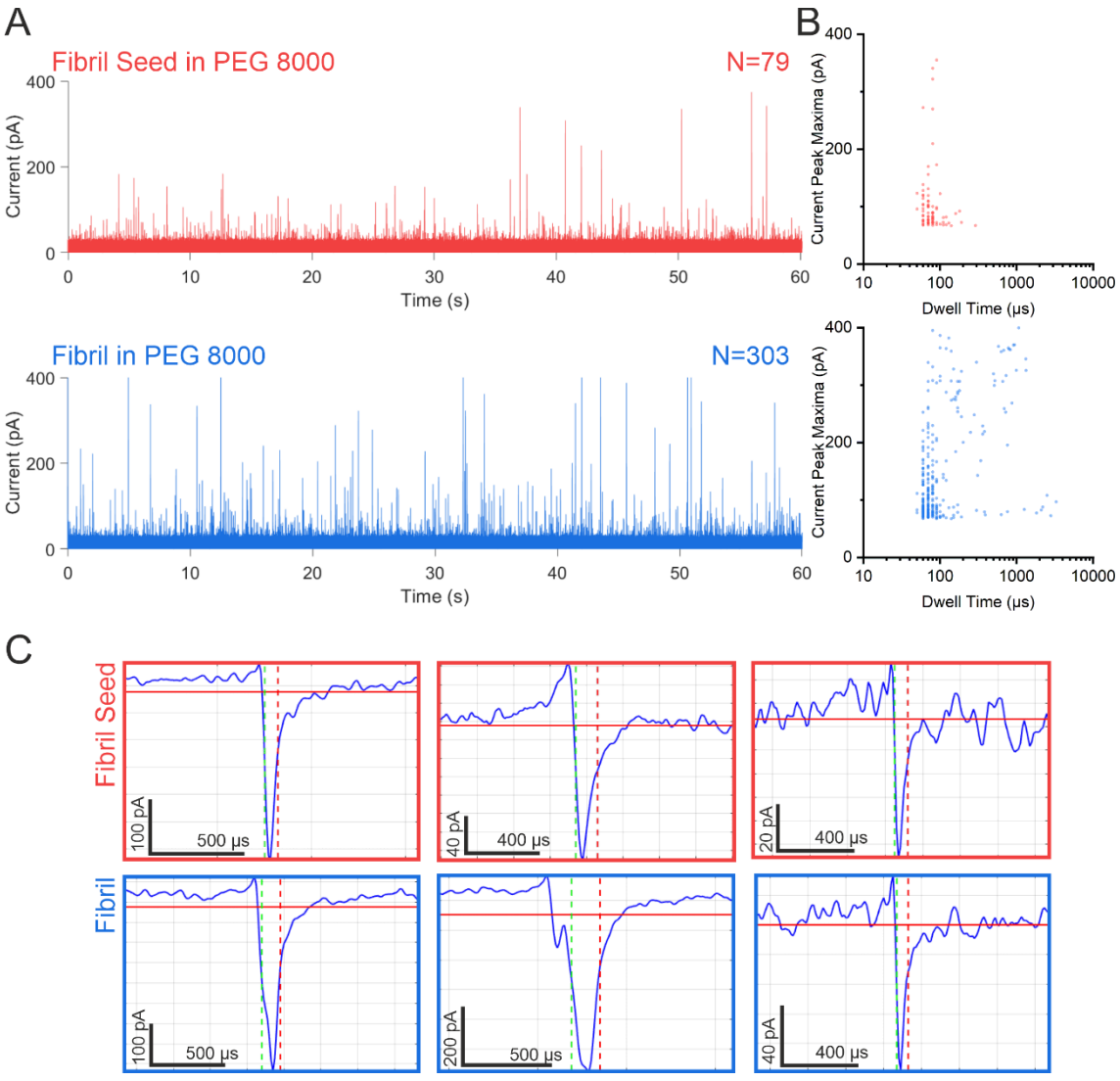

Figure 4.40. Molecular crowding with 50% (w/v) PEG 8000 enhances the detection of α-synuclein amyloid fibrils. *The baseline adjusted current trace is shown for the fibril seeds and fibrils in 50% (w/v) PEG 8000 (A) with scatter plot to show the dwell time as function of the current peak maxima for each event (B). Example translocation signals were shown for each trace which were randomly sampled (C). N refers to the total number of events recorded. Three 60 second traces were used to calculate the molecule count.*

In contrast, the 50% (w/v) PEG 8000 PBS bath enhanced the detection efficiency for the α-synuclein fibril seed and fibril with a molecule count of 101 ± 11 and 422 ± 61 respectively (Figure 4.40).

Although the particle concentration was higher for the fibril seeds, there were less molecule counts. This could be because the fibrils were larger and elicited a larger current amplitude change and longer dwell time, while the fibril seeds were smaller and less readily detected in the PEG crowded bath. The population scatter of the fibril seed and fibril in the 50% (w/v) PEG 8000 showed a different distribution between them. The more homogenous distribution of the fibril seed was potentially due to their narrower length distribution, on the other hand, the broad population distribution of the of the fibril was subsequently due to their heterogeneity in their lengths (Figure 4.39B). The average current peak maxima as well as the dwell time for the fibril seed of 107 ± 7 pA and 83 ± 9 μs were statistically significantly smaller than the fibril of 172 ± 7 pA and 220 ± 22 μs, with the increase in the dwell time reflected by the longer length of the fibril.

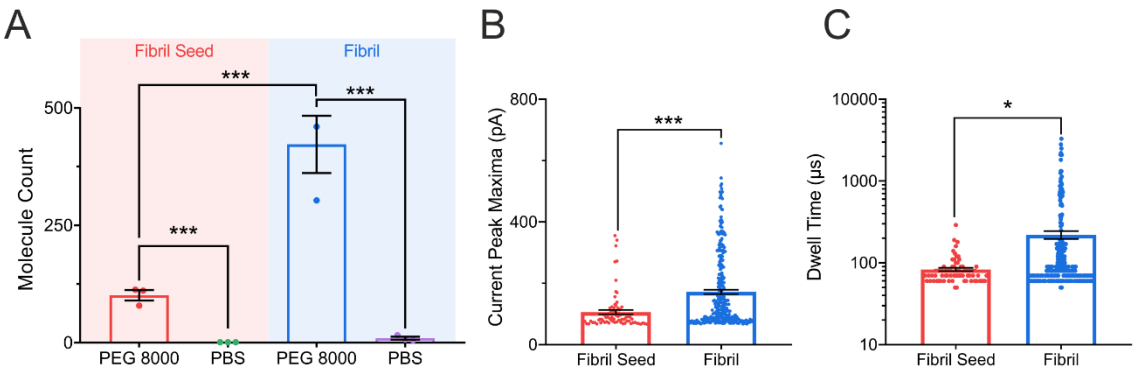

Figure 4.41. Statistical analysis on the translocation effects of PEG crowded bath on fibrils and fibril seeds. *Three 60 second traces were used to calculate the molecule count. PEG 8000 increased the number of events counted for both the fibril seeds and fibrils over that of the fibrils in PBS (A). Moreover, with PEG 8000, the fibrils had a significantly higher current peak maxima (B) and longer dwell time (C) than the fibril seeds. The data points in bar chart (B) and (C) correspond to individual events from Figure 4.39 and Figure 4.40. Error bars are ± S.E.M. Asterisks indicate P-values (*, P<0.5; ***, P<0.01). One-way ANOVA was used for (A), Mann-whitney tests were used for (B) and (C).*

These experiments and data suggest that enhancement brought by the PEG crowded PBS bath is not exclusive to only the detection of DNA plasmids and globular proteins. It also helps the detection of different DNA topology, even smaller globular proteins like the BSA and filamentous proteins such as the α-synuclein fibrils of different length.

4.4 Discussion

4.4.1 Summary and highlights

I demonstrated that the nanopipette single molecule detection system could detect the translocation of DNA plasmids into a PBS bath, but could not detect the protein β-galactosidase (Section 4.3.2). However, the addition of high molecular weight crowders, such as high molecular weight PEG 8000 and BSA at high concentrations into the electrolyte bath enhanced the sensitivity of the nanopipette for single molecule detection of both DNA and proteins. In addition, increasing the percentage of the PEG 8000 and BSA in the electrolyte bath resulted in a corresponding increase in the current amplitude for DNA, with the most pronounced increase observed at high concentration (50% (w/v)) of PEG 8000. Furthermore, PEG 8000 at 50% (w/v), but not 50% (w/v) PEG 4000, improved the detection efficiency for the protein β-galactosidase, by enhancing the SNR (Section 4.3.3). The improved detection efficiency achieved with PEG 8000 aided the characterization of the topology states of DNA plasmids and of α-synuclein fibrils of different lengths.

4.4.2 Signal enhancement and macromolecular crowding

The addition of the macromolecular crowder – PEG at high concentration enhances the detection of plasmids and proteins. The use of PEG to induce macromolecular crowding to enhance the detection of the translocation of the ssDNA has been shown before (Yao et al., 2020). In that study, ssDNA was mixed with up to 40% of PEG 4000 (determined to be the most effective size in that study) and ssDNA was driven towards the biological α-HL nanopore into the PEG-free electrolyte chamber. In contrast, here I used solid-state quartz nanopore to deliver DNA plasmid and proteins into the highly crowded bath electrolyte created by PEG 8000 at 50% (w/v). Although we both only formed a crowded bath on one side of the nanopore, in my system the DNA plasmids were delivered towards instead of away from the crowded bath.

A key difference between the studies, was that here a glass nanopipette with a diameter of <30 nm was used, while the α-HL nanopore used by Yao *et al.* has a diameter of 2.6 nm, according to the crystal structure of α-HL (Song et al., 1996;

Yao et al., 2020). The hydrodynamic radius of PEG molecules can be estimated by using the formula $R_{hyd} = 0.0145 \times M_{w,\,PEG}^{0.57}$, where R_{hyd} is the hydrodynamic radius in nm, $M_{W,\,PEG}$ is the molecular weight of the PEG in g/mol and subsequently the diameter of the molecule (Linegar et al., 2010). For the α-HL nanopore, a smaller PEG with a molecular weight below 1000 g/mol can access the nanopore, and subsequently affects the overall conductivity of the pore as it further reduces the size of the biological nanopore (Stojilkovic et al., 2003; Reiner et al., 2010; Balijepalli et al., 2013; Aksoyoglu et al., 2016). The calculated diameter of PEG 200, PEG 1000, PEG 4000 and PEG 8000 are 0.6 nm, 1.5 nm, 3.3 nm and 4.9 nm respectively and can all pass through a <30 nm wide nanopore by diffusion. In contrast, only the PEG 1000 and smaller can access inside of the α-HL nanopore, the PEG 4000 and 8000 will be physically excluded from the nanopore (Aksoyoglu et al., 2016; Yao et al., 2020). This core difference subsequently suggests a different underlying mechanism to the improvement in single molecule detection observed in my system.

Yao *et al.* utilised an entropy driven model to explain the observed improvement in the detected event translocation frequency where the PEG 4000 (and higher molecular weight PEGs) induced excluded volume effects, which generated a greater effective attraction force between the ssDNA and the α-HL nanopore. This enhancement was not observed when lower molecular weight PEGs such as PEG 200 were used, which are small enough to access the inside of a α-HL nanopore (Yao et al., 2020). However, this model may not apply to the system developed in this thesis, because it is delivering the biomolecules from the uncrowded environment to a crowded environment. As such the interaction between the nanopore and the biomolecule should not be affected by the existence of PEG outside the nanopore. Furthermore, PEG 8000 is small enough to diffuse into the nanopipette used here, yet the detection efficiencies for DNA and protein are enhanced, this is in direct contrast to the observations made by Yao *et al.* that the enhancement occurs only when PEG is unable to get into the pore (Yao et al., 2020). This suggests that the entropy model cannot completely explain the observations in this thesis, suggesting that there is another mechanism at play.

In future work, to test experimentally the entropy driven model, a narrower nanopipette of <10 nm diameter could be fabricated (Navikas et al., 2020; Shigyou et al., 2020), and PEG with a molecular weight of ≥ 35,000 could be used to

generate the PEG crowded PBS bath. The calculated hydrodynamic diameter of the 35,000 PEG would be around 11.2 nm which should not be able to enter the <10 nm nanopipette. Additionally, the PEG size dependent signal enhancement observed for the translocation of β-galactosidase and DNA plasmids indicates that the current amplitude can be further enhanced by using a higher molecular weight PEG, which also increases the excluded volume effects (Knowles et al., 2011; Ziębacz et al., 2011).

4.4.3 PEG and polymer electrolyte

The generation of the PEG crowded bath requires the addition of PEG at high concentration to the 1× PBS. The effect of PEG crowded bath was shown to be concentration dependent, with 50% (w/v) showing the greatest enhancement for the detection of DNA plasmids and of globular and filamentous proteins. Coincidentally, the mixing of PEG at high concentration with electrolyte is the first step in the generation of the polymer electrolyte in the battery related research field (Li, Xiaowei et al., 2019; Zhou, D. et al., 2019; Foran et al., 2020; Ding et al., 2021).

The concept of polymer electrolyte dates back to 1973 when Fenton *et al.* first mixed alkali metal salts with PEG in methanol, then followed by the evaporation of the methanol to create a low conductivity PEG-salt mixture (Fenton et al., 1973). Later, studies demonstrated that the ternary PEG-salt-water polymer electrolyte mixture would further improve its conductivity (Tanzella et al., 1981; Hashmi, 1998; Foran et al., 2020). It has been shown that the addition of PEG to electrolyte such as 0.1 M KCl, regardless of the PEG size, lowers the conductivity of the solution from *c.a.* 12 mS/cm at 0% PEG down to 3 mS/cm at 33% PEG (Stojilkovic et al., 2003). The mechanism behind the reduction in the conductivity is commonly accepted to be due to the chelation of cations by the PEG chains in the mixture, the chelation of the cations in the solution hindered the mobilities of the cations and consequently reduced the conductivity of the solution. This mechanism is further supported by molecular dynamic (MD) simulations (Tasaki, Kenzabu, 1996; Tasaki, K., 1999; Ohki et al., 2007; Tao and Cummings, 2007; Ren et al., 2011; Zhang, Z. et al., 2015; Poudel et al., 2017).

The experimental system developed in this thesis of PEG crowded electrolyte shares the same fundamentals properties as the ternary PEG-salt-water polymer electrolyte mixture, although 1× PBS is not a typical choice for the generation of polymer electrolyte, it is nonetheless an electrolyte. The 1× PBS used in this thesis contains 137 mM of NaCl, 3 mM KCl, 8 mM Na_2HPO_4 and 1.5 mM KH_2PO_4, thus the main species of cation is the Na^+ cation, and Na^+ cation has shown to be chelated by the PEG chain via MD simulations (Zhang, Z. et al., 2015). In this study, Zhang *et al*. generated a MD model that is based on a mixture of 1.1 M LiCl 50% PEG 20000 electrolyte mixture, this composition is similar to the PEG crowded PBS bath. The simulation showed that Na^+ and K^+ cations are both chelated by the PEG chain, but Li^+ cation is not chelated, *i.e.* Na^+ and K^+ interact with the PEG chain but not for Li^+ (Zhang, Z. et al., 2015). Indeed, by studying the translocation behaviour of PEG molecules through the α-HL biological nanopore in different electrolyte baths including LiCl, NaCl and KCl, studies have shown that the PEG is neutral and has no net charge when LiCl is used, but polycation-like when NaCl or KCl is used as the electrolyte (Breton et al., 2013; Machado et al., 2016).

The interactions between the cation and the PEG chain should be investigated in future work. As the PEG crowded bath is relatively easy to generate, a range of different alkali metal halides can be tested, including the LiCl, KCl, NaCl. The LiCl containing PEG crowded bath is of particular interest, firstly, the Li^+ cation's relatively free to move property inside the PEG polymer electrolyte mixture; and secondly LiCl significantly slows down the translocation speed of DNA in translocation experiments with solid-state nanopores (Kowalczyk et al., 2012). This is due to the Li^+ cations having a higher affinity towards dsDNA and they can effectively shield the charge of the DNA (Gebala et al., 2015; Gebala et al., 2016). Thus, the translocation dynamics of a biomolecule into a LiCl PEG crowded bath could also be different from those observed in a PBS crowded bath. Additionally, the modified mobilities of cations should alter the nanofluidics properties of a conical nanopore, as demonstrated by the modified current-voltage profile (White, H.S. and Bund, 2008; Yusko, Erik C. et al., 2009; Luo et al., 2012; Perera et al., 2015; Lan et al., 2016; Rabinowitz et al., 2019). The nanofluidic properties should also be studied in the future as this inevitably affects the single molecule translocation signal (Chen, K. et al., 2017).

4.4.4 Probing the formation of amyloid aggregates

In this chapter, I showed that the PEG crowded PBS bath can detect and potentially discriminate between α-synuclein fibrils of different lengths diluted in PBS. This could be explored further, by calibrating the system with fibrils of different lengths with the PEG crowded PBS bath, it would produce a fibril length standard curve similar to the column calibrants of size-exclusion chromatography. This standard curve could then be used to determine the lengths of α-synuclein fibrils without the need for electron microscopy or AFM imaging. Furthermore, the process of the aggregation of α-synuclein into amyloid aggregates could also be studied using this approach.

The nanopore is an ideal tool to study the aggregation process of amyloid proteins, because both amyloid aggregation reaction and nanopore detection are carried out inside electrolyte. The process of aggregation generates aggregates of different sizes, these aggregates could be simultaneously monitored and discriminated by the nanopore over the course of multiple days. The aggregation of different amyloid proteins has been studied with solid-state nanopores over the course of hours to days (Yusko, Erik C. et al., 2012; Martyushenko et al., 2015; Balme et al., 2016; Hu, R. et al., 2016; Giamblanco et al., 2018a; Houghtaling, J. et al., 2018; Li, Xiaoqing et al., 2019; Giamblanco et al., 2020a; Giamblanco et al., 2020b). Whilst these studies demonstrated the formation of different sizes of aggregates, they were carried out in electrolytes containing high concentrations (0.5 M to 2 M) of salts, the salt concentration is higher than the physiological relevant buffer like the 1×PBS. The salt concentration inside the electrolyte is an important parameter, as various studies have shown that differences in the solution ionic strengths led to the formation of structurally different amyloid aggregates as well as modification in the aggregation kinetics (Sicorello et al., 2009; Morel et al., 2010; Goto et al., 2017; Roeters et al., 2017; Adachi et al., 2018; Flynn et al., 2018; de Oliveira and Silva, 2019).

Using the PEG crowded PBS bath, the aggregation process could be carried out under physiological conditions in the nanopipette while simultaneously collecting data on the size of the aggregates over time. This approach would be an excellent complement to other techniques that study the kinetic of amyloid fibrils, such as the thioflavin-T amyloid fibril kinetic assay (Meisl et al., 2018; Michaels et al., 2018; Törnquist et al., 2018). However, the rate of the assembly could be different

in a plate versus the nanopipette which is a confined space. Additionally, the PEG molecule itself is also an anti-fouling agent and it is often used to coat the nanopore to prevent materials from clogging or absorb into the nanopore wall (Balme et al., 2016; Giamblanco et al., 2018a; Giamblanco et al., 2018b; Giamblanco et al., 2020a; Giamblanco et al., 2020b; Ma, T. et al., 2021), this anti-fouling property will also aid the characterisation of the amyloid aggregation process.

Thesis Conclusions

This thesis contains two main themes: the development of a quantitative nanoinjection platform for the delivery of biomolecules into cells (Chapter 3) and the use of macromolecular crowding to enhance the detection of biomolecules translocating through the nanopipette's nanopore (Chapter 4) (Figure 4.42).

In Chapter 3, different biomolecules including DNA plasmids, the enzyme β-galactosidase and fluorescently labelled α-synuclein fibrils were quantitatively nanoinjected into different cells including primary neurons, and subsequently showed that the concept of quantitative nanoinjection can be realised, and this intracellular delivery method does not interfere the cell viability and the structure of the nanoinjected biomolecules. During the nanoinjection, I observed that the translocation signals were enhanced during the delivery, and this could be because the intracellular environment is highly crowded, and this crowded environment modifies the translocation signals.

In Chapter 4, the macromolecular crowded environment was further studied by adding high concentration of PEG or BSA into a PBS electrolyte bath to mimic the intracellular environment. Single molecule translocation experiments were performed inside these baths and I showed that the addition of PEG and BSA to the PBS bath both enhanced the translocation signals of the DNA plasmids and the protein β-galactosidase. Further experiments showed multiple applications of the PEG crowded bath, such as the detection of α-synuclein fibrils of different length and the analysis of DNA plasmid topology.

The alteration of the translocation events characteristics when carried out inside the macromolecular crowded bath indicated that the electrolyte bath condition is an important factor for the nanopipette, this observation hinted that the intracellular space could affect the characteristics of the events in similar manner. However, the PEG or BSA macromolecular crowded PBS bath is a static mimic of an extremely dynamic intracellular space, additional factors should be considered such as viscosity and the mobility of ions in order to further understand the mechanism of signal enhancement. Furthermore, the intracellular space is heterogeneously crowded with different proteins and organelles (Ellis, 2001; Mittal et al., 2015; Gnutt and Ebbinghaus, 2016; Rivas and Minton, 2016), thus it

would be of interest to study a heterogeneously crowded mimic of the intracellular environment in the future.

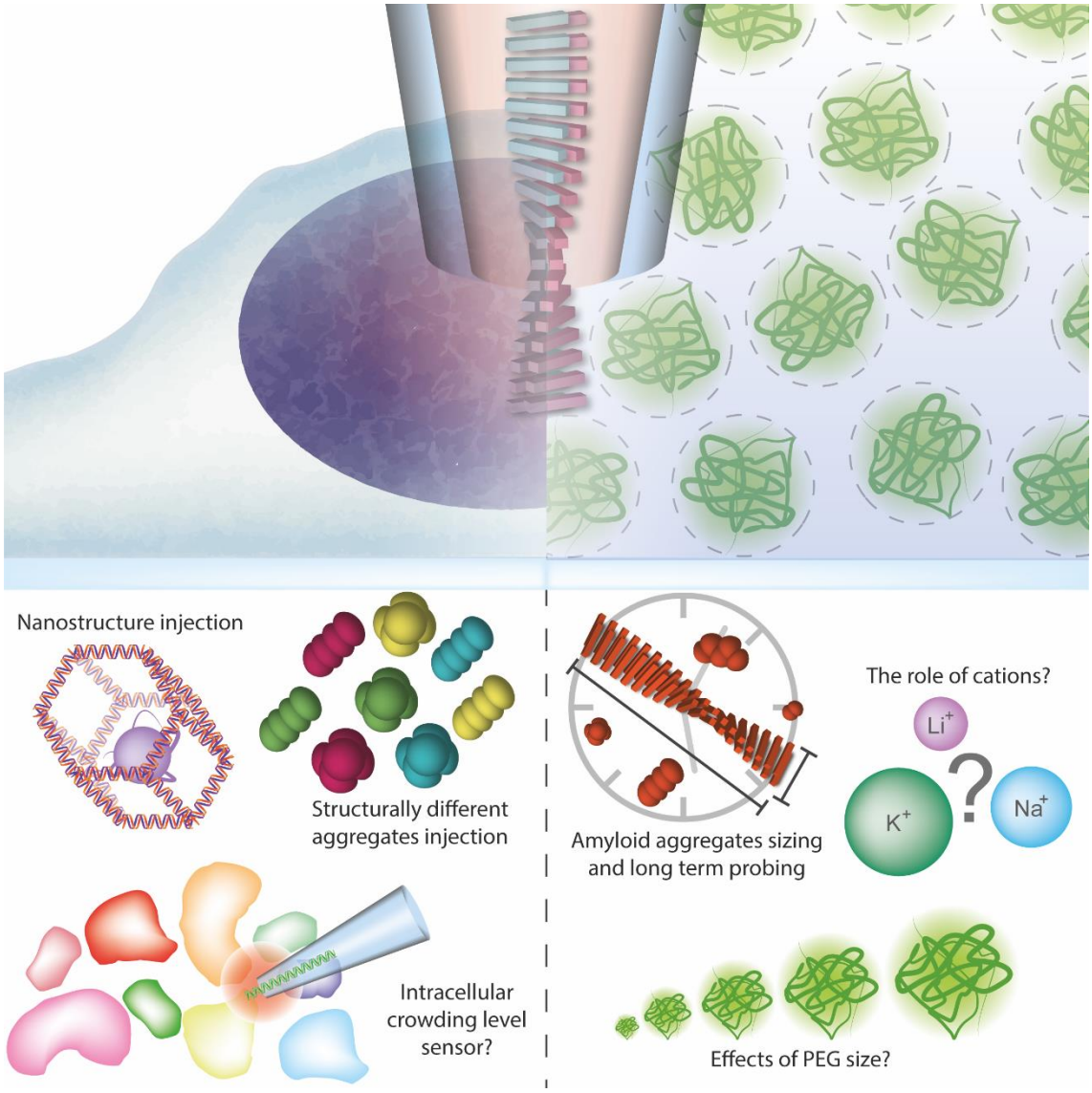

Figure 4.42. Schematic illustration to summarise the thesis and future follow-up. *The left depicts the quantitative nanoinjection of molecules into the cell via the nanopipette and its potential applications. These include the injection of nanostructures to study and control the intracellular dynamics, the quantitative injection of structurally different aggregates to study the cell response and nanoinjection as an intracellular crowding level sensor. The right depicts the macromolecular crowded bath assisted single molecule detection of molecules via the nanopipette and its future applications. These include the sizing of amyloid aggregates and probing the amyloid aggregation under physiological conditions. With regards to the understanding the underlying reasons for the signal enhancement, the role of cations and the effect of PEG size could be investigated.*

The work from this thesis has a number of potential applications (Figure 4.42). For quantitative nanoinjection, these include:

- The quantitative injection of higher order nanostructures that can either release siRNAs inside the cell (Douglas et al., 2012; Bujold et al., 2016; Bujold et al., 2018), this can potentially be used to assess and control cellular dynamic in a more precise manner, through controlling the number of nanostructures that will be delivered into the cell and subsequently precisely control the gene expression level.
- The injection of structurally different amyloid aggregates, it has been shown that amyloid aggregates can have different structures and that these elicit different cellular response (Bousset, L. et al., 2013; Peelaerts et al., 2015b; Chou et al., 2021). Using the quantitative nanoinjection approach, not only could the relationship between structure and function correlation be investigated inside the cell, but the number of these structures required to elicit cellular response could be quantified.
- Lastly, since the cellular environment may alter the characteristics of the translocation signals of biomolecules during nanoinjection, I propose that these alteration in the translocation signals can be used to probe the crowding level inside the cell. Further development will be needed and the established FRET based intracellular crowding sensor (Boersma et al., 2015; Murade and Shubeita, 2019) can be easily implemented into the current set-up to test whether translocation signals correlate to the level of crowding inside the cell.

For the macromolecular crowding assisted detection, future studies could explore:

- Amyloid assembly reactions. By first correlating the dimensions of aggregates of known size with their translocation signals. Then, this information could be used to probe the process and kinetics of the aggregation of proteins into amyloid fibrils over the course of multiple days (Yusko, Erik C. et al., 2012; Martyushenko et al., 2015; Balme et al., 2016; Hu, R. et al., 2016; Giamblanco et al., 2018a; Houghtaling, J. et al., 2018; Li, Xiaoqing et al., 2019; Giamblanco et al., 2020a; Giamblanco et al., 2020b). Using the PEG crowded bath assisted detection method, aggregation could be carried out in physiologically relevant buffer system instead of the high salt conditions often used. This application could complement other kinetic assays of amyloid formation and has potential to observe aggregates

formed early in the aggregation reactions (Meisl et al., 2018; Michaels et al., 2018; Törnquist et al., 2018).

- The PEG crowded electrolyte bath should also be further studied by generating the PEG crowded bath with different alkali halide metals. In particular, the unique role of cations should be further investigated, since various polymer electrolyte-related research shown that Li^+ cations do not interact with the PEG chain, but Na^+ and K^+ cations are chelated by the PEG chain (Tasaki, Kenzabu, 1996; Tasaki, K., 1999; Ohki et al., 2007; Tao and Cummings, 2007; Ren et al., 2011; Zhang, Z. et al., 2015; Poudel et al., 2017). The hindered cations alters the ion mobility in the bath solution and as a result affects the nanofluidic physics of the nanopipette (White, H.S. and Bund, 2008; Yusko, Erik C. et al., 2009; Luo et al., 2012; Perera et al., 2015; Lan et al., 2016; Rabinowitz et al., 2019), this consequently affect the single molecule translocation signals (Chen, K. et al., 2017).
- Lastly, the role of the PEG size should also be investigated, as the results showed that PEG 8000 enhanced the signals better than the PEG 4000 at equivalent concentration. Increasing the size of PEG also increases the excluded volume effects (Knowles et al., 2011), this can be tested by generating the PEG crowded bath with PEG of a wide range of molecular weights.

In summary, in this thesis I demonstrated that quantitative nanoinjection can be performed with a nanopipette and SICM. Secondly, I demonstrated that modifying the electrolyte bath with macromolecular crowding agents enhances the detection of biomolecules.

Bibliography

Actis, P. 2018. Sampling from Single Cells. *Small Methods.* **2**(3), p1700300.

Actis, P., Maalouf, M.M., Kim, H.J., Lohith, A., Vilozny, B., Seger, R.A. and Pourmand, N. 2013. Compartmental Genomics in Living Cells Revealed by Single-Cell Nanobiopsy. *ACS Nano.* **8**(1), pp.546-553.

Adachi, M., Noji, M., So, M., Sasahara, K., Kardos, J., Naiki, H. and Goto, Y. 2018. Aggregation-phase diagrams of β2-microglobulin reveal temperature and salt effects on competitive formation of amyloids versus amorphous aggregates. *Journal of Biological Chemistry.* **293**(38), pp.14775-14785.

Adam Seger, R., Actis, P., Penfold, C., Maalouf, M., Vilozny, B. and Pourmand, N. 2012. Voltage controlled nano-injection system for single-cell surgery. *Nanoscale.* **4**(19), pp.5843-5846.

Adamo, A., Arione, A., Sharei, A. and Jensen, K.F. 2013. Flow-Through Comb Electroporation Device for Delivery of Macromolecules. *Analytical Chemistry.* **85**(3), pp.1637-1641.

Adli, M. 2018. The CRISPR tool kit for genome editing and beyond. *Nature Communications.* **9**(1), p1911.

Ahmed, S., Fujita, S. and Matsumura, K. 2016. Enhanced protein internalization and efficient endosomal escape using polyampholyte-modified liposomes and freeze concentration. *Nanoscale.* **8**(35), pp.15888-15901.

Aksimentiev, A. 2010. Deciphering ionic current signatures of DNA transport through a nanopore. *Nanoscale.* **2**(4), p468.

Aksoyoglu, M.A., Podgornik, R., Bezrukov, S.M., Gurnev, P.A., Muthukumar, M. and Parsegian, V.A. 2016. Size-dependent forced PEG partitioning into channels: VDAC, OmpC, and α-hemolysin. *Proceedings of the National Academy of Sciences.* **113**(32), pp.9003-9008.

Alam, P., Bousset, L., Melki, R. and Otzen, D.E. 2019. α-synuclein oligomers and fibrils: a spectrum of species, a spectrum of toxicities. *Journal of Neurochemistry.* **150**(5), pp.522-534.

Apel, P.Y., Blonskaya, I.V., Orelovitch, O.L., Ramirez, P. and Sartowska, B.A. 2011. Effect of nanopore geometry on ion current rectification. *Nanotechnology.* **22**(17), p175302.

Aramesh, M., Forró, C., Dorwling-Carter, L., Lüchtefeld, I., Schlotter, T., Ihle, S.J., Shorubalko, I., Hosseini, V., Momotenko, D., Zambelli, T., Klotzsch, E. and Vörös, J. 2019. Localized detection of ions and biomolecules with a force-controlled scanning nanopore microscope. *Nature Nanotechnology.* **14**(8), pp.791-798.

Aubrey, L.D., Blakeman, B.J.F., Lutter, L., Serpell, C.J., Tuite, M.F., Serpell, L.C. and Xue, W.-F. 2020. Quantification of amyloid fibril polymorphism by nano-

morphometry reveals the individuality of filament assembly. *bioRxiv.* p2020.2001.2014.905877.

Babakinejad, B., Jönsson, P., López Córdoba, A., Actis, P., Novak, P., Takahashi, Y., Shevchuk, A., Anand, U., Anand, P., Drews, A., Ferrer-Montiel, A., Klenerman, D. and Korchev, Y.E. 2013. Local Delivery of Molecules from a Nanopipette for Quantitative Receptor Mapping on Live Cells. *Analytical Chemistry.* **85**(19), pp.9333-9342.

Babayekhorasani, F., Dunstan, D.E., Krishnamoorti, R. and Conrad, J.C. 2016. Nanoparticle diffusion in crowded and confined media. *Soft Matter.* **12**(40), pp.8407-8416.

Badowski, C., Iskander, A., Gaspar, D., Zeugolis, D.I. and Raghunath, M. 2018. Molecular Crowding – (in Cell Culture). In: Gimble, J.M., et al. eds. *Cell Engineering and Regeneration.* Springer International Publishing, pp.1-27.

Bagnoli, J.W., Ziegenhain, C., Janjic, A., Wange, L.E., Vieth, B., Parekh, S., Geuder, J., Hellmann, I. and Enard, W. 2018. Sensitive and powerful single-cell RNA sequencing using mcSCRB-seq. *Nature Communications.* **9**(1), p2937.

Bai, H., Lester, G.M.S., Petishnok, Laura C. and Dean, David A. 2017. Cytoplasmic transport and nuclear import of plasmid DNA. *Bioscience Reports.* **37**(6), pBSR20160616.

Balijepalli, A., Robertson, J.W.F., Reiner, J.E., Kasianowicz, J.J. and Pastor, R.W. 2013. Theory of Polymer–Nanopore Interactions Refined Using Molecular Dynamics Simulations. *Journal of the American Chemical Society.* **135**(18), pp.7064-7072.

Balme, S., Coulon, P.E., Lepoitevin, M., Charlot, B., Yandrapalli, N., Favard, C., Muriaux, D., Bechelany, M. and Janot, J.-M. 2016. Influence of Adsorption on Proteins and Amyloid Detection by Silicon Nitride Nanopore. *Langmuir.* **32**(35), pp.8916-8925.

Bangham, A.D., Hill, M.W. and Miller, N.G.A. 1974. Preparation and Use of Liposomes as Models of Biological Membranes. pp.1-68.

Bangham, A.D. and Horne, R.W. 1964. Negative staining of phospholipids and their structural modification by surface-active agents as observed in the electron microscope. *Journal of Molecular Biology.* **8**(5), pp.660-IN610.

Barber, M.A. 1904. A new method of isolating micro-organisms. *J. Kans. Med. Soc.* **4**, pp.489-494.

Bartesaghi, A., Matthies, D., Banerjee, S., Merk, A. and Subramaniam, S. 2014. Structure of β-galactosidase at 3.2-A resolution obtained by cryo-electron microscopy. *Proceedings of the National Academy of Sciences.* **111**(32), pp.11709-11714.

Bayrhuber, M., Meins, T., Habeck, M., Becker, S., Giller, K., Villinger, S., Vonrhein, C., Griesinger, C., Zweckstetter, M. and Zeth, K. 2008. Structure of the human voltage-dependent anion channel. *Proceedings of the National Academy of Sciences.* **105**(40), pp.15370-15375.

Behrens, S.H. and Grier, D.G. 2001. The charge of glass and silica surfaces. *The Journal of Chemical Physics.* **115**(14), pp.6716-6721.

Bell, N.A.W. and Keyser, U.F. 2016. Digitally encoded DNA nanostructures for multiplexed, single-molecule protein sensing with nanopores. *Nature Nanotechnology.* **11**(7), pp.645-651.

Binnig, G., Quate, C.F. and Gerber, C. 1986. Atomic Force Microscope. *Physical Review Letters.* **56**(9), pp.930-933.

Boersma, A.J., Zuhorn, I.S. and Poolman, B. 2015. A sensor for quantification of macromolecular crowding in living cells. *Nature Methods.* **12**(3), pp.227-229.

Bortner, C.D. and Cidlowski, J.A. 2020. Ions, the Movement of Water and the Apoptotic Volume Decrease. *Frontiers in Cell and Developmental Biology.* **8**.

Bottomley, L.A. 1998. Scanning Probe Microscopy. *Analytical Chemistry.* **70**(12), pp.425-476.

Bousset, L., Pieri, L., Ruiz-Arlandis, G., Gath, J., Jensen, P.H., Habenstein, B., Madiona, K., Olieric, V., Bockmann, A., Meier, B.H. and Melki, R. 2013. Structural and functional characterization of two alpha-synuclein strains. *Nature Communications.* **4**, p2575.

Bousset, L., Pieri, L., Ruiz-Arlandis, G., Gath, J., Jensen, P.H., Habenstein, B., Madiona, K., Olieric, V., Böckmann, A., Meier, B.H. and Melki, R. 2013. Structural and functional characterization of two alpha-synuclein strains. *Nature Communications.* **4**(1).

Boyer, P.D., Krebs, E.G., Sigman, D.S., Tamanoi, F., Dalbey, R.E., Hackney, D.D. and Tamanoi, F. 1970. *The enzymes.* 3rd ed. New York ; London: Academic Press.

Bozzuto, G. and Molinari, A. 2015. Liposomes as nanomedical devices. *Int J Nanomedicine.* **10**, pp.975-999.

Breton, M.F., Discala, F., Bacri, L., Foster, D., Pelta, J. and Oukhaled, A. 2013. Exploration of Neutral Versus Polyelectrolyte Behavior of Poly(ethylene glycol)s in Alkali Ion Solutions using Single-Nanopore Recording. *The Journal of Physical Chemistry Letters.* **4**(13), pp.2202-2208.

Bujold, K.E., Hsu, J.C.C. and Sleiman, H.F. 2016. Optimized DNA "Nanosuitcases" for Encapsulation and Conditional Release of siRNA. *Journal of the American Chemical Society.* **138**(42), pp.14030-14038.

Bujold, K.E., Lacroix, A. and Sleiman, H.F. 2018. DNA Nanostructures at the Interface with Biology. *Chem.* **4**(3), pp.495-521.

Bürgel, S.C., Escobedo, C., Haandbæk, N. and Hierlemann, A. 2015. On-chip electroporation and impedance spectroscopy of single-cells. *Sensors and Actuators B: Chemical.* **210**, pp.82-90.

Burré, J., Vivona, S., Diao, J., Sharma, M., Brunger, A.T. and Südhof, T.C. 2013. Properties of native brain α-synuclein. *Nature.* **498**(7453), pp.E4-E6.

Cai, Y., Zhou, H., Zhu, Y., Sun, Q., Ji, Y., Xue, A., Wang, Y., Chen, W., Yu, X., Wang, L., Chen, H., Li, C., Luo, T. and Deng, H. 2020. Elimination of senescent cells by β-galactosidase-targeted prodrug attenuates inflammation and restores physical function in aged mice. *Cell Research.* **30**(7), pp.574-589.

Calander, N. 2009. Analyte Concentration at the Tip of a Nanopipette. *Analytical Chemistry.* **81**(20), pp.8347-8353.

Cao, D., Song, Y., Peng, J., Ma, R., Guo, J., Chen, J., Li, X., Jiang, Y., Wang, E. and Xu, L. 2019. Advances in Atomic Force Microscopy: Weakly Perturbative Imaging of the Interfacial Water. *Frontiers in Chemistry.* **7**, p626.

Cao, Y., Chen, H., Qiu, R., Hanna, M., Ma, E., Hjort, M., Zhang, A., Lewis, R.S., Wu, J.C. and Melosh, N.A. 2018. Universal intracellular biomolecule delivery with precise dosage control. *Science Advances.* **4**(10), peaat8131.

Cao, Y., Ma, E., Cestellos-Blanco, S., Zhang, B., Qiu, R., Su, Y., Doudna, J.A. and Yang, P. 2019. Nontoxic nanopore electroporation for effective intracellular delivery of biological macromolecules. *Proceedings of the National Academy of Sciences.* **116**(16), pp.7899-7904.

Caragine, C.M., Haley, S.C. and Zidovska, A. 2018. Surface Fluctuations and Coalescence of Nucleolar Droplets in the Human Cell Nucleus. *Physical Review Letters.* **121**(14), p148101.

Carter, B. and Zhao, K. 2020. The epigenetic basis of cellular heterogeneity. *Nature Reviews Genetics.* **22**(4), pp.235-250.

Carter, M. and Shieh, J. 2015. Gene Delivery Strategies. In: Carter, M. and Shieh, J. eds. *Guide to Research Techniques in Neuroscience.* Elsevier, pp.239-252.

Cascella, R., Chen, S.W., Bigi, A., Camino, J.D., Xu, C.K., Dobson, C.M., Chiti, F., Cremades, N. and Cecchi, C. 2021. The release of toxic oligomers from α-synuclein fibrils induces dysfunction in neuronal cells. *Nature Communications.* **12**(1).

Cautain, B., Hill, R., de Pedro, N. and Link, W. 2015. Components and regulation of nuclear transport processes. *The FEBS Journal.* **282**(3), pp.445-462.

Chakroun, T., Evsyukov, V., Nykänen, N.-P., Höllerhage, M., Schmidt, A., Kamp, F., Ruf, V.C., Wurst, W., Rösler, T.W. and Höglinger, G.U. 2020. Alpha-synuclein fragments trigger distinct aggregation pathways. *Cell Death & Disease.* **11**(2), p84.

Chandrashekaran, S. 2004. KpnI restriction endonuclease and methyltransferase exhibit contrasting mode of sequence recognition. *Nucleic Acids Research.* **32**(10), pp.3148-3155.

Chang, L., Hu, J., Chen, F., Chen, Z., Shi, J., Yang, Z., Li, Y. and Lee, L.J. 2016. Nanoscale bio-platforms for living cell interrogation: current status and future perspectives. *Nanoscale.* **8**(6), pp.3181-3206.

Charron, M., Briggs, K., King, S., Waugh, M. and Tabard-Cossa, V. 2019. Precise DNA Concentration Measurements with Nanopores by Controlled Counting. *Analytical Chemistry.* **91**(19), pp.12228-12237.

Chatin, B., Mevel, M., Devalliere, J., Dallet, L., Haudebourg, T., Peuziat, P., Colombani, T., Berchel, M., Lambert, O., Edelman, A. and Pitard, B. 2015. Liposome-based Formulation for Intracellular Delivery of Functional Proteins. *Mol Ther Nucleic Acids.* **4**, pe244.

Chau, C., Actis, P. and Hewitt, E. 2020. Methods for protein delivery into cells: from current approaches to future perspectives. *Biochem Soc Trans.* **48**(2), pp.357-365.

Chau, C.C., Hewitt, E.W. and Actis, P. 2021. The role of macromolecular crowding in single-entity electrochemistry: Friend or foe? *Current Opinion in Electrochemistry.* **25**, p100654.

Chaverra-Rodriguez, D., Macias, V.M., Hughes, G.L., Pujhari, S., Suzuki, Y., Peterson, D.R., Kim, D., McKeand, S. and Rasgon, J.L. 2018. Targeted delivery of CRISPR-Cas9 ribonucleoprotein into arthropod ovaries for heritable germline gene editing. *Nature Communications.* **9**(1), p3008.

Chen, B.B., Lv, J., Wang, X.Y. and Qian, R.C. 2019. Probing the Membrane Vibration of Single Living Cells by Using Nanopipettes. *ChemBioChem.* **21**(5), pp.650-655.

Chen, C.C., Zhou, Y. and Baker, L.A. 2012. Scanning Ion Conductance Microscopy. *Annual Review of Analytical Chemistry.* **5**(1), pp.207-228.

Chen, C.C., Zhou, Y., Morris, C.A., Hou, J. and Baker, L.A. 2013. Scanning Ion Conductance Microscopy Measurement of Paracellular Channel Conductance in Tight Junctions. *Analytical Chemistry.* **85**(7), pp.3621-3628.

Chen, K., Bell, N.A.W., Kong, J., Tian, Y. and Keyser, U.F. 2017. Direction- and Salt-Dependent Ionic Current Signatures for DNA Sensing with Asymmetric Nanopores. *Biophysical Journal.* **112**(4), pp.674-682.

Chen, K., Zhu, J., Bošković, F. and Keyser, U.F. 2020. Nanopore-Based DNA Hard Drives for Rewritable and Secure Data Storage. *Nano Letters.* **20**(5), pp.3754-3760.

Chen, Q. and Liu, Z. 2019. Fabrication and Applications of Solid-State Nanopores. *Sensors.* **19**(8), p1886.

Chen, S.W., Drakulic, S., Deas, E., Ouberai, M., Aprile, F.A., Arranz, R., Ness, S., Roodveldt, C., Guilliams, T., De-Genst, E.J., Klenerman, D., Wood, N.W., Knowles, T.P.J., Alfonso, C., Rivas, G., Abramov, A.Y., Valpuesta, J.M., Dobson, C.M. and Cremades, N. 2015. Structural characterization of toxic oligomers that are kinetically trapped during α-synuclein fibril formation. *Proceedings of the National Academy of Sciences.* **112**(16), pp.E1994-E2003.

Chen, Y., Sukhorukov, G.B. and Novak, P. 2018. Visualising nanoscale restructuring of a cellular membrane triggered by polyelectrolyte microcapsules. *Nanoscale.* **10**(35), pp.16902-16910.

Chen, Z., Cao, Y., Lin, C.-W., Alvarez, S., Oh, D., Yang, P. and Groves, J.T. 2021. Nanopore-mediated protein delivery enabling three-color single-molecule tracking in living cells. *Proceedings of the National Academy of Sciences.* **118**(5), pe2012229118.

Cheng, C., Jia, J.-L. and Ran, S.-Y. 2015. Polyethylene glycol and divalent salt-induced DNA reentrant condensation revealed by single molecule measurements. *Soft Matter.* **11**(19), pp.3927-3935.

Cheung, M.C., LaCroix, R., McKenna, B.K., Liu, L., Winkelman, J. and Ehrlich, D.J. 2013. Intracellular protein and nucleic acid measured in eight cell types using deep-ultraviolet mass mapping. *Cytometry Part A.* **83A**(6), pp.540-551.

Chiki, A., Ricci, J., Hegde, R., Abriata, L.A., Reif, A. and Lashuel, H.A. 2020. Site-specific phosphorylation of Huntingtin exon 1 recombinant proteins enabled by the discovery of novel kinases. *bioRxiv.* p2020.2007.2023.217968.

Chiti, F. and Dobson, C.M. 2017. Protein Misfolding, Amyloid Formation, and Human Disease: A Summary of Progress Over the Last Decade. *Annual Review of Biochemistry.* **86**(1), pp.27-68.

Cho, S.W., Lee, J.Y., Carroll, D., Kim, J.S. and Lee, J.H. 2013. Heritable Gene Knockout in Caenorhabditis elegans by Direct Injection of Cas9–sgRNA Ribonucleoproteins. *Genetics.* **195**(3), pp.1177-1180.

Chou, Q.-L., Alik, A., Marquier, F., Melki, R., Treussart, F. and Simonneau, M. 2021. Impact of α-synuclein fibrillar strains and ß-amyloid assemblies on mouse cortical neurons endo-lysosomal logistics. *bioRxiv.* p2021.2005.2015.444288.

Chow, Y.T., Chen, S., Liu, C., Liu, C., Li, L., Kong, C.W.M., Cheng, S.H., Li, R.A. and Sun, D. 2016a. A High-Throughput Automated Microinjection System for Human Cells With Small Size. *IEEE/ASME Transactions on Mechatronics.* **21**(2), pp.838-850.

Chow, Y.T., Chen, S., Wang, R., Liu, C., Kong, C.-w., Li, R.A., Cheng, S.H. and Sun, D. 2016b. Single Cell Transfection through Precise Microinjection with Quantitatively Controlled Injection Volumes. *Scientific Reports.* **6**(1), p24127.

Clarke, J., Wu, H.-C., Jayasinghe, L., Patel, A., Reid, S. and Bayley, H. 2009. Continuous base identification for single-molecule nanopore DNA sequencing. *Nature Nanotechnology.* **4**(4), pp.265-270.

Clarke, R.W., Novak, P., Zhukov, A., Tyler, E.J., Cano-Jaimez, M., Drews, A., Richards, O., Volynski, K., Bishop, C. and Klenerman, D. 2016. Low Stress Ion Conductance Microscopy of Sub-Cellular Stiffness. *Soft Matter.* **12**(38), pp.7953-7958.

Clarke, R.W., Zhukov, A., Richards, O., Johnson, N., Ostanin, V. and Klenerman, D. 2012. Pipette–Surface Interaction: Current Enhancement and Intrinsic Force. *Journal of the American Chemical Society.* **135**(1), pp.322-329.

Cleal, K., He, L., Watson, P.D. and Jones, A.T. 2013. Endocytosis, intracellular traffic and fate of cell penetrating peptide based conjugates and nanoparticles. *Curr Pharm Des.* **19**(16), pp.2878-2894.

Clift, D., McEwan, W.A., Labzin, L.I., Konieczny, V., Mogessie, B., James, L.C. and Schuh, M. 2017. A Method for the Acute and Rapid Degradation of Endogenous Proteins. *Cell.* **171**(7), pp.1692-1706 e1618.

Clift, D., So, C., McEwan, W.A., James, L.C. and Schuh, M. 2018. Acute and rapid degradation of endogenous proteins by Trim-Away. *Nature Protocols.* **13**(10), pp.2149-2175.

Cohen, J.A. 2003. Electrophoretic Characterization of Liposomes. *Methods in Enzymology.* **367**, pp.148-176.

Colletier, J.P., Chaize, B., Winterhalter, M. and Fournier, D. 2002. Protein encapsulation in liposomes: efficiency depends on interactions between protein and phospholipid bilayer. *BMC Biotechnol.* **2**, p9.

Conic, S., Desplancq, D., Ferrand, A., Fischer, V., Heyer, V., Reina San Martin, B., Pontabry, J., Oulad-Abdelghani, M., Babu, N.K., Wright, G.D., Molina, N., Weiss, E. and Tora, L. 2018. Imaging of native transcription factors and histone phosphorylation at high resolution in live cells. *J Cell Biol.* **217**(4), pp.1537-1552.

Coulter, W.H. 1953. *Means for counting particles suspended in a fluid*.

Cox, D.B.T., Platt, R.J. and Zhang, F. 2015. Therapeutic genome editing: prospects and challenges. *Nature Medicine.* **21**(2), pp.121-131.

Cremades, N., Cohen, S.I., Deas, E., Abramov, A.Y., Chen, A.Y., Orte, A., Sandal, M., Clarke, R.W., Dunne, P., Aprile, F.A., Bertoncini, C.W., Wood, N.W., Knowles, T.P., Dobson, C.M. and Klenerman, D. 2012. Direct observation of the interconversion of normal and toxic forms of alpha-synuclein. *Cell.* **149**(5), pp.1048-1059.

Cremades, N., Cohen, Samuel I.A., Deas, E., Abramov, Andrey Y., Chen, Allen Y., Orte, A., Sandal, M., Clarke, Richard W., Dunne, P., Aprile, Francesco A., Bertoncini, Carlos W., Wood, Nicholas W., Knowles, Tuomas P.J., Dobson, Christopher M. and Klenerman, D. 2012. Direct Observation of the Interconversion of Normal and Toxic Forms of α-Synuclein. *Cell.* **149**(5), pp.1048-1059.

Cressiot, B., Oukhaled, A., Patriarche, G., Pastoriza-Gallego, M., Betton, J.-M., Auvray, L., Muthukumar, M., Bacri, L. and Pelta, J. 2012. Protein Transport through a Narrow Solid-State Nanopore at High Voltage: Experiments and Theory. *ACS Nano.* **6**(7), pp.6236-6243.

D'Angelo, M.A., Raices, M., Panowski, S.H. and Hetzer, M.W. 2009. Age-dependent deterioration of nuclear pore complexes causes a loss of nuclear integrity in postmitotic cells. *Cell.* **136**(2), pp.284-295.

Danzer, K.M., Krebs, S.K., Wolff, M., Birk, G. and Hengerer, B. 2009. Seeding induced by α-synuclein oligomers provides evidence for spreading of α-synuclein pathology. *Journal of Neurochemistry.* **111**(1), pp.192-203.

De Cecco, E., Celauro, L., Vanni, S., Grandolfo, M., Bistaffa, E., Moda, F., Aguzzi, A. and Legname, G. 2020. The uptake of tau amyloid fibrils is facilitated by the cellular prion protein and hampers prion propagation in cultured cells. *Journal of Neurochemistry.* pAhead of Print.

de Oliveira, G.A.P. and Silva, J.L. 2019. Alpha-synuclein stepwise aggregation reveals features of an early onset mutation in Parkinson's disease. *Communications Biology.* **2**(1), p374.

DeBlois, R.W. and Bean, C.P. 1970. Counting and Sizing of Submicron Particles by the Resistive Pulse Technique. *Review of Scientific Instruments.* **41**(7), pp.909-916.

Déjardin, P., Vasina, E.N., Berezkin, V.V., Sobolev, V.D. and Volkov, V.I. 2005. Streaming Potential in Cylindrical Pores of Poly(ethylene terephthalate) Track-Etched Membranes: Variation of Apparent ζ Potential with Pore Radius. *Langmuir.* **21**(10), pp.4680-4685.

Del Linz, S., Willman, E., Caldwell, M., Klenerman, D., Fernández, A. and Moss, G. 2014. Contact-Free Scanning and Imaging with the Scanning Ion Conductance Microscope. *Analytical Chemistry.* **86**(5), pp.2353-2360.

Ding, W.-Q., Lv, F., Xu, N., Wu, M.-T., Liu, J. and Gao, X.-P. 2021. Polyethylene Oxide-Based Solid-State Composite Polymer Electrolytes for Rechargeable Lithium Batteries. *ACS Applied Energy Materials.* **4**(5), pp.4581-4601.

Distler, J.H.W., Jungel, A., Kurowska-Stolarska, M., Michel, B.A., Gay, R.E., Gay, S. and Distler, O. 2005. Nucleofection: a new, highly efficient transfection method for primary human keratinocytes*. *Experimental Dermatology.* **14**(4), pp.315-320.

Dix, J.A. and Verkman, A.S. 2008. Crowding Effects on Diffusion in Solutions and Cells. *Annual Review of Biophysics.* **37**(1), pp.247-263.

Dixon, C., Platani, M., Makarov, A. and Schirmer, E. 2017. Microinjection of Antibodies Targeting the Lamin A/C Histone-Binding Site Blocks Mitotic Entry and Reveals Separate Chromatin Interactions with HP1, CenpB and PML. *Cells.* **6**(2), p9.

Doherty, G.J. and McMahon, H.T. 2009. Mechanisms of Endocytosis. *Annual Review of Biochemistry.* **78**(1), pp.857-902.

Doudna, J.A. and Charpentier, E. 2014. The new frontier of genome engineering with CRISPR-Cas9. *Science.* **346**(6213), p1258096.

Dougherty, P.G., Sahni, A. and Pei, D. 2019. Understanding Cell Penetration of Cyclic Peptides. *Chemical Reviews.* **119**(17), pp.10241-10287.

Douglas, S.M., Bachelet, I. and Church, G.M. 2012. A Logic-Gated Nanorobot for Targeted Transport of Molecular Payloads. *Science.* **335**(6070), pp.831-834.

Doura, T., Kamiya, M., Obata, F., Yamaguchi, Y., Hiyama, T.Y., Matsuda, T., Fukamizu, A., Noda, M., Miura, M. and Urano, Y. 2016. Detection of LacZ-Positive Cells in Living Tissue with Single-Cell Resolution. *Angewandte Chemie International Edition.* **55**(33), pp.9620-9624.

Drews, A., Flint, J., Shivji, N., Jönsson, P., Wirthensohn, D., De Genst, E., Vincke, C., Muyldermans, S., Dobson, C. and Klenerman, D. 2016. Individual aggregates of amyloid beta induce temporary calcium influx through the cell membrane of neuronal cells. *Scientific Reports.* **6**(1), p31910.

Duncan, A.L., Reddy, T., Koldsø, H., Hélie, J., Fowler, P.W., Chavent, M. and Sansom, M.S.P. 2017. Protein crowding and lipid complexity influence the nanoscale dynamic organization of ion channels in cell membranes. *Scientific Reports.* **7**(1).

Eiriksdottir, E., Konate, K., Langel, U., Divita, G. and Deshayes, S. 2010. Secondary structure of cell-penetrating peptides controls membrane interaction and insertion. *Biochim Biophys Acta.* **1798**(6), pp.1119-1128.

Eisenberg, D.S. and Sawaya, M.R. 2017. Structural Studies of Amyloid Proteins at the Molecular Level. *Annual Review of Biochemistry.* **86**(1), pp.69-95.

Ellis, R.J. 2001. Macromolecular crowding: an important but neglected aspect of the intracellular environment. *Current Opinion in Structural Biology.* **11**(1), pp.114-119.

Evdokimov, A.G., Pokross, M.E., Egorov, N.S., Zaraisky, A.G., Yampolsky, I.V., Merzlyak, E.M., Shkoporov, A.N., Sander, I., Lukyanov, K.A. and Chudakov, D.M. 2006. Structural basis for the fast maturation of Arthropoda green fluorescent protein. *EMBO reports.* **7**(10), pp.1006-1012.

Experton, J., Wu, X. and Martin, C.R. 2017. From Ion Current to Electroosmotic Flow Rectification in Asymmetric Nanopore Membranes. *Nanomaterials.* **7**(12), p445.

Faller, M. 2004. The Structure of a Mycobacterial Outer-Membrane Channel. *Science.* **303**(5661), pp.1189-1192.

Fares, M.B., Jagannath, S. and Lashuel, H.A. 2021. Reverse engineering Lewy bodies: how far have we come and how far can we go? *Nature Reviews Neuroscience.* **22**(2), pp.111-131.

Fenton, D.E., Parker, J.M. and Wright, P.V. 1973. Complexes of alkali metal ions with poly(ethylene oxide). *Polymer.* **14**(11), p589.

Figard, L. and Sokac, A.M. 2014. A membrane reservoir at the cell surface. *BioArchitecture.* **4**(2), pp.39-46.

Flynn, J.D., McGlinchey, R.P., Walker, R.L. and Lee, J.C. 2018. Structural features of α-synuclein amyloid fibrils revealed by Raman spectroscopy. *Journal of Biological Chemistry.* **293**(3), pp.767-776.

Fologea, D., Brandin, E., Uplinger, J., Branton, D. and Li, J. 2007. DNA conformation and base number simultaneously determined in a nanopore. *Electrophoresis.* **28**(18), pp.3186-3192.

Fologea, D., Uplinger, J., Thomas, B., McNabb, D.S. and Li, J. 2005. Slowing DNA Translocation in a Solid-State Nanopore. *Nano Letters.* **5**(9), pp.1734-1737.

Foran, G., Mankovsky, D., Verdier, N., Lepage, D., Prébé, A., Aymé-Perrot, D. and Dollé, M. 2020. The Impact of Absorbed Solvent on the Performance of Solid Polymer Electrolytes for Use in Solid-State Lithium Batteries. *iScience.* **23**(10), p101597.

Fraccari, R.L., Carminati, M., Piantanida, G., Leontidou, T., Ferrari, G. and Albrecht, T. 2016. High-bandwidth detection of short DNA in nanopipettes. *Faraday Discussions.* **193**, pp.459-470.

Fragasso, A., Schmid, S. and Dekker, C. 2020. Comparing Current Noise in Biological and Solid-State Nanopores. *ACS Nano.* **14**(2), pp.1338-1349.

Frankel, A.D. and Pabo, C.O. 1988. Cellular uptake of the tat protein from human immunodeficiency virus. *Cell.* **55**(6), pp.1189-1193.

Fretz, M.M., Hogset, A., Koning, G.A., Jiskoot, W. and Storm, G. 2007. Cytosolic delivery of liposomally targeted proteins induced by photochemical internalization. *Pharm Res.* **24**(11), pp.2040-2047.

Freundt, E.C., Maynard, N., Clancy, E.K., Roy, S., Bousset, L., Sourigues, Y., Covert, M., Melki, R., Kirkegaard, K. and Brahic, M. 2012. Neuron-to-neuron transmission of α-synuclein fibrils through axonal transport. *Annals of Neurology.* **72**(4), pp.517-524.

Fu, A., Tang, R., Hardie, J., Farkas, M.E. and Rotello, V.M. 2014. Promises and pitfalls of intracellular delivery of proteins. *Bioconjug Chem.* **25**(9), pp.1602-1608.

Fusco, G., Chen, S.W., Williamson, P.T.F., Cascella, R., Perni, M., Jarvis, J.A., Cecchi, C., Vendruscolo, M., Chiti, F., Cremades, N., Ying, L., Dobson, C.M. and De Simone, A. 2017. Structural basis of membrane disruption and cellular toxicity by α-synuclein oligomers. *Science.* **358**(6369), pp.1440-1443.

Ganjam, G.K., Bolte, K., Matschke, L.A., Neitemeier, S., Dolga, A.M., Höllerhage, M., Höglinger, G.U., Adamczyk, A., Decher, N., Oertel, W.H. and Culmsee, C. 2019. Mitochondrial damage by α-synuclein causes cell death in human dopaminergic neurons. *Cell Death & Disease.* **10**(11).

García-Pérez, B.E., Villagómez-Palatto, D.A., Castañeda-Sánchez, J.I., Coral-Vázquez, R.M., Ramírez-Sánchez, I., Ordoñez-Razo, R.M. and Luna-Herrera, J. 2011. Innate response of human endothelial cells infected with mycobacteria. *Immunobiology.* **216**(8), pp.925-935.

Gaudelli, N.M., Komor, A.C., Rees, H.A., Packer, M.S., Badran, A.H., Bryson, D.I. and Liu, D.R. 2017. Programmable base editing of A*T to G*C in genomic DNA without DNA cleavage. *Nature.* **551**(7681), pp.464-471.

Gebala, M., Bonilla, S., Bisaria, N. and Herschlag, D. 2016. Does Cation Size Affect Occupancy and Electrostatic Screening of the Nucleic Acid Ion Atmosphere? *Journal of the American Chemical Society.* **138**(34), pp.10925-10934.

Gebala, M., Giambaşu, G.M., Lipfert, J., Bisaria, N., Bonilla, S., Li, G., York, D.M. and Herschlag, D. 2015. Cation–Anion Interactions within the Nucleic Acid Ion Atmosphere Revealed by Ion Counting. *Journal of the American Chemical Society.* **137**(46), pp.14705-14715.

Geiler-Samerotte, K.A., Dion, M.F., Budnik, B.A., Wang, S.M., Hartl, D.L. and Drummond, D.A. 2010. Misfolded proteins impose a dosage-dependent fitness cost and trigger a cytosolic unfolded protein response in yeast. *Proceedings of the National Academy of Sciences.* **108**(2), pp.680-685.

Gentet, L.J., Stuart, G.J. and Clements, J.D. 2000. Direct Measurement of Specific Membrane Capacitance in Neurons. *Biophysical Journal.* **79**(1), pp.314-320.

Giamblanco, N., Coglitore, D., Gubbiotti, A., Ma, T., Balanzat, E., Janot, J.M., Chinappi, M. and Balme, S. 2018a. Amyloid Growth, Inhibition, and Real-Time Enzymatic Degradation Revealed with Single Conical Nanopore. *Anal Chem.* **90**(21), pp.12900-12908.

Giamblanco, N., Coglitore, D., Janot, J.M., Coulon, P.E., Charlot, B. and Balme, S. 2018b. Detection of protein aggregate morphology through single antifouling nanopore. *Sensors and Actuators B: Chemical.* **260**, pp.736-745.

Giamblanco, N., Fichou, Y., Janot, J.M., Balanzat, E., Han, S. and Balme, S. 2020a. Mechanisms of Heparin-Induced Tau Aggregation Revealed by a Single Nanopore. *ACS Sensors.* **5**(4), pp.1158-1167.

Giamblanco, N., Janot, J.M., Gubbiotti, A., Chinappi, M. and Balme, S. 2020b. Characterization of Food Amyloid Protein Digestion by Conical Nanopore. *Small Methods.* p1900703.

Ginzberg, M.B., Kafri, R. and Kirschner, M. 2015. On being the right (cell) size. *Science.* **348**(6236), pp.1245075-1245075.

Glass, Z., Lee, M., Li, Y. and Xu, Q. 2018. Engineering the Delivery System for CRISPR-Based Genome Editing. *Trends in Biotechnology.* **36**(2), pp.173-185.

Glynn, M.W. and McAllister, A.K. 2006. Immunocytochemistry and quantification of protein colocalization in cultured neurons. *Nature Protocols.* **1**(3), pp.1287-1296.

Gnutt, D. and Ebbinghaus, S. 2016. The macromolecular crowding effect – from in vitro into the cell. *Biological Chemistry.* **397**(1), pp.37-44.

Gnutt, D., Gao, M., Brylski, O., Heyden, M. and Ebbinghaus, S. 2015. Excluded-Volume Effects in Living Cells. *Angewandte Chemie International Edition.* **54**(8), pp.2548-2551.

Goins, A.B., Sanabria, H. and Waxham, M.N. 2008. Macromolecular Crowding and Size Effects on Probe Microviscosity. *Biophysical Journal.* **95**(11), pp.5362-5373.

Goldman, S.L., MacKay, M., Afshinnekoo, E., Melnick, A.M., Wu, S. and Mason, C.E. 2019. The Impact of Heterogeneity on Single-Cell Sequencing. *Frontiers in Genetics.* **10**.

Golowasch, J., Thomas, G., Taylor, A.L., Patel, A., Pineda, A., Khalil, C. and Nadim, F. 2009. Membrane Capacitance Measurements Revisited: Dependence of Capacitance Value on Measurement Method in Nonisopotential Neurons. *Journal of Neurophysiology.* **102**(4), pp.2161-2175.

Golshadi, M., Wright, L.K., Dickerson, I.M. and Schrlau, M.G. 2016. High-Efficiency Gene Transfection of Cells through Carbon Nanotube Arrays. *Small.* **12**(22), pp.3014-3020.

Golzio, M., Teissie, J. and Rols, M.P. 2002. Direct visualization at the single-cell level of electrically mediated gene delivery. *Proceedings of the National Academy of Sciences.* **99**(3), pp.1292-1297.

Goto, Y., Adachi, M., Muta, H. and So, M. 2017. Salt-induced formations of partially folded intermediates and amyloid fibrils suggests a common underlying mechanism. *Biophysical Reviews.* **10**(2), pp.493-502.

Graf, M., Lihter, M., Thakur, M., Georgiou, V., Topolancik, J., Ilic, B.R., Liu, K., Feng, J., Astier, Y. and Radenovic, A. 2019. Fabrication and practical applications of molybdenum disulfide nanopores. *Nature Protocols.* **14**(4), pp.1130-1168.

Grant, B.D. and Donaldson, J.G. 2009. Pathways and mechanisms of endocytic recycling. *Nature Reviews Molecular Cell Biology.* **10**(9), pp.597-608.

Graumann, K. and Evans, D.E. 2017. The Nuclear Envelope - Structure and Protein Interactions. In: Roberts, J. ed. *Annual Plant Reviews online.* John Wiley & Sons, Ltd., pp.19-56.

Gribaudo, S., Tixador, P., Bousset, L., Fenyi, A., Lino, P., Melki, R., Peyrin, J.-M. and Perrier, A.L. 2019. Propagation of α-Synuclein Strains within Human Reconstructed Neuronal Network. *Stem Cell Reports.* **12**(2), pp.230-244.

Grosberg, A.Y. and Rabin, Y. 2010. DNA capture into a nanopore: Interplay of diffusion and electrohydrodynamics. *The Journal of Chemical Physics.* **133**(16), p165102.

Guerrero-Ferreira, R., Kovacik, L., Ni, D. and Stahlberg, H. 2020. New insights on the structure of alpha-synuclein fibrils using cryo-electron microscopy. *Current Opinion in Neurobiology.* **61**, pp.89-95.

Guerrero-Ferreira, R., Taylor, N.M.I., Arteni, A.-A., Kumari, P., Mona, D., Ringler, P., Britschgi, M., Lauer, M.E., Makky, A., Verasdonck, J., Riek, R., Melki, R., Meier, B.H., Böckmann, A., Bousset, L. and Stahlberg, H. 2019. Two new polymorphic structures of human full-length alpha-synuclein fibrils solved by cryo-electron microscopy. *eLife.* **8**.

Guillaume-Gentil, O., Grindberg, R.V., Kooger, R., Dorwling-Carter, L., Martinez, V., Ossola, D., Pilhofer, M., Zambelli, T. and Vorholt, J.A. 2016. Tunable Single-Cell Extraction for Molecular Analyses. *Cell.* **166**(2), pp.506-516.

Guillaume-Gentil, O., Potthoff, E., Ossola, D., Dorig, P., Zambelli, T. and Vorholt, J.A. 2013. Force-controlled fluidic injection into single cell nuclei. *Small.* **9**(11), pp.1904-1907.

Halff, E.F., Versteeg, M., Brondijk, T.H.C. and Huizinga, E.G. 2014. When less becomes more: Optimization of protein expression in HEK293–EBNA1 cells using plasmid titration – A case study for NLRs. *Protein Expression and Purification.* **99**, pp.27-34.

Hall, D. and Minton, A.P. 2003. Macromolecular crowding: qualitative and semiquantitative successes, quantitative challenges. *Biochimica et Biophysica Acta (BBA) - Proteins and Proteomics.* **1649**(2), pp.127-139.

Hansma, P., Drake, B., Marti, O., Gould, S. and Prater, C. 1989. The scanning ion-conductance microscope. *Science.* **243**(4891), pp.641-643.

Happel, P., Hoffmann, G., Mann, S.A. and Dietzel, I.D. 2003. Monitoring cell movements and volume changes with pulse-mode scanning ion conductance microscopy. *Journal of Microscopy.* **212**(2), pp.144-151.

Harrell, C.C., Choi, Y., Horne, L.P., Baker, L.A., Siwy, Z.S. and Martin, C.R. 2006. Resistive-Pulse DNA Detection with a Conical Nanopore Sensor†. *Langmuir.* **22**(25), pp.10837-10843.

Hashmi, S.A. 1998. Influence of water absorption on poly–ethylene oxide-based polymer electrolytes complexed with ammonium, sodium and magnesium perchlorates. *Journal of Materials Science.* **33**(4), pp.989-993.

Hasin, Y., Seldin, M. and Lusis, A. 2017. Multi-omics approaches to disease. *Genome Biology.* **18**(1).

He, G., Feng, J., Zhang, A., Zhou, L., Wen, R., Wu, J., Yang, C., Yang, J., Li, C., Chen, D., Wang, J., Hu, N. and Xie, X. 2019. Multifunctional Branched Nanostraw-Electroporation Platform for Intracellular Regulation and Monitoring of Circulating Tumor Cells. *Nano Letters.* **19**(10), pp.7201-7209.

He, Y., Tsutsui, M., Scheicher, Ralph H., Fan, C., Taniguchi, M. and Kawai, T. 2013. Mechanism of How Salt-Gradient-Induced Charges Affect the Translocation of DNA Molecules through a Nanopore. *Biophysical Journal.* **105**(3), pp.776-782.

He, Z., Zhu, Y. and Gu, H. 2013. A new method for the determination of critical polyethylene glycol concentration for selective precipitation of DNA fragments. *Applied Microbiology and Biotechnology.* **97**(20), pp.9175-9183.

Heath, G.R., Kots, E., Robertson, J.L., Lansky, S., Khelashvili, G., Weinstein, H. and Scheuring, S. 2021. Localization atomic force microscopy. *Nature.* **594**(7863), pp.385-390.

Hebisch, E., Hjort, M., Volpati, D. and Prinz, C.N. 2021. Nanostraw-Assisted Cellular Injection of Fluorescent Nanodiamonds via Direct Membrane Opening. *Small.* p2006421.

Hennig, S., van de Linde, S., Lummer, M., Simonis, M., Huser, T. and Sauer, M. 2015. Instant Live-Cell Super-Resolution Imaging of Cellular Structures by Nanoinjection of Fluorescent Probes. *Nano Letters.* **15**(2), pp.1374-1381.

Higgins, N.P. and Vologodskii, A.V. 2015. Topological Behavior of Plasmid DNA. *Microbiology Spectrum.* **3**(2).

Higgins, S.G. and Stevens, M.M. 2017. Extracting the contents of living cells. *Science.* **356**(6336), pp.379-380.

Hijaz, B.A. and Volpicelli-Daley, L.A. 2020. Initiation and propagation of α-synuclein aggregation in the nervous system. *Molecular Neurodegeneration.* **15**(1).

Hinchcliffe, E.H., Day, C.A., Karanjeet, K.B., Fadness, S., Langfald, A., Vaughan, K.T. and Dong, Z. 2016. Chromosome missegregation during anaphase triggers p53 cell cycle arrest through histone H3.3 Ser31 phosphorylation. *Nature Cell Biology.* **18**(6), pp.668-675.

Hirose, H., Takeuchi, T., Osakada, H., Pujals, S., Katayama, S., Nakase, I., Kobayashi, S., Haraguchi, T. and Futaki, S. 2012. Transient focal membrane deformation induced by arginine-rich peptides leads to their direct penetration into cells. *Mol Ther.* **20**(5), pp.984-993.

Hoffmann, E.K., Lambert, I.H. and Pedersen, S.F. 2009. Physiology of Cell Volume Regulation in Vertebrates. *Physiological Reviews.* **89**(1), pp.193-277.

Hong, P., Koza, S. and Bouvier, E.S.P. 2012. A Review Size-Exclusion Chromatography for the Analysis of Protein Biotherapeutics and Their Aggregates. *Journal of Liquid Chromatography & Related Technologies.* **35**(20), pp.2923-2950.

Hossan, M.R., Dutta, D., Islam, N. and Dutta, P. 2018. Review: Electric field driven pumping in microfluidic device. *Electrophoresis.* **39**(5-6), pp.702-731.

Houghtaling, J., List, J. and Mayer, M. 2018. Nanopore-Based, Rapid Characterization of Individual Amyloid Particles in Solution: Concepts, Challenges, and Prospects. *Small.* **14**(46), pe1802412.

Houghtaling, J., Ying, C., Eggenberger, O.M., Fennouri, A., Nandivada, S., Acharjee, M., Li, J., Hall, A.R. and Mayer, M. 2019. Estimation of Shape, Volume, and Dipole Moment of Individual Proteins Freely Transiting a Synthetic Nanopore. *ACS Nano.* **13**(5), pp.5231-5242.

Howorka, S., Cheley, S. and Bayley, H. 2001. Sequence-specific detection of individual DNA strands using engineered nanopores. *Nature Biotechnology.* **19**(7), pp.636-639.

Howorka, S. and Siwy, Z.S. 2020. Reading amino acids in a nanopore. *Nature Biotechnology.* **38**(2), pp.159-160.

Hu, R., Diao, J., Li, J., Tang, Z., Li, X., Leitz, J., Long, J., Liu, J., Yu, D. and Zhao, Q. 2016. Intrinsic and membrane-facilitated alpha-synuclein oligomerization revealed by label-free detection through solid-state nanopores. *Scientific Reports.* **6**(1), p20776.

Hu, X., Hu, J., Tian, J., Ge, Z., Zhang, G., Luo, K. and Liu, S. 2013. Polyprodrug Amphiphiles: Hierarchical Assemblies for Shape-Regulated Cellular Internalization, Trafficking, and Drug Delivery. *Journal of the American Chemical Society.* **135**(46), pp.17617-17629.

Huang, G., Voet, A. and Maglia, G. 2019. FraC nanopores with adjustable diameter identify the mass of opposite-charge peptides with 44 dalton resolution. *Nature Communications.* **10**(1), p835.

Huang, J.A., Caprettini, V., Zhao, Y., Melle, G., Maccaferri, N., Deleye, L., Zambrana-Puyalto, X., Ardini, M., Tantussi, F., Dipalo, M. and De Angelis, F. 2019. On-Demand Intracellular Delivery of Single Particles in Single Cells by 3D Hollow Nanoelectrodes. *Nano Letters.* **19**(2), pp.722-731.

Hunter, M., Yuan, P., Vavilala, D. and Fox, M. 2019. Optimization of Protein Expression in Mammalian Cells. *Current Protocols in Protein Science.* **95**(1), pe77.

Hwang, B., Lee, J.H. and Bang, D. 2018. Single-cell RNA sequencing technologies and bioinformatics

pipelines. *Experimental & Molecular Medicine.* **50**(8), pp.1-14.

Iadanza, M.G., Jackson, M.P., Hewitt, E.W., Ranson, N.A. and Radford, S.E. 2018. A new era for understanding amyloid structures and disease. *Nature Reviews Molecular Cell Biology.* **19**(12), pp.755-773.

Iadanza, M.G., Jackson, M.P., Radford, S.E. and Ranson, N.A. 2016. MpUL-multi: Software for Calculation of Amyloid Fibril Mass per Unit Length from TB-TEM Images. *Scientific Reports.* **6**(1), p21078.

Inglut, C.T., Sorrin, A.J., Kuruppu, T., Vig, S., Cicalo, J., Ahmad, H. and Huang, H.C. 2020. Immunological and Toxicological Considerations for the Design of Liposomes. *Nanomaterials.* **10**(2), p190.

Íñigo-Marco, I., Valencia, M., Larrea, L., Bugallo, R., Martínez-Goikoetxea, M., Zuriguel, I. and Arrasate, M. 2017. E46K α-synuclein pathological mutation causes cell-autonomous toxicity without altering protein turnover or aggregation. *Proceedings of the National Academy of Sciences.* **114**(39), pp.E8274-E8283.

Iqbal, S.M., Akin, D. and Bashir, R. 2007. Solid-state nanopore channels with DNA selectivity. *Nature Nanotechnology.* **2**(4), pp.243-248.

Itahana, K., Itahana, Y. and Dimri, G.P. 2013. Colorimetric Detection of Senescence-Associated β Galactosidase. *Methods in Molecular Biology.* **965**, pp.143-156.

Ivanov, A.P., Actis, P., Jonsson, P., Klenerman, D., Korchev, Y. and Edel, J.B. 2015. On-Demand Delivery of Single DNA Molecules Using Nanopipets. *ACS Nano.* **9**(4), pp.3587-3595.

Jacobs, D., Hoogerheide, D.P., Rovini, A., Jiang, Z., Lee, J.C., Rostovtseva, T.K. and Bezrukov, S.M. 2019. Probing Membrane Association of α-Synuclein Domains with VDAC Nanopore Reveals Unexpected Binding Pattern. *Scientific Reports.* **9**(1), p4580.

Jain, M., Fiddes, I.T., Miga, K.H., Olsen, H.E., Paten, B. and Akeson, M. 2015. Improved data analysis for the MinION nanopore sequencer. *Nature Methods.* **12**(4), pp.351-356.

Jakhria, T., Hellewell, A.L., Porter, M.Y., Jackson, M.P., Tipping, K.W., Xue, W.-F., Radford, S.E. and Hewitt, E.W. 2014. β2-Microglobulin Amyloid Fibrils Are Nanoparticles That Disrupt Lysosomal Membrane Protein Trafficking and Inhibit Protein Degradation by Lysosomes. *Journal of Biological Chemistry.* **289**(52), pp.35781-35794.

Jalili, N. and Laxminarayana, K. 2004. A review of atomic force microscopy imaging systems: application to molecular metrology and biological sciences. *Mechatronics.* **14**(8), pp.907-945.

Jansen, R., Embden, J.D.A.v., Gaastra, W. and Schouls, L.M. 2002. Identification of genes that are associated with DNA repeats in prokaryotes. *Molecular Microbiology.* **43**(6), pp.1565-1575.

Jayant, K., Wenzel, M., Bando, Y., Hamm, J.P., Mandriota, N., Rabinowitz, J.H., Plante, I.J., Owen, J.S., Sahin, O., Shepard, K.L. and Yuste, R. 2019. Flexible Nanopipettes for Minimally Invasive Intracellular Electrophysiology In Vivo. *Cell Reports.* **26**(1), pp.266-278 e265.

Jimenez, A.J., Maiuri, P., Lafaurie-Janvore, J., Divoux, S., Piel, M. and Perez, F. 2014. ESCRT Machinery Is Required for Plasma Membrane Repair. *Science.* **343**(6174), pp.1247136-1247136.

Jin, P., Mukaibo, H., Horne, L.P., Bishop, G.W. and Martin, C.R. 2010. Electroosmotic Flow Rectification in Pyramidal-Pore Mica Membranes. *Journal of the American Chemical Society.* **132**(7), pp.2118-2119.

Juers, D.H., Matthews, B.W. and Huber, R.E. 2012. LacZ β-galactosidase: Structure and function of an enzyme of historical and molecular biological importance. *Protein Science.* **21**(12), pp.1792-1807.

Jung, G.-E., Noh, H., Shin, Y.K., Kahng, S.-J., Baik, K.Y., Kim, H.-B., Cho, N.-J. and Cho, S.-J. 2015. Closed-loop ARS mode for scanning ion conductance microscopy with improved speed and stability for live cell imaging applications. *Nanoscale.* **7**(25), pp.10989-10997.

Kaczmarczyk, S.J., Sitaraman, K., Young, H.A., Hughes, S.H. and Chatterjee, D.K. 2011. Protein delivery using engineered virus-like particles. *Proceedings of the National Academy of Sciences.* **108**(41), pp.16998-17003.

Kafri, M., Metzl-Raz, E., Jona, G. and Barkai, N. 2016. The Cost of Protein Production. *Cell Reports.* **14**(1), pp.22-31.

Kahle, P.J., Hassink, G.C., Raiss, C.C., Segers-Nolten, I.M.J., van Wezel, R.J.A., Subramaniam, V., le Feber, J. and Claessens, M.M.A.E. 2018. Exogenous α-synuclein hinders synaptic communication in cultured cortical primary rat neurons. *Plos One.* **13**(3), pe0193763.

Kaksonen, M. and Roux, A. 2018. Mechanisms of clathrin-mediated endocytosis. *Nature Reviews Molecular Cell Biology.* **19**(5), pp.313-326.

Kaminski Schierle, G.S., Bertoncini, C.W., Chan, F.T.S., van der Goot, A.T., Schwedler, S., Skepper, J., Schlachter, S., van Ham, T., Esposito, A., Kumita, J.R., Nollen, E.A.A., Dobson, C.M. and Kaminski, C.F. 2011. A FRET Sensor for Non-Invasive Imaging of Amyloid Formation in Vivo. *ChemPhysChem.* **12**(3), pp.673-680.

Kang, W., Yavari, F., Minary-Jolandan, M., Giraldo-Vela, J.P., Safi, A., McNaughton, R.L., Parpoil, V. and Espinosa, H.D. 2013. Nanofountain Probe Electroporation (NFP-E) of Single Cells. *Nano Letters.* **13**(6), pp.2448-2457.

Karbstein, K. and Hancock, R. 2012. Structure of Metaphase Chromosomes: A Role for Effects of Macromolecular Crowding. *PLOS ONE.* **7**(4), pe36045.

Kasianowicz, J.J., Brandin, E., Branton, D. and Deamer, D.W. 1996. Characterization of individual polynucleotide molecules using a membrane channel. *Proceedings of the National Academy of Sciences.* **93**(24), pp.13770-13773.

Ke, P.C., Zhou, R., Serpell, L.C., Riek, R., Knowles, T.P.J., Lashuel, H.A., Gazit, E., Hamley, I.W., Davis, T.P., Fändrich, M., Otzen, D.E., Chapman, M.R., Dobson, C.M., Eisenberg, D.S. and Mezzenga, R. 2020. Half a century of amyloids: past, present and future. *Chemical Society Reviews.* **49**(15), pp.5473-5509.

Keppeke, G., Andrade, L.E.C., Grieshaber, S.S. and Chan, E.K.L. 2015. Microinjection of specific anti-IMPDH2 antibodies induces disassembly of cytoplasmic rods/rings that are primarily stationary and stable structures. *Cell & Bioscience.* **5**(1), p1.

Kim, J.-s., Choi, D.-K., Park, S.-w., Shin, S.-M., Bae, J., Kim, D.-M., Yoo, T.H. and Kim, Y.-S. 2015. Quantitative assessment of cellular uptake and cytosolic access of antibody in living cells by an enhanced split GFP complementation assay. *Biochemical and Biophysical Research Communications.* **467**(4), pp.771-777.

Kim, S., Kim, D., Cho, S.W., Kim, J. and Kim, J.S. 2014. Highly efficient RNA-guided genome editing in human cells via delivery of purified Cas9 ribonucleoproteins. *Genome Res.* **24**(6), pp.1012-1019.

Kim, T.K. and Eberwine, J.H. 2010. Mammalian cell transfection: the present and the future. *Analytical and Bioanalytical Chemistry.* **397**(8), pp.3173-3178.

Kintaka, R., Makanae, K. and Moriya, H. 2016. Cellular growth defects triggered by an overload of protein localization processes. *Scientific Reports.* **6**(1).

Kirton, H.M., Pettinger, L. and Gamper, N. 2013. Transient Overexpression of Genes in Neurons Using Nucleofection. *Methods in Molecular Biology.* **998**, pp.55-64.

Klenerman, D., Shevchuk, A., Novak, P., Korchev, Y.E. and Davis, S.J. 2013. Imaging the cell surface and its organization down to the level of single molecules. *Philosophical Transactions of the Royal Society B: Biological Sciences.* **368**(1611), p20120027.

Knowles, D.B., LaCroix, A.S., Deines, N.F., Shkel, I. and Record, M.T. 2011. Separation of preferential interaction and excluded volume effects on DNA duplex and hairpin stability. *Proceedings of the National Academy of Sciences.* **108**(31), pp.12699-12704.

Kolašinac, R., Jaksch, S., Dreissen, G., Braeutigam, A., Merkel, R. and Csiszár, A. 2019. Influence of Environmental Conditions on the Fusion of Cationic Liposomes with Living Mammalian Cells. *Nanomaterials.* **9**(7), p1025.

Kong, J., Wu, H., Liu, L., Xie, X., Wu, L., Ye, X. and Liu, Q. 2013. Silicon Nitride Nanopores for Nanoparticle Sensing. *Journal of Nanoscience and Nanotechnology.* **13**(6), pp.4010-4016.

König, I., Soranno, A., Nettels, D. and Schuler, B. 2021. Impact of In-Cell and In-Vitro Crowding on the Conformations and Dynamics of an Intrinsically Disordered Protein. *Angewandte Chemie International Edition.* **60**(19), pp.10724-10729.

Konopka, M.C., Shkel, I.A., Cayley, S., Record, M.T. and Weisshaar, J.C. 2006. Crowding and Confinement Effects on Protein Diffusion In Vivo. *Journal of Bacteriology.* **188**(17), pp.6115-6123.

Kotnik, T., Rems, L., Tarek, M. and Miklavčič, D. 2019. Membrane Electroporation and Electropermeabilization: Mechanisms and Models. *Annual Review of Biophysics.* **48**(1), pp.63-91.

Kowalczyk, S.W. and Dekker, C. 2012. Measurement of the Docking Time of a DNA Molecule onto a Solid-State Nanopore. *Nano Letters.* **12**(8), pp.4159-4163.

Kowalczyk, S.W., Wells, D.B., Aksimentiev, A. and Dekker, C. 2012. Slowing down DNA Translocation through a Nanopore in Lithium Chloride. *Nano Letters.* **12**(2), pp.1038-1044.

Kristensen, M., de Groot, A.M., Berthelsen, J., Franzyk, H., Sijts, A. and Nielsen, H.M. 2015. Conjugation of Cell-Penetrating Peptides to Parathyroid Hormone Affects Its Structure, Potency, and Transepithelial Permeation. *Bioconjugate Chemistry.* **26**(3), pp.477-488.

Kumar Sharma, R., Agrawal, I., Dai, L., Doyle, P.S. and Garaj, S. 2019. Complex DNA knots detected with a nanopore sensor. *Nature Communications.* **10**(1), p4473.

Kumari, S., Mg, S. and Mayor, S. 2010. Endocytosis unplugged: multiple ways to enter the cell. *Cell Research.* **20**(3), pp.256-275.

Kumei, Y., Nakajima, T., Sato, A., Kamata, N. and Enomoto, S. 1989. Reduction of G1 phase duration and enhancement of c-myc gene expression in HeLa cells at hypergravity. *J Cell Sci.* **93 (Pt 2)**, pp.221-226.

Kurata, K., Yoshii, T., Uchida, S., Fukunaga, T. and Takamatsu, H. 2012. Visualization of electroporation-induced temperature rise using temperature-sensitive ink. *International Journal of Heat and Mass Transfer.* **55**(23-24), pp.7207-7212.

Kurz, V., Tanaka, T. and Timp, G. 2014. Single Cell Transfection with Single Molecule Resolution Using a Synthetic Nanopore. *Nano Letters.* **14**(2), pp.604-611.

Kuznetsova, I., Turoverov, K. and Uversky, V. 2014. What Macromolecular Crowding Can Do to a Protein. *International Journal of Molecular Sciences.* **15**(12), pp.23090-23140.

Laforge, F.O., Carpino, J., Rotenberg, S.A. and Mirkin, M.V. 2007. Electrochemical attosyringe. *Proceedings of the National Academy of Sciences.* **104**(29), pp.11895-11900.

Lan, W.-J., Edwards, M.A., Luo, L., Perera, R.T., Wu, X., Martin, C.R. and White, H.S. 2016. Voltage-Rectified Current and Fluid Flow in Conical Nanopores. *Accounts of Chemical Research.* **49**(11), pp.2605-2613.

Lan, W.-J., Kubeil, C., Xiong, J.-W., Bund, A. and White, H.S. 2014. Effect of Surface Charge on the Resistive Pulse Waveshape during Particle Translocation through Glass Nanopores. *The Journal of Physical Chemistry C.* **118**(5), pp.2726-2734.

Laohakunakorn, N., Gollnick, B., Moreno-Herrero, F., Aarts, D.G.A.L., Dullens, R.P.A., Ghosal, S. and Keyser, U.F. 2013. A Landau–Squire Nanojet. *Nano Letters.* **13**(11), pp.5141-5146.

Laohakunakorn, N. and Keyser, U.F. 2015. Electroosmotic flow rectification in conical nanopores. *Nanotechnology.* **26**(27), p275202.

Laohakunakorn, N., Thacker, V.V., Muthukumar, M. and Keyser, U.F. 2014. Electroosmotic Flow Reversal Outside Glass Nanopores. *Nano Letters.* **15**(1), pp.695-702.

Lappalainen, K., Jaaskelainen, I., Syrjanen, K., Urtti, A. and Syrjanen, S. 1994. Comparison of cell proliferation and toxicity assays using two cationic liposomes. *Pharm Res.* **11**(8), pp.1127-1131.

Larimi, M.G., Mayse, L.A. and Movileanu, L. 2019. Interactions of a Polypeptide with a Protein Nanopore Under Crowding Conditions. *ACS Nano.* **13**(4), pp.4469-4477.

Laszlo, A.H., Derrington, I.M. and Gundlach, J.H. 2016. MspA nanopore as a single-molecule tool: From sequencing to SPRNT. *Methods.* **105**, pp.75-89.

Lebeaupin, T., Smith, R. and Huet, S. 2018. The Multiple Effects of Molecular Crowding in the Cell Nucleus. In: Lavelle, C. and Victor, J.M. eds. *Nuclear Architecture and Dynamics.* Elsevier, pp.209-232.

Lechardeur, D., Sohn, K.J., Haardt, M., Joshi, P.B., Monck, M., Graham, R.W., Beatty, B., Squire, J., O'Brodovich, H. and Lukacs, G.L. 1999. Metabolic instability of plasmid DNA in the cytosol: a potential barrier to gene transfer. *Gene Therapy.* **6**(4), pp.482-497.

Lee, B.Y., Han, J.A., Im, J.S., Morrone, A., Johung, K., Goodwin, E.C., Kleijer, W.J., DiMaio, D. and Hwang, E.S. 2006. Senescence-associated β-galactosidase is lysosomal β-galactosidase. *Aging Cell.* **5**(2), pp.187-195.

Lee, Y.-W., Luther, D.C., Kretzmann, J.A., Burden, A., Jeon, T., Zhai, S. and Rotello, V.M. 2019. Protein Delivery into the Cell Cytosol using Non-Viral Nanocarriers. *Theranostics.* **9**(11), pp.3280-3292.

Lenz, P., Bacot, S.M., Frazier-Jessen, M.R. and Feldman, G.M. 2003. Nucleoporation of dendritic cells: efficient gene transfer by electroporation into human monocyte-derived dendritic cells. *FEBS Letters.* **538**(1-3), pp.149-154.

Leo-Macias, A., Agullo-Pascual, E., Sanchez-Alonso, J.L., Keegan, S., Lin, X., Arcos, T., Feng Xia, L., Korchev, Y.E., Gorelik, J., Fenyö, D., Rothenberg, E. and Delmar, M. 2016. Nanoscale visualization of functional adhesion/excitability nodes at the intercalated disc. *Nature Communications.* **7**(1), p10342.

Li, B., Ponjavic, A., Chen, W.-H., Hopkins, L., Hughes, C., Ye, Y., Bryant, C. and Klenerman, D. 2021. Single-Molecule Light-Sheet Microscopy with Local Nanopipette Delivery. *Analytical Chemistry.* **93**(8), pp.4092-4099.

Li, C. and Pielak, G.J. 2009. Using NMR to Distinguish Viscosity Effects from Nonspecific Protein Binding under Crowded Conditions. *Journal of the American Chemical Society.* **131**(4), pp.1368-1369.

Li, J. and Talaga, D.S. 2010. The distribution of DNA translocation times in solid-state nanopores. *Journal of Physics: Condensed Matter.* **22**(45), p454129.

Li, W., Bell, N.A.W., Hernández-Ainsa, S., Thacker, V.V., Thackray, A.M., Bujdoso, R. and Keyser, U.F. 2013. Single Protein Molecule Detection by Glass Nanopores. *ACS Nano.* **7**(5), pp.4129-4134.

Li, X., Cheng, S., Zheng, Y. and Li, C.Y. 2019. Morphology control in semicrystalline solid polymer electrolytes for lithium batteries. *Molecular Systems Design & Engineering.* **4**(4), pp.793-803.

Li, X., Jiang, Y., Chong, S. and Walt, D.R. 2018. Bottom-up single-molecule strategy for understanding subunit function of tetrameric β-galactosidase. *Proceedings of the National Academy of Sciences.* **115**(33), pp.8346-8351.

Li, X., Tong, X., Lu, W., Yu, D., Diao, J. and Zhao, Q. 2019. Label-free detection of early oligomerization of α-synuclein and its mutants A30P/E46K through solid-state nanopores. *Nanoscale.* **11**(13), pp.6480-6488.

Li, Y., Eshein, A., Virk, R.K.A., Eid, A., Wu, W., Frederick, J., VanDerway, D., Gladstein, S., Huang, K., Shim, A.R., Anthony, N.M., Bauer, G.M., Zhou, X., Agrawal, V., Pujadas, E.M., Jain, S., Esteve, G., Chandler, J.E., Nguyen, T.-Q., Bleher, R., de Pablo, J.J., Szleifer, I., Dravid, V.P., Almassalha, L.M. and Backman, V. 2021. Nanoscale chromatin imaging and analysis platform bridges 4D chromatin organization with molecular function. *Science Advances.* **7**(1), peabe4310.

Li, Y., Wu, M., Zhao, D., Wei, Z., Zhong, W., Wang, X., Liang, Z. and Li, Z. 2015. Electroporation on microchips: the harmful effects of pH changes and scaling down. *Scientific Reports.* **5**(1), p17817.

Lin, S., Staahl, B.T., Alla, R.K. and Doudna, J.A. 2014. Enhanced homology-directed human genome engineering by controlled timing of CRISPR/Cas9 delivery. *eLife.* **3**, pe04766.

Linegar, K.L., Adeniran, A.E., Kostko, A.F. and Anisimov, M.A. 2010. Hydrodynamic radius of polyethylene glycol in solution obtained by dynamic light scattering. *Colloid Journal.* **72**(2), pp.279-281.

Liu, J., Wen, J., Zhang, Z., Liu, H. and Sun, Y. 2015. Voyage inside the cell: Microsystems and nanoengineering for intracellular measurement and manipulation. *Microsystems & Nanoengineering.* **1**(1), p15020.

Loman, N.J. and Watson, M. 2015. Successful test launch for nanopore sequencing. *Nature Methods.* **12**(4), pp.303-304.

Löwe, M., Kalacheva, M., Boersma, A.J. and Kedrov, A. 2020. The more the merrier: effects of macromolecular crowding on the structure and dynamics of biological membranes. *The FEBS Journal.* **287**(23), pp.5039-5067.

Lu, V.B., Williams, D.J., Won, Y.-J. and Ikeda, S.R. 2009. Intranuclear Microinjection of DNA into Dissociated Adult Mammalian Neurons. *Journal of Visualized Experiments.* (34), p1614.

Luan, B., Wang, D., Zhou, R., Harrer, S., Peng, H. and Stolovitzky, G. 2012. Dynamics of DNA translocation in a solid-state nanopore immersed in aqueous glycerol. *Nanotechnology.* **23**(45), p455102.

Luft, C. and Ketteler, R. 2015. Electroporation Knows No Boundaries: The Use of Electrostimulation for siRNA Delivery in Cells and Tissues. *J Biomol Screen.* **20**(8), pp.932-942.

Luk, K.C., Kehm, V., Carroll, J., Zhang, B., O'Brien, P., Trojanowski, J.Q. and Lee, V.M.Y. 2012. Pathological -Synuclein Transmission Initiates Parkinson-like Neurodegeneration in Nontransgenic Mice. *Science.* **338**(6109), pp.949-953.

Luo, L., Holden, D.A., Lan, W.-J. and White, H.S. 2012. Tunable Negative Differential Electrolyte Resistance in a Conical Nanopore in Glass. *ACS Nano.* **6**(7), pp.6507-6514.

Lutter, L., Serpell, C.J., Tuite, M.F. and Xue, W.-F. 2019. The molecular lifecycle of amyloid – Mechanism of assembly, mesoscopic organisation, polymorphism, suprastructures, and biological consequences. *Biochimica et Biophysica Acta (BBA) - Proteins and Proteomics.* **1867**(11), p140257.

Lyon, A.R., MacLeod, K.T., Zhang, Y., Garcia, E., Kanda, G.K., Lab, M.J., Korchev, Y.E., Harding, S.E. and Gorelik, J. 2009. Loss of T-tubules and other changes to surface topography in ventricular myocytes from failing human and rat heart. *Proceedings of the National Academy of Sciences.* **106**(16), pp.6854-6859.

Ma, L., Li, Z., Yuan, Z., Huang, C., Siwy, Z.S. and Qiu, Y. 2020. Modulation of Ionic Current Rectification in Ultrashort Conical Nanopores. *Analytical Chemistry.* **92**(24), pp.16188-16196.

Ma, T., Arroyo, N., Marc Janot, J., Picaud, F. and Balme, S. 2021. Conformation of Polyethylene Glycol inside Confined Space: Simulation and Experimental Approaches. *Nanomaterials.* **11**(1), p244.

Macaulay, I.C., Ponting, C.P. and Voet, T. 2017. Single-Cell Multiomics: Multiple Measurements from Single Cells. *Trends in Genetics.* **33**(2), pp.155-168.

Machado, D.C., Júnior, J.J.S., Melo, M.C.A., Silva, A.M.B., Fontes, A. and Rodrigues, C.G. 2016. Effects of alkali and ammonium ions in the detection of poly(ethyleneglycol) by alpha-hemolysin nanopore sensor. *RSC Advances.* **6**(61), pp.56647-56655.

Madani, F., Lindberg, S., Langel, U., Futaki, S. and Graslund, A. 2011. Mechanisms of cellular uptake of cell-penetrating peptides. *J Biophys.* **2011**, p414729.

Mahul-Mellier, A.-L., Burtscher, J., Maharjan, N., Weerens, L., Croisier, M., Kuttler, F., Leleu, M., Knott, G.W. and Lashuel, H.A. 2020. The process of Lewy body formation, rather than simply α-synuclein fibrillization, is one of the major drivers of neurodegeneration. *Proceedings of the National Academy of Sciences.* **117**(9), pp.4971-4982.

Maity, H., Muttathukattil, A.N. and Reddy, G. 2018. Salt Effects on Protein Folding Thermodynamics. *The Journal of Physical Chemistry Letters.* **9**(17), pp.5063-5070.

Majorek, K.A., Porebski, P.J., Dayal, A., Zimmerman, M.D., Jablonska, K., Stewart, A.J., Chruszcz, M. and Minor, W. 2012. Structural and immunologic characterization of bovine, horse, and rabbit serum albumins. *Molecular Immunology.* **52**(3-4), pp.174-182.

Mao, X., Ou, M.T., Karuppagounder, S.S., Kam, T.I., Yin, X., Xiong, Y., Ge, P., Umanah, G.E., Brahmachari, S., Shin, J.H., Kang, H.C., Zhang, J., Xu, J., Chen, R., Park, H., Andrabi, S.A., Kang, S.U., Goncalves, R.A., Liang, Y., Zhang, S., Qi, C., Lam, S., Keiler, J.A., Tyson, J., Kim, D., Panicker, N., Yun, S.P., Workman, C.J., Vignali, D.A.A., Dawson, V.L., Ko, H.S. and Dawson, T.M. 2016. Pathological -synuclein transmission initiated by binding lymphocyte-activation gene 3. *Science.* **353**(6307), pp.aah3374-aah3374.

Mardoum, W.M., Gorczyca, S.M., Regan, K.E., Wu, T.-C. and Robertson-Anderson, R.M. 2018. Crowding Induces Entropically-Driven Changes to DNA Dynamics That Depend on Crowder Structure and Ionic Conditions. *Frontiers in Physics.* **6**, p53.

Marfori, M., Mynott, A., Ellis, J.J., Mehdi, A.M., Saunders, N.F.W., Curmi, P.M., Forwood, J.K., Bodén, M. and Kobe, B. 2011. Molecular basis for specificity of nuclear import and prediction of nuclear localization. *Biochimica et Biophysica Acta (BBA) - Molecular Cell Research.* **1813**(9), pp.1562-1577.

Marschall, A.L., Zhang, C., Frenzel, A., Schirrmann, T., Hust, M., Perez, F. and Dubel, S. 2014. Delivery of antibodies to the cytosol: debunking the myths. *MAbs.* **6**(4), pp.943-956.

Martyushenko, N., Bell, N.A., Lamboll, R.D. and Keyser, U.F. 2015. Nanopore analysis of amyloid fibrils formed by lysozyme aggregation. *Analyst.* **140**(14), pp.4882-4886.

Mathe, J., Manrao, E.A., Derrington, I.M., Pavlenok, M., Niederweis, M. and Gundlach, J.H. 2011. Nucleotide Discrimination with DNA Immobilized in the MspA Nanopore. *PLOS ONE.* **6**(10), pe25723.

Mc Hugh, J., Andresen, K. and Keyser, U.F. 2019. Cation dependent electroosmotic flow in glass nanopores. *Applied Physics Letters.* **115**(11), p113702.

McKelvey, K., Kinnear, S.L., Perry, D., Momotenko, D. and Unwin, P.R. 2014. Surface Charge Mapping with a Nanopipette. *Journal of the American Chemical Society.* **136**(39), pp.13735-13744.

McKnight, T.E., Melechko, A.V., Hensley, D.K., Mann, D.G.J., Griffin, G.D. and Simpson, M.L. 2004. Tracking Gene Expression after DNA Delivery Using Spatially Indexed Nanofiber Arrays. *Nano Letters.* **4**(7), pp.1213-1219.

Medda, L., Monduzzi, M. and Salis, A. 2015. The molecular motion of bovine serum albumin under physiological conditions is ion specific. *Chemical Communications.* **51**(30), pp.6663-6666.

Meisl, G., Michaels, T.C.T., Linse, S. and Knowles, T.P.J. 2018. Kinetic Analysis of Amyloid Formation. In: Einar M. Sigurdsson, M.C., María Gasset ed. *Amyloid Proteins.* Springer, pp.181-196.

Meister, A., Gabi, M., Behr, P., Studer, P., Vörös, J.n., Niedermann, P., Bitterli, J., Polesel-Maris, J.r.m., Liley, M., Heinzelmann, H. and Zambelli, T. 2009. FluidFM: Combining Atomic Force Microscopy and Nanofluidics in a Universal Liquid Delivery System for Single Cell Applications and Beyond. *Nano Letters.* **9**(6), pp.2501-2507.

Merchant, C.A., Healy, K., Wanunu, M., Ray, V., Peterman, N., Bartel, J., Fischbein, M.D., Venta, K., Luo, Z., Johnson, A.T.C. and Drndić, M. 2010. DNA Translocation through Graphene Nanopores. *Nano Letters.* **10**(8), pp.2915-2921.

Michaels, T.C.T., Šarić, A., Habchi, J., Chia, S., Meisl, G., Vendruscolo, M., Dobson, C.M. and Knowles, T.P.J. 2018. Chemical Kinetics for Bridging Molecular Mechanisms and Macroscopic Measurements of Amyloid Fibril Formation. *Annual Review of Physical Chemistry.* **69**(1), pp.273-298.

Micutkova, L., Hermann, M., Offterdinger, M., Hess, M.W., Matscheski, A., Pircher, H., Mück, C., Ebner, H.-L., Laich, A., Ferrando-May, E., Zwerschke, W., Huber, L.A. and Jansen-Dürr, P. 2012. Analysis of the cellular uptake and nuclear delivery of insulin-like growth factor binding protein-3 in human osteosarcoma cells. *International Journal of Cancer.* **130**(7), pp.1544-1557.

Mika, Jacek T., Thompson, Alexander J., Dent, Michael R., Brooks, Nicholas J., Michiels, J., Hofkens, J. and Kuimova, Marina K. 2016. Measuring the Viscosity of the Escherichia coli Plasma Membrane Using Molecular Rotors. *Biophysical Journal.* **111**(7), pp.1528-1540.

Miles, B.N., Ivanov, A.P., Wilson, K.A., Doğan, F., Japrung, D. and Edel, J.B. 2013. Single molecule sensing with solid-state nanopores: novel materials, methods, and applications. *Chem. Soc. Rev.* **42**(1), pp.15-28.

Minaschek, G., Bereiter-Hahn, J. and Bertholdt, G. 1989. Quantitation of the volume of liquid injected into cells by means of pressure. *Exp Cell Res.* **183**(2), pp.434-442.

Mincarelli, L., Lister, A., Lipscombe, J. and Macaulay, I.C. 2018. Defining Cell Identity with Single-Cell Omics. *Proteomics.* **18**(18), p1700312.

Miragoli, M., Moshkov, A., Novak, P., Shevchuk, A., Nikolaev, V.O., El-Hamamsy, I., Potter, C.M.F., Wright, P., Kadir, S.H.S.A., Lyon, A.R., Mitchell, J.A., Chester, A.H., Klenerman, D., Lab, M.J., Korchev, Y.E., Harding, S.E. and Gorelik, J. 2011. Scanning ion conductance microscopy: a convergent high-resolution technology for multi-parametric analysis of living cardiovascular cells. *Journal of The Royal Society Interface.* **8**(60), pp.913-925.

Mitchenall, L.A., Hipkin, R.E., Piperakis, M.M., Burton, N.P. and Maxwell, A. 2018. A rapid high-resolution method for resolving DNA topoisomers. *BMC Research Notes.* **11**(1), p37.

Mittal, S., Chowhan, R.K. and Singh, L.R. 2015. Macromolecular crowding: Macromolecules friend or foe. *Biochimica et Biophysica Acta (BBA) - General Subjects.* **1850**(9), pp.1822-1831.

Miyagi, T., Yamanaka, Y., Harada, Y., Narumi, S., Hayamizu, Y., Kuroda, M. and Kanekura, K. 2021. An improved molecular crowding sensor CRONOS for detection of crowding changes in membrane-less organelles under pathological conditions. *bioRxiv.* p2021.2003.2031.437991.

Moe, A.M., Golding, A.E. and Bement, W.M. 2015. Cell healing: Calcium, repair and regeneration. *Seminars in Cell & Developmental Biology.* **45**, pp.18-23.

Morel, B., Varela, L., Azuaga, A.I. and Conejero-Lara, F. 2010. Environmental Conditions Affect the Kinetics of Nucleation of Amyloid Fibrils and Determine Their Morphology. *Biophysical Journal.* **99**(11), pp.3801-3810.

Moriya, H. and Cohen-Fix, O. 2015. Quantitative nature of overexpression experiments. *Molecular Biology of the Cell.* **26**(22), pp.3932-3939.

Mourão, Márcio A., Hakim, Joe B. and Schnell, S. 2014. Connecting the Dots: The Effects of Macromolecular Crowding on Cell Physiology. *Biophysical Journal.* **107**(12), pp.2761-2766.

Mugele, F. and Baret, J.-C. 2005. Electrowetting: from basics to applications. *Journal of Physics: Condensed Matter.* **17**(28), pp.R705-R774.

Mukherjee, P., Nathamgari, S.S.P., Kessler, J.A. and Espinosa, H.D. 2018. Combined Numerical and Experimental Investigation of Localized Electroporation-Based Cell Transfection and Sampling. *ACS Nano.* **12**(12), pp.12118-12128.

Murade, C.U. and Shubeita, G.T. 2019. A Molecular Sensor Reveals Differences in Macromolecular Crowding between the Cytoplasm and Nucleoplasm. *ACS Sensors.* **4**(7), pp.1835-1843.

Muthukumar, M., Plesa, C. and Dekker, C. 2015. Single-molecule sensing with nanopores. *Physics Today.* **68**(8), pp.40-46.

Nakajima, M., Mizutani, Y., Iwata, F. and Ushiki, T. 2018. Scanning ion conductance microscopy for visualizing the three-dimensional surface topography of cells and tissues. *Seminars in Cell & Developmental Biology.* **73**, pp.125-131.

Nan, Z., Xu, Q., Zhang, Y. and Ge, W. 2019. Force-Sensing Robotic Microinjection System for Automated Multi-Cell Injection With Consistent Quality. *IEEE Access.* **7**, pp.55543-55553.

Nashimoto, Y., Takahashi, Y., Zhou, Y., Ito, H., Ida, H., Ino, K., Matsue, T. and Shiku, H. 2016. Evaluation of mRNA Localization Using Double Barrel Scanning Ion Conductance Microscopy. *ACS Nano.* **10**(7), pp.6915-6922.

Navikas, V., Leitão, S.M., Marion, S., Davis, S.J., Drake, B., Fantner, G.E. and Radenovic, A. 2020. High-Throughput Nanocapillary Filling Enabled by Microwave Radiation for Scanning Ion Conductance Microscopy Imaging. *ACS Applied Nano Materials.* **3**(8), pp.7829-7834.

Nettesheim, G., Nabti, I., Murade, C.U., Jaffe, G.R., King, S.J. and Shubeita, G.T. 2020. Macromolecular crowding acts as a physical regulator of intracellular transport. *Nature Physics.* **16**(11), pp.1144-1151.

Neumann, E., Schaefer-Ridder, M., Wang, Y. and Hofschneider, P.H. 1982. Gene transfer into mouse lyoma cells by electroporation in high electric fields. *EMBO J.* **1**(7), pp.841-845.

Niedzwiecki, D.J., Chou, Y.C., Xia, Z., Thei, F. and Drndić, M. 2020. Detection of single analyte and environmental samples with silicon nitride nanopores: Antarctic dirt

particulates and DNA in artificial seawater. *Review of Scientific Instruments.* **91**(3), p031301.

Nirmalraj, P.N., List, J., Battacharya, S., Howe, G., Xu, L., Thompson, D. and Mayer, M. 2020. Complete aggregation pathway of amyloid β (1-40) and (1-42) resolved on an atomically clean interface. *Science Advances.* **6**(15), peaaz6014.

Nishizawa, K., Fujiwara, K., Ikenaga, M., Nakajo, N., Yanagisawa, M. and Mizuno, D. 2017. Universal glass-forming behavior of in vitro and living cytoplasm. *Scientific Reports.* **7**(1), p15143.

Nouri, R., Tang, Z. and Guan, W. 2019. Quantitative Analysis of Factors Affecting the Event Rate in Glass Nanopore Sensors. *ACS Sensors.* **4**(11), pp.3007-3013.

Novak, P., Gorelik, J., Vivekananda, U., Shevchuk, Andrew I., Ermolyuk, Yaroslav S., Bailey, Russell J., Bushby, Andrew J., Moss, Guy W.J., Rusakov, Dmitri A., Klenerman, D., Kullmann, Dimitri M., Volynski, Kirill E. and Korchev, Yuri E. 2013. Nanoscale-Targeted Patch-Clamp Recordings of Functional Presynaptic Ion Channels. *Neuron.* **79**(6), pp.1067-1077.

Novak, P., Li, C., Shevchuk, A.I., Stepanyan, R., Caldwell, M., Hughes, S., Smart, T.G., Gorelik, J., Ostanin, V.P., Lab, M.J., Moss, G.W.J., Frolenkov, G.I., Klenerman, D. and Korchev, Y.E. 2009. Nanoscale live-cell imaging using hopping probe ion conductance microscopy. *Nature Methods.* **6**(4), pp.279-281.

Novak, P., Shevchuk, A., Ruenraroengsak, P., Miragoli, M., Thorley, A.J., Klenerman, D., Lab, M.J., Tetley, T.D., Gorelik, J. and Korchev, Y.E. 2014. Imaging Single Nanoparticle Interactions with Human Lung Cells Using Fast Ion Conductance Microscopy. *Nano Letters.* **14**(3), pp.1202-1207.

O'Dea, S., Annibaldi, V., Gallagher, L., Mulholland, J., Molloy, E.L., Breen, C.J., Gilbert, J.L., Martin, D.S., Maguire, M. and Curry, F.R. 2017. Vector-free intracellular delivery by reversible permeabilization. *PLOS ONE.* **12**(3), pe0174779.

Obataya, I., Nakamura, C., Han, S., Nakamura, N. and Miyake, J. 2005. Mechanical sensing of the penetration of various nanoneedles into a living cell using atomic force microscopy. *Biosens Bioelectron.* **20**(8), pp.1652-1655.

Ohki, T., Harada, M. and Okada, T. 2007. Structural and Thermodynamic Aspects of Ionic Solvation in Concentrated Aqueous Poly(ethylene glycol). *The Journal of Physical Chemistry B.* **111**(25), pp.7245-7252.

Orynbayeva, Z., Singhal, R., Vitol, E.A., Schrlau, M.G., Papazoglou, E., Friedman, G. and Gogotsi, Y. 2012. Physiological validation of cell health upon probing with carbon nanotube endoscope and its benefit for single-cell interrogation. *Nanomedicine.* **8**(5), pp.590-598.

Ouldali, H., Sarthak, K., Ensslen, T., Piguet, F., Manivet, P., Pelta, J., Behrends, J.C., Aksimentiev, A. and Oukhaled, A. 2019. Electrical recognition of the twenty proteinogenic amino acids using an aerolysin nanopore. *Nature Biotechnology.* **38**(2), pp.176-181.

Page, A., Perry, D. and Unwin, P.R. 2017. Multifunctional scanning ion conductance microscopy. *Proceedings of the Royal Society A: Mathematical, Physical and Engineering Sciences.* **473**(2200), p20160889.

Page, A., Perry, D., Young, P., Mitchell, D., Frenguelli, B.G. and Unwin, P.R. 2016. Fast Nanoscale Surface Charge Mapping with Pulsed-Potential Scanning Ion Conductance Microscopy. *Analytical Chemistry.* **88**(22), pp.10854-10859.

Pan, R., Hu, K., Jia, R., Rotenberg, S.A., Jiang, D. and Mirkin, M.V. 2020. Resistive-Pulse Sensing Inside Single Living Cells. *Journal of the American Chemical Society.* **142**(12), pp.5778-5784.

Park, S.-H., Kukushkin, Y., Gupta, R., Chen, T., Konagai, A., Hipp, Mark S., Hayer-Hartl, M. and Hartl, F.U. 2013. PolyQ Proteins Interfere with Nuclear Degradation of Cytosolic Proteins by Sequestering the Sis1p Chaperone. *Cell.* **154**(1), pp.134-145.

Paslawski, W., Andreasen, M., Nielsen, S.B., Lorenzen, N., Thomsen, K., Kaspersen, J.D., Pedersen, J.S. and Otzen, D.E. 2014a. High Stability and Cooperative Unfolding of α-Synuclein Oligomers. *Biochemistry.* **53**(39), pp.6252-6263.

Paslawski, W., Mysling, S., Thomsen, K., Jørgensen, T.J.D. and Otzen, D.E. 2014b. Co-existence of Two Different α-Synuclein Oligomers with Different Core Structures Determined by Hydrogen/Deuterium Exchange Mass Spectrometry. *Angewandte Chemie International Edition.* **53**(29), pp.7560-7563.

Patel, S.G., Sayers, E.J., He, L., Narayan, R., Williams, T.L., Mills, E.M., Allemann, R.K., Luk, L.Y.P., Jones, A.T. and Tsai, Y.H. 2019. Cell-penetrating peptide sequence and modification dependent uptake and subcellular distribution of green florescent protein in different cell lines. *Scientific Reports.* **9**(1), p6298.

Patterson, D., Schwarz, B., Avera, J., Western, B., Hicks, M., Krugler, P., Terra, M., Uchida, M., McCoy, K. and Douglas, T. 2017. Sortase-Mediated Ligation as a Modular Approach for the Covalent Attachment of Proteins to the Exterior of the Bacteriophage P22 Virus-like Particle. *Bioconjug Chem.* **28**(8), pp.2114-2124.

Peelaerts, W., Bousset, L., Van der Perren, A., Moskalyuk, A., Pulizzi, R., Giugliano, M., Van den Haute, C., Melki, R. and Baekelandt, V. 2015a. alpha-Synuclein strains cause distinct synucleinopathies after local and systemic administration. *Nature.* **522**(7556), pp.340-344.

Peelaerts, W., Bousset, L., Van der Perren, A., Moskalyuk, A., Pulizzi, R., Giugliano, M., Van den Haute, C., Melki, R. and Baekelandt, V. 2015b. α-Synuclein strains cause distinct synucleinopathies after local and systemic administration. *Nature.* **522**(7556), pp.340-344.

Pei, D. and Buyanova, M. 2019. Overcoming Endosomal Entrapment in Drug Delivery. *Bioconjug Chem.* **30**(2), pp.273-283.

Perera, R.T., Johnson, R.P., Edwards, M.A. and White, H.S. 2015. Effect of the Electric Double Layer on the Activation Energy of Ion Transport in Conical Nanopores. *The Journal of Physical Chemistry C.* **119**(43), pp.24299-24306.

Perry, D., Al Botros, R., Momotenko, D., Kinnear, S.L. and Unwin, P.R. 2015. Simultaneous Nanoscale Surface Charge and Topographical Mapping. *ACS Nano.* **9**(7), pp.7266-7276.

Perry, D., Momotenko, D., Lazenby, R.A., Kang, M. and Unwin, P.R. 2016a. Characterization of Nanopipettes. *Analytical Chemistry.* **88**(10), pp.5523-5530.

Perry, D., Page, A., Chen, B., Frenguelli, B.G. and Unwin, P.R. 2017. Differential-Concentration Scanning Ion Conductance Microscopy. *Analytical Chemistry.* **89**(22), pp.12458-12465.

Perry, D., Paulose Nadappuram, B., Momotenko, D., Voyias, P.D., Page, A., Tripathi, G., Frenguelli, B.G. and Unwin, P.R. 2016b. Surface Charge Visualization at Viable Living Cells. *Journal of the American Chemical Society.* **138**(9), pp.3152-3160.

Persson, H., Køber, C., Mølhave, K., Samuelson, L., Tegenfeldt, J.O., Oredsson, S. and Prinz, C.N. 2013. Fibroblasts Cultured on Nanowires Exhibit Low Motility, Impaired Cell Division, and DNA Damage. *Small.* **9**(23), pp.4006-4016.

Persson, H., Li, Z., Tegenfeldt, J.O., Oredsson, S. and Prinz, C.N. 2015. From immobilized cells to motile cells on a bed-of-nails: effects of vertical nanowire array density on cell behaviour. *Scientific Reports.* **5**(1), p18535.

Pieri, L., Madiona, K., Bousset, L. and Melki, R. 2012. Fibrillar α-Synuclein and Huntingtin Exon 1 Assemblies Are Toxic to the Cells. *Biophysical Journal.* **102**(12), pp.2894-2905.

Plesa, C., Kowalczyk, S.W., Zinsmeester, R., Grosberg, A.Y., Rabin, Y. and Dekker, C. 2013. Fast translocation of proteins through solid state nanopores. *Nano Letters.* **13**(2), pp.658-663.

Plett, T.S., Cai, W., Le Thai, M., Vlassiouk, I.V., Penner, R.M. and Siwy, Z.S. 2017. Solid-State Ionic Diodes Demonstrated in Conical Nanopores. *The Journal of Physical Chemistry C.* **121**(11), pp.6170-6176.

Porter, K.R., Fonte, V. and Weiss, G. 1974. A scanning microscope study of the topography of HeLa cells. *Cancer Res.* **34**(6), pp.1385-1394.

Poudel, L., Podgornik, R. and Ching, W.-Y. 2017. The Hydration Effect and Selectivity of Alkali Metal Ions on Poly(ethylene glycol) Models in Cyclic and Linear Topology. *The Journal of Physical Chemistry A.* **121**(24), pp.4721-4731.

Qi, L.S., Larson, M.H., Gilbert, L.A., Doudna, J.A., Weissman, J.S., Arkin, A.P. and Lim, W.A. 2013. Repurposing CRISPR as an RNA-guided platform for sequence-specific control of gene expression. *Cell.* **152**(5), pp.1173-1183.

Qian, R.-C., Lv, J. and Long, Y.-T. 2018. Ultrafast Mapping of Subcellular Domains via Nanopipette-Based Electroosmotically Modulated Delivery into a Single Living Cell. *Analytical Chemistry.* **90**(22), pp.13744-13750.

Qian, Z., LaRochelle, J.R., Jiang, B., Lian, W., Hard, R.L., Selner, N.G., Luechapanichkul, R., Barrios, A.M. and Pei, D. 2014. Early endosomal escape of a cyclic cell-

penetrating peptide allows effective cytosolic cargo delivery. *Biochemistry.* **53**(24), pp.4034-4046.

Qiu, H., Yan, H., Tang, J., Zeng, Z. and Liu, P. 2012. A study on the influence of ethanol over the primary cultured rat cortical neurons by using the scanning electron microscopy. *Micron.* **43**(2-3), pp.135-140.

Rabinowitz, J., Edwards, M.A., Whittier, E., Jayant, K. and Shepard, K.L. 2019. Nanoscale Fluid Vortices and Nonlinear Electroosmotic Flow Drive Ion Current Rectification in the Presence of Concentration Gradients. *The Journal of Physical Chemistry A.* **123**(38), pp.8285-8293.

Rahman, M., Stott, M.A., Harrington, M., Li, Y., Sampad, M.J.N., Lancaster, L., Yuzvinsky, T.D., Noller, H.F., Hawkins, A.R. and Schmidt, H. 2019. On demand delivery and analysis of single molecules on a programmable nanopore-optofluidic device. *Nature Communications.* **10**(1), p3712.

Raveendran, M., Leach, A.R., Hopes, T., Aspden, J.L. and Actis, P. 2020a. Ribosome Fingerprinting with a Solid-State Nanopore. *ACS Sensors.* **5**(11), pp.3533-3539.

Raveendran, M., Lee, A.J., Sharma, R., Wälti, C. and Actis, P. 2020b. Rational design of DNA nanostructures for single molecule biosensing. *Nature Communications.* **11**(1), p4384.

Raveendran, M., Lee, A.J., Wälti, C. and Actis, P. 2018. Analysis of 2D DNA Origami with Nanopipettes. *ChemElectroChem.* **5**(20), pp.3014-3020.

Reiner, J.E., Kasianowicz, J.J., Nablo, B.J. and Robertson, J.W.F. 2010. Theory for polymer analysis using nanopore-based single-molecule mass spectrometry. *Proceedings of the National Academy of Sciences.* **107**(27), pp.12080-12085.

Ren, C.-l., Tian, W.-d., Szleifer, I. and Ma, Y.-q. 2011. Specific Salt Effects on Poly(ethylene oxide) Electrolyte Solutions. *Macromolecules.* **44**(6), pp.1719-1727.

Restrepo-Pérez, L., Wong, C.H., Maglia, G., Dekker, C. and Joo, C. 2019. Label-Free Detection of Post-translational Modifications with a Nanopore. *Nano Letters.* **19**(11), pp.7957-7964.

Rey, N.L., Bousset, L., George, S., Madaj, Z., Meyerdirk, L., Schulz, E., Steiner, J.A., Melki, R. and Brundin, P. 2019. α-Synuclein conformational strains spread, seed and target neuronal cells differentially after injection into the olfactory bulb. *Acta Neuropathologica Communications.* **7**(1).

Rey, N.L., Petit, G.H., Bousset, L., Melki, R. and Brundin, P. 2013. Transfer of human α-synuclein from the olfactory bulb to interconnected brain regions in mice. *Acta Neuropathologica.* **126**(4), pp.555-573.

Rheinlaender, J. and Schäffer, T.E. 2009. Image formation, resolution, and height measurement in scanning ion conductance microscopy. *Journal of Applied Physics.* **105**(9), p094905.

Rheinlaender, J. and Schäffer, T.E. 2013. Mapping the mechanical stiffness of live cells with the scanning ion conductance microscope. *Soft Matter.* **9**(12), p3230.

Rheinlaender, J. and Schäffer, T.E. 2015. Lateral Resolution and Image Formation in Scanning Ion Conductance Microscopy. *Analytical Chemistry.* **87**(14), pp.7117-7124.

Richardson, C.D., Ray, G.J., Bray, N.L. and Corn, J.E. 2016. Non-homologous DNA increases gene disruption efficiency by altering DNA repair outcomes. *Nature Communications.* **7**(1), p12463.

Richter, K., Nessling, M. and Lichter, P. 2008. Macromolecular crowding and its potential impact on nuclear function. *Biochimica et Biophysica Acta (BBA) - Molecular Cell Research.* **1783**(11), pp.2100-2107.

Rivas, G. and Minton, A.P. 2016. Macromolecular Crowding In Vitro , In Vivo , and In Between. *Trends in Biochemical Sciences.* **41**(11), pp.970-981.

Roeters, S.J., Iyer, A., Pletikapić, G., Kogan, V., Subramaniam, V. and Woutersen, S. 2017. Evidence for Intramolecular Antiparallel Beta-Sheet Structure in Alpha-Synuclein Fibrils from a Combination of Two-Dimensional Infrared Spectroscopy and Atomic Force Microscopy. *Scientific Reports.* **7**(1), p41051.

Rosdy, M., Grisoni, B. and Clauss, L.-C. 1991. Proliferation of normal human keratinocytes on silicons substrates. *Biomaterials.* **12**(5), pp.511-517.

Rossi, A., Dahm, R. and Macchi, P. 2017. Transfection of Cultured Primary Neurons. In: S., A.K., et al. eds. *Stem Cell Technologies in Neuroscience. Neuromethods.* Humana Press, New York, NY., pp.55-78.

Rout, M.P., Sali, A., Wente, S.R., Russel, D., Kim, S.J., Trivedi, J.M., Mironska, R., Raveh, B. and Timney, B.L. 2016. Simple rules for passive diffusion through the nuclear pore complex. *Journal of Cell Biology.* **215**(1), pp.57-76.

Rowe, I., Anishkin, A., Kamaraju, K., Yoshimura, K. and Sukharev, S. 2014. The cytoplasmic cage domain of the mechanosensitive channel MscS is a sensor of macromolecular crowding. *Journal of General Physiology.* **143**(5), pp.543-557.

Ruseska, I. and Zimmer, A. 2020. Internalization mechanisms of cell-penetrating peptides. *Beilstein Journal of Nanotechnology.* **11**, pp.101-123.

Sabari, B.R., Dall'Agnese, A. and Young, R.A. 2020. Biomolecular Condensates in the Nucleus. *Trends in Biochemical Sciences.* **45**(11), pp.961-977.

Sang, J.C., Hidari, E., Meisl, G., Ranasinghe, R.T., Spillantini, M.G. and Klenerman, D. 2021. Super-resolution imaging reveals α-synuclein seeded aggregation in SH-SY5Y cells. *Communications Biology.* **4**(1), p613.

Santra, T.S., Kar, S., Chang, H.-Y. and Tseng, F.-G. 2020. Nano-localized single-cell nano-electroporation. *Lab on a Chip.* **20**(22), pp.4194-4204.

Santra, T.S. and Tseng, F.-G. 2016. Electroporation for Single-Cell Analysis. In: F.G., T. and T., S. eds. *Essentials of Single-Cell Analysis. Series in BioEngineering.* Springer, Berlin, Heidelberg, pp.55-83.

Sarkar, M., Lu, J. and Pielak, G.J. 2014. Protein Crowder Charge and Protein Stability. *Biochemistry.* **53**(10), pp.1601-1606.

Sasaki, Y., Miyoshi, D. and Sugimoto, N. 2006. Effect of molecular crowding on DNA polymerase activity. *Biotechnology Journal.* **1**(4), pp.440-446.

Schierbaum, N., Hack, M., Betz, O. and Schäffer, T.E. 2018. Macro-SICM: A Scanning Ion Conductance Microscope for Large-Range Imaging. *Analytical Chemistry.* **90**(8), pp.5048-5054.

Schmiderer, L., Subramaniam, A., Žemaitis, K., Bäckström, A., Yudovich, D., Soboleva, S., Galeev, R., Prinz, C.N., Larsson, J. and Hjort, M. 2020. Efficient and nontoxic biomolecule delivery to primary human hematopoietic stem cells using nanostraws. *Proceedings of the National Academy of Sciences.* **117**(35), pp.21267-21273.

Schweighauser, M., Shi, Y., Tarutani, A., Kametani, F., Murzin, A.G., Ghetti, B., Matsubara, T., Tomita, T., Ando, T., Hasegawa, K., Murayama, S., Yoshida, M., Hasegawa, M., Scheres, S.H.W. and Goedert, M. 2020. Structures of α-synuclein filaments from multiple system atrophy. *Nature.* **585**(7825), pp.464-469.

Seifert, J., Rheinlaender, J., Novak, P., Korchev, Y.E. and Schäffer, T.E. 2015. Comparison of Atomic Force Microscopy and Scanning Ion Conductance Microscopy for Live Cell Imaging. *Langmuir.* **31**(24), pp.6807-6813.

Sen, O., Saurin, A.T. and Higgins, J.M.G. 2018. The live cell DNA stain SiR-Hoechst induces DNA damage responses and impairs cell cycle progression. *Scientific Reports.* **8**(1), p7898.

Sharp, K.A. 2015. Analysis of the size dependence of macromolecular crowding shows that smaller is better. *Proceedings of the National Academy of Sciences.* **112**(26), pp.7990-7995.

Shekar, S., Niedzwiecki, D.J., Chien, C.-C., Ong, P., Fleischer, D.A., Lin, J., Rosenstein, J.K., Drndić, M. and Shepard, K.L. 2016. Measurement of DNA Translocation Dynamics in a Solid-State Nanopore at 100 ns Temporal Resolution. *Nano Letters.* **16**(7), pp.4483-4489.

Shen, Y., Zhang, Z. and Fukuda, T. 2015. Bending spring rate investigation of nanopipette for cell injection. *Nanotechnology.* **26**(15), p155702.

Shevchuk, A., Tokar, S., Gopal, S., Sanchez-Alonso, Jose L., Tarasov, Andrei I., Vélez-Ortega, A.C., Chiappini, C., Rorsman, P., Stevens, Molly M., Gorelik, J., Frolenkov, Gregory I., Klenerman, D. and Korchev, Yuri E. 2016. Angular Approach Scanning Ion Conductance Microscopy. *Biophysical Journal.* **110**(10), pp.2252-2265.

Shevchuk, A.I., Frolenkov, G.I., Sanchez, D., James, P.S., Freedman, N., Lab, M.J., Jones, R., Klenerman, D. and Korchev, Y.E. 2006. Imaging Proteins in Membranes of Living Cells by High-Resolution Scanning Ion Conductance Microscopy. *Angewandte Chemie International Edition.* **45**(14), pp.2212-2216.

Shevchuk, A.I., Novak, P., Taylor, M., Diakonov, I.A., Ziyadeh-Isleem, A., Bitoun, M., Guicheney, P., Lab, M.J., Gorelik, J., Merrifield, C.J., Klenerman, D. and Korchev, Y.E.

2012. An alternative mechanism of clathrin-coated pit closure revealed by ion conductance microscopy. *The Journal of Cell Biology.* **197**(4), pp.499-508.

Shigyou, K., Sun, L., Yajima, R., Takigaura, S., Tajima, M., Furusho, H., Kikuchi, Y., Miyazawa, K., Fukuma, T., Taoka, A., Ando, T. and Watanabe, S. 2020. Geometrical Characterization of Glass Nanopipettes with Sub-10 nm Pore Diameter by Transmission Electron Microscopy. *Analytical Chemistry.* **92**(23), pp.15388-15393.

Shiotari, A. and Sugimoto, Y. 2017. Ultrahigh-resolution imaging of water networks by atomic force microscopy. *Nature Communications.* **8**(1), p14313.

Shu, Z., Chen, H.H., Zhou, X. and Gao, D. 2017. Assessment of Cryoprotectant Concentration by Electrical Conductivity Measurement and Its Applications in Cryopreservation. In: Shahat, A.E. ed. *Electrical Resistivity and Conductivity.* IntechOpen.

Si, W. and Aksimentiev, A. 2017. Nanopore Sensing of Protein Folding. *ACS Nano.* **11**(7), pp.7091-7100.

Sicorello, A., Torrassa, S., Soldi, G., Gianni, S., Travaglini-Allocatelli, C., Taddei, N., Relini, A. and Chiti, F. 2009. Agitation and High Ionic Strength Induce Amyloidogenesis of a Folded PDZ Domain in Native Conditions. *Biophysical Journal.* **96**(6), pp.2289-2298.

Simonis, M., Hubner, W., Wilking, A., Huser, T. and Hennig, S. 2017. Survival rate of eukaryotic cells following electrophoretic nanoinjection. *Scientific Reports.* **7**(1), p41277.

Simonis, M., Sandmeyer, A., Greiner, J., Kaltschmidt, B., Huser, T. and Hennig, S. 2019. MoNa - A Cost-Efficient, Portable System for the Nanoinjection of Living Cells. *Scientific Reports.* **9**(1), p5480.

Singh, S., Dwarakanath, B.S. and Mathew, T.L. 2004. DNA ligand Hoechst-33342 enhances UV induced cytotoxicity in human glioma cell lines. *Journal of Photochemistry and Photobiology B: Biology.* **77**(1-3), pp.45-54.

Singhal, R., Orynbayeva, Z., Kalyana Sundaram, R.V., Niu, J.J., Bhattacharyya, S., Vitol, E.A., Schrlau, M.G., Papazoglou, E.S., Friedman, G. and Gogotsi, Y. 2011. Multifunctional carbon-nanotube cellular endoscopes. *Nature Nanotechnology.* **6**(1), pp.57-64.

Siwy, Z., Heins, E., Harrell, C.C., Kohli, P. and Martin, C.R. 2004. Conical-Nanotube Ion-Current Rectifiers: The Role of Surface Charge. *Journal of the American Chemical Society.* **126**(35), pp.10850-10851.

Smeets, R.M.M., Keyser, U.F., Krapf, D., Wu, M.-Y., Dekker, N.H. and Dekker, C. 2006. Salt Dependence of Ion Transport and DNA Translocation through Solid-State Nanopores. *Nano Letters.* **6**(1), pp.89-95.

Smith, K.C., Son, R.S., Gowrishankar, T.R. and Weaver, J.C. 2014. Emergence of a large pore subpopulation during electroporating pulses. *Bioelectrochemistry.* **100**, pp.3-10.

Smith, R.A. and McInnes, I.B. 1986. Phase contrast and electron microscopical observations of adult mouse dorsal root ganglion cells maintained in primary culture. *J Anat.* **145**, pp.1-12.

Smith, S.A., Selby, L.I., Johnston, A.P.R. and Such, G.K. 2018. The Endosomal Escape of Nanoparticles: Toward More Efficient Cellular Delivery. *Bioconjugate Chemistry.* **30**(2), pp.263-272.

So, C., Seres, K.B., Steyer, A.M., Mönnich, E., Clift, D., Pejkovska, A., Möbius, W. and Schuh, M. 2019. A liquid-like spindle domain promotes acentrosomal spindle assembly in mammalian oocytes. *Science.* **364**(6447), peaat9557.

Song, L., Hobaugh, M.R., Shustak, C., Cheley, S., Bayley, H. and Gouaux, J.E. 1996. Structure of Staphylococcal alpha -Hemolysin, a Heptameric Transmembrane Pore. *Science.* **274**(5294), pp.1859-1865.

Spillantini, M.G., Schmidt, M.L., Lee, V.M.Y., Trojanowski, J.Q., Jakes, R. and Goedert, M. 1997. α-Synuclein in Lewy bodies. *Nature.* **388**(6645), pp.839-840.

Spitzer, J. 2011. From Water and Ions to Crowded Biomacromolecules: In Vivo Structuring of a Prokaryotic Cell. *Microbiology and Molecular Biology Reviews.* **75**(3), pp.491-506.

Stagg, L., Zhang, S.Q., Cheung, M.S. and Wittung-Stafshede, P. 2007. Molecular crowding enhances native structure and stability of α/β protein flavodoxin. *Proceedings of the National Academy of Sciences.* **104**(48), pp.18976-18981.

Stanley, J. and Pourmand, N. 2020. Nanopipettes—The past and the present. *APL Materials.* **8**(10), p100902.

Steinbock, L.J., Otto, O., Chimerel, C., Gornall, J. and Keyser, U.F. 2010. Detecting DNA Folding with Nanocapillaries. *Nano Letters.* **10**(7), pp.2493-2497.

Stewart, M. 2007. Molecular mechanism of the nuclear protein import cycle. *Nature Reviews Molecular Cell Biology.* **8**(3), pp.195-208.

Stewart, M.P., Langer, R. and Jensen, K.F. 2018. Intracellular Delivery by Membrane Disruption: Mechanisms, Strategies, and Concepts. *Chem Rev.* **118**(16), pp.7409-7531.

Stiefel, P., Schmidt, F.I., Dörig, P., Behr, P., Zambelli, T., Vorholt, J.A. and Mercer, J. 2012. Cooperative Vaccinia Infection Demonstrated at the Single-Cell Level Using FluidFM. *Nano Letters.* **12**(8), pp.4219-4227.

Stoddart, D., Heron, A.J., Mikhailova, E., Maglia, G. and Bayley, H. 2009. Single-nucleotide discrimination in immobilized DNA oligonucleotides with a biological nanopore. *Proceedings of the National Academy of Sciences.* **106**(19), pp.7702-7707.

Stojilkovic, K.S., Berezhkovskii, A.M., Zitserman, V.Y. and Bezrukov, S.M. 2003. Conductivity and microviscosity of electrolyte solutions containing polyethylene glycols. *The Journal of Chemical Physics.* **119**(13), pp.6973-6978.

Stuart, T. and Satija, R. 2019. Integrative single-cell analysis. *Nature Reviews Genetics.* **20**(5), pp.257-272.

Sze, J.Y.Y., Ivanov, A.P., Cass, A.E.G. and Edel, J.B. 2017. Single molecule multiplexed nanopore protein screening in human serum using aptamer modified DNA carriers. *Nature Communications.* **8**(1), p1552.

Takahashi, Y., Murakami, Y., Nagamine, K., Shiku, H., Aoyagi, S., Yasukawa, T., Kanzaki, M. and Matsue, T. 2010. Topographic imaging of convoluted surface of live cells by scanning ion conductance microscopy in a standing approach mode. *Physical Chemistry Chemical Physics.* **12**(34), p10012.

Takahashi, Y., Zhou, Y., Miyamoto, T., Higashi, H., Nakamichi, N., Takeda, Y., Kato, Y., Korchev, Y. and Fukuma, T. 2019. High-Speed SICM for the Visualization of Nanoscale Dynamic Structural Changes in Hippocampal Neurons. *Analytical Chemistry.* **92**(2), pp.2159-2167.

Talaga, D.S. and Li, J. 2009. Single-Molecule Protein Unfolding in Solid State Nanopores. *Journal of the American Chemical Society.* **131**(26), pp.9287-9297.

Tanaka, K., Caaveiro, J.M.M., Morante, K., González-Mañas, J.M. and Tsumoto, K. 2015. Structural basis for self-assembly of a cytolytic pore lined by protein and lipid. *Nature Communications.* **6**(1), p6337.

Tanenbaum, M.E., Gilbert, L.A., Qi, L.S., Weissman, J.S. and Vale, R.D. 2014. A protein-tagging system for signal amplification in gene expression and fluorescence imaging. *Cell.* **159**(3), pp.635-646.

Tang, R., Kim, C.S., Solfiell, D.J., Rana, S., Mout, R., Velázquez-Delgado, E.M., Chompoosor, A., Jeong, Y., Yan, B., Zhu, Z.-J., Kim, C., Hardy, J.A. and Rotello, V.M. 2013. Direct Delivery of Functional Proteins and Enzymes to the Cytosol Using Nanoparticle-Stabilized Nanocapsules. *ACS Nano.* **7**(8), pp.6667-6673.

Tanzella, F.L., Bailey, W., Frydrych, D., Farrington, G.C. and Story, H.S. 1981. Ion transport in peo-alkali salt complex polymeric electrolytes. *Solid State Ionics.* **5**, pp.681-684.

Tao, Z. and Cummings, P.T. 2007. Molecular dynamics simulation of inorganic ions in PEO aqueous solution. *Molecular Simulation.* **33**(15), pp.1255-1260.

Tasaki, K. 1996. Poly(oxyethylene)−Water Interactions: A Molecular Dynamics Study. *Journal of the American Chemical Society.* **118**(35), pp.8459-8469.

Tasaki, K. 1999. Poly(oxyethylene)–cation interactions in aqueous solution: a molecular dynamics study. *Computational and Theoretical Polymer Science.* **9**(3-4), pp.271-284.

Tay, A. and Melosh, N. 2019. Transfection with Nanostructure Electro-Injection is Minimally Perturbative. *Advanced Therapeutics.* **2**(12), p1900133.

Törnquist, M., Michaels, T.C.T., Sanagavarapu, K., Yang, X., Meisl, G., Cohen, S.I.A., Knowles, T.P.J. and Linse, S. 2018. Secondary nucleation in amyloid formation. *Chemical Communications.* **54**(63), pp.8667-8684.

Torres-Perez, J.V., Naeem, H., Thompson, C.L., Knight, M.M. and Novak, P. 2020. Nanoscale Mapping Reveals Functional Differences in Ion Channels Populating the Membrane of Primary Cilia. *Cell Physiol Biochem.* **54**(1), pp.15-26.

Tóth, E.N., Lohith, A., Mondal, M., Guo, J., Fukamizu, A. and Pourmand, N. 2018. Single-cell nanobiopsy reveals compartmentalization of mRNAs within neuronal cells. *Journal of Biological Chemistry.* **293**(13), pp.4940-4951.

Tseng, S., Lin, S.-C., Lin, C.-Y. and Hsu, J.-P. 2016. Influences of Cone Angle and Surface Charge Density on the Ion Current Rectification Behavior of a Conical Nanopore. *The Journal of Physical Chemistry C.* **120**(44), pp.25620-25627.

Tuttle, M.D., Comellas, G., Nieuwkoop, A.J., Covell, D.J., Berthold, D.A., Kloepper, K.D., Courtney, J.M., Kim, J.K., Barclay, A.M., Kendall, A., Wan, W., Stubbs, G., Schwieters, C.D., Lee, V.M.Y., George, J.M. and Rienstra, C.M. 2016. Solid-state NMR structure of a pathogenic fibril of full-length human α-synuclein. *Nature Structural & Molecular Biology.* **23**(5), pp.409-415.

Umehara, S., Pourmand, N., Webb, C.D., Davis, R.W., Yasuda, K. and Karhanek, M. 2006. Current Rectification with Poly-l-Lysine-Coated Quartz Nanopipettes. *Nano Letters.* **6**(11), pp.2486-2492.

Ushiki, T., Nakajima, M., Choi, M., Cho, S.-J. and Iwata, F. 2012. Scanning ion conductance microscopy for imaging biological samples in liquid: A comparative study with atomic force microscopy and scanning electron microscopy. *Micron.* **43**(12), pp.1390-1398.

Usov, I. and Mezzenga, R. 2015. FiberApp: An Open-Source Software for Tracking and Analyzing Polymers, Filaments, Biomacromolecules, and Fibrous Objects. *Macromolecules.* **48**(5), pp.1269-1280.

van den Berg, J., Boersma, A.J. and Poolman, B. 2017. Microorganisms maintain crowding homeostasis. *Nature Reviews Microbiology.* **15**(5), pp.309-318.

VanDersarl, J.J., Xu, A.M. and Melosh, N.A. 2012. Nanostraws for direct fluidic intracellular access. *Nano Letters.* **12**(8), pp.3881-3886.

Vaquer-Alicea, J. and Diamond, M.I. 2019. Propagation of Protein Aggregation in Neurodegenerative Diseases. *Annual Review of Biochemistry.* **88**(1), pp.785-810.

Varongchayakul, N., Song, J., Meller, A. and Grinstaff, M.W. 2018. Single-molecule protein sensing in a nanopore: a tutorial. *Chemical Society Reviews.* **47**(23), pp.8512-8524.

Venslauskas, M.S. and Satkauskas, S. 2015. Mechanisms of transfer of bioactive molecules through the cell membrane by electroporation. *Eur Biophys J.* **44**(5), pp.277-289.

Vivekananda, U., Novak, P., Bello, O.D., Korchev, Y.E., Krishnakumar, S.S., Volynski, K.E. and Kullmann, D.M. 2017. Kv1.1 channelopathy abolishes presynaptic spike width modulation by subthreshold somatic depolarization. *Proceedings of the National Academy of Sciences.* **114**(9), pp.2395-2400.

Voelkel, C., Galla, M., Maetzig, T., Warlich, E., Kuehle, J., Zychlinski, D., Bode, J., Cantz, T., Schambach, A. and Baum, C. 2010. Protein transduction from retroviral Gag precursors. *Proceedings of the National Academy of Sciences.* **107**(17), pp.7805-7810.

Wang, H.X., Li, M., Lee, C.M., Chakraborty, S., Kim, H.W., Bao, G. and Leong, K.W. 2017. CRISPR/Cas9-Based Genome Editing for Disease Modeling and Therapy: Challenges and Opportunities for Nonviral Delivery. *Chemical Reviews.* **117**(15), pp.9874-9906.

Wang, J., Zhang, M., Zhai, J. and Jiang, L. 2014. Theoretical simulation of the ion current rectification (ICR) in nano-pores based on the Poisson-Nernst-Planck (PNP) model. *Phys Chem Chem Phys.* **16**(1), pp.23-32.

Wang, M., Wu, B., Shah, S.N., Lu, P. and Lu, Q. 2018. Saponins as Natural Adjuvant for Antisense Morpholino Oligonucleotides Delivery In Vitro and in mdx Mice. *Molecular Therapy - Nucleic Acids.* **11**, pp.192-202.

Wang, P., Yu, I., Feig, M. and Sugita, Y. 2017. Influence of protein crowder size on hydration structure and dynamics in macromolecular crowding. *Chemical Physics Letters.* **671**, pp.63-70.

Wang, S., Zhao, Z., Haque, F. and Guo, P. 2018. Engineering of protein nanopores for sequencing, chemical or protein sensing and disease diagnosis. *Current Opinion in Biotechnology.* **51**, pp.80-89.

Wang, V., Ermann, N. and Keyser, U.F. 2019. Current Enhancement in Solid-State Nanopores Depends on Three-Dimensional DNA Structure. *Nano Letters.* **19**(8), pp.5661-5666.

Wang, X., Wilkinson, M.D., Lin, X., Ren, R., Willison, K.R., Ivanov, A.P., Baum, J. and Edel, J.B. 2020. Single-molecule nanopore sensing of actin dynamics and drug binding. *Chemical Science.* **11**(4), pp.970-979.

Wanunu, M., Liu, Q., Wu, H., Wu, L., Xie, X., Kong, J., Ye, X. and Liu, L. 2012. Voltage-Driven Translocation of DNA through a High Throughput Conical Solid-State Nanopore. *PLOS ONE.* **7**(9), pe46014.

Wanunu, M., Morrison, W., Rabin, Y., Grosberg, A.Y. and Meller, A. 2009. Electrostatic focusing of unlabelled DNA into nanoscale pores using a salt gradient. *Nature Nanotechnology.* **5**(2), pp.160-165.

Wei, R., Martin, T.G., Rant, U. and Dietz, H. 2012. DNA Origami Gatekeepers for Solid-State Nanopores. *Angewandte Chemie International Edition.* **51**(20), pp.4864-4867.

White, H.S. and Bund, A. 2008. Ion Current Rectification at Nanopores in Glass Membranes. *Langmuir.* **24**(5), pp.2212-2218.

White, J.M. and Whittaker, G.R. 2016. Fusion of Enveloped Viruses in Endosomes. *Traffic.* **17**(6), pp.593-614.

Witt, S.N., Domert, J., Sackmann, C., Severinsson, E., Agholme, L., Bergström, J., Ingelsson, M. and Hallbeck, M. 2016. Aggregated Alpha-Synuclein Transfer Efficiently between Cultured Human Neuron-Like Cells and Localize to Lysosomes. *Plos One.* **11**(12), pe0168700.

Wloka, C., Van Meervelt, V., van Gelder, D., Danda, N., Jager, N., Williams, C.P. and Maglia, G. 2017. Label-Free and Real-Time Detection of Protein Ubiquitination with a Biological Nanopore. *ACS Nano.* **11**(5), pp.4387-4394.

Wörheide, M.A., Krumsiek, J., Kastenmüller, G. and Arnold, M. 2021. Multi-omics integration in biomedical research – A metabolomics-centric review. *Analytica Chimica Acta.* **1141**, pp.144-162.

Wu, G., Homann, S., Hofmann, C., Gorin, A.M., Nguyen, H.C.X., Huynh, D., Hamid, P., Maithel, N., Yacoubian, V., Mu, W., Kossyvakis, A., Sen Roy, S., Yang, O.O. and Kelesidis, T. 2017. A novel rapid and reproducible flow cytometric method for optimization of transfection efficiency in cells. *PLOS ONE.* **12**(9), pe0182941.

Wu, L., Liu, H., Zhao, W., Wang, L., Hou, C., Liu, Q. and Lu, Z. 2014. Electrically facilitated translocation of protein through solid nanopore. *Nanoscale Research Letters.* **9**(1), p140.

Xie, X., Xu, A.M., Leal-Ortiz, S., Cao, Y., Garner, C.C. and Melosh, N.A. 2013. Nanostraw–Electroporation System for Highly Efficient Intracellular Delivery and Transfection. *ACS Nano.* **7**(5), pp.4351-4358.

Xu, A.M., Wang, D.S., Shieh, P., Cao, Y. and Melosh, N.A. 2017. Direct Intracellular Delivery of Cell-Impermeable Probes of Protein Glycosylation by Using Nanostraws. *ChemBioChem.* **18**(7), pp.623-628.

Xu, Q. 2018. Review of Microinjection Systems. In: Xu, Q. ed. *Micromachines for Biological Micromanipulation.* Springer, Cham, pp.15-47.

Xu, X., Costa, A. and Burgess, D.J. 2012. Protein Encapsulation in Unilamellar Liposomes: High Encapsulation Efficiency and A Novel Technique to Assess Lipid-Protein Interaction. *Pharmaceutical Research.* **29**(7), pp.1919-1931.

Xue, L., Yamazaki, H., Ren, R., Wanunu, M., Ivanov, A.P. and Edel, J.B. 2020. Solid-state nanopore sensors. *Nature Reviews Materials.* **5**(12), pp.931-951.

Yang, R., Lemaître, V., Huang, C., Haddadi, A., McNaughton, R. and Espinosa, H.D. 2018. Monoclonal Cell Line Generation and CRISPR/Cas9 Manipulation via Single-Cell Electroporation. *Small.* **14**(12), p1702495.

Yao, F., Peng, X., Su, Z., Tian, L., Guo, Y. and Kang, X.F. 2020. Crowding-Induced DNA Translocation through a Protein Nanopore. *Analytical Chemistry.* **92**(5), pp.3827-3833.

Yu, R.-J., Lu, S.-M., Xu, S.-W., Li, Y.-J., Xu, Q., Ying, Y.-L. and Long, Y.-T. 2019. Single molecule sensing of amyloid-β aggregation by confined glass nanopores. *Chemical Science.* **10**(46), pp.10728-10732.

Yusko, E.C., An, R. and Mayer, M. 2009. Electroosmotic Flow Can Generate Ion Current Rectification in Nano- and Micropores. *ACS Nano.* **4**(1), pp.477-487.

Yusko, E.C., Bruhn, B.R., Eggenberger, O.M., Houghtaling, J., Rollings, R.C., Walsh, N.C., Nandivada, S., Pindrus, M., Hall, A.R., Sept, D., Li, J., Kalonia, D.S. and Mayer, M. 2017. Real-time shape approximation and fingerprinting of single proteins using a nanopore. *Nature Nanotechnology.* **12**(4), pp.360-367.

Yusko, E.C., Johnson, J.M., Majd, S., Prangkio, P., Rollings, R.C., Li, J., Yang, J. and Mayer, M. 2011. Controlling protein translocation through nanopores with bio-inspired fluid walls. *Nature Nanotechnology.* **6**(4), pp.253-260.

Yusko, E.C., Prangkio, P., Sept, D., Rollings, R.C., Li, J. and Mayer, M. 2012. Single-Particle Characterization of Aβ Oligomers in Solution. *ACS Nano.* **6**(7), pp.5909-5919.

Zdanowicz, M. and Chroboczek, J. 2016. Virus-like particles as drug delivery vectors. *Acta Biochim Pol.* **63**(3), pp.469-473.

Zhang, D., Wu, L., Chen, J. and Liang, Y. 2012. Effects of macromolecular crowding on the structural stability of human α-lactalbumin. *Acta Biochimica et Biophysica Sinica.* **44**(8), pp.703-711.

Zhang, Y., Takahashi, Y., Hong, S.P., Liu, F., Bednarska, J., Goff, P.S., Novak, P., Shevchuk, A., Gopal, S., Barozzi, I., Magnani, L., Sakai, H., Suguru, Y., Fujii, T., Erofeev, A., Gorelkin, P., Majouga, A., Weiss, D.J., Edwards, C., Ivanov, A.P., Klenerman, D., Sviderskaya, E.V., Edel, J.B. and Korchev, Y. 2019. High-resolution label-free 3D mapping of extracellular pH of single living cells. *Nature Communications.* **10**(1), p5610.

Zhang, Y., Wu, G., Si, W., Ma, J., Yuan, Z., Xie, X., Liu, L., Sha, J., Li, D. and Chen, Y. 2017. Ionic current modulation from DNA translocation through nanopores under high ionic strength and concentration gradients. *Nanoscale.* **9**(2), pp.930-939.

Zhang, Z., Ohl, M., Diallo, S.O., Jalarvo, N.H., Hong, K., Han, Y., Smith, G.S. and Do, C. 2015. Dynamics of Water Associated with Lithium Ions Distributed in Polyethylene Oxide. *Physical Review Letters.* **115**(19).

Zhao, D., Huang, D., Li, Y., Wu, M., Zhong, W., Cheng, Q., Wang, X., Wu, Y., Zhou, X., Wei, Z., Li, Z. and Liang, Z. 2016. A Flow-Through Cell Electroporation Device for Rapidly and Efficiently Transfecting Massive Amounts of Cells in vitro and ex vivo. *Scientific Reports.* **6**(1), p18469.

Zhao, H., Traganos, F., Dobrucki, J., Wlodkowic, D. and Darzynkiewicz, Z. 2009. Induction of DNA damage response by the supravital probes of nucleic acids. *Cytometry Part A.* **75A**(6), pp.510-519.

Zhou, D., Shanmukaraj, D., Tkacheva, A., Armand, M. and Wang, G. 2019. Polymer Electrolytes for Lithium-Based Batteries: Advances and Prospects. *Chem.* **5**(9), pp.2326-2352.

Zhou, L., Gong, Y., Hou, J. and Baker, L.A. 2017. Quantitative Visualization of Nanoscale Ion Transport. *Analytical Chemistry.* **89**(24), pp.13603-13609.

Zhou, L., Gong, Y., Sunq, A., Hou, J. and Baker, L.A. 2016. Capturing Rare Conductance in Epithelia with Potentiometric-Scanning Ion Conductance Microscopy. *Analytical Chemistry.* **88**(19), pp.9630-9637.

Zhou, Y., Saito, M., Miyamoto, T., Novak, P., Shevchuk, A.I., Korchev, Y.E., Fukuma, T. and Takahashi, Y. 2018. Nanoscale Imaging of Primary Cilia with Scanning Ion Conductance Microscopy. *Analytical Chemistry.* **90**(4), pp.2891-2895.

Zhu, C., Huang, K., Siepser, N.P. and Baker, L.A. 2020. Scanning Ion Conductance Microscopy. *Chemical Reviews.*

Zhu, T., Luo, C., Huang, J., Xiong, C., Ouyang, Q. and Fang, J. 2009. Electroporation based on hydrodynamic focusing of microfluidics with low dc voltage. *Biomedical Microdevices.* **12**(1), pp.35-40.

Ziębacz, N., Wieczorek, S.A., Kalwarczyk, T., Fiałkowski, M. and Hołyst, R. 2011. Crossover regime for the diffusion of nanoparticles in polyethylene glycol solutions: influence of the depletion layer. *Soft Matter.* **7**(16), p7181.

Zimmerman, S.B. and Trach, S.O. 1991. Estimation of macromolecule concentrations and excluded volume effects for the cytoplasm of Escherichia coli. *Journal of Molecular Biology.* **222**(3), pp.599-620.

Zinchenko, A., Chen, Q., Berezhnoy, N.V., Wang, S. and Nordenskiöld, L. 2020. Compaction and self-association of megabase-sized chromatin are induced by anionic protein crowding. *Soft Matter.* **16**(18), pp.4366-4372.

Appendix – A

The following pages contains information that is related to Chapter 3 Section 0 Figure 3.35. Figure 3.35 shows eight scatter plots that are associated with another eight attempts of β-galactosidase quantitative nanoinjection. Here the before and after injection fluorescent images of these eight nanoinjection attempts are shown (Appendix Figure 1 to Appendix Figure 8). The nanoinjection traces are also shown alongside the associated population scatter plots.

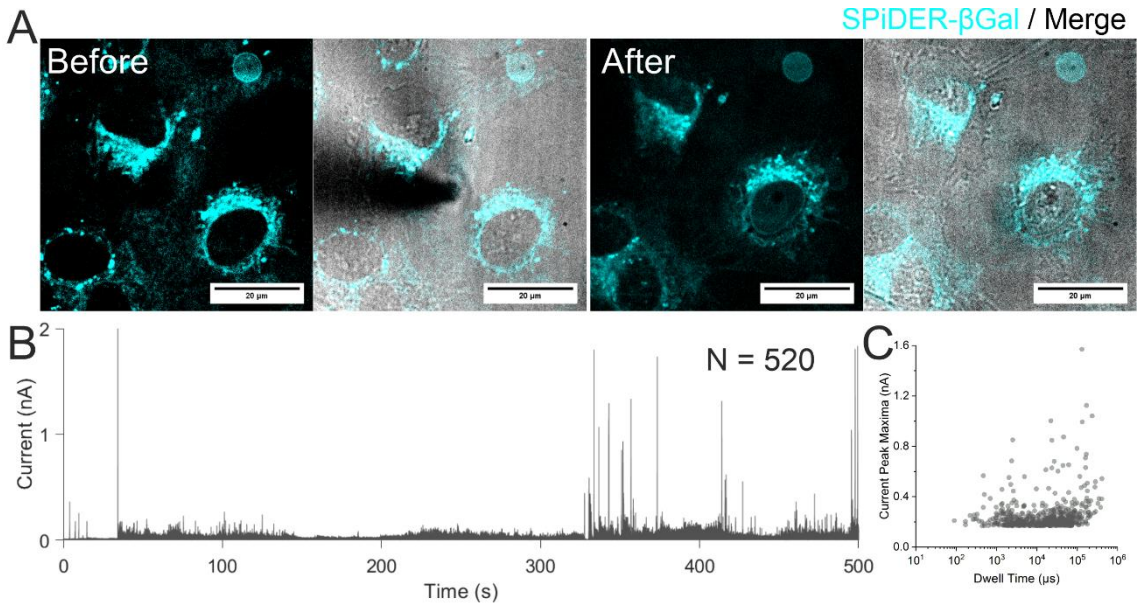

Appendix Figure 1. Intracellular quantitative nanoinjection of the enzyme β-galactosidase – 1. *The purified β-galatosidase was diluted to 1 µM with PBS was used to fill the nanopipette. The SPiDER-βGal was added to the SICM imaging buffer at a final concentration of 2 µM. (A) Fluorescent and brightfield images of the SPiDER-βGal channel and brightfield were taken before the nanoinjection. Once inside the cell, a voltage of -700 mV was used to deliver the β-galactosidase into the nucleus. The fluorescent and brightfield images were taken after the nanoinjection. (B) 520 molecules were recorded from the current trace during the injection and (C) the population scatter produced from the trace.*

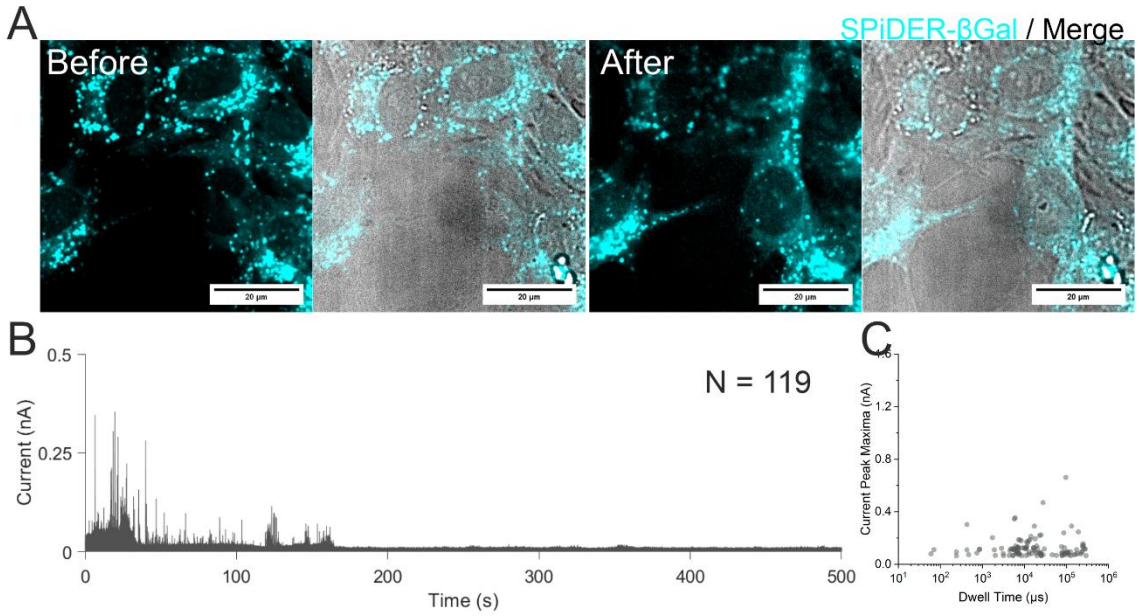

Appendix Figure 2. Intracellular quantitative nanoinjection of the enzyme β-galactosidase – 2. *The purified β-galatosidase was diluted to 1 µM with PBS was used to fill the nanopipette. The SPiDER-βGal was added to the SICM imaging buffer at a final concentration of 2 µM. (A) Fluorescent and brightfield images of the SPiDER-βGal channel and brightfield were taken before the nanoinjection. Once inside the cell, a voltage of -700 mV was used to deliver the β-galactosidase into the nucleus. The fluorescent and brightfield images were taken after the nanoinjection. (B) 119 molecules were recorded from the current trace during the injection and (C) the population scatter produced from the trace.*

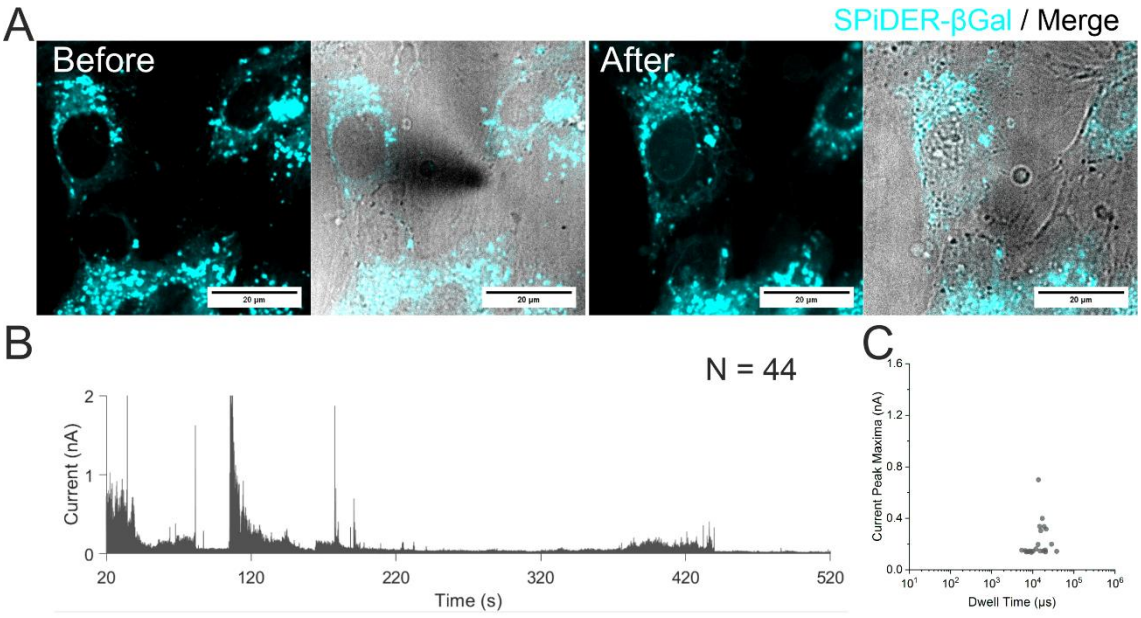

Appendix Figure 3. Intracellular quantitative nanoinjection of the enzyme β-galactosidase – 1. *The purified β-galatosidase was diluted to 1 µM with PBS was used to fill the nanopipette. The SPiDER-βGal was added to the SICM imaging buffer at a final concentration of 2 µM. (A) Fluorescent and brightfield images of the SPiDER-βGal channel and brightfield were taken before the nanoinjection. Once inside the cell, a voltage of -700 mV was used to deliver the β-galactosidase into the nucleus. The fluorescent and brightfield images were taken after the nanoinjection. (B) 44 molecules were recorded from the current trace during the injection and (C) the population scatter produced from the trace.*

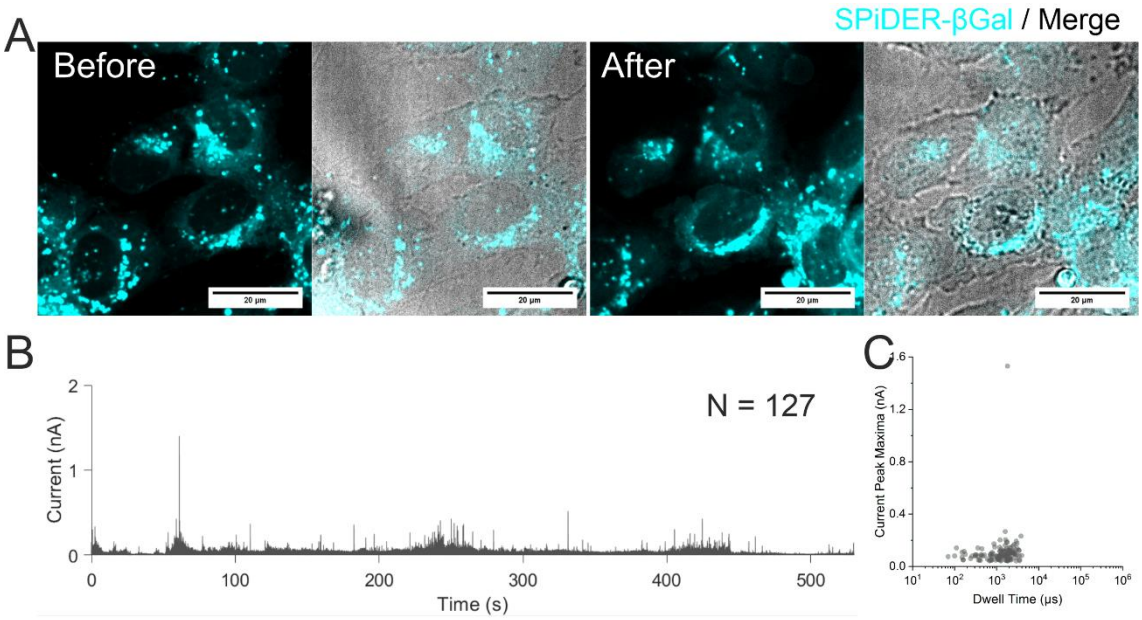

Appendix Figure 4. Intracellular quantitative nanoinjection of the enzyme β-galactosidase – 1. *The purified β-galatosidase was diluted to 1 µM with PBS was used to fill the nanopipette. The SPiDER-βGal was added to the SICM imaging buffer at a final concentration of 2 µM. (A) Fluorescent and brightfield images of the SPiDER-βGal channel and brightfield were taken before the nanoinjection. Once inside the cell, a voltage of -700 mV was used to deliver the β-galactosidase into the nucleus. The fluorescent and brightfield images were taken after the nanoinjection. (B) 127 molecules were recorded from the current trace during the injection and (C) the population scatter produced from the trace.*

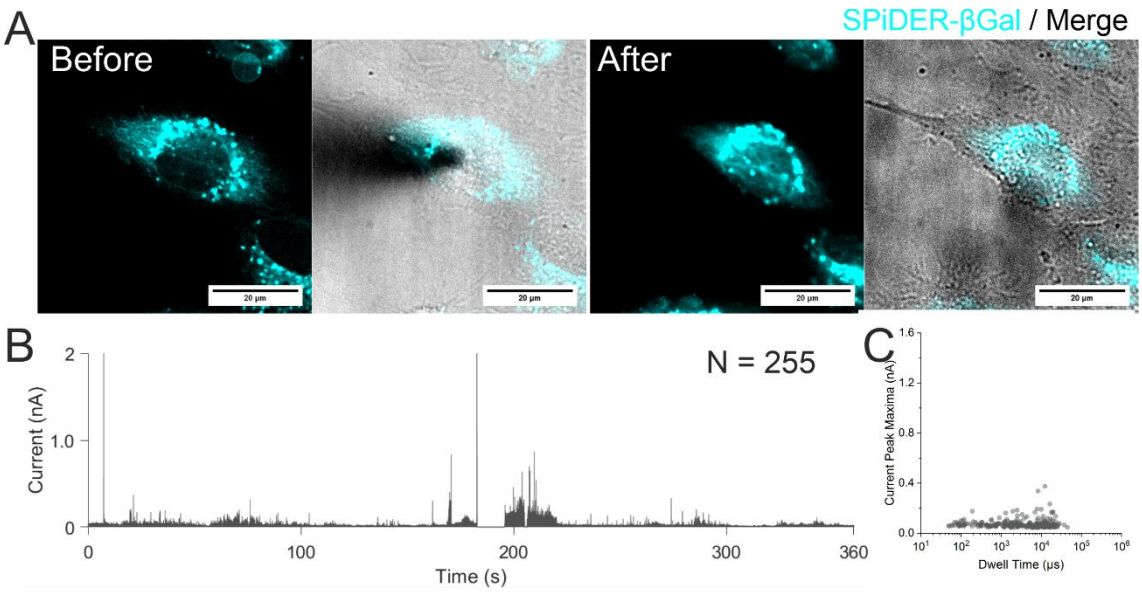

Appendix Figure 5. Intracellular quantitative nanoinjection of the enzyme β-galactosidase – 1. *The purified β-galatosidase was diluted to 1 µM with PBS was used to fill the nanopipette. The SPiDER-βGal was added to the SICM imaging buffer at a final concentration of 2 µM. (A) Fluorescent and brightfield images of the SPiDER-βGal channel and brightfield were taken before the nanoinjection. Once inside the cell, a voltage of -700 mV was used to deliver the β-galactosidase into the nucleus. The fluorescent and brightfield images were taken after the nanoinjection. (B) 255 molecules were recorded from the current trace during the injection and (C) the population scatter produced from the trace.*

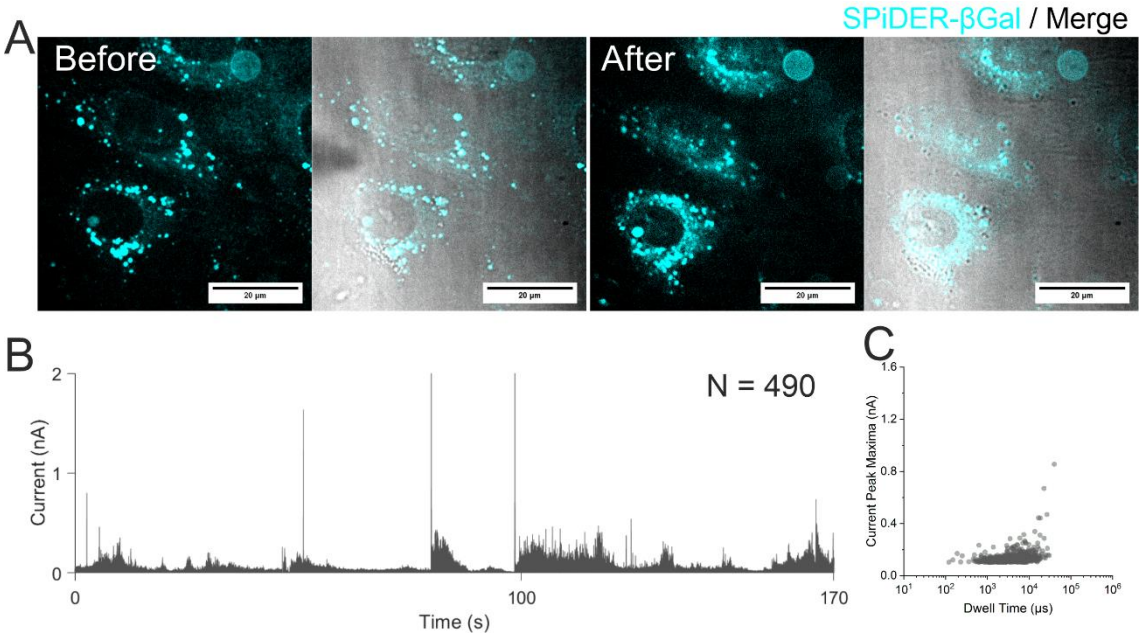

Appendix Figure 6. Intracellular quantitative nanoinjection of the enzyme β-galactosidase – 1. *The purified β-galatosidase was diluted to 1 µM with PBS was used to fill the nanopipette. The SPiDER-βGal was added to the SICM imaging buffer at a final concentration of 2 µM. (A) Fluorescent and brightfield images of the SPiDER-βGal channel and brightfield were taken before the nanoinjection. Once inside the cell, a voltage of -700 mV was used to deliver the β-galactosidase into the nucleus. The fluorescent and brightfield images were taken after the nanoinjection. (B) 490 molecules were recorded from the current trace during the injection and (C) the population scatter produced from the trace.*

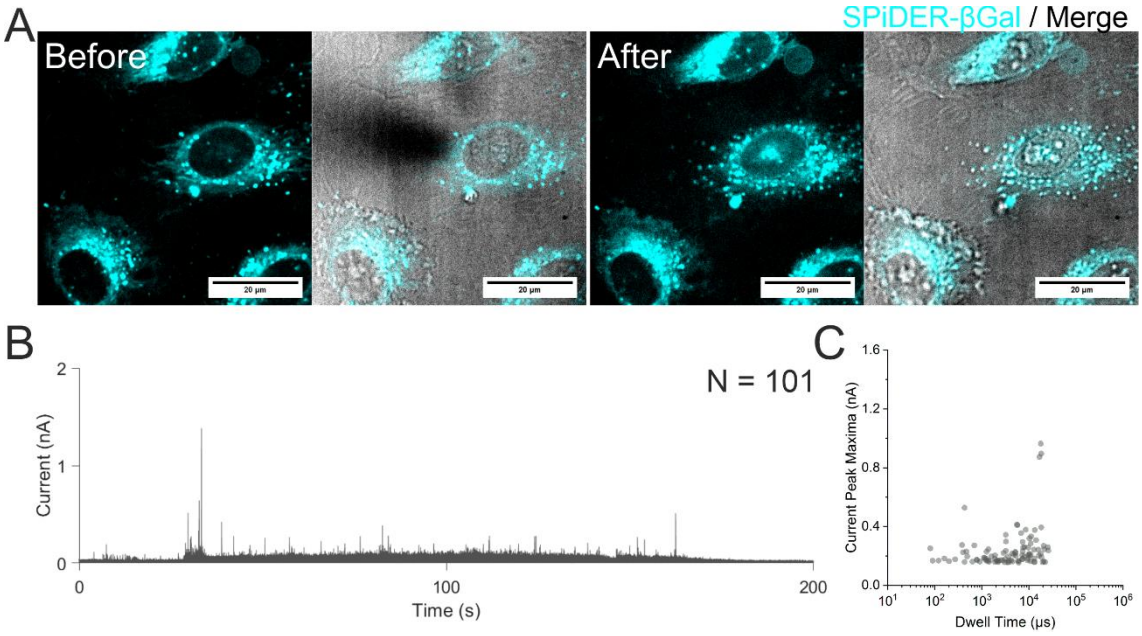

Appendix Figure 7. Intracellular quantitative nanoinjection of the enzyme β-galactosidase – 1. *The purified β-galatosidase was diluted to 1 µM with PBS was used to fill the nanopipette. The SPiDER-βGal was added to the SICM imaging buffer at a final concentration of 2 µM. (A) Fluorescent and brightfield images of the SPiDER-βGal channel and brightfield were taken before the nanoinjection. Once inside the cell, a voltage of -700 mV was used to deliver the β-galactosidase into the nucleus. The fluorescent and brightfield images were taken after the nanoinjection. (B) 101 molecules were recorded from the current trace during the injection and (C) the population scatter produced from the trace.*

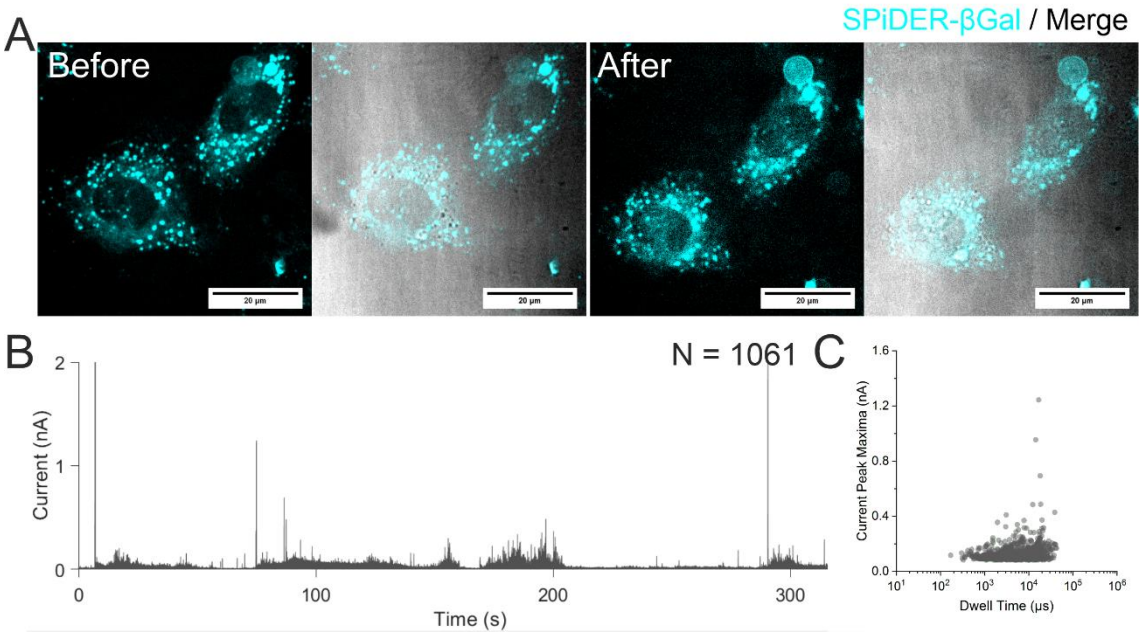

Appendix Figure 8. Intracellular quantitative nanoinjection of the enzyme β-galactosidase – 1. *The purified β-galatosidase was diluted to 1 µM with PBS was used to fill the nanopipette. The SPiDER-βGal was added to the SICM imaging buffer at a final concentration of 2 µM. (A) Fluorescent and brightfield images of the SPiDER-βGal channel and brightfield were taken before the nanoinjection. Once inside the cell, a voltage of -700 mV was used to deliver the β-galactosidase into the nucleus. The fluorescent and brightfield images were taken after the nanoinjection. (B) 1061 molecules were recorded from the current trace during the injection and (C) the population scatter produced from the trace.*